MECHANO-ELECTROCHEMICAL INTERACTIONS AND STOCHASTICS IN INTERCALATION ELECTRODES

A Dissertation

by

PALLAB BARAI

Submitted to the Office of Graduate and Professional Studies of
Texas A&M University
in partial fulfillment of the requirements for the degree of

DOCTOR OF PHILOSOPHY

Chair of Committee,	Partha P. Mukherjee
Committee Members,	Perla Balbuena
	Yalchin Efendiev
	Debjyoti Banerjee
	Kandler Smith
Head of Department,	Andreas A. Polycarpou

December 2015

Major Subject: Mechanical Engineering

ABSTRACT

Lithium ion battery (LIB) is replacing all the other battery chemistries from the portable electronic and automotive market due to its superior energy and power density. During operation, transport of lithium atoms within the active particles through diffusion process induces large amount of diffusion induced stress (DIS). A computational methodology has been developed that is capable of estimating the concentration gradient, subsequent DIS and formation of microcracks within graphite active particles. Nucleation of these microcracks form large spanning cracks, which not only impedes the transport of lithium within the solid phase but also acts as fresh sites for the formation of solid electrolyte interface (SEI). Active particles of smaller size (<5μm) and operation at lower rates experiences negligible capacity fade due to microcrack formation. Damage evolution in brittle media occurs initially in a random fashion and towards the end localized propagation is observed. Grain/grain-boundary microstructures with smaller grain sizes display higher strength against crack propagation.

By solving the dynamic momentum balance equation, the acoustic emission spectra and jump in energy release rate (avalanche), observed in experiments can be predicted. Since only brittle crack propagation is being considered, evolution of mechanical damage happens in the first three cycles, and then saturates. A reduced order model (ROM) has been developed that can predict the amount of mechanical degradation as a function of particle size and rate of operation. A pseudo 2D computational methodology has been demonstrated that can predict the increase in mass

transport resistance and performance decay in lithium ion batteries due to mechanical degradation. Under drive cycle operation, it is safe to use anode particles of radius smaller than 10μm from the capacity fade perspective. Transport of lithium inside high capacity anode materials (such as, Si, Sn) occurs through two phase diffusion process. This gives rise to DIS and fracture at the two phase interface and the particle surface due to high volume expansion. Usage of functionally graded Si with reduced elastic modulus close to the surface is capable of minimizing the microcrack formation. Creep deformation can be significant in Sn active particles during operation at low rates.

This thesis is dedicated to my parents, sister and wife.

ACKNOWLEDGEMENTS

I would like to thank my PhD adviser and mentor, Prof. Partha P. Mukherjee (Mechanical Engineering, TAMU), for his continuous encouragement as well as technical and financial support during my PhD career. I would also like to thank my committee members, Prof. Perla B. Balbuena (Chemical Engineering, TAMU), Prof. Yalchin Efendiev (Department of Mathematics, TAMU), Prof. Debjyoti Banerjee (Mechanical Engineering, TAMU), and Dr. Kandler Smith (National Renewable Energy Laboratory, Golden, CO), for their guidance and support throughout the course of this research. I would also like to convey my special thanks to Dr. Kandler Smith for his kind mentorship and help during my internship at NREL and agreeing to serve as a member in my PhD thesis committee.

Special thanks to my lab mates at ETSL for their kind cooperation and support during the span of my PhD research. Thanks also go to my friends and colleagues and the department faculty and staff for making my time at Texas A&M University a great experience.

Finally, I would like to thank my mother, father and sister for their encouragement and to my wife for her patience and love.

NOMENCLATURE

Chapter II

k_n spring stiffness along the axial direction

k_s spring stiffness along the shear direction

$c\left(\vec{x},t\right)$ space and time dependent Li ion concentration

$\vec{x}$ space domain

t time domain

$\underset{\approx}{D}\left(\vec{x},t\right)$ space and time dependent diffusion coefficient tensor

D_{scalar} constant scalar value of the diffusivity

k_{cond} ionic conductivity

$\vec{n}$ direction normal to the surface

i current over particle surface

F Faraday's constant

$\underset{\approx}{I}$ Identity tensor

$\vec{B}$ body force vector

$\vec{f}$ local force vector

$\vec{u}$ local displacement vector

$\left[T\right]$ transformation tensor

$\vec{F}$ global force vector

$\vec{U}$ global displacement vector

$\left[K_g\right]$ global stiffness matrix

$\left[k_l\right]$ local stiffness matrix

Δc increment in Li ion concentration

l length of spring element

Δu^d diffusion induced displacement

$E\left(c\right)$ concentration dependent Young's modulus

E_0 Young's modulus with zero Li ion concentration

$c_{\max}$ maximum stoichiometric Li ion concentration

k parameter which governs hardening or softening material

V actual cell potential

E_{ocp} open circuit potential

E_{ocp}^0 OCP at the standard state with unit activities

R universal gas constant

T temperature

n number of electrons associated with the reaction

$a_{products}$ activity of products

$a_{reactants}$ activity of reactants

i_0 exchange current density

a activity

k_0 reaction rate constant

Greek

$\underset{\sim}{\sigma}(\bar{x})$ stress tensor

ω diffusion expansion coefficient

Ψ energy in each spring

Ψ_t threshold energy for each spring

α damage parameter for diffusivity

η overpotential

ν_i stoichiometric coefficient

α_t transfer coefficient

Chapter IV

$c(x, y, t)$ spatio-temporal variation of lithium-ion concentration

x, y space domain

t time domain

D scalar diffusion coefficient

n direction normal to the surface

I current over particle surface

F Faraday's constant

S available surface area in the electrode

$[M]$ global mass matrix

$[C]$	global damping matrix
$[K]$	global stiffness matrix
$\{\ddot{U}\}$	acceleration vector
$\{\dot{U}\}$	velocity vector
$\{U\}$	displacement vector
$\{F\}$	global force vector
$[k_i]$	local stiffness matrix
$[c_i]$	local damping matrix
$[m_i]$	local mass matrix
$[T_l]$	local orientation matrix
k_n	normal component of spring stiffness
k_s	transverse component of spring stiffness
E	Young's modulus
G	shear modulus
c_n	normal component of damping coefficient
m	half of the mass of each spring
$\{u_d\}$	diffusion induced local displacement vector
Δu_d	local concentration gradient induced displacement
ω	diffusion expansion coefficient

Δc	concentration gradient
l	length of the spring
$\ddot{u}_{i+1}$	acceleration of a single node at (i+1)-th time instant
$\dot{u}_{i+1}$	velocity of a single node at (i+1)-th time instant
u_{i+1}	displacement of a single node at (i+1)-th time instant
$\ddot{u}_i$	acceleration of a single node at (i)-th time instant
$\dot{u}_i$	velocity of a single node at (i)-th time instant
u_i	displacement of a single node at (i)-th time instant
Δt	time increment
M	mass of a node
C	damping of a node
K	stiffness of a node
F_{i+1}	force at a node at the (i+1)-th time instant
$\hat{K}_{i+1}$	modified stiffness matrix
$\hat{F}_{i+1}$	modified right hand side force vector
$\vec{F}_g$	global force vector of a spring
$\vec{u}_g$	global displacement vector for a spring
D_e	scalar diffusion coefficient

Greek

ω	diffusion expansion coefficient
ψ	energy in each spring
ψ_t	threshold energy for each spring
ψ_{mean}	mean threshold energy
α	effect of microcrack on diffusivity
β, γ	parameters of the average acceleration method

Chapter V

a_s	specific surface area
A	area of the electrode current collector interface
$Ahtp$	amp-hour throughput
$\Delta Ahtp$	incremental amp-hour throughput
$A_{\max}$	maximum amount of damage
c_e	space and time dependent lithium ion concentration within electrolyte
$c_{e,init}$	initial electrolyte concentration
c_s	space and time dependent lithium concentration within the solid phase
$c_{s,s}$	solid phase concentration at the surface of the active particles
D_e^{eff}	effective diffusivity of the electrolyte phase
D_e	diffusivity of the electrolyte phase
D_s	diffusivity within the solid phase

D_s^{eff} effective solid phase diffusivity

f_{bb} fraction of broken bonds

F Faraday's constant

I applied current

j reaction current density

j_0 exchange current density

L total thickness of the electrode

L_a thickness of the anode portion of the electrode

L_c thickness of the cathode portion of the electrode

m_{rate} rate of damage evolution

r radial direction within the solid phase

R universal gas constant

R_{cell} electrolyte resistance

R_s outer radius of the solid active particle

t time domain

t_+ transference number

T cell temperature, reference temperature

U open circuit potential

x spatial dimension along the thickness of the electrode

z charge number of the diffusing species

Greek

α_a	anodic transfer coefficient
α_c	cathodic transfer coefficient
γ	an exponent to capture the effect of microcrack on diffusivity
δ_{sep}	thickness of the separator
ε	porosity of the electrolyte phase
η	overpotential for positive or negative electrode
κ	conductivity of electrolyte
κ^{eff}	effective electrolyte conductivity
κ_d	conductivity of charged particles within the electrolyte
κ_d^{eff}	effective conductivity of the charged particles within the electrolyte
σ	conductivity of the solid phase
σ^{eff}	effective conductivity of the solid phase
ϕ_e	electrolyte phase potential
$\phi_{e,0}$	electrolyte phase potential at the previous step
ϕ_s	solid phase potential
$\phi_{s,0}$	solid phase potential at the previous step

TABLE OF CONTENTS

LIST OF FIGURES

LIST OF TABLES

CHAPTER I

INTRODUCTION, BACKGROUND AND SIGNIFICANCE

Every man-made device in the world requires energy to perform its functionalities in the desired fashion. There exist several sources of energy in the world (such as, fossil fuel, wind, water etc.), and various techniques have been developed to capture those energies and convert them into a useful form. These extracted energies can be used for making the life of human much easier. Invention of steam engine can be considered as a major milestone in that respect where heat energy gets converted into kinetic energy of a large locomotive vehicle. The maximum efficiency of these engines, which involve the conversion of some other form of energy into heat, is always restricted by the Carnot efficiency. If conversion of energy can be somehow conducted without transforming it into thermal energy, higher efficiencies may be attained. Fuel cell is a device that directly converts chemical energy into electrical energy, which can again be easily converted into kinetic motion. Thus fuel cell has the potential to show higher efficiency. Batteries act as a device that can convert electrical energy into chemical energy and store it for large amount of time. Thus, the main purpose of a battery is to store energy for some time and then deliver it whenever needed. In general, in a battery electrical energy is converted into chemical energy and stored in that form. This chemical energy is converted back into electrical form according to requirement (see [1, 2]).

Batteries can be broadly divided into two categories: rechargeable and non-rechargeable. In non-rechargeable batteries, once the chemical energy is converted into electricity, it cannot store any more energy again. On the other hand, rechargeable batteries can convert chemical energy into electricity several times. Once the rechargeable battery delivers all its energy, it can be charged again by applying electrical energy in the reverse direction. Since these rechargeable batteries can be recharged and used for long time, increasing the lifetime of these secondary batteries has always been a matter of research (see Ref. [3]).

Based on their commercial availability, different chemistries have been under investigation for usage in secondary battery systems. The first generation rechargeable batteries used lead (Pb) – acid chemistry. Next came the metal hydride batteries (MH). The Nickel (NiMH) metal hydride chemistry was used in most of the commercially successful MH batteries. Even some of the hybrid electric vehicles (Toyota Prius) use NiMH battery chemistry. Recently, due to their high energy and power density, lithium ion battery (LIB) is being extensively used in the commercial battery market. The lithium ion chemistry is being used in the batteries of both electronic devices as well as electric vehicles. Development of fully electric commercial vehicle was possible because of the mass production of lithium ion batteries. All the recent electric vehicles (Nissan Leaf, Chevrolet Volt, Tesla) uses secondary batteries constructed based on lithium ion chemistry (see Ref. [4]).

The materials used to manufacture a LIB are expensive. Also the complicated fabrication procedure adds up to the total cost. Thus, once a LIB is constructed, it is very

important to be able to use it for long enough time so that the money spent on building a LIB is evened out. As a rule of thumb, any LIB is supposed to be used for 5 years, irrespective of whether the battery is being used in an electronic device or an electric vehicle. Assuming that a battery will be charged and discharged once every day, in its entire lifetime of five years a lithium ion cell is approximately cycled (charge – discharge) for 1825 times. Sustaining the charge – discharge ability for that many cycles along with keeping the cell safe for use, is a very big challenge. Due to several physico-chemical factors, capacity of every lithium ion cell decreases and its internal resistance increases with time. Most of the electric vehicles follow the rule of thumb that 20% decrease in capacity or 50% increase in internal resistance indicates the end of life (EOL) for most of the LIBs. Understanding the mechanisms behind this capacity fade and/or resistance increase is very important to improve the performance of the lithium ion batteries. Prevention of some of these degradation mechanisms can significantly increase the lifetime of LIBs (see Ref. [5]).

The deterioration usually experienced by LIBs can be broadly categorized into two divisions: chemical degradation and mechanical degradation. During operation, lots of side reactions happen inside the LIBs, which consume cyclable Li ions from the cell and eventually results in loss of capacity. Also some form of thin films develops, which increases the internal resistance. These types of degradation resulting from side reactions are categorized as chemical degradation. On the other hand, due to the mechanical stresses that develop during operation, fracture may occur within the electrode materials. These cracks have the potential to isolate portions of the electrode that does not

participate in chemical reactions, rendering it useless. Delamination of the electrode from the current collector can result in significant increase in resistance. These types of fracture and detachment of portions of electrode fall under the category of mechanical degradation. Historically, the chemical degradation has been studied more thoroughly and majority of the focus has been to develop materials that can prevent chemical degradation. Understanding the reason behind mechanical degradation has not been investigated in the past. Recently, due to the increased industrial requirement, research focus has been shifted towards understanding the reason behind mechanical degradation and how it can be prevented. The mechanical degradation can also be categorized into multiple mechanisms. Some of them are listed below (see Ref. [6]):

- Fracture within electrode active particles
- Detachment of active particles from the conductive additives
- Delamination of the electrode from the current collectors

There exist several mechanical degradation techniques that are coupled with the chemical degradation procedure and when they work together, it can result in very rapid capacity fade and render the lithium ion cell useless within 50 – 100 cycles. The coupling between mechanical and chemical degradation is also being extensively studied. In the last 5-6 years, significant research work has been conducted to characterize the mechanical degradation from different angles and 2-3 PhD thesis have also been written based on these works. In this particular research, we will try to capture the evolution of mechanical damage within the LIB electrode using a technique that has never been implemented in the context of lithium ion battery before.

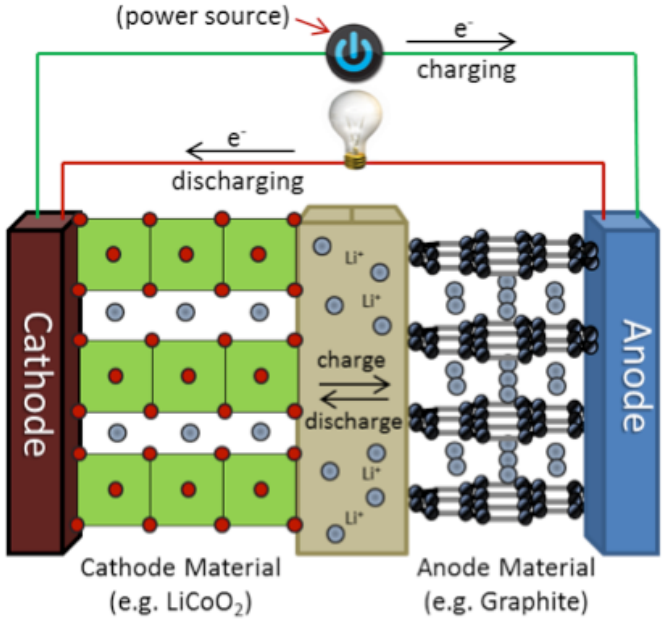

Fig: 1.1. *Schematic representation of a lithium ion battery along with all its components.*

Figure 1.1 gives a brief overview of what exists and goes on inside a lithium ion battery during operation. Starting from the left first comes the cathode current collector made of aluminum (Al) foil. Next is the cathode material, which is usually a blend of $LiCoO_2$, $LiNiO_2$ and/or $LiMnO_2$. Then there is a layer of porous polymer that acts as the separator and keeps the cathode material separate from the anode material. The anode material usually consists of graphite. Finally, copper (Cu) current collector is used in the anode side. During the discharge process, lithium ions move from the anode graphite to the cathode side. Electrons move in the same direction (anode to cathode) outside the cell and delivers energy to external devices. During the charge process, lithium ions

move from cathode to anode and the electrons move in the same direction through an external circuit consuming power from outside sources.

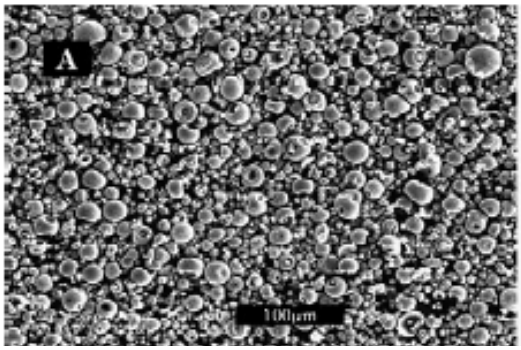

Fig: 1.2. *SEM image of the microstructure of a cathode electrode for $LiFePO_4$/carbon composite (adopted from Liu et al Electrochemica Acta 2009 54 5656 – 5659 (Ref. [7])).*

All the chemical reactions occur within the electrode of the lithium ion battery. Neither the cathode nor the anode possesses a simple microstructure. There exist multiple phases within both the electrodes. Figure 1.2 shows an SEM image of the distribution of different phases within an electrode. The active particles are responsible for hosting the lithium ions during operation. The combination of binder and conductive additives are not very well visible here. It helps to increase the electronic conductivity within the electrode and gives mechanical stability to the battery. The transparent portion is void, through which flow of electrolyte occurs. This electrolyte is responsible for carrying lithium ions from one electrode to the other during operation. In this research we focus on a single active particle and analyze the transport of lithium ions through diffusion. Because of the concentration gradient, stress develops within the active particles that give rise to formation of cracks (see Ref. [8]).

1.1 Literature review

Recent years have witnessed an unprecedented research emphasis on lithium-ion batteries toward improved performance, life and safety, especially for electric drive vehicles. Fundamental understanding of the underlying degradation mechanisms, limiting battery life, is of critical importance. Fracture due to diffusion-induced stress (DIS) of electrode active particles has been identified as one of the critical factors for capacity fade and impedance rise in lithium-ion batteries (LIB)[9]. High-capacity anode materials, for example, exhibit rapid capacity fade resulting from mechanical degradation due to excessive volume change and fracture of the active particles [10] as well as rupture of the SEI layer. [11] On the other hand cathode materials also experience significant mechanical degradation due to fracture during operation. [12, 13] Crack formation in cathode materials has been suggested to occur primarily because of the phase transition that occurs during lithium insertion and extraction. [14] It was, however, argued by Zhao *et al.,* that the potential for fracture formation in cathode materials increases even more under high rate operations. [14] This mechanical degradation may result in isolation of portions of active particles and eventual loss of connectivity and active sites. [10] When the diffusion induced tensile stress exceeds the fracture threshold, existing initial flaws can propagate or new microcracks can develop inside the active particles [15]. Several studies have been conducted to characterize the critical size of the initial imperfection that can propagate during lithiation and delithiation (see Ref. [14, 16]). Orientation of the initial pre-existing crack also impacts its probability of crack propagation [17]. With reduced particle size, less stress was

observed during lithiation and delithiation (see Ref. [18-20]). In some of the computational models reported in the literature, the particles were assumed to be free from imperfection while solving for lithium diffusion in the electrode active particles (see Ref. [18, 21]). Although, in practical scenarios, electrode active particles contain imperfections and defects, which generate during the fabrication process or they develop due to diffusion induced stress (see [22]). Existences of mesopores (2 – 50 nm) inside graphite particles were also observed [23]. Other notable works on stress generation and fracture in Li ion battery active particles can be found in these articles [24-26].

Most of the computational analysis conducted assumes the elastic moduli of the active particles to be independent of Li ion concentration. From Density Functional Theory (DFT) analysis it has been reported that the elastic moduli of electrode particles can vary with the concentration of Li ions (see Ref. [27, 28]). Dependence of elastic moduli and fracture threshold on the Li ion concentration has also been analyzed from a continuum perspective[29]. In the present article, we analyze the effect of concentration dependent elastic moduli on the total amount of damage that develops during operational conditions.

Presence of microstructural defect impacts the diffusion of Li ions inside the active particles[22]. According to the authors, till date little or no research has been conducted to capture the effect of microscopic imperfections on the diffusion of Li ions. In this article a methodology has been developed to capture the initiation and propagation of microstructural damage and their impact on diffusion of Li ions within active particles. In some of the earlier continuum based studies, formation and

propagation of a single crack has been considered[16, 17]. In this analysis, formation of multiple cracks is possible, which allows for multiple pathways of strain energy release that can lead to significantly different results than the single crack analysis. Figure 1.3 shows the SEM image of a graphite active particle with typical crack formation and the existence of transgranular crack[22]. Presence of transgranular cracks in a typical graphite intercalation particle forms the base for our present study on the formation and propagation of fracture within a single spherical electrode active particle.

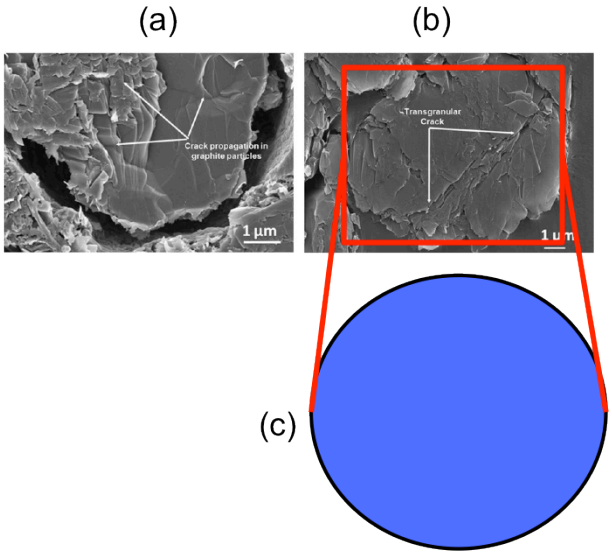

Fig:1.3. *(a) SEM image of a typical hairline crack propagation in a graphite electrode particle. (b) SEM image of a transgranular crack in a graphite particle (adopted from Harris et al. Mat. Res,. 2010) [22]. (c) Schematic diagram of a single particle adopted in the present study. Presence of a intraparticle crack in the graphite active material provided the motivation to study fracture formation in active electrode particles.*

Fracture initiation, propagation and failure of solid materials present an extremely challenging domain of study for materials scientists as well as structural engineers [30-32]. Linear elastic fracture mechanics (LEFM) have been successful in

capturing the propagation of a pre-existing notch in a homogeneous linearly elastic solid material [15]. LEFM uses Griffith energy criterion, which determines the motion of a propagating crack by balancing the energy that is dissipated because of the formation of a new surface with the energy due to the externally applied load [33]. Several new theories have been developed based on the LEFM to understand the impact of plastic zone around the notch tip in the propagation of cracks for ductile materials. Two important concepts usually overlooked by continuum based fracture theory are the effect of disorder and the impact of other pre-existing cracks on the propagation of a notch [30]. Material heterogeneity due to the formation of grain – grain boundary microstructure, presence of interstitials and defects lead to the generation of disorder in solids [34]. A realistic brittle solid develop multiple microcracks under externally applied loads, which eventually contribute in the dissipation of strain energy, along with the notch under investigation [35]. Statistical techniques are used extensively to model the inherent disorder and long-range interactions observed in failure of brittle or quasi-brittle materials[30, 31, 36-46]. Several experimentally observed features such as non-smooth fracture trajectories [36, 37, 44], distribution of fracture strength [31, 32, 35, 47], and occurrence of avalanche during propagation of a crack front [44] have been explained successfully using statistical methods.

At elevated temperature, brittle solids, such as ceramics, are subjected to thermal stresses of high magnitude. Steady state or transient non-isothermal operating conditions induces micro-cracking that can lead to catastrophic failure [48]. Microcracks develop because of the mismatch in grain orientation and anisotropy in the thermal expansion

coefficient of the crystal structure [48-51]. More microcracks are observed for larger grain sizes or highly oriented grains [49, 50]. During propagation, whether a developed microcrack will follow the grain boundary or enter a grain interior, depends on the grain – grain boundary stiffness ratio [51]. Hasselman and Singh have studied temperature gradient induced cracks from a continuum perspective. Their model can describe stable and unstable crack propagation incorporating some preliminary effects of crack interaction in a highly transient thermal stress field [52]. More detailed analysis concluded that under thermal shock loading, preexisting flaws propagates unstably only till an extent [53]. Stable propagation of multiple interacting cracks produces the experimentally observed fracture patterns [54, 55].

The random fuse model (RFM), first introduced by Arcangelis et al., and is capable of simulating the stochastic evolution of stiffness observed during formation and propagation of brittle fracture [56 42]. A two dimensional electrical network of fuses with only one degree of freedom at each node was considered in this model. Random fuse model (RFM) was extended to three dimensions to capture the crack avalanche behavior during brittle fragmentation observed through acoustic emission [44]. To better characterize the experiments, network models with more than one degree of freedom per node were considered. Random spring models consist of two degrees of freedom (in 2D) and three degrees of freedom (in 3D), which are the displacements of each node along the axis [44, 57]. To incorporate the rotational degrees of freedom in each node, the random beam network model was developed. In 2D, two displacements and one rotational degree of freedom [58] and in 3D, three rotational degrees of freedom along

with three displacements are the features of a network of random beams [37]. Brittle fracture surface roughness coefficient of 2/3 in 2D and ½ in 3D was mostly observed in the literature using both random spring and random beam network models. Plasticity was also incorporated into random network models to characterize the strain localization observed in ductile materials before failure [37, 45, 59]. Using energy based fracture criterion in a three dimensional random lattice spring model, initiation and propagation of cracks in polymer blends were simulated [60]. Random network models have been used recently to characterize the non-universality of roughness exponents in quasistatic brittle fracture in the presence of extended correlations and anisotropy [36]. Effect of microstructure in the quasistatic failure behavior of heterogeneous concrete materials under externally applied load has been simulated using random beam network models [61]. Experimentally observed oscillations of crack velocity and micro-branching in the dynamic fracture of amorphous as well as crystalline materials with grain/grain-boundary microstructure have been captured using the random network models [36, 62].

Acoustic emission (AE) is a nondestructive experimental technique, which has been recently employed to study mechanical degradation in LIB electrodes.[63-65] In AE, piezoelectric sensors are placed on the material under study. Formation of microcracks release strain energy to its surrounding, which travels through the material as mechanical vibration. These stress waves are detected by the piezoelectric actuators located on the material surface as sound waves.[66] The AE technique renders a non-destructive procedure for the detection of microcrack formation, nucleation and propagation. The methodology of acoustic emission has been used quite extensively to

detect the mechanical degradation in solid materials.[67, 68] This unique experimental tool can detect sound waves of different frequencies, which correspond to different degradation mechanisms. In composite materials, fracture initiation can occur because of multiple reasons, such as rupture of fibers, microcrack formation in the matrix phase, fiber – matrix delamination/debonding etc. Each degradation mechanism emanates stress waves of different magnitude and frequency, which can be successfully detected by piezoelectric sensors. Acoustic emission technique provides a very useful tool for detecting the amount as well as type of mechanical damage in composite materials.[69] Estimation of fracture toughness under "Mode – I" crack propagation in several geological materials (such as, rocks) have been conducted by using the acoustic emission technique.[70] Fracture and fatigue behavior and health monitoring of numerous structural components (such as steam pipes, pressure vessels) can be conducted by calculating the acoustic emission counts, peak levels and cumulative energy release rates.[66] Acoustic emission methodologies have also been used to detect the amount of degradation observed in several materials (such as, wood, aluminum, gypsum, plastic etc.) exposed to open flames [71]. Detection of stress corrosion cracking (see [72, 73]) and health monitoring of tensioned structural members[74] can also be conducted using the acoustic emission scheme.

For almost a decade, the scientific community is well aware of the formation of cracks in the lithium ion battery electrode active particles during the lithiation – delithiation cycles.[13, 29] However, only recently this versatile nondestructive acoustic emission tool received significant attention for the detection of mechanical damage in

electrode materials. In the late nineties, a research group from Japan attempted to characterize the amount of fracture in the manganese dioxide cathodes used in secondary lithium ion batteries (see [64]). They were able to show that mechanical degradation saturates after five/six lithiation – delithiation cycles (see Ref. [64]). In the past few years, the AE technique was employed to investigate the amount of damage in high-capacity LIB anode materials.[40, 63, 65, 75, 76] Gas generation during operation inside lithium-ion batteries has also been experimentally characterized using acoustic emission response[77]. Structural and morphological impacts of lithiation and delithiation on the conversion type electrodes have been investigated using the AE technique[78]. Recently, Woodford *et al*. used AE to study damage evolution in $LiCoO_2$ cathode.[79, 80]

In several industrial applications, such as metal cutting, efforts have been devoted to computationally model the dynamic behavior of realistic solids to predict the acoustic emission activity under externally applied loads.[81] In the physics community, to investigate the fracture of disordered media under uniaxial tensile load, statistical analysis was conducted to correlate energy release rate with damage evolution till specimen failure.[82] In this study, a two-dimensional disordered lattice network was subjected to uniaxial tensile load to capture the microcrack formation and the corresponding energy release by plotting the acoustic emission spectra (acceleration with respect to time curve). In the statistical physics community, computational efforts were invested in the investigation of the speed of crack propagation in a disordered specimen subjected to uniaxial tensile load.[83] In lithium-ion batteries, significant research has been conducted to computationally characterize the stress – strain relations observed in

electrode active particles (see [17, 29, 84]). On the contrary, relatively fewer efforts focused on the formation and propagation of cracks inside lithium-ion battery electrodes [10, 16, 17, 29, 63, 79, 85]. To the best of our knowledge, no computational study has been conducted to capture and/or predict the acoustic emission response (spectra) observed during lithiation – delithiation cycling of LIB active particles. In this paper, a computational method has been developed that can capture the dynamic change in lithium concentration gradient in a two-dimensional domain. The concentration gradient has been coupled with a dynamic lattice spring model (DLSM), which can estimate the stress generation and predict the formation of microcracks. Propagation of strain energy released from the rupture of the spring network is estimated by solving the dynamic momentum balance equation. Acceleration of nodes located on the surface of the particle corresponds to the acoustic emission spectra. The computational technique developed in this study is capable of predicting the acoustic emission response during lithiation – delithiation of LIB electrode and allows for local probing of mechanical damage detection and monitoring.

Due to their high energy and power density, lithium-ion batteries (LIBs) are being used extensively in the electrification of the automotive industry through the development of electric and hybrid electric vehicles (EVs and HEVs) [5, 86, 87]. Several mechanisms exist that can cause a reduction in the capacity of LIBs and subsequent loss of life [88-91]. Growth of a solid electrolyte interface (SEI) layer on the carbon active particles of the anode is the major reason behind the loss of cyclable lithium ions [11, 92, 93]. Lithium plating at low temperatures also results in loss of lithium and

subsequent capacity fade [94]. Delamination of the current collector from the electrode due to gas evolution in the electrolyte can significantly increase the internal resistance of the lithium-ion cell [95]. Crack propagation, rupture, and isolation of portions of active particles can also cause loss of active sites where lithium atoms can intercalate, resulting in effective capacity fade [10]. In the past two to three decades, capacity fade due to the formation of SEI [11, 92, 96-99] and lithium plating [100, 101] have been investigated thoroughly. On the other hand, resistance growth and capacity fade due to delamination and site loss have not been explored extensively. In the recent past, some research initiatives have focused on characterizing the generation of diffusion-induced stress within the active particles [102]. A computational methodology was developed to capture the formation of cracks based on the material heterogeneity of the anode active particles [85]. In the present article, the authors have developed a comprehensive reduced order model (ROM) that can characterize the impact of microcrack formation (within anode active particles) on the electrode-level performance of LIBs.

The first effort towards development of computational models to characterize the behavior of porous battery electrodes was conducted by Newman [103, 104], which is more commonly known as the "porous electrode theory." Several researchers have extended the pioneering work of Newman by incorporating the effect of transport limitations [105], electrode thickness [106] and separator [99, 105].

The presence of two different porous electrodes (cathode and anode) was also taken into consideration while modeling LIBs [107]. Experiments were also conducted to estimate different parameters and validate the porous electrode theory [107].

Transport of lithium ions through the electrolyte phase occurs via two mechanisms, diffusion (estimated using conductivity) and migration (measured by transference number). Analysis of the competition between these two mechanisms on the cell performance was conducted to obtain optimum values for each of the parameters [107]. Analytical expressions for maximum energy and power density obtainable from a LIB as a function of design parameters (such as, porosity, electrode, and/or separator thickness) were also developed [106]. Relaxation phenomena inside dual lithium-ion insertion cells and their impact on the performance have also been studied [107]. Impacts of ambient temperature and heat generation within the electrochemical cell on the overall performance of LIBs were investigated by modifying the porous electrode theory to incorporate the effect of temperature [67, 108, 109]. A multi-scale multi-domain model has been developed by extending the porous electrode theory to capture the behavior of LIBs at different length scales (such as particle level, electrode level, and cell level) [110]. The effect of stress generation inside electrode active particles has been incorporated within the porous electrode theory to study its impact on cell performance [21, 111]. The porous electrode theory has also been extended to incorporate system-level parameters, such as, cost, life, and safety of the LIB [112].

Detailed modeling of a physical phenomenon requires solution of partial differential equations that derive from either mass conservation, momentum balance, and/or energy conservation principles. For complex geometry and variable physical parameters, these partial differential equations need to be discretized using some numerical technique (finite difference, finite volume, or finite element method), and a

series of linear algebraic equations needs to be solved to obtain the correct solution [113]. Reduced order modeling is a technique that gives reasonably good approximate solutions to these partial differential equations without using any numerical discretization technique [114, 115]. Reduced order solutions are also applicable only under certain operational constraints and may fail severely when applied to situations away from those constraints. Application of reduced order modeling significantly decreases the number of unknowns that need to be solved for. Development of ROMs for complicated physical systems significantly helps in the implementation of control-based theories [116]. A ROM of diffusion within the solid active particles has already been incorporated within the porous electrode theory [117, 118]. ROMs of the entire porous electrode theory have also been developed to capture the cell performance under high charge-discharge rates [114, 115]. From a phenomenological perspective, ROMs have been developed to capture the mechanical degradation of active materials [10]. Coupling of mechanical and chemical degradation using ROMs has been conducted to investigate the enhancement in capacity fade due to SEI growth on microcracks located on active particle surfaces [119]. ROMs for estimating cell life have been used extensively for EV and drive cycle applications [120]. ROMs for capacity fade due to lithium loss and reduction of active sites have been developed and used to explain experimentally observed data under different operating conditions [89].

Next generation lithium ion batteries are supposed to use high capacity cathode as well as anode materials [121]. Layered-layered composite cathode structures, usually denoted as $xLi_2MnO_3 \cdot (1-x)LiMO_2$ (M = Mn, Ni, Co), has received attention due to

excessively high rechargeable capacity of 250mAh/g when cycled between 4.6V and 2.0V (see [122-124]). Except some minor gas generation due to oxygen release, these high capacity layered composite cathode materials do not experience severe volume expansion during lithiation process [122]. High capacity anode materials include silicon (Si), tin (Sn) or germanium (Ge), which can show almost ten times higher theoretical specific energy than graphite (see [18, 109, 125]). The theoretical capacity of silicon is 4200mAh/g and the same for tin is 994mAh/g [88]. Significant research work has been conducted to construct silicon based anode electrodes for lithium ion battery. Some studies focused on Si nanowires (see [18, 126]) and others developed silicon based composite anodes (see [119, 127-130]). From the perspective of commercial applications, Panasonic Corporation announced the development of high capacity lithium ion battery with Si-alloy anodes [131]. When used inside a realistic lithium ion battery electrode, the effective capacity of Si and Sn decrease to some extent, but still displays around thrice the capacity of graphite based anodes (see [132]). However, usage of Si based high capacity anode materials within LIB suffers from significant loss of capacity with charge-discharge cycles [129]. Most of the novel Si architectures constructed experimentally experienced more than 20% capacity-fade within the first 50 cycles (see [18, 133]).

The reason behind this severe capacity fade within high capacity anode materials is the fact that they experience severe volume expansion-contraction during the lithiation-delithiation phenomenon [119]. Si and Sn anode active particles expand around 300% to 400% depending on the amount of lithiation [134, 135]. This gives rise

to significant amount of microcrack formation, nucleation and propagation within the active particles. Figure 3(a) in Lee et al. PNAS (2012) shows an experimentally observed SEM image of mechanical degradation in silicon (Si) active particle after the lithiation process [42]. Generation of microcrack on the particle surface enhances the formation of solid electrolyte interface (SEI) layer, which subsequently leads to capacity fade [11]. High volume expansion and contraction of the active particles apply large magnitude of tensile and compressive stresses on the SEI layer, which is susceptible to fracture, and successive detachment from the active particles. Fresh active particle surface comes in contact with the electrolyte where SEI layer can form leading to additional loss of cyclable lithium (for similar concept see [119]). Severe mechanical degradation and subsequent pulverization of the active particles has the potential to completely isolate some of the active particles [136, 137]. Detachment of portions of active particles from the electron carrying current collectors leads to loss of active sites for lithium intercalation, which gets reflected as severe capacity fade. Some computational research has been conducted to elucidate the reason behind large stress generation (see [138, 139]).

Transport of lithium ions though the Si and Sn based high capacity anode materials occur via the two-phase diffusion mechanism. During lithiation, the crystalline Si changes into amorphous Li_xSi compound, which is usually separated by a moving two-phase front [140]. It can be assumed that after the first lithiation process, the entire Si behaves like an amorphous material and transport of Li happens via single phase diffusion process [141]. Hence, the governing equation for single phase diffusion has

been adopted to characterize the transport of lithium within silicon active particles [138, 141]. However, experimentally obtained SEM images show that significant amount of mechanical degradation occur within the first lithiation process [42, 138, 142]. Because of the conversion from crystalline Si to amorphous Li_xSi compound, the first lithiation process must be modeled using a two-phase diffusion technique. To analyze the magnitude of stress generation within Si active particles, Huang et al. adopted a two-phase concentration profile for transport of silicon [143]. The effects of high or low rates of reaction were not captured successfully. A Cahn-Hilliard equation based two phase transport model was adopted by Chen et al. to model the combined kinetics of diffusion and movement of the two-phase front [139]. The effects of particle size and rate of lithiation-delithiation within silicon were appropriately captured. A similar governing equation that is capable of predicting the phase separation and diffusion within Si active particles has been be adopted in the present study.

Severe capacity fade observed in Si anode electrode is attributed to the extremely large magnitude of mechanical deformation and particle fragmentation during the lithiation-delithiation process [11]. Hence, several computational studies have been conducted to study the large volume expansion and subsequent stress generation within Si anodes during the lithiation process (see [138, 141]). In silicon thin films and nanowires, possibility of pre-existing cracks to propagate during the lithiation-delithiation process has been investigated (see [14, 144]). The effect of surface energy in nano-sized Si particles and wires to eliminate the microcrack formation has also been studied [29]. Elasto-plastic deformation of the silicon active material was taken into

consideration in some of the computational analysis (see [121, 139, 141]). Adhesion strength between the silicon active particle and Cu have been investigated to elucidate the operating conditions at which delamination of the electrode form the current collector can happen [145]. Delamination strength for silicon and carbon conductive additives has also been studied using ab-initio computational techniques [146]. Effect of mechanical stress generation on the electrochemical potential of thin film silicon electrode has also been investigated [141, 147]. However, there exist no detailed numerical analyses that can predict the nucleation and propagation of microcracks and pulverization of high capacity anode materials during the lithiation-delithiation process.

Lithium ion batteries are usually assembled in the factory in a discharged state [43]. Then they are charged in a relatively slow rate that stabilizes the anode active particles via the formation of a thin solid-electrolyte-interphase (SEI) layer [148]. Also the cell becomes ready to discharge and deliver power to the external circuit. For graphite based anode materials, the initial slow lithiation process is a relatively benign phenomenon and does not lead to any major mechanical degradation [85]. However, for high capacity anode materials, such as Si and Sn, the lithiation process occurs via a two-phase diffusion process [139]. Large volume expansion followed by severe mechanical degradation occurs within high capacity anode materials during the first lithiation process [149]. The new crack fronts that open up, allows the formation of larger amounts of SEI, which results in significant loss of cyclable lithium [11]. Pulverization of the anode active particles during lithiation-delithiation cycles, has the potential to detach them form the binders and conductive additives [136]. This result in loss of active sites

for lithium intercalation, which is also characterized as capacity fade due to site-loss. There exist two main reasons behind this major mechanical degradation observed within high capacity anode active materials [147]:

a) Transport of lithium occurs via a two-phase diffusion process, which gives rise to very large concentration gradient induced load at the two-phase interface boundary.

b) Large volume expansion during lithiation causes the lithium rich phase to move outward along the radial direction resulting in generation of tensile stress at the particle surface.

Prevention of these major forms of capacity deterioration in Si and Sn based anode materials is necessary to successfully implement them in commercial lithium ion battery systems [88, 121]. In the results and discussion section, how the developed computational methodology can capture the formation and propagation of microcracks will be discussed in details. Different techniques that are capable of minimizing the overall mechanical degradation of high capacity anode materials will also be investigated.

1.2 Hypothesis

According to several literatures, presence of spanning cracks has been extensively observed in the SEM images of used electrode active particles (see Ref. [27, 63, 134]). Those spanning cracks were not there in the pristine unused particles. From these SEM and TEM images, it has been hypothesized that those cracks developed during operation of the electrochemical cell. Similar to formation of microcracks under temperature gradient induced loading, diffusion induced stress inside the active particles

can also generate significant amount of microcracks. One hypothesis is that the stress generated by lithium ion concentration gradients is sufficient to create mechanical damage within electrode active particles. Nucleation of these microcracks has the potential to form large cracks. Since the stress concentration factor at the tip of a crack front is usually higher, they can propagate and form spanning cracks. In phase separating materials, even under small rates of operation, formation of macroscopic cracks have been observed. In high capacity anode materials (such as, Si) large volume expansion occurs during the lithiation process and subsequently cracks are observed along the periphery due to anisotropy in the expansion process (see [42]).

1.3 Objective

The overarching objective of this particular research is to develop understanding about the mechano-electrochemical aspects of lithium ion battery. In this regard the following research goals have been narrowed down to be accomplished as a part of this PhD research.

1.3.1 Objective: 1

Checking the correctness of the above-mentioned hypothesis is the first objective of this research. A computational methodology have been developed that can solve for the formation of concentration gradient within the active particles. Based on the concentration gradient, diffusion induced stress acts on the active particles. The developed computational methodology has the capability to capture the formation of microcracks due to this diffusion-induced stress (DIS). More precisely, the objective of this research is to understand how and when under DIS the microscopic cracks develop

and under what condition they nucleate and propagate to form spanning cracks. Design as well as operating conditions, which can reduce the formation of mechanical damage, will also be investigated in this study.

1.3.2 Objective: 2

Experimental diagnosis of damage evolution can be conducted using the acoustic emission (AE) technique. The second objective of this research work has been to develop another computational methodology that can predict the experimentally observed acoustic response during fracture of an electrode active particle. Energy released during formation of a microscopic damage propagates through the solid media as a stress wave and hits the boundary of the structure. Acceleration at any point on the surface of the solid can be detected by placing an actuator. The developed computational scheme captures the propagation of stress waves through the solid media and tries to predict the acceleration response usually detected by the actuator. This methodology should potentially be applicable to predict the acoustic emission response observed in other physico-chemical systems by appropriately tuning the elastic modulus and damping coefficient of the solid material.

1.3.3 Objective: 3

The third objective of this research is to extend the particle damage model for phase separating materials. In high capacity anodes (such as Si, Sn), lithium intercalation and extraction cannot be successfully captured using the simple Fick's law. A more sophisticated phase separating model, which takes into account the formation of multiple phases during lithiation and delithiation, needs to be developed. Significant

concentration gradients will appear between the two phases, which can potentially lead to significant amount of mechanical damage. Also due to the high volume expansion of the lithiated phase, severe tensile stress develops at the surface of the active particles, which has the potential to create significant amount of microcracks. A thorough study will be conducted to understand from where the microcrack evolution initiates for high capacity anode active materials during lithiation/delithiation process. Methodologies regarding how to mitigate the fracture evolution within high capacity anode materials will also be investigated.

1.3.4 Objective: 4

Finally, impact of mechanical degradation on life of lithium ion cells will be discussed. A reduced order model will be developed to predict the amount of mechanical degradation without solving the time consuming momentum balance equation. Reduction in diffusivity due to increasing mechanical degradation has also been modeled. A power law expression can be estimated to capture the effective diffusivity as a function of microcrack density. Increase in mass transport resistance and reduction in effective capacity can be modeled using the porous electrode theory. To achieve that goal, an in-house pseudo-2D LIB model has been developed along the thickness direction of the cell. During operation, evolution of mechanical degradation along the thickness direction will be analyzed using the developed model.

A brief overview of what is being presented in this thesis is provided below. The background of Mechano-electrochemical aspects in lithium ion battery electrode active particle is provided here. Chapter II applies the damage evolution on a single particle.

Chapter III talks about the properties of fracture in a brittle media due to diffusion induced stress. Chapter IV will discuss about prediction of acoustic emission spectra. Chapter V contains the details about developing porous electrode theory model and the effect of mechanical degradation on the cell level capacity fade. Mechanical degradation observed in high capacity anode materials will be discussed in Chapter VI. Finally, in Chapter VII, the thesis will be concluded and the future research goals will be elaborated.

CHAPTER II

INTERCALATION INDUCED STRESS AND FRACTURE IN ELECTRODE ACTIVE PARTICLES*

The stochastic methodology, developed in this work, is based on a ***random lattice spring*** formalism coupled with solid-state diffusion of lithium in active particles and performance prediction analysis.

2.1 Computational methodology

The concept of a network of electrical fuse with randomly distributed "burn out" threshold to analyze the fracture behavior in a brittle solid material was first introduced by Arcangelis and Redner[150]. This Random Fuse Model (RFM) uses only one degree of freedom at each node, which is not sufficient to capture the Poisson's ratio observed in solid materials. Instead of electrical fuse, spring with resistance to central force only, can be assumed as the connecting element between the nodes. This model gives two degrees of freedom in 2D and three degrees of freedom in 3D analysis. But the Poisson's ratio depends on the connectivity of each node. Central force spring network shows a constant Poisson's ratio of zero for a square lattice (coordination number four) and 1/3 for a triangular lattice (coordination number six)[57]. When the elemental forces are no longer restricted to be only along the axial direction and a second spring constant is

introduced along the shear direction, different Poisson's ratio can be modeled with this modified lattice spring network (see Ref. [151]). The Poisson's ratio for a 2D modified lattice spring network with coordination number six (also known as the Born model) is given as,

$$\nu = \frac{k_n - k_s}{3k_n + k_s} \tag{2.1}$$

where, k_n is the spring stiffness along the axial direction and k_s is the spring stiffness along the shear direction. By keeping $k_n = 1$, as k_s varies from zero to one ($0 < k_s < 1$), Poisson's ratio of the network changes from 1/3 to zero ($1/3 > \nu > 0$).

To capture the diffusion of Li ions inside the entire electrode, a pseudo-2D model was developed by Doyle *et al*.[152] and Fuller *et al*.[107], where the problem was solved with variations along one spatial direction perpendicular to the cell and represent the gradients in the electrode particles by a representative spherically symmetric particle at each node. According to this pseudo-2D model, only the radial variation of Li ion concentration within the solid active particle has been captured. Because of the presence of microscopic imperfections within the active particles[22], azimuthal variation of Li ion concentration cannot be ruled out. Hence, in the current study, Li ion distribution inside the active particle along both radial and azimuthal direction has been taken into consideration. Ionic conductivity of the electrolyte has been assumed to be very large which results in zero ion concentration gradient in the electrolyte phase. Hence, the active particle is subjected to constant galvanostatic current from all directions, irrespective of its distance from the current collector. Under the same assumption of very

high ionic conductivity of the electrolyte phase, capacity of the cell will be limited by the diffusion of Li ions inside the solid active electrode particle[153]. The distribution of Li ion concentration inside the solid phase has been calculated by solving the diffusion equation as provided below,

$$\frac{\partial c\left(\vec{x},t\right)}{\partial t} = \vec{\nabla}\cdot\left(\underset{\sim}{D}\left(\vec{x},t\right)\cdot\vec{\nabla}c\left(\vec{x},t\right)\right)$$

$$\text{and } -k_{cond}\frac{\partial c\left(\vec{x},t\right)}{\partial n} = \frac{i}{F} \text{ at the outer boundary} \tag{2.2}$$

Here $c\left(\vec{x},t\right)$ is the space $\left(\vec{x}\right)$ and time $\left(t\right)$ dependent Li ion concentration inside the active particle, $\underset{\sim}{D}\left(\vec{x},t\right)$ is the space and time dependent diffusion coefficient tensor, k_{cond} is the ionic conductivity, $\vec{n}$ signifies the direction normal to the surface, i is the current over particle surface and F is the Faraday constant. For homogeneous and isotropic materials, $\underset{\sim}{D}\left(\vec{x},t\right) = D_{scalar}\underset{\sim}{I}$ and is independent of space and time (here, $\underset{\sim}{I}$ is the identity tensor). Coupling with Li diffusion, the resultant stress generation is incorporated through the Li concentration profile inside the electrode.

The quasistatic force equilibrium equation has been solved to determine the stress distribution inside the electrode.

$$\frac{\partial \underset{\sim}{\sigma}\left(\vec{x}\right)}{\partial \vec{x}} + \vec{B} = \rho\ddot{\vec{u}} = 0 \quad \text{with, } u_i = \bar{u}_i \, on \, S_u \; and \; \sigma_{ij}n_j = t_i = \bar{t}_i \, on \, S_t \tag{2.3}$$

Here, $\underset{\sim}{\sigma}\left(\vec{x}\right)$ is the stress tensor, $\vec{B}$ is the body force vector which is assumed to be zero for this particular problem $\left(\vec{B}=0\right)$ and $\vec{u}\left(\vec{x}\right)$ is the space dependent displacement

vector. Since the diffusion of Li ions inside the solid active particle is very slow, mechanical equilibrium is reached as soon as the Li ions diffuse. As a result, quasistatic analysis of the mechanical equilibrium is sufficient.

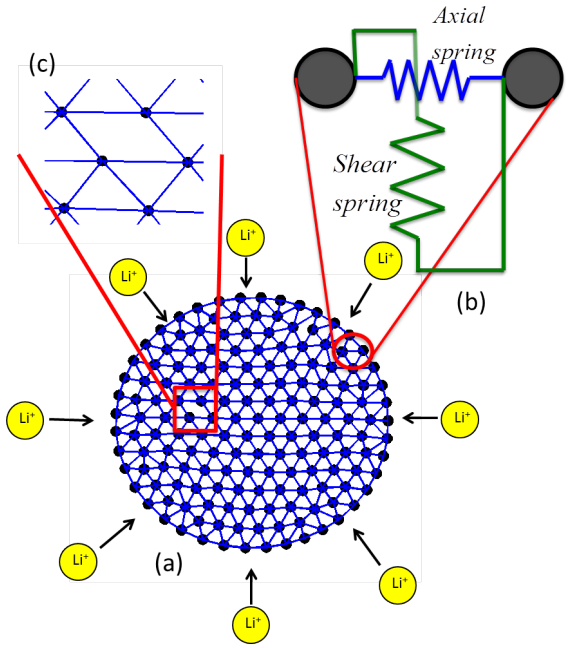

Fig: 2.1. *A schematic representation of the lattice spring model adopted in the current analysis. (a) Discretization of the circular domain into springs. Lithium ions intercalate or deintercalate from the outer surface. (b) Magnified visualization of each spring. All the mass is assumed to be lumped at each node. The springs show axial as well as shear stiffness. (c) A magnified visualization of a broken spring.*

Random spring type elements were considered to discretize the above-mentioned equation (see Eq. (2.3)). Figure 2.1 shows the triangular mesh under consideration for the current analysis. Each node in this mesh is attached to six other neighboring nodes by a spring, which leads to a coordination number of six. The springs display stiffness not only along the axial direction, but also along the transverse direction making this technique equivalent to born model (see Fig: 2.1(b)). The local force vs. displacement relation for each spring is given as follows,

$$\begin{bmatrix} f_{x1} \\ f_{y1} \\ f_{x2} \\ f_{y2} \end{bmatrix} = \begin{bmatrix} k_n & 0 & -k_n & 0 \\ 0 & k_s & 0 & -k_s \\ -k_n & 0 & k_n & 0 \\ 0 & -k_s & 0 & k_s \end{bmatrix} \begin{bmatrix} u_{x1} \\ u_{y1} \\ u_{x2} \\ u_{y2} \end{bmatrix} \tag{2.4}$$

where, $\vec{f}$ is the local force vector and $\vec{u}$ is the local displacement vector. Global forces and displacements are related to the local forces and displacements through the relations $\vec{F} = \left[T\right]^T \vec{f}$ and $\vec{U} = \left[T\right]^T \vec{u}$, where $\left[T\right]$ is the transformation matrix. Global stiffness matrix is constructed from the local stiffness matrix using the relation,

$$\left[K_g\right] = \sum_{\substack{all\,the \\ elements}} \left[T\right]^T \left[k_l\right]\left[T\right] \tag{2.5}$$

Stress generated due to the diffusion of Li is incorporated as an axial displacement inside the spring (see [17, 102]).

$$\Delta u^d = \omega \cdot \Delta c \cdot l \tag{2.6}$$

where, ω is the diffusion expansion coefficient that has a typical value of $1.14\times10^{-6} m^3/mol$ for graphite[17], Δc is the incremental change in Li ion concentration, l is the length of the spring type element and Δu^d is the diffusion induced displacement. The force vector due to diffusion-induced stress is defined as,

$$\vec{F}^d = \left[T\right]^T \vec{f}^d = \left[T\right]^T \left[k_l\right] \Delta \vec{u}^d \tag{2.7}$$

Energy in each spring is calculated according to $\Psi = \frac{1}{2} \vec{F}_{spring} \cdot \vec{u}_{spring}$. Here, $\vec{F}_{spring}$ and $\vec{u}_{spring}$ are the global force and displacement vectors in each spring. The electrode material is assumed to display brittle fracture behavior (see Ref. [37]). Mean value of the

breaking threshold of each spring is estimated using an energy equivalence scheme. Exact value of breaking threshold is assigned as a uniformly distributed random number with the mean calculated above $\left(\Psi_t\right)$. If the energy in a particular spring is greater than the energy threshold for that spring ($\Psi > \Psi_t$), the spring is irreversibly removed from the network (see Fig: 2.1(c)). For graphite, the average fracture energy threshold per unit area (Ψ_{ua}) has been given as 2 J/m^2 (see [17]). Actual mean value of fracture threshold for a particular spring is obtained by multiplying the average fracture energy threshold per unit area with the area associated with that spring $\left(\Psi_{mean} = \Psi_{ua} \cdot A_{spring}\right)$[15, 17, 44, 151]. Here, A_{spring} signifies the area associated with each spring type element in the two-dimensional circular cross sectional region. The propensity of every brittle material to fracture under tensile loading conditions is much higher than compressive type load [15]. Hence, the energy threshold under compression is assumed to be few orders of magnitude higher than the energy threshold under tension.

In the above-mentioned theory, diffusion of Li ions within the solid electrode material affects the mechanical response. But the macroscopic damage and fracture inside the electrode active particle have no impact on the diffusion process. In practical scenario, if the material develops internal damage, it is supposed to have some impact on the diffusion of Li ions. Figure 2.2 depicts a phenomenological methodology that has been implemented to capture the impact of mechanical damage on the diffusion process. In the absence of any damage within the solid material, Li ion diffuses through the bulk with its original diffusion coefficient, $D_{scalar} = D_{original}$ (see Eq. (2.2) and Fig: 2.2(a)).

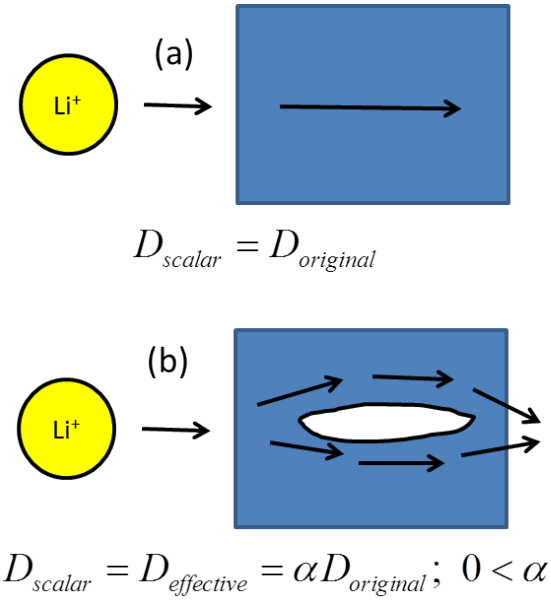

Fig: 2.2. *Schematic diagram of the mechanism adopted to couple the effect of mechanical damage with diffusion of Li ions. (a) When there is no internal damage within the bulk material, Li ions diffuse through the solid freely and display the original diffusion coefficient for undamaged material. (b) When there is mechanical damage within the particle, Li ions need to move in a tortuous pathway around the crack. Increased tortuosity reduces the diffusion coefficient of Li ions, which is taken into account through the introduction of the parameter* α *that varies between 0 and 1.*

With the presence of mechanical damage within the bulk electrode material, the diffusing Li ions encounter major obstructions. It takes a tortuous pathway to avoid the internal micro-crack (see Fig: 2.2(b)), which results in reduction of diffusivity of Li ions. Changes in diffusion coefficient due to internal mechanical damage are modeled by introducing a scale parameter ($0 < \alpha < 1$), and the modified diffusion coefficient is defined as $D_{scalar} = \alpha D_{original}$. In damage mechanics of solid materials, for isotropic damage, a reduced Young's modulus is defined to take into consideration the impact of microcracks [15, 154]. Introduction of the α parameter has been motivated from an analogy to solid mechanics. Physically, the damage parameter α captures the effect of mechanical damage on the diffusion process. The two limiting cases of $\alpha = 1$ correspond

to undamaged material and $\alpha = 0$ correspond to zero diffusion through the completely damaged bulk material. Estimation of exact value of the damage parameter α from a computational perspective requires analysis based on lower length scale simulations (such as, molecular dynamics or MD). Otherwise, empirical procedure based on comparison with experimental results can be adopted to determine the value of α. In the present study, different parametric values of α will be considered and the impact on Li ion diffusion will be investigated. Degradation in battery performance will also be reported for a particular value of the α parameter.

In most of the analysis reported till date, constant values of elastic moduli have been assumed. But concentration dependent elastic moduli are observed for most of the active materials used in anode or cathode electrodes[27, 28]. Following the correlation reported by Deshpande et al.[29], variation in concentration dependent Young's modulus $E(c)$ is given as,

$$E(c) = E_0\left(1 + k\frac{c}{c_{\max}}\right) \tag{2.8}$$

Here, E_0 is the Young's modulus with zero stoichiometric Li concentration, c is the current Li ion concentration and $c_{\max}$ is the maximum stoichiometric Li ion concentration within the active material. The parameter k signifies whether the material stiffens $(k > 0)$ or softens $(k < 0)$ due to Li insertion.

The numerical scheme to solve the coupled diffusion mechanics problem will be described here. Initially, Eq. (2.2) has been solved to obtain the time dependent Li ion

concentration profile inside the cross section of the active particle. A volume averaging scheme has been adopted to evaluate the mean ion concentration [29]. Average ion concentration is subtracted from the local Li ion concentration at each computational node to obtain the value of Δc in Eq. (2.6). Diffusion induced displacement has been obtained from Eq. (2.6). The corresponding diffusion induced force in global coordinate system has been derived from Eq. (2.7). The diffusion induced force vector assembled over all the spring type elements, constitute the right hand side (RHS) vector of the set of linear algebraic equations to be solved. Stiffness matrix for the entire system has been obtained by assembling the global stiffness matrix for each of the spring type elements (see Eq. (2.5)). Derivation to obtain the set of linear algebraic equations from Eq. (2.3) has been adopted from textbooks regarding introduction to finite element method[155, 156]. Finally, the set of algebraic equations were solved using the "linsolve" function in MATLAB and the equilibrium displacements under an intermediate Li ion concentration gradient were computed. Under the equilibrium displacement, force and energy in each spring were computed and the springs, which exceeded the fracture energy threshold, were removed from the network one by one. Based on the location of the broken bonds, diffusion coefficients at the corresponding nodes were modified according to the value of α parameter. Li ion concentration for the next time step was estimated by solving Eq. (2.2) with the modified set of diffusion coefficients.

Performance is estimated based on the Li-ion surface concentration at the active particle/electrolyte interface. This relies on the single particle formalism for performance prediction of a LIB cell sandwich presented by White and co-workers [157]. Recently,

the performance prediction methodology was enhanced to study the morphological influence on the electrochemical and transport behavior in 3-D electrode architectures for LIBs, and is detailed in the work by Martin *et al [158]*. In this regard, it is important to note the significant effort invested in computational modeling and theoretical analysis to study electrochemical, transport and performance attributes of LIBs (see Ref. [18, 107, 112, 117, 152, 159-164]). Briefly, the Butler-Volmer Equation is used to solve for the electrode overpotential, η_i (i = n, p for negative and positive electrodes, respectively). Below is shown the appropriate form of this equation for this study.

$$j_{Li,i} = k_i c_e^{\alpha_n} \left(c_{\max,i} - c_{surf,i}\right)^{\alpha_n} c_{surf,i}^{\alpha_p} \left[e^{\frac{\alpha_n F}{RT}\eta_i} - e^{\frac{\alpha_p F}{RT}\eta_i} \right] \tag{2.9}$$

In the above equation, c_e, and $c_{surf,i}$ are the electrolyte concentration, taken to be constant at the initial value of 1000 mol/m^3, and the surface concentration of the i^{th} electrode, respectively. Additionally, α_p and α_n are the transfer coefficients taken to be 0.5 for both the anode and cathode. Furthermore, the equilibrium potentials for the anode and cathode are determined from empirically derived functions of Li-ion surface concentration, as shown below[157].

$$\begin{aligned} U_n = {} & .13966 + .68920e^{-49.20361x_n} + .41903e^{-254.40067x_n} - e^{49.97886x_n - 43.37888} - \\ & .028221\arctan(22.52300x_n - 3.65328) \\ & -.01308\arctan(28.34801x_n - 13.43960) \end{aligned} \tag{2.10}$$

$$\begin{aligned} U_p = {} & 4.04596 + e^{-42.30027x_p + 16.56714} - .04880\arctan(50.01833x_p - 26.48897) - \\ & .05447\arctan(18.99678x_p - 12.32362) - e^{78.24095x_p - 78.68074} \end{aligned} \tag{2.11}$$

In the above equations, x_i is the ratio of the surface concentration to the maximum intercalation concentration for the particular material, also referred to as the *surface state of charge* (SOC), as given in Eqn. (2.12).

$$SOC = x_i = \frac{c_{surf,i}}{c_{\max,i}},\ i = n, p \tag{2.12}$$

Having knowledge of the equilibrium potential and overpotential values at each electrode, the voltage across the cell sandwich can be calculated using the following expression, assuming there is no potential drop in the electrolyte phase.

$$V = \left|\left(U_p - U_n\right) + \left(\eta_p - \eta_n\right)\right| \tag{2.13}$$

The performance curves in terms of cell potential vs. state of charge are estimated.

2.2 Results and discussion

Due to the diffusion process, concentration of Li inside the active particle is not uniform during the lithiation or delithiation process. Distribution of Li ions inside the

Table 2.1. Material parameters used for simulating graphite anode are given below.

Name	Material parameters (Graphite)
Diffusion coefficient $\left(D_{scalar}\right)$	$3.9\text{x}10^{-14}$ m^2/s
Expansion coefficient $\left(\omega\right)$	$1.14\text{x}10^{-6}$ m^3/mol
Young's modulus $\left(E\right)$	70.57 GPa
Poisson's ratio $\left(\nu\right)$	0.277
Mean fracture energy threshold per unit area $\left(\Psi_{ua}\right)$	2 J/m^2
Radius of particle $\left(R\right)$	12.5 μm
Maximum stoichiometric Li ion concentration $\left(c_{\max}\right)$	30000 mol/m^3
Operating temperature $\left(T\right)$	298 K

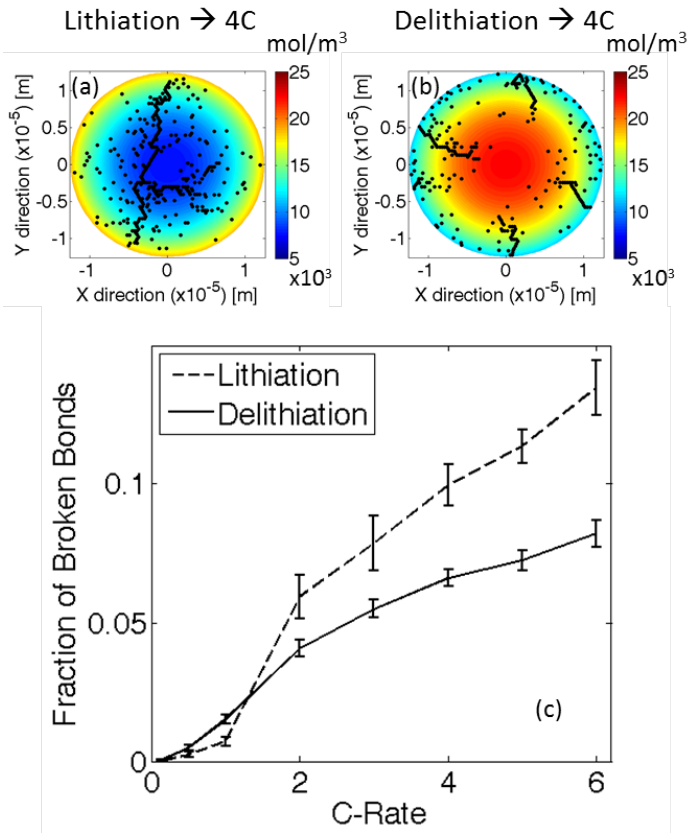

Fig: 2.3. *Evolution of brittle damage during the first lithiation or delithiation of an electrode active particle. (a) Central notch observed during lithiation process. (b) Multiple peripheral cracks appear during the delithiation process. (c) Evolution of damage with respect to C-rate during lithiation and delithiation. The color-bar in (a) and (b) signifies the distribution of Li ion concentration inside the particle in mol/m^3 units.*

electrode particle is obtained by solving Eq. (2.2). Parameters used to solve the diffusion equation are given in Table 2.1. Distribution of Li ions inside the circular cross section of an active particle at a rate of 4C is shown in Fig: 2.3(a) and Fig: 2.3(b) for lithiation and delithiation respectively. For both lithiation and delithiation, the difference in ion concentration between the center and surface is approximately 3 kmol/m^3 at 1C and 10 kmol/m^3 at 4C. This difference in Li ion concentration results in stress generation to

achieve mechanical equilibrium within the active particles. This diffusion-induced stress (DIS) causes damage initiation and nucleation while the battery is in operation. Applying this Li ion distribution into the mechanical equilibrium equation (Eq. (2.3)), force in each of the lattice spring element is calculated. Based on the energy threshold criterion mentioned in the computational methodology section, evolution of damage within the active particle is calculated. Figures 2.3(a) and 2.3(b) also show typical crack patterns during lithiation and delithiation (superimposed on the Li ion concentration profile). Lack of lithium in the central region generates tensile stress at the time of lithiation, which leads to a single central crack. Delithiation induces tensile stress close to the surface of the active particles. For Li de-intercalation, tensile stress develops close to the periphery and during Li intercalation tensile stress is observed close to the center of the particle (see Figure 2.3). Since the propensity of fracture initiation and nucleation under tensile stress is much higher than that under compressive stress [15], during lithiation cracks develop close to the center of the active particle. No cracks develop in the peripheral region during lithiation because compressive stress acts there (even though the magnitude of stress is high there). This gives rise to multiple peripheral cracks. Similar mechanisms of crack formation have been discussed by Bhandarkar and Gao[14, 144]. Amount of damage within the active particle is characterized by the fraction of broken bonds (see Ref. [51, 165]). Figure 2.3(c) shows the amount of damage during lithiation and delithiation process as C-rate increases. For lithiation, negligible damage is observed till 1C, whereas, significant increase in the amount of damage is observed for 2C and higher C-rates. During delithiation negligible damage occurs till 0.5C, and the

fraction of broken bonds starts to increase from 1C onwards. Lithiation at a rate larger than 4C and delithiation at rates higher than 6C leads to more than 10% damage within the active electrode particle. In the two-way coupled analysis, impact of such large amount of internal damage on the diffusion of Li ions within the active particles will be analyzed.

Because of the imperfection in manufacturing processes, cracks can pre-exist within the active particles (see Ref. [22, 28]). Possibility of these pre-existing cracks to propagate depends on the location of the crack and the type of loading the particle experiences [17]. Figure 2.4 presents a analysis whether a crack will propagate during lithiation or delithiation. Fig: 2.4(a), 2.4(b) and 2.4(c) show pristine particles without any pre-existing crack, with a central crack and a peripheral crack respectively. Fig: 2.4(d), 2.4(e) and 2.4(f) correspond to lithiation process and formation of central crack within the three pristine particles. Fig: 2.4(g), 2.4(h) and 2.4(i) correspond to delithiation and formation of peripheral cracks. During lithiation, because of the tensile force close to the center of the particle, the central crack propagates and the peripheral crack remains intact. Opposite phenomena is observed during delithiation, when tensile stress develops close to the periphery of the particle and the peripheral crack propagates. The central pre-existing crack remains unchanged during delithiation. For subsequent lithiation – delithiation cycles increment in damage is minimal (see Fig: 2.5). As a result the pre-existing crack does not propagate significantly in subsequent cycles. Propagation of cracks is supposed to occur during uncontrolled discharge process (charging is controlled in nature and usually happens in a low C-rate). During discharge, anode

experiences delithiation and cathode experiences lithiation. Central imperfection in anode and peripheral imperfection in cathode is less detrimental for the durability of the active particles because the pre-existing cracks have a smaller possibility of propagation under high discharge rates.

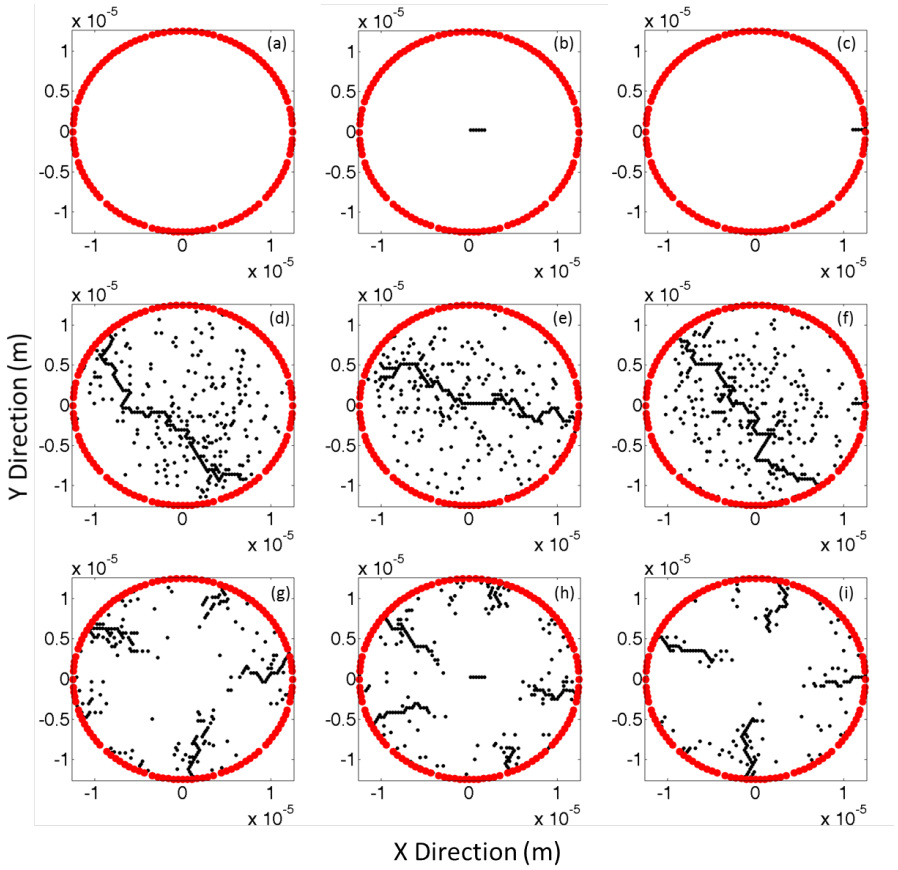

Fig: 2.4. *Different fracture scenario during lithiation and delithiation is shown here. (a) A pristine electrode particle without any initial crack. (b) Electrode particle with central initial crack. (c) Electrode particle with peripheral initial crack. (d) Formation of central crack during lithiation. (e) For the electrode with central initial crack, during lithiation, the central crack propagates. (f) For the electrode with peripheral initial crack, during lithiation, the peripheral crack remains unaffected. (g) Formation of peripheral crack during delithiation. (h) For the electrode with central initial crack, during delithiation the central crack does not propagate. (i) For the electrode with peripheral initial crack, during delithiation, the peripheral crack propagates.*

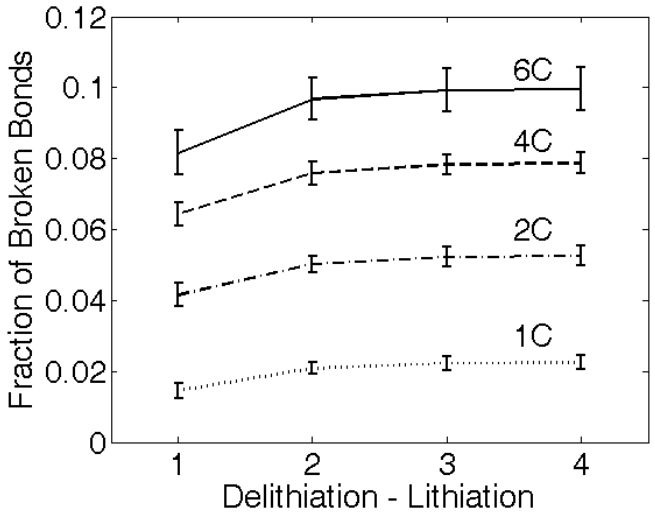

Fig: 2.5. *Increase in the fraction of broken bonds for subsequent delithiation and lithiation at four different C-rates. Along the delithiation – lithiation axis 1, 2, 3 and 4 signifies first delithiation, first lithiation, second delithiation and second lithiation respectively. For all the four C-rates examined here, total amount of damage saturates after two delithiation – lithiation cycles.*

Since the first lithiation or delithiation at high C-rates can create close to 10% damage inside active particles, it is important to assess the extent of damage upon cycling. Figure 2.5 displays the amount of damage for subsequent delithiation and lithiation in an active particle at four different C-rates. The numbers 1, 2, 3 and 4 along the abscissa of Fig: 2.5 represent subsequent delithiation, lithiation, and delithiation and lithiation process. At 4C, during the first delithiation, damage increases from 0% to 6.5%. Lithiation on the delithiated particle increases the amount of broken bond from 6.5% to 7.5%. From the earlier results, peripheral cracks are generated during delithiation (Fig. 2.4(g)), whereas, central imperfections propagate during lithiation (Fig. 2.4(d)). These two types of cracks are not supposed to impact the formation of each other. However lithiation on a delithiated particle increases the amount of broken bonds by only 1% at 4C, whereas, lithiation on a pristine particle can create as large as 10%

damage at the same C-rate. This discrepancy in damage evolution happens because of the strain energy release within the existing peripheral cracks. Subsequent delithiation and lithiation increases the damage to 7.9% and 8.0% respectively. These averaged values of damage and the error bars in Fig. 2.5 have been obtained using 10 samples at each data point. This indicates that the total amount of damage in an active particle tends to saturate after the first two cycles. For 1C, amount of damage remains constant after the first delithiation – lithiation cycle. For higher C-rates (4C and 6C), amount of damage increases during the second delithiation – lithiation cycle but the increment is very small. Saturation of damage occurs because of the fact that initially developed cracks provide strain relief during subsequent delithiation and lithiation, and new cracks do not form to a significant extent [166]. Important point to be noted here is that the developed model captures the evolution of only brittle type damage. For charge – discharge cycles over long time, can cause fatigue within the material and the existing cracks can propagate. Elevated temperature at certain regions within the electrode can also incur creep deformation and propagation of already developed crack fronts.

Inside electrode particles, diffusion induced stress is not uniform. For delithiation maximum tensile force is observed at the periphery, which decreases towards the center and converts into compressive force very close to the central region of the electrode. Force concentration at the crack tip tries to increase with increasing initial crack length. But the tensile force that acts perpendicular to the initial crack at the crack tip decreases with increasing crack length. Because of these two competing mechanisms, there exists a critical crack length at which maximum force concentration is observed at the tip. In Fig:

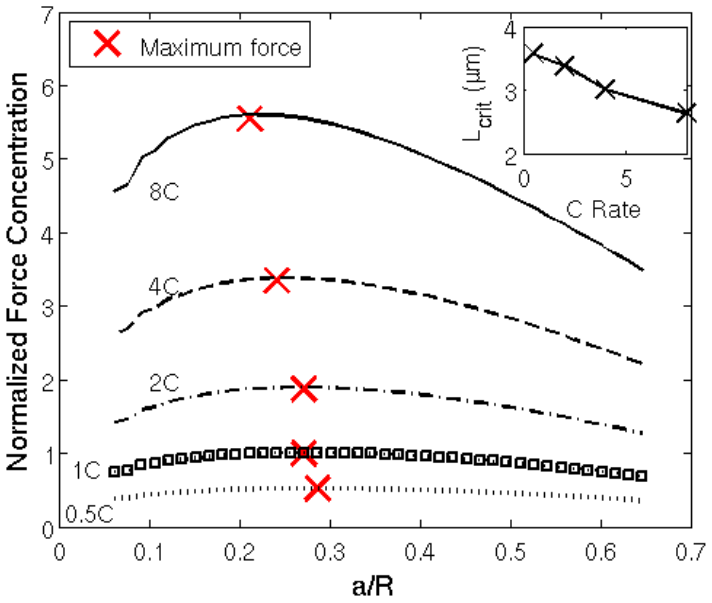

Fig: 2.6. *Force concentration at the crack tip is plotted for different initial peripheral crack sizes. Initial crack size at which maximum force concentration is observed (critical crack length) depends on the C-rate. Inset shows a plot of how the critical crack length decreases with increasing C-rate. These results were calculated on a particle with diameter 25μm.*

2.6, normalized force concentration has been plotted against the initial crack length for different C-rates. "a" is the initial crack length and "R" is the radius of the electrode particle. Force values have been normalized by dividing each of the individual forces by the maximum force obtained at 1C. The cross mark indicates the critical initial crack length at which maximum force concentration is observed for different C-rates. An interesting phenomenon observed in Fig: 2.6 are that with increasing C-rate, the critical initial crack length decreases. The figure in the inset indicates that for an active particle with 25μm diameter, the critical crack length at which maximum tensile force is observed decreases from 3.6μm at 0.5C to 2.6μm at 8C. For extremely high C-rates, very high concentration gradient is observed close to the periphery. As a consequence, tensile force at the crack tip decreases rapidly with increasing crack size and a smaller critical

crack length is observed. At smaller C-rates, where larger initial cracks are more vulnerable, the net tensile force acting at the crack tip may not be significant enough for the crack to propagate. For large C-rates, very small initial cracks encounter a destabilizing effect. With increasing crack length the force acting at the crack tip increases and it has the ability to induce enough kinetic energy to the crack front to span through the entire particle and cause terminal failure [16]. However, the simulations conducted by the authors were not able to capture any such scenario, because it is based on quasistatic mechanics, and the dynamic crack propagation aspects have not been modeled. From these results, it can be concluded that, for high C-rate applications, small pre-existing cracks can be more detrimental than larger imperfections.

Equilibrium state of a system is defined by the minimum energy configuration it can attain. For elastic, brittle, electrode active particles with zero potential and kinetic

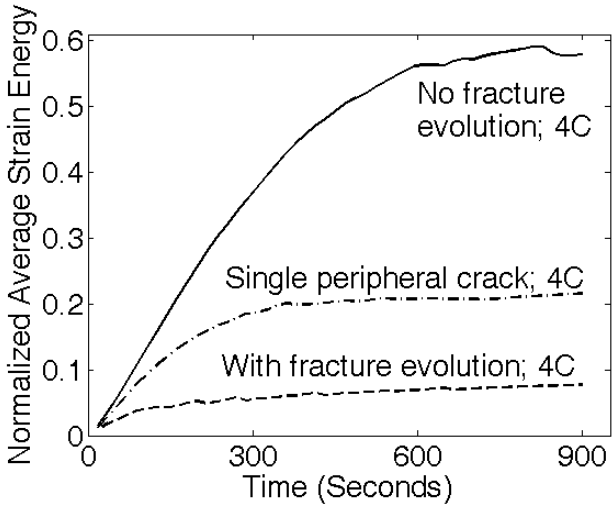

Fig: 2.7. *During delithiation evolution of strain energy with respect to time is plotted for different fracture scenarios at 4C. When no fracture is considered, maximum strain energy is observed (solid line). Presence of a single peripheral crack can significantly reduce the average strain energy (dash – dot line). When damage is allowed to evolve freely, strain energy is always bounded below a certain limit (dash – dash line).*

energy, all the energy is because of the contribution from elastic strain energy. During galvanostatic discharge process at 4C, evolution of average strain energy of an active particle has been calculated and plotted in Fig: 2.7. Similar strain energy calculations for potentiostatic charging process have been reported elsewhere (see Ref. [22, 167]). The mean fracture threshold to obtain the "normalized average strain energy" value divides the average strain energy. When no fracture evolution is taken into consideration, energy of the particle is very high (solid line in Fig: 2.7). Presence of a small peripheral crack can reduce the strain energy significantly (Ref. [22]) (dash – dot line in Fig: 2.7). When complete evolution of fracture is allowed, strain energy of the particle is bound within a certain limit, which is much less than the mean fracture threshold of that particle (dash – dash line in Fig: 2.7). Since minimum strain energy is attained with the evolution of fracture, it is more likely that most of the electrode active particles will experience internal damage under high C-rate conditions. Another important finding from Fig: 2.7 are the magnitude of the normalized average strain energy. From general understanding, the active particle can experience fracture only when its "normalized average strain energy" approaches unity. However, when fracture evolution is allowed, the normalized value of the strain energy never goes above 0.1. But, the damage is already around 6.5% (from Fig: 2.5), which seems to be counter-intuitive. The aspects of localization and material heterogeneity must be introduced to explain this apparent discrepancy. Because of material heterogeneity, the fracture energy threshold for each spring varies over a wide range of values. At low externally applied concentration gradient, some bonds with low fracture threshold energy can break. Force carried by these broken bonds gets

distributed in the surrounding elements and increases the force concentration. Hence, the localization effect becomes more prominent and starts to affect the overall fracture evolution. Because of this localization, even though the "normalized average strain energy" lies much below the fracture threshold energy, significant internal damage and cracks develop within the material. An important assumption is the values of fracture threshold energy for each element were calculated randomly according to a Uniform distribution.

The significant amount of damage observed in electrode particles under high C-rate conditions can be significantly mitigated by reducing the particle size[19, 29, 149]. Figure 2.8(a) shows the Li ion concentration profile and distribution of broken bonds at 4C for an electrode particle with 3.125μm diameter. Concentration and broken bond profile for a particle with 25μm diameter under the same 4C discharge is shown in Fig: 2.8(b). Well-developed cracks are clearly visible within the 25μm particle, whereas, the smaller particle contains much less internal damage. Figure 2.8(c) shows the reduction in total amount of broken bonds with decreasing particle size. The error-bars have been obtained by averaging the results over 10 different samples. For discharge at a rate of 4C, a 25μm particle experiences approximately 7.0% damage. However, an electrode particle with 800nm diameter shows less than 1.0% damage. Usage of nanometer sized electrode particles for reducing the damage is very much evident from this analysis. Similar reduction in damage has been observed in 1C and 2C as well. For smaller sized particles the diffusion gradient is smaller as compared to larger sized particles. Since magnitude of stress generated in electrode particles is solely governed by Li ion

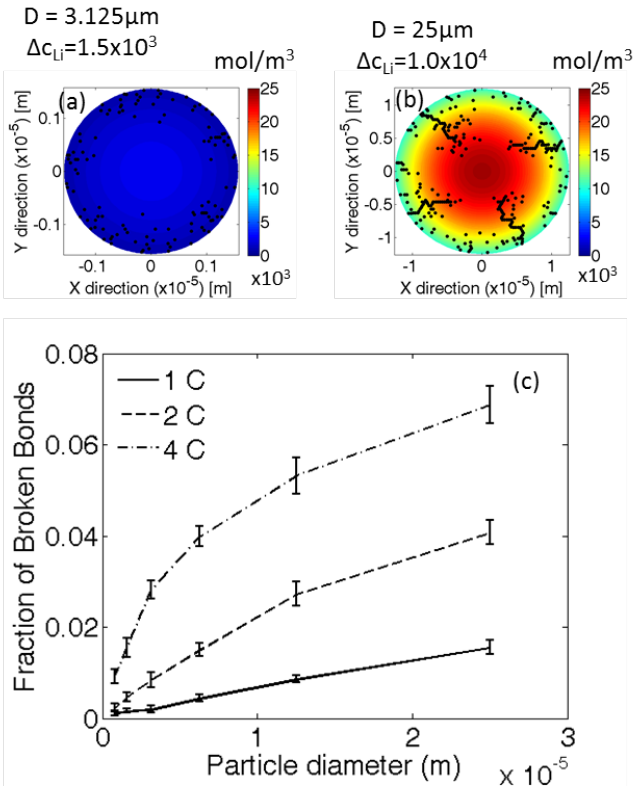

Fig: 2.8. *With decreasing particle size, development of total amount of damage in the particle also reduces. (a) Formation of less damage in a particle with diameter 3.125µm. (b) More damage evolved in a larger particle with diameter 25µm. (c) Reduction in total amount of damage with decreasing particle size is observed for all the C-rates of 1C, 2C and 4C.*

concentration gradient, lesser magnitude of stress (force in the springs) is developed in smaller particles than the larger ones. Since stress generation in electrode particles is governed solely by the Li ion concentration gradient, less stress (force in the springs) is developed in smaller particles than the larger ones. Since the material is same, fracture threshold energy for both smaller and larger particles remains unchanged. Hence, larger force in the 25µm particle leads to more internal damage and fracture. Less force is developed in the smaller particle, which results in smaller amount of damage.

All the analysis reported till now was obtained using one-way coupling mechanism. Two-way coupled simulations have been conducted to characterize the impact of mechanical damage on the diffusion of Li ions. Figure 2.9 depicts the changes in Li ion distribution within the active particle due to mechanical fracture. Figure 2.9(a) and 2.9(b) shows the distortion in concentration profile for $\alpha = 0.9$ and $\alpha = 0.6$ respectively. For $\alpha = 0.9$ almost symmetric Li ion distribution is observed, whereas, with $\alpha = 0.6$ significant distortion in the concentration profile close to the periphery is evident. Average concentration of Li ions on the particle surface has been plotted in Fig: 2.9(c) for different values of α (solid line). Maximum and minimum values of surface concentration have also been plotted. The error-bars have been obtained by averaging over 10 samples. With $\alpha = 1.0$, there is no impact of mechanical damage on the diffusion process. This results in axisymmetric diffusion profile with average, maximum and minimum concentrations having the same value. As the value of α decreases, impact of mechanical damage on the diffusion process increases. Fracture induces asymmetry in the Li ion concentration profile. With decreasing α, maximum and minimum values of ion concentration increases and decreases respectively. The average surface concentration has also been observed to increase. With smaller values of α (= 0.6), induced mechanical damage reduces the diffusion coefficient. Hence, during delithiation, it becomes more difficult for the Li ions to get out of the electrode particles and results in increased surface concentration. Thus, mechanical damage has a deteriorating impact on the movement of Li ions within the active particles. During delithiation, the cracks are observed to develop close to the periphery of the particle. In

the present simulation, it has been assumed that no electrolyte flows inside the active particles through the cracks formed on the outer surface. If electrolytes were allowed to flow inside the electrode particles, completely different boundary condition for the diffusion equation has to be considered. Formation and propagation of crack fronts expose fresh electrode surface to the electrolyte, which is extremely vulnerable to SEI formation and capacity fade [119].

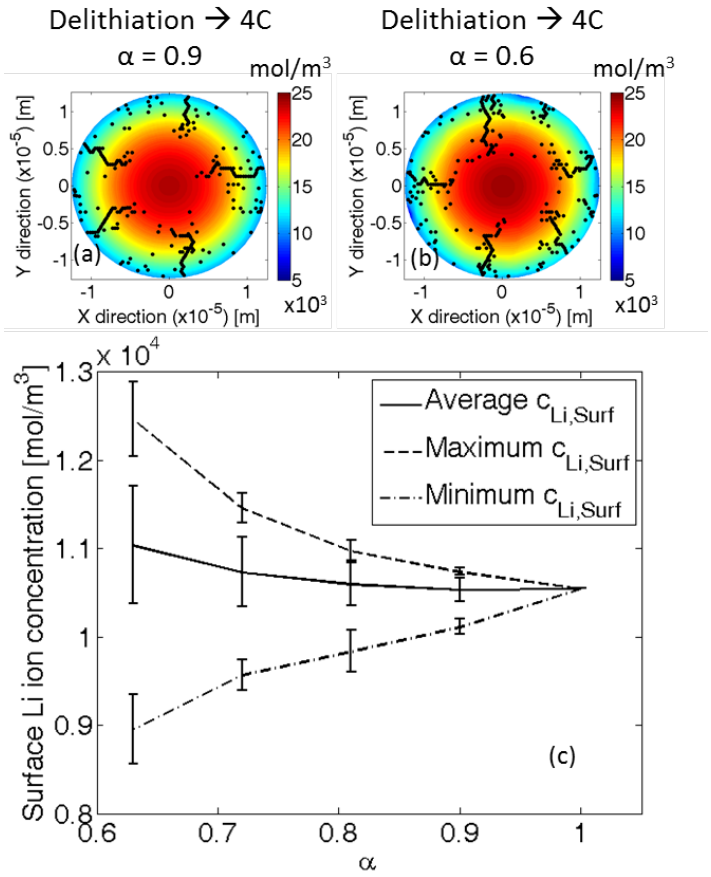

Fig: 2.9. *Implementation of the two way coupled analysis reveals that with evolution of fracture, Li ion concentration profile within the particle changes and loses its azimuthal symmetry. (a) Li ion concentration profile looks symmetric along the azimuthal direction for α = 0.9. (b) Lack of symmetry along the azimuthal direction is clearly visible with α = 0.6. (c) With decreasing α, the average surface concentration of Li ions increases. Maximum and minimum surface concentration also changes as the value of α is reduced.*

The increase in average surface concentration of lithium-ion due to mechanical damage has a significant impact on the performance of the cell. Figure 2.10(a) and 2.10(b) shows the cell potential vs. surface SOC behavior during discharge at 2C and 4C respectively. Three different values of α (= 1.0, 0.7 and 0.6) have been taken into consideration. Voltage drop due to transport limitation of lithium is of emphasis in this study. In the current simulations, it has been assumed that the electrolyte conducts Li ions much faster than the electrode material and capacity loss due to mass transport limitation is solely because of diffusion of Li ions within the active particles. For both 2C and 4C, as the value of α decrease, the capacity loss due to lithium transport increases. Since the amount of fracture developed at 4C is much larger than that at 2C, loss of capacity is higher in Fig: 2.10(b) than 2.10(a). It is important to note that the effect of the formation of SEI on capacity loss has not been taken into consideration. The capacity loss underscores the influence hindered lithium diffusion due to higher tortuosity from underlying fracture. Hence, the impact of mechanical damage must be taken into consideration while analyzing the battery performance at high C-rates.

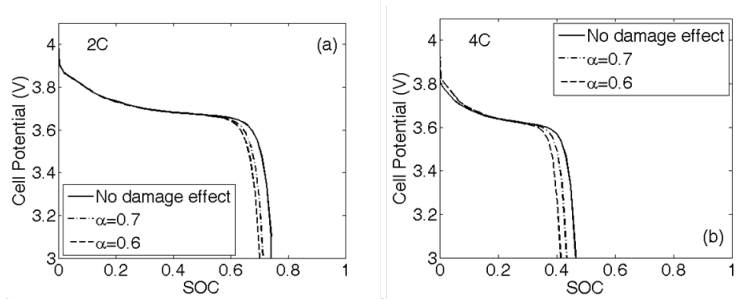

Fig: 2.10. *With decreasing value of α, the concentration of Li ions on the particle surface varies significantly. This change affects the overall performance of the electrochemical cell. Operating cell potential vs. state of charge (SOC) is plotted for discharge rates of 2C and 4C. As the value of α decrease, capacity of the cell also reduces. This image implies that internal mechanical damage can impact the overall capacity of the battery.*

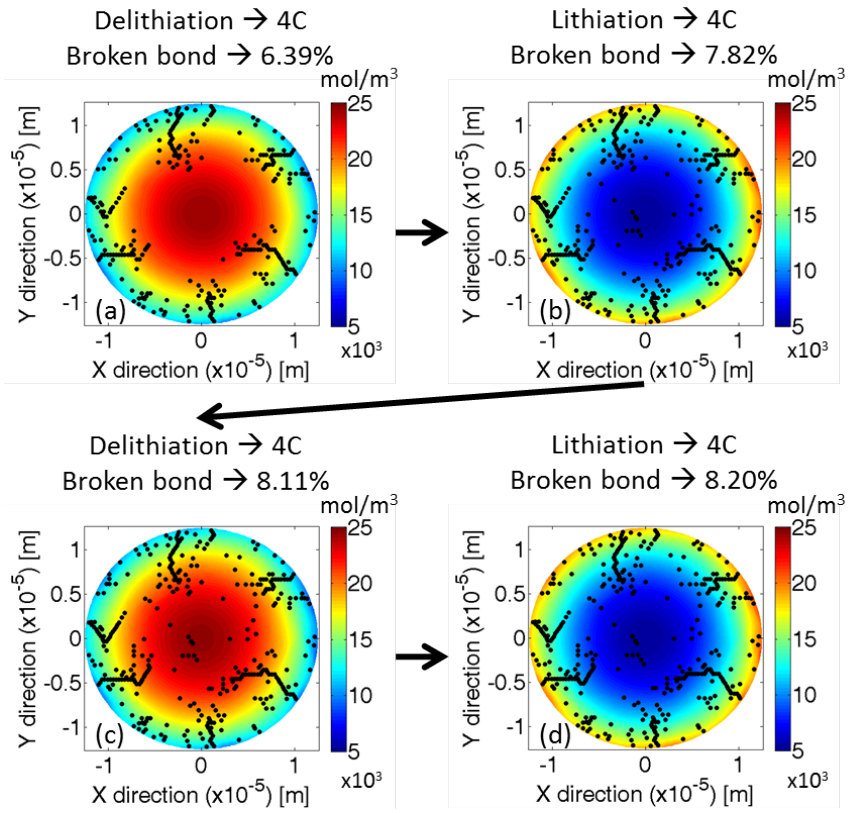

Fig: 2.11. *Fracture pattern superimposed on the concentration profile for a two-way coupled simulation with α = 0.6. (a) Delithiation in a pristine anode particle that result in peripheral cracks. (b) Lithiation on the previously delithiated electrode particle does not result in the formation of a significant damage in the central region. (c) Subsequent delithiation increases the peripheral damage in a smaller amount. (d) Further lithiation causes very small increment in overall damage of the electrode particle. Significant distortion in the Li ion concentration profile is observed for coupled simulations. All the concentration values are shown in moles/m^3 unit.*

The next question that should be answered is how significantly the modified Li ion concentration affects the evolution and nucleation of damage. Simulations have been conducted to visualize the impact of different values of α on the formation of internal damage. For large values of α (such as, $\alpha > 0.8$), impact of mechanical damage on Li ion concentration is not significant and almost equivalent to the undamaged scenario. For $\alpha = 0.6$ the Li ion concentration profile is shown in Fig: 2.11. Figure 2.11(a),

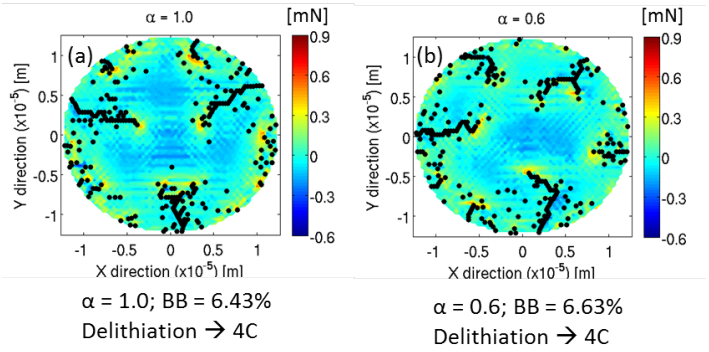

Fig: 2.12. *Fracture profile superimposed on force contour plots. Significant tensile force concentration is observed at the crack tip. Compressive force is detected at the center of the particle. (a) Force contour for delithiation at 4C with α = 1.0. (b) Force contour for delithiation at 4C with α = 0.6.*

2.11(b), 2.11(c) and 2.11(d) correspond to subsequent delithiation, lithiation, delithiation and lithiation respectively, on the same electrode particle. In Fig: 2.11, total amount of damage has also been mentioned for subsequent delithiation and lithiation processes at 4C. Saturation of the number of broken bonds signifies that even for $\alpha = 0.6$, because of the strain relief provided by already existing cracks, total amount of damage saturates after approximately two delithiation – lithiation cycles (also see Fig: 2.5). Under both one-way as well as two-way coupled scenario, force distribution within the particle during delithiation can specify the probability of increase in damage. For a pristine particle without any damage, during delithiation, the central portion is subjected to compressive force, whereas, the peripheral region experiences tensile force. Figure 2.12(a) and 2.12(b) shows the force distribution at the end of discharge with α = 1.0 and α = 0.6 respectively. Because of the crack propagation, regions that were under compression at the beginning of delithiation can experience tensile force towards the end of the process. Significantly higher tensile force concentration has been observed at the crack tips for both the values of α. Since with increasing crack size force acting at the

crack tips decreases, strain energy at the crack tips can drop below the fracture energy threshold resulting in a saturation of total amount of damage.

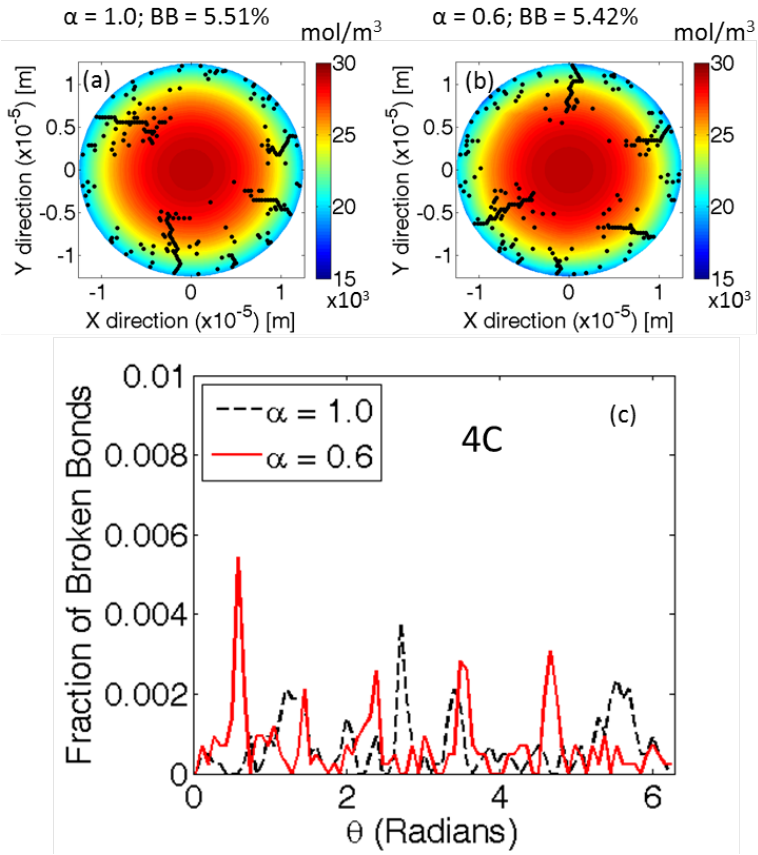

Fig: 2.13. *Comparison between the amounts of localized damage (fraction of broken bonds) for one-way (α = 1.0) and two-way coupled (α = 0.6) analysis. Damage is evaluated at different locations along the θ direction. More localization is observed (in terms of larger peaks) for α = 0.6 (the two-way coupled scenario).*

Even though with α = 1.0 and α = 0.6, total amount of mechanical damage is almost the same, significant difference can be observed in terms of localization of the mechanical failure. To analyze how localized the development of mechanical damage has been, Fig: 2.13(c) show the fraction of broken bonds along the azimuthal direction for α = 1.0 and α = 0.6. Fig: 2.13(a) and 2.13(b) displays the concentration profile and

fracture pattern that has been plotted in Fig: 2.13(c). Larger peaks are evident from the figure for α = 0.6 than α = 1.0. Hence, more localized damage for α = 0.6 has been observed. Here, α = 1.0 corresponds to one-way coupling. Hence, two-way coupling can lead to significant amount of localization as compared to its one-way coupled counterpart.

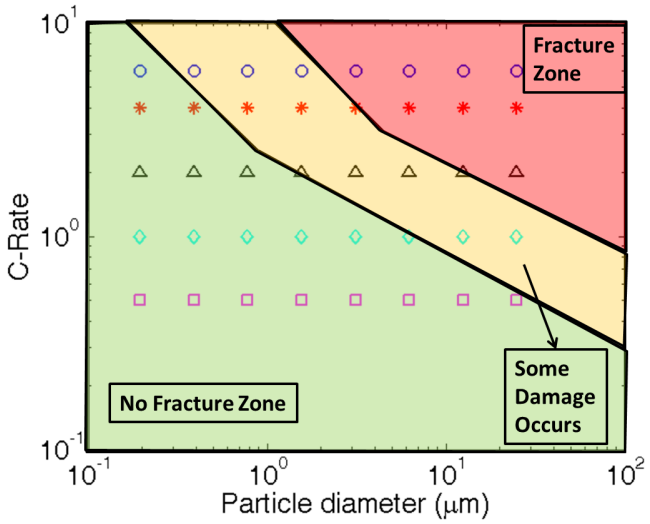

Fig: 2.14. *Fracture map of different particle sizes with respect to increasing C-rates is shown here. All the calculations have been conducted on a graphite anode particle under galvanostatic discharge process under the assumption of two-way coupling with α = 0.6. "No fracture" corresponds to very little amount of internal damage (< 0.5%). "Some damage" corresponds to formation of macroscopic damage in the range of 0.5% to 3%. "Fracture zone" signifies operating conditions which results in more than 3% mechanical damage.*

A *fracture phase-map* (see Fig: 2.14) has been developed to characterize the safe/unsafe operating regime in terms of particle size and C-rate. Two-way coupled analysis with α = 0.6 has been considered here. For one-way coupled analysis, it has already been reported in Fig. 2.8 that decreases in particle size results in reduction of macroscopic damage. Similarly for two-way coupled computation, either very small C-rate or very small particle size will definitely give rise to reduced amount of mechanical

damage. From the fracture map shown in Fig: 2.14, it is evident that discharge at C-rates less than or equal to 0.5C will never give rise to any significant damage for particles as large as 25μm. On the other hand, particles with 200nm diameter will never go through any mechanical damage for C-rates as large as 6C. An intermediate domain has been defined where some macroscopic damage is observed, but it is not severe from the perspective of short-term operations. Major amount of fracture has been observed during the first delithiation for large particle sizes and relatively higher C-rates. For the purpose of realistic operations, combinations of particle size and C-rate, which lie in the no fracture zone, are preferable. Combinations that lie in the intermediate zone, are preferable for short-term applications, but also have the potential for creep and fatigue failure during long term operations. Operating conditions which lie in the fracture zone must be avoided; otherwise they lead to significant amount of fracture, SEI formation and eventual loss of capacity during the first delithiation – lithiation cycle.

Elastic moduli of the electrode material are usually dependent on the Li ion concentration. DFT analysis shows that for graphite the Young's modulus can increase by three times with increasing concentration of active species (see Ref. [22, 27]). Based on the concentration dependent elastic moduli correlations described by Deshpande *et al*.[29], the evolution of fracture in different electrode active particles, which show hardening or softening behavior with Li insertion, has been simulated. Figure 2.15(a) and 2.15(b) show a comparative analysis for total amount of damage, over two

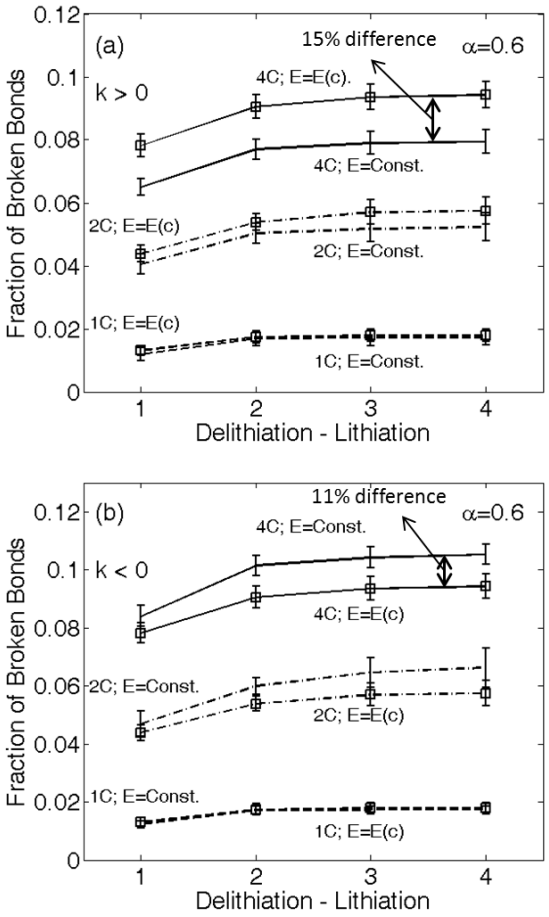

Fig: 2.15. *Total amount of damage is plotted for two delithiation – lithiation cycles. When concentration dependent elastic moduli are taken into consideration, fraction of broken bonds can be significantly different from the analysis with constant elastic moduli. This effect is more prominent for higher C-rates (> 2C). The entire analysis is conducted with α = 0.6. (a) Electrode material stiffens with Li insertion, which results in enhanced damage. (b) Electrode material softens with Li insertion, which results in damage mitigation.*

delithiation – lithiation cycles, between constant elastic moduli and Li ion concentration dependent elastic moduli. Two-way coupling analysis with α = 0.6 has been considered here. For very small C-rate applications, both concentration dependent and concentration independent elastic moduli lead to almost same amount of macroscopic damage (see 1C in Fig: 2.15(a) and 2.15(b)). However, for higher C-rate applications (see 4C in Fig:

2.15(a)), where increasing Li concentration stiffens the material, leads to larger amount of broken bonds for concentration dependent elastic moduli. On the other hand, where increasing Li concentration softens the material, large C-rate operating conditions (see 4C in Fig: 2.15(b)) lead to reduction of macroscopic mechanical damage. Towards the end of the second delithiation – lithiation cycle, approximately 15% extra damage has been observed for stiffening type of materials. Approximately 11% less damage has been observed for active particles that soften with increasing Li concentration. Even with concentration dependent elastic moduli, for both hardening and softening type of materials, saturation of the macroscopic damage signifies that strain energy is released by the existing cracks which hinders the formation of internal damage as well as reduces the probability of existing crack front propagation. It is an important point to note that for silicon anode, with increasing Li ion concentration, elastic moduli decreases [28, 29]. Since, in this analysis small strain and small displacement has been assumed, and Si actually goes through very large deformation, the present analysis precludes accurate quantification for Si anodes under operation. However, the qualitative trend can be captured correctly and is applicable to other intercalation materials, which show softening behavior. This study underscores the criticality of the stiffening/softening material behavior with intercalation for reduced damage evolution in electrode active material while from electrochemical standpoint higher capacity is a desirable feature.

Evolution of strain energy for hardening and softening type electrode material is reported in Fig: 2.16(a) and 2.16(b), respectively. For active particles, where Li insertion causes the material to harden, shows very high stiffness (and equivalently large force) at

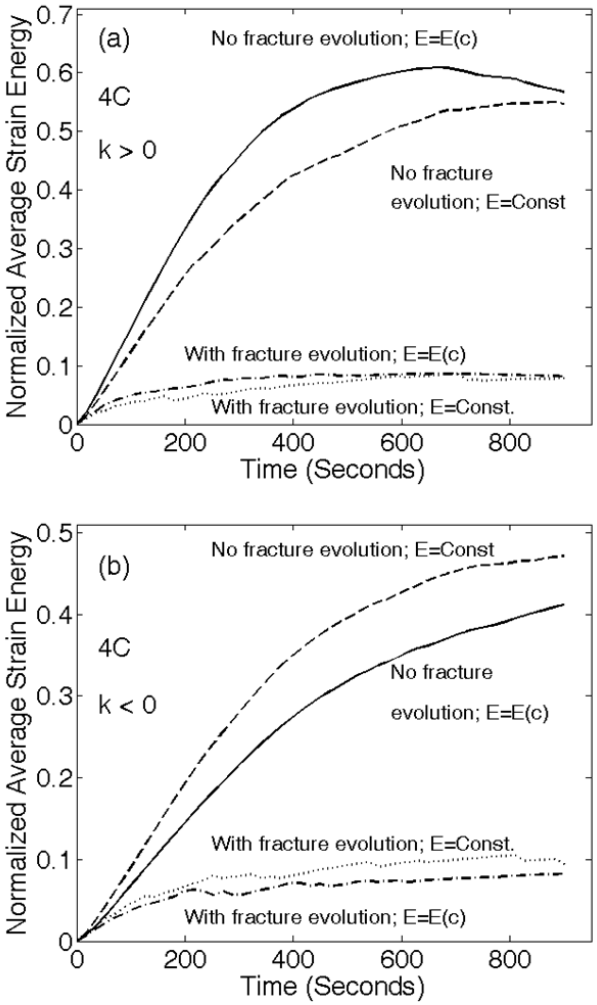

Fig: 2.16. *Strain energy evolution of representative anode materials during delithiation. (a) Hardening behavior is observed with increasing stoichiometric Li concentration (e.g. Graphite). (b) Softening behavior is observed with increasing stoichiometric Li concentration (e.g. Silicon). Since, for hardening type material, more strain energy has to be released, more damage is observed. Whereas, for softening type materials less strain energy release is required, which results in reduced amount of mechanical damage.*

the beginning of delithiation. This leads to higher strain energy as compared to constant elastic moduli scenario when fracture evolution is not taken into consideration (see Fig: 2.16(a)). For materials where Li insertion causes softening, low stiffness (and less force) is observed at the initiation of delithiation. Under no fracture scenario, softening type

material results in smaller strain energy than its constant elastic moduli counterpart (see Fig: 2.16(b)). With fracture evolution, for both constant elastic moduli and Li concentration dependent elastic moduli, strain energy saturates to an almost constant value for both hardening and softening type material (see Fig: 2.16(a) and 2.16(b)). Since, for hardening type material, the average strain energy has to drop by an amount that is more than the constant elastic moduli case, more bond breaks for these types of materials. Opposite behavior is observed for the softening type material that results in reduced amount of damage. For hardening type material, strain energy evolution curve without fracture scenario, dips down at the end of delithiation (see solid line in Fig: 2.16(a)). Whereas, for softening type material, strain energy evolution curve without fracture, rises steadily at the end of delithiation (see solid line in Fig: 2.16(b)). This happens because of softening (or hardening) induced by lack of Li ions at the end of delithiation in the hardening (or softening) type material.

2.3 Conclusion

A stochastic methodology based on the lattice spring model, coupled with solid-state lithium diffusion and performance analysis has been developed to characterize mechanical fracture in lithium-ion battery electrode active particles. Galvanostatic discharge process in graphite electrodes was primarily considered. Peripheral crack during delithiation and central crack during lithiation has been observed. Higher C-rates can lead to significantly larger amount of damage. Due to strain energy release, total amount of damage saturates after two or three delithiation – lithiation cycles at the same C-rate. Using two-way coupled analysis, dependence of mechanical damage on solid-

state lithium diffusion has also been captured. Hindered lithium diffusion owing to increased tortuosity emanating from crack formation leads to capacity loss. Concentration dependent elastic moduli further lead to the formation of significantly larger amount of damage under high C-rates.

A key question that needs to be answered is how the formation of cracks in electrode particles during operational conditions can be minimized. The importance of critical particle size has been emphasized. Furthermore, the presence of pre-existing cracks results in strain energy release and leads toward potential reduction in further formation and propagation of new cracks. Hence, addition of initial pre-existing imperfections (e.g. microcracks) might be considered as a potential pathway toward intercalation materials development with improved damage resistance attributes. It has also been observed that materials, which soften with lithium intercalation, lead to reduce amount of mechanical damage during the first delithiation process. A fracture phase-map has been developed to characterize the safe/unsafe operating regime in terms of particle size and C-rate. Finally, the importance of underlying stochastic and fracture mechanics due to diffusion induced stress requires enhanced insight toward developing possible mitigation strategies for reduced mechanical degradation and thereby improved performance and life of lithium-ion batteries.

CHAPTER III

STATISTICAL ANALYSIS OF DAMAGE BEHAVIOR IN INTERCALATION MATERIALS*

In the previous chapter it has been discussed in details that under diffusion induced stress, significant amount of mechanical degradation can occur. Some statistical properties of damage evolution and characterization of fracture surface roughness under gradient loading conditions will be analyzed in this chapter.

3.1 Computational methodology

Random spring model (RSM) has been used in this study to characterize the damage and failure of materials under diffusion induced stresses. The random threshold spring model consists of a two-dimensional triangular lattice network of size $L \times L$. Figure 3.1(a) demonstrates a general two-dimensional lattice spring network with $L = 6$. Unlike the random fuse model, these 2D lattice springs have two degrees of freedom at each node (displacement along x and y directions). Each spring connects the two nearest neighbor nodes in the lattice network. Modifications were made to the basic RSM to include shear stiffness (G) in each spring along with its axial stiffness (E), which makes it equivalent to the Random Born Model (RBM). However, angle between two springs in the born model is not conserved, which makes the model *not* rotationally

*Under preparation: "Stochastics of diffusion induced damage in intercalation materials" by P. Barai and P. P. Mukherjee (for submission in *Journal of the Mechanics and Physics of Solids*)

invariant and rigid body rotations of a network can store energy [57].

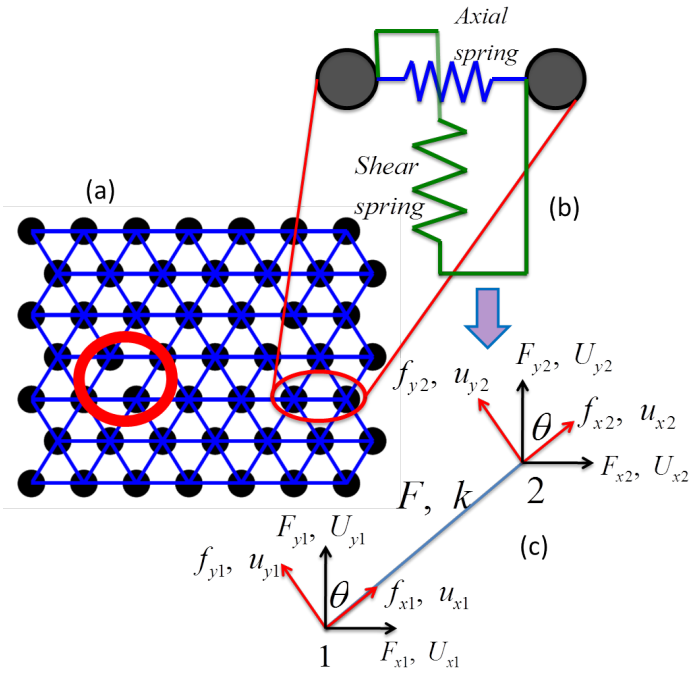

Fig: 3.1. *(a) Schematic representation of the lattice spring network that has been taken under consideration in this investigation. (b) Entire mass of the system is assumed to be concentrated at each node. The nodes are connected by axial as well as shear springs. (c) Global and local force and displacement at each node.*

In random born model we start with a fully intact lattice system with springs having unit length $(l=1)$, unit square cross section $(A=1)$, Young's modulus $E=1$ and shear modulus $G=0.2$. Axial stiffness of each spring is defined as $k_n=\frac{AE}{l}$ and shear stiffness of each spring is given by $k_s=\frac{AG}{l}$. Figure 3.1 shows schematic diagram of the lattice network adopted in random born model. The Poisson's ratio for a 2D lattice network of Born type elements with coordination number six is given as,

$$\nu_{PR}=\frac{k_n-k_s}{3k_n+k_s} \tag{3.1}$$

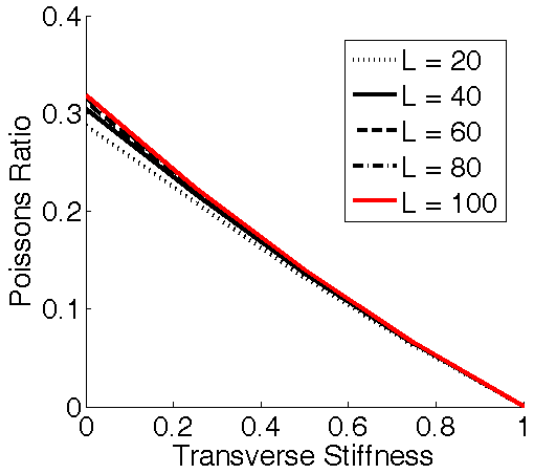

Fig: 3.2. *Decrease in Poisson's ratio of the triangular lattice network with increasing shear stiffness of the springs. For zero transverse stiffness, Poisson's ratio of the lattice network asymptotically approaches 1/3 for increasing system size. As the transverse stiffness is increased to 1.0, Poisson's ratio for network of all sizes decreases to zero.*

With zero value of the shear modulus $(G = 0)$, the triangular network of springs show a constant Poisson's ratio (ν_{PR}) of $1/3$ [47]. As the shear modulus is increased from zero to unity (*G=0* to *G=1*), keeping the Young's modulus equal to unity $(E = 1)$, Poisson's ratio (ν_{PR}) of the network decreases from $1/3$ to 0. Figure 3.2 shows the linear variation of Poisson's ratio with constant E but changing values of G for different lattice sizes. Applying unit displacement along the vertical direction and measuring the displacement of the lattice along the horizontal direction have estimated Poisson's ratio. Size effect in the calculated value of Poisson's ratio is evident from Fig. 3.2, where with increasing lattice size the value of ν saturates to 1/3 at $G = 0$. Even though there are two modes of deformation, axial and shear displacements, only one energy based breaking threshold (ψ_t) has been defined in this model. Since the loading

is defined by concentration gradients, higher concentration is observed in one side of the lattice and lower concentration on the other side. Hence periodic boundary condition is not applicable along the horizontal direction.

From Fig. 3.1(c), force in each of the spring is calculated along the axial and shear directions in the local coordinate frame. The axial force is defined as $f_n = k_n\left(u_{x2} - u_{x1}\right)$ and the forces in transverse directions are given as $f_s = k_s\left(u_{y2} - u_{y1}\right)$. The local force – displacement relationship in a matrix form is given as,

$$\begin{bmatrix} f_{x1} \\ f_{y1} \\ f_{x2} \\ f_{y2} \end{bmatrix} = \begin{bmatrix} k_n & 0 & -k_n & 0 \\ 0 & k_s & 0 & -k_s \\ -k_n & 0 & k_n & 0 \\ 0 & -k_s & 0 & k_s \end{bmatrix} \begin{bmatrix} u_{x1} \\ u_{y1} \\ u_{x2} \\ u_{y2} \end{bmatrix} \tag{3.2}$$

where, $\vec{f}$ is the local force vector and $\vec{u}$ is the local displacement vector. Global forces and displacements are related to the local forces and displacements through the relations $\vec{F} = \left[T\right]^T \vec{f}$ and $\vec{U} = \left[T\right]^T \vec{u}$, where $\left[T\right]$ is the transformation matrix. The rotation matrix $\left[T\right]$ is defined in terms of the angle the spring makes with the horizontal direction (denoted as θ).

$$\left[T\right] = \begin{bmatrix} \cos\theta & \sin\theta & 0 & 0 \\ -\sin\theta & \cos\theta & 0 & 0 \\ 0 & 0 & \cos\theta & \sin\theta \\ 0 & 0 & -\sin\theta & \cos\theta \end{bmatrix} \tag{3.3}$$

Global stiffness matrix is constructed from the local stiffness matrix using the relation $\left[K_g\right] = \sum \left[T\right]^T \left[k_l\right]\left[T\right]$. Concentration gradient induced loading inside the lattice

network is calculated in terms of concentration induced displacement and corresponding force. The expression $\Delta u^d = \omega \cdot \Delta c \cdot l$ shows concentration gradient induced displacement along the local axial direction. Here, ω is the diffusion expansion coefficient that has a typical value of $1.14 \times 10^{-6} m^3 / mol$ for graphite, Δc is the incremental change in the concentration of the intercalation material, l is the length of the spring type element and Δu^d is the diffusion induced displacement. Force vector in each spring due to concentration gradient is obtained as, $\vec{F}^d = \left[T\right]^T \vec{f}^d = \left[T\right]^T \left[k_l\right] \Delta \vec{u}^d$. Considering the intercalation-induced force as externally applied load, the system is equilibrated by solving a set of linear algebraic equations of the form $\left[K_g\right] \cdot \vec{U} = \vec{F}_d$, using the LU decomposition method. The equilibrium global displacement values are converted to the local coordinate system and local forces in each spring are calculated using Eq. (3.2).

Fracture in each of the springs is defined in terms of an energy threshold criterion. Energy in each spring is calculated according to $\psi = \frac{1}{2} \vec{F} \cdot \vec{U} = \frac{1}{2} \vec{f} \cdot \vec{u}$. Here, $\vec{F}\left(\vec{f}\right)$ and $\vec{U}\left(\vec{u}\right)$ are the global (local) force and displacement vectors for each of the springs. The host material inside which intercalation happens is assumed to display brittle fracture behavior. As the energy in a spring exceeds its breaking threshold $\left(\psi > \psi_t\right)$, it is irreversibly removed from the network (see Fig. 3.1(a)). The forces are redistributed instantaneously which implies that stress relaxation happens much faster than the breaking of a bond, hence, the quasistatic assumption is applied. After one bond

is broken, the lattice network is re-equilibrated before breaking subsequent bonds. This process of increasing the concentration induced load and removing bond one at a time is continued until a spanning crack develops and the lattice system falls apart. In the random Born model, threshold energy for each spring is obtained from a uniform probability distribution between [0, 1]. Randomly distributed fracture threshold energy is capable of capturing the inherent disorder observed in any realistic brittle material. Different lattice system sizes of L = [40, 60, 80, 100, 120, 140] are considered in this study. To reduce the statistical disorder induced error, large numbers of sample have been simulated for each lattice size and each type of loading conditions.

3.2 Concentration gradient induced loading

During operation the intercalating particles diffuse inside the host materials, which creates concentration gradients and hence stresses are developed that leads to fracture. At different spatial locations of the host material, various concentration gradients are observed. The observed concentration is higher in one end and lower in the other. This linear concentration profile is modeled as, concentration $c(x) = \Delta + \varepsilon(x)$, where Δ is assumed to be unity $(\Delta = 1)$ and $\varepsilon(x)$ varies as a function of x and changes from $-\delta$ at the left end to $+\delta$ at the right end of the lattice $(-\delta < \varepsilon(x) < +\delta)$. Here δ can vary between 0 and 1. Figure 3.3 shows an illustrative schematic diagram of the concentration loading profile on the lattice network. Three different values of the δ parameter have been taken into consideration in this article, $\delta = [0.1, 0.5, 0.9]$. Higher values of δ correspond to very fast intercalation or de-intercalation of the diffusing

species. Similarly lower value of δ signifies slow intercalation/de-intercalation phenomena. In a realistic Li ion battery, during high discharge rates, very fast de-intercalation of Li ions occurs. Here, the entire possible low $(\delta = 0.1)$, medium $(\delta = 0.5)$ and high $(\delta = 0.9)$ concentration gradient scenarios are taken into consideration.

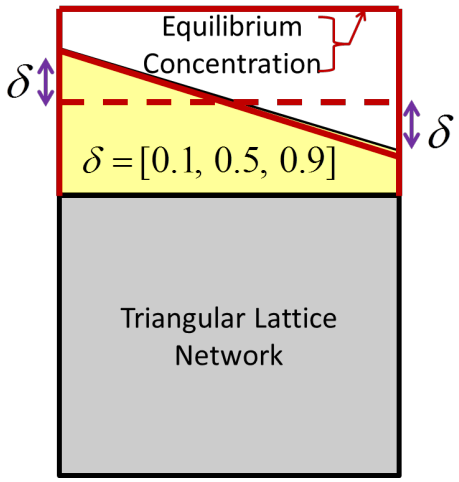

Fig: 3.3. *Schematic diagram representing the concentration or temperature profile applied on the body. The parameter* δ *signifies steepness of the temperature gradient. For* $\delta = 0.1$*, the temperature gradient is almost uniform throughout the network. Higher values of* δ *such as* $\delta = 0.5$ *or* $\delta = 0.9$ *corresponds to more steep temperature gradients. Total area under the temperature profile curve has been kept constant.*

3.3 Results and discussion

In this section, the effect of concentration gradient on the fracture behavior of elastic brittle solids has been investigated. In a 2D triangular lattice network of random Born model, concentration gradient is applied, and the evolution of damage along with formation of fracture has been observed. The effect of grain/grain-boundary microstructure has not been taken into account. Fraction of broken bonds, reduction in

stiffness, localization of damage and roughness exponent of the final crack line has been analyzed. Another set of simulations was conducted taking into consideration the grain interior (GI) and grain-boundary (GB) microstructure of the brittle material. Effect of grain/grain-boundary stiffness ratio on the fracture strength and crack propagation path (intergranular or transgranular) has been analyzed. Finally, effect of grain size on the stiffness and ultimate strength of the material has been estimated.

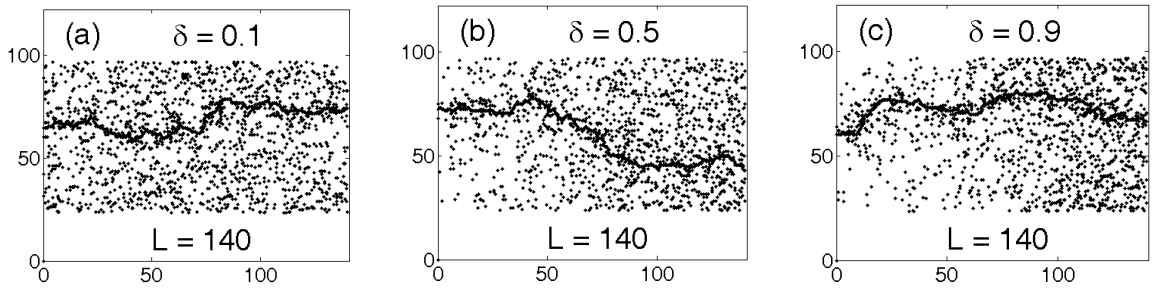

Fig: 3.4. *Fracture profile in a 140x140 triangular lattice network. (a)* $\delta = 0.1$*, (b)* $\delta = 0.5$ *and (c)* $\delta = 0.9$*. For* $\delta = 0.1$*, almost uniform broken bond profile has been observed. With increasing values of* δ*, it is evident that more broken bonds are observed on the right side where the loading gradient is significantly higher. For* $\delta = 0.5$ *and* $\delta = 0.9$*, on the left side much less damage evolution occurs.*

Under some applied concentration gradient, as shown in Fig. 3.3, damage evolves and finally a spanning crack develops. Damage and fracture profile at failure is presented in Fig. 3.4 for three different gradient values $\left(\delta = \left[0.1, 0.5, 0.9\right]\right)$ in a 140x140 lattice network without any GI/GB microstructure. Figure 3.4(a) shows that damage evolves almost uniformly for $\delta = 0.1$. Figure 3.4(b) indicates that as the concentration gradient increases to $\delta = 0.5$, more localized damage is observed on the region with larger values of the concentration gradient. Finally in Fig. 3.4(c), under a very high concentration gradient of $\delta = 0.9$, major damage evolution occurs on the right side and

very few bonds break on the region which experiences very low deviation of concentration from the equilibrium value. The impact of concentration gradient in fracture formation is very clear from Fig. 3.4. In these simulations, as well as in the following ones, some elements, which are very close to the top and bottom boundary, are assumed to be unbreakable. This approximation is made to remove the boundary effect, which can create undesirable stress concentration and hence fracture initiation close to the top or bottom boundary. In the following, effect of concentration gradient will be statistically characterized by taking different parameters into account, which acts as damage and failure indicators.

3.4 Scaling laws without GI/GB microstructure

For disordered brittle materials under tensile loading, fracture propagation was assumed to be coalescence of microscopic damage which follows percolation behavior [168]. This proposition was negated by Nukala et al. (see [169]) where the authors proposed that diffused damage evolves till a peak load. Beyond that point, stress concentration at the crack tip dominates and more localized crack propagation occurs under uniform tensile loading. The peak load depends on the inherent disorder of the material. Here we aim to analyze whether fracture propagates in a percolated or localized manner under diffusion induced stress. Hansen and Schmittbuhl (see [168]) reported that for percolation scaling, $p_{fbb} \propto N_{el}^{-1/2\nu}$, where p_{fbb} is the average value of the fraction of broken bonds (calculated over 100 samples), N_{el} is the number of elements and ν is an exponent ($\nu = 3/4$ for 2D systems). For fracture developed by diffusion-induced stress in 2D triangular lattice networks, the power law relation

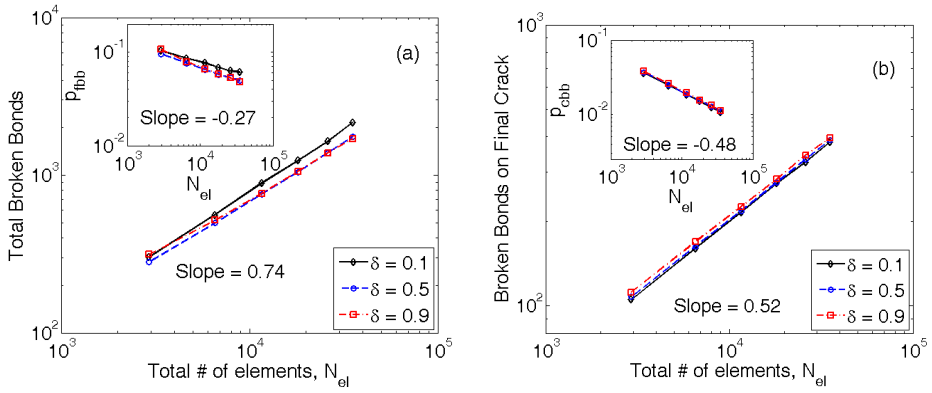

Fig: 3.5. *Power law scaling of broken bonds for a triangular spring lattice network. (a) Total number of broken bonds increases with increasing system size. It follows a power law relation, which can be represented as,* $n_{bb} \propto N_{el}^{0.74}$. *Mean fraction of broken bonds* $\left(p_{fbb}\right)$ *follow power law relation given as,* $p_{fbb} \propto N_{el}^{-0.27}$ *(inset). (b) Broken bonds on final crack also follows a power law relation with total number of elements with a different exponent,* $n_{cbb} \propto N_{el}^{0.52}$. *Mean fraction of bonds on final crack* $\left(p_{cbb}\right)$ *also shows power law relation,* $p_{cbb} \propto N_{el}^{-0.48}$.

observed is given by, $p_{fbb} \propto N_{el}^{-0.27}$ (see Fig: 3.5(a), inset). Since the exponent obtained (-0.27) does not match with the percolation limit (-0.375), it can be concluded that fracture evolution does not occur in a completely diffused manner. The exponent obtained here resembles very closely to that reported by Nukala et al. [169], $p_{fbb} \propto N_{el}^{-0.25}$ for triangular lattice network. Hence, fracture in brittle media under diffusion induced stress can be characterized as some sort of correlated percolation phenomena.

With increasing system size the total number of broken bonds also increases. A power law relation hold between them, which is expressed as, $n_{bb} \propto N_{el}^{0.74}$, where n_{bb} is the total number of broken bonds (see Fig. 3.5(a)). Different values of the gradient parameter δ do not impact the power law relation significantly. Here system sizes taken

into consideration are, L = [40, 60, 80, 100, 120, 140]. To characterize the pattern of the final crack line (whether it is extremely tortuous or relatively flat), the total number of broken bonds on the final crack line $\left(n_{cbb}\right)$ has been plotted against the number of elements within the system $\left(N_{el}\right)$. According to Fig. 3.5(b), $n_{cbb} \propto N_{el}^{0.52}$, which signifies that the number of broken bonds on the final crack increases as the square root of the total number of elements in the system. In 2D lattice networks, the system size L and the total number of elements can be assumed to be correlated as, $N_{el} \propto L^2$. Substituting this back into the power law relation for broken bonds on final crack, $n_{cbb} \propto \left(L^2\right)^{0.52}$, which can be approximately written as, $n_{cbb} \propto L^{1.04}$. Hence the total number of broken bonds on the final spanning cracks scales almost linearly with system size. Collapse of the three different lines for the three different values of δ signifies the universality of the power law relation. Similarly, another power law type expression can be developed for the fraction of broken bonds on the final crack, which is expressed as $p_{cbb} \propto N_{el}^{-0.48}$ (see Fig. 3.5(b), inset). Scaling analysis of the crack line gives insight about the tortuosity of the final fracture pathway. In the power law relation $n_{cbb} \propto L^n$, value of the exponent $n > 1$ signifies a tortuous pathway, whereas, $n \approx 1$ corresponds to a relatively straight crack line. In the current simulation, $n = 1.04$ signifies a relatively straight crack path with very little tortuosity. The loading gradient δ, has very little impact on the power law exponents.

As mentioned in the earlier paragraph, fracture in disordered media is not entirely a percolation phenomenon. Then the question is how we can characterize the failure of lattice networks under diffusion induced stresses. Figure 3.6(a) shows the variation in applied load with increasing number of broken bonds. As the loading gradient δ increases, the peak load decreases. Major crack propagation occurs after the first peak load without increasing the diffusion induced force at all. This phenomenon is characterized as an avalanche phenomenon. For loading gradients of $\delta = 0.1$ and $\delta = 0.5$, the spanning crack develops during the crack propagation after reaching the peak load. But for $\delta = 0.9$, after the first peak load major crack propagation happens without any increase in load, but the sample does not fail. Because of very small magnitude of diffusion induced stress on the left side of the domain (see Fig: 3.3 and Fig. 3.4), very high loading gradients require high magnitudes of concentration values for the propagating crack to span through the entire lattice. The load multiplier for $\delta = 0.9$ is observed to increase beyond the previously obtained peak value. It was proposed that under uniformly distributed uniaxial tensile load, fracture propagates in a diffused manner till the peak load (see [30, 169]). High stress concentration driven localized nucleation and propagation of the crack front occurs beyond the peak load. The question is, whether a similar combination of diffused damage evolution in pre-peak and localized propagation of fracture happens for post-peak regime under diffusion induced loading. To answer this question, fraction of broken bonds has been plotted against total number of elements in Fig. 3.6(b) for the pre-peak regime. Results indicate that the fraction of broken bonds at peak load follows a power law relation given by

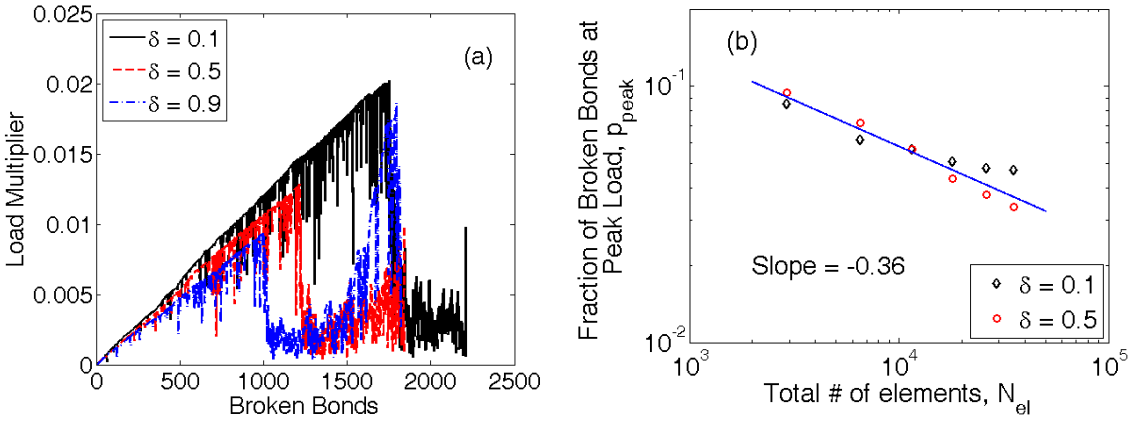

Fig: 3.6. *(a) Avalanche phenomena observed during the fracture of brittle materials under diffusion induced stress. As the loading gradient increases, peak load is attained more quickly. After the peak load a catastrophic failure follows, which are more prominent for loading gradients of* $\delta = 0.1$ *and* $\delta = 0.5$*. Different behavior is observed for very high loading gradient of* $\delta = 0.9$*, where after approaching the first peak load major crack propagation occurs. But for a spanning crack to develop, significant increase in diffusion induced force is required, which is higher than the first peak load observed earlier. (b) For* $\delta = 0.1$ *and* $\delta = 0.5$*, the fraction of broken bonds at peak load varies as* $p_{peak} \propto N_{el}^{-0.36}$*. The exponent -0.36 resembles very closely to the percolation value.*

$p_{peak} \propto N_{el}^{-0.36}$. The slope of -0.36 resembles very closely to the value or -0.37 reported earlier in the literature [168]. Hence, it can be concluded that even under diffusion induced loading, uncorrelated evolution of damage occurs till the peak load, and after that localized propagation of crack is observed. Since there exist multiple peaks under concentration loading gradient of $\delta = 0.9$, in Fig. 3.6(b) only two loading gradients ($\delta = 0.1$ and $\delta = 0.5$) have been considered for which determination of the desired peak load is relatively easier. Since multiple samples under loading gradient $\delta = 0.9$ show two peaks, and the second peak may exceed the first one, there is a possibility that the peak detection algorithm would select the second one as the only peak. Inclusion of all the broken bonds prior to the second peak would contain some spring elements, which

broke in a localized fashion, and lead to a wrong conclusion. From the lithiation – delithiation perspective, under very high loading gradient very small amount of de-intercalation can lead to formation of small cracks. Delithiation for long time under high gradient would generate multiple crack fronts which are very small in size [85]. Whereas, deintercalation with a small loading gradient would lead to formation of very few crack fronts, but they would continue for a long distance, resulting in single spanning cracks (usually observed in graphite after long operations [22]).

Since each and every bond in the lattice spring network contributes to the overall stiffness of the system, as each bond breaks it contributes to the reduction of the overall stiffness. Figure 3.7 shows how the stiffness evolves from the initial pristine state to zero stiffness that occurs at complete rupture of the lattice network. All the three loading gradients (Fig. 3.7(a) shows $\delta = 0.1$, Fig. 3.7(b) shows $\delta = 0.5$ and Fig. 3.7(c) shows $\delta = 0.9$) display two distinct regions of stiffness evolution. In the initial phase where fracture evolves in a diffusive fashion, the stiffness drops at a very slow rate following a linear relation. Similar correlation between stiffness and fraction of broken bonds in a micro-cracked sample has been reported earlier for ceramics under non-uniform thermal expansion induced micro-cracking (see [51]). As the diffusion induced loading increases, more damage evolves in a percolative fashion which eventually nucleates and form microcracks. Localization of these microscopic domains of damage gives rise to macroscopic cracks. When the stress concentration at the tip of a macroscopic crack becomes sufficiently large, it can make the crack to propagate without any increment in externally applied diffusion induced force. During this localized crack propagation,

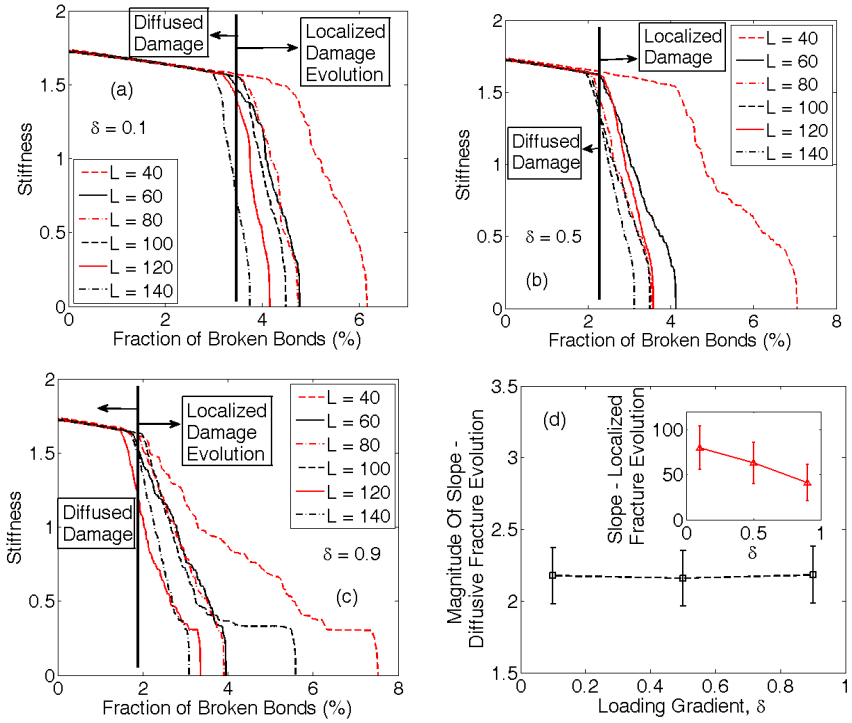

Fig: 3.7. *Reduction in stiffness of the system with increasing number of broken bonds. (a)* $\delta = 0.1$ *(b)* $\delta = 0.5$ *(c)* $\delta = 0.9$ *and (d) Values of the slope for different loading gradients. Evolution of fracture can be divided into two regimes. In the first region fracture initiates in a diffusive manner. The stiffness decreases slowly and linearly in this region. In the second regime, nucleation and propagation of cracks occur. Hence the stiffness decreases drastically. The exact region where diffused and localized damage evolution occurs has also been explicitly pointed out. For smaller values of* δ *, reduction in stiffness in the second region is more catastrophic. For larger values of* δ *, in the second region stiffness decreases relatively slowly.*

stiffness of the lattice network starts to drop drastically with increasing fraction of broken bonds. The rate at which stiffness decreases with increasing fraction of broken bonds at the localization zone changes inversely with the applied loading gradient. Figure 3.7(d) demonstrates the universality of the stiffness reduction rate in the percolation zone. For all the loading gradients and all the system sizes, the stiffness vs. fraction of broken bonds curve can be represented by the equation, $E_{eff} = E_0 - 2.2f$, where, E_{eff} is the effective stiffness of the network, E_0 is the initial stiffness with no

damage and f is the fraction of broken bonds. Universality of the slope can be attributed to the fact that evolution of damage occurs in a diffusive manner, which does not depend on the loading gradient or system size. In the localized fracture propagation zone, rate of reduction in stiffness depends on the loading gradient. Figure 3.7(d) (inset) shows the variation in slope with different values of δ. For smaller values of the loading gradient, larger slope signifies that once the localized crack propagation starts, it leads to catastrophic failure of the system very quickly. For $\delta = 0.9$, a smaller value of the slope signifies that the system takes more time to rupture. But the transition from diffusive damage to localized damage occurs much earlier for high loading gradients. From Fig. 3.7(a), 3.7(b) and 3.7(c) it can be concluded that transition from percolative to localized damage propagation occurs at 4%, 3% and 2% broken bond fraction for loading gradients of $\delta = 0.1$, $\delta = 0.5$ and $\delta = 0.9$ respectively.

As the concentration loading gradient (δ) increases, the diffusion induced stress on one side of the lattice structure becomes much larger than the other side (see Figure 3.3). Because of such non-uniform stress gradient, transition from diffused fracture evolution to localized crack propagation happens much quickly under high concentration loading gradients. Let f_{bb} be the fraction of broken bonds at which the transition in the modes of fracture propagation occur. In Fig 3.8(a), the cumulative distribution of the transition broken bonds for different system sizes and different concentration loading gradients are plotted. The plot in the inset shows the unscaled values of f_{bb}. In the main plot, the fraction of transition broken bonds have been scaled using the relation

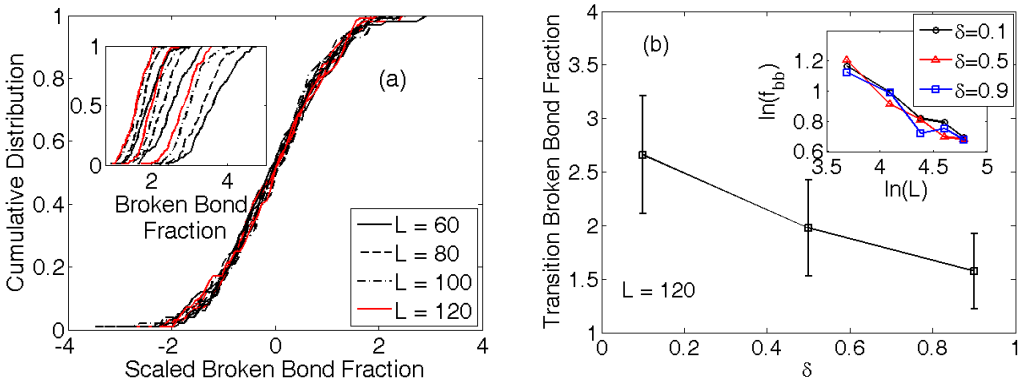

Fig: 3.8. *(a) Cumulative distribution of the scaled transition broken bond fraction for all the loading gradients of* $\delta = 0.1$, $\delta = 0.5$ *and* $\delta = 0.9$. *Inset shows cumulative distribution of transition broken bond fraction without scaling. The scaling law adopted in the main plot is given as [(transition broken bond fraction - mean)/standard deviation]. Symmetric behavior of the scaled distribution around zero signifies that it follows the normal distribution very closely. (b) With increasing value of the loading gradient* δ, *the transition occurs at a lower fraction of broken bonds (here shown for system size L = 120). The figure in the inset shows that the transition broken bond fraction changes with the system size according to a power law relation which is valid for all the three values of* δ.

$\frac{\left(f_{bb} - \mu_{fbb}\right)}{\sigma_{fbb}}$, where, μ_{fbb} and σ_{fbb} are the mean and standard deviation of the fraction of transition broken bonds, respectively. Symmetric nature of the curve on both sides of the zero point shows that the values of f_{bb} follows a normal distribution. In Fig. 3.8(b), decrease in the fraction of broken bonds at transition $\left(f_{bb}\right)$ is plotted with increasing value of δ, for a system size of $L = 120$. This relation reconfirms the statement made earlier in this paragraph that under high loading gradients, transition from diffused to localized fracture propagation happens much earlier with less number of broken bonds. The plot in the inset of Fig 3.8(b) indicates that for all the values of δ, fraction of broken bonds at transition $\left(f_{bb}\right)$ follows a power law relation with system size $\left(L\right)$. It

was explained earlier that the total number of broken bonds at failure follows a power law relation with total number of elements (see Fig. 3.5). As a natural extension to that theory, power law correlation between f_{bb} and L is expected. The slope in the inset plot of Fig 3.8(b) has been estimated to be -0.5, which leads to a correlation of $f_{bb} \propto L^{-0.5}$. This inverse power law relation signifies that, as the system size increases, the fraction of broken bonds at transition will asymptotically converge towards a particular value $\left(f_{bb}^{asy}\right)$, which can be again characterized as a function of δ $\left(f_{bb}^{asy} = f_{bb}^{asy}(\delta)\right)$.

The stiffness of a network of lattice springs is always directly proportional to the number of intact (or unbroken) springs. Let's define the stiffness at which the transition from diffused to localized crack propagation occur, as the transition stiffness $\left(k_{bb}\right)$. The number of broken bonds at which transition from diffused damage to localized damage occur depends on the loading gradient (see Fig 3.8(b)). Consequently, the transition stiffness should also depend on the loading gradient $\left(\delta\right)$ and system size $\left(L\right)$. Figure 3.9(a) shows the cumulative distribution of the scaled transition stiffness. The scaling have been conducted using the formula $\frac{\left(k_{bb} - \mu_{fbb}\right)}{\sigma_{fbb}}$, where μ_{kbb} and σ_{kbb} are the mean and standard deviation of the transition stiffness, respectively. For all the system sizes taken into consideration, collapse of the scaled distribution around the point 0.0 signifies that the transition stiffness follows a Gaussian distribution. The figure in the inset of Fig 3.9(a) gives an example of the cumulative distribution of the unscaled transition stiffness. As shown in Fig. 3.8(b), with increasing concentration gradient $\left(\delta\right)$, the

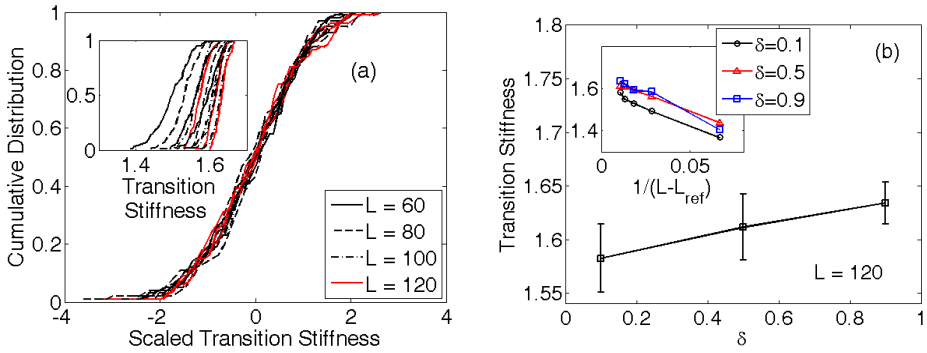

Fig: 3.9. *(a) Cumulative distribution of the scaled transition stiffness for all the loading gradients of* $\delta = 0.1$, $\delta = 0.5$ *and* $\delta = 0.9$. *Inset shows cumulative distribution of transition stiffness without scaling. The main plots display cumulative distribution of [(transition stiffness - mean)/standard deviation]. Symmetric behavior of the scaled distribution around zero signifies that it follows the normal distribution very closely. (b) For system size of L=120, the transition stiffness increases for larger values of the loading gradient. Inset shows that for all the values of* δ, *the transition stiffness is inversely proportional to the system size.*

fraction of broken bonds at the transition point, decreases. Since more number of broken bonds lead to smaller values of stiffness, the transition stiffness is supposed to increase with increasing concentration loading gradient (δ). Figure 3.9(b) shows a similar trend of increasing transition stiffness for higher values of δ observed in a system of size $L = 120$. Scaling of the mean value of transition stiffness with system size (L) has been demonstrated in the inset of Fig 3.9(b). The plot of transition stiffness vs. inverse of system size shows a straight line for all the three values of concentration gradient, $\delta = 0.1$, $\delta = 0.5$ and $\delta = 0.9$. The power law relation can be written as $k_{bb} \propto \left(L - L_{ref}\right)^{-1}$, where, L_{ref} is some reference system size. The slope of the straight line for all the values of δ is also similar signifying that the proportionality constant in the power law relation is universal for all concentration loading gradients. Similar to the

fraction of broken bonds at transition (see the previous paragraph), the transition stiffness also asymptotically converges towards a particular value $\left(k_{bb}^{asy}\right)$.

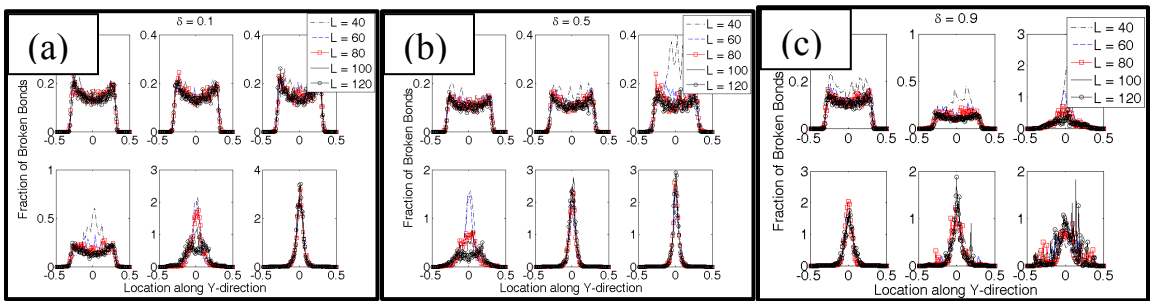

Fig: 3.10. *Localization of total number of broken bonds along vertical direction in six equal divisions of the total time. (a) For* $\delta = 0.1$*, in the first three time divisions, diffusive fracture evolution occurs. Localization of fracture is observed in the last two time divisions. (b) For* $\delta = 0.5$*, first three time divisions show diffusive fracture evolution. Localization initiates in the fourth time division and the last two divisions display extreme localization. (c) For* $\delta = 0.9$*, localization is observed in the third, fourth and fifth time steps, but less localization happens in the last time division. This is attributed to the fact that under high loading gradients, before the development of a spanning crack, diffusive fracture evolution occurs in some samples (see Fig: 3.7).*

3.5 Damage localization

In the previous section, it was argued that damage evolution occurs in a diffusive method till a particular point. Because of the dominance of stress concentration at crack tips over the disorder effect, localized evolution of damage is observed towards the end of the fracture process. To verify the applicability of this theory, localization of damage has been analyzed along the vertical (y - direction) as well as the horizontal (x - direction) direction. Figure 3.10 shows the localization of damage observed in the vertical direction for different system sizes $\left(L = \left[40, 60, 80, 100, 120\right]\right)$ under each of the three loading gradients of $\delta = 0.1$ (Fig. 3.10(a)), $\delta = 0.5$ (Fig. 3.10(b)) and $\delta = 0.9$ (Fig. 3.10(c)). The plotted values were obtained by averaging over 100 samples.

Averaging the profiles for determination of localization is rather a delicate task, because formation of the localized crack does not necessarily occur at the center of the sample. The localized crack can form anywhere along the length of the lattice in the vertical direction. Thus, performing a simple average leads to a flat profile that corresponds to absence of localization. There exist two different methods of averaging the damage profile, which can lead to clear observation of localization when averaged over multiple samples [37, 44, 169]. One way is to shift the interval at which maximum damage is observed to the center, and then average. The other way is to shift the center of mass of the damage profile to the center of the system before averaging. The first methodology gives rise to an unnatural peak at the center which comes because of the excessive emphasis on existing noise. The second methodology of shifting the damage profile by its center of mass, have been adopted widely because of the smooth and overlapping peak observed by this procedure [45]. In the current simulation, fracture was not allowed to occur in certain regions at the top and bottom of the lattice to avoid the boundary effect. Thus, while averaging over different realizations, certain portions on top and bottom of the lattice, where fracture was not allowed to occur, have been neglected.

In Fig 3.10, for all the three values of concentration gradient, the entire process of damage evolution and formation of a spanning crack have been divided into six equal divisions. Each interval contains the same number of broken bonds. An inspection over all the six intervals of Fig 3.10(a) reveals that, under concentration loading gradient of $\delta = 0.1$, localization happens only towards the end of the breaking process. Very little or no localization is observed in the first four time intervals. Initiation of localization is

visible in the fifth interval. Finally, significant localization along with overlap of the profiles for different sizes, have been observed in the final interval. Linear scaling law has been used in this analysis to collapse the data for different sizes (L), which can be written as $\langle \Delta p(y,L) \rangle = f\left((y - L/2)/L \right)$ (see Ref. [168]). Figure 3.10(b) shows how the damage localizes under loading gradient of $\delta = 0.5$. Since higher concentration gradient signifies more force on one end than the other, the crack propagation starts much quickly. As evident from Fig 3.10(b), diffused damage evolution is observed for the first three time steps. Initiation of localization occurs in the fourth time interval. In the fifth and final time intervals, major localization with sharp peaks has been observed. Collapse of the data has also been observed for different system sizes under a linear scaling law (see Ref. [169]). Success of the linear scaling law to collapse the data can be attributed to the fact that the fractions of damage at each strip $\langle \Delta p(y,L) \rangle$ have not been scaled with the peak value. In Fig 3.10(c), distribution of damage observed under a loading gradient of $\delta = 0.9$ has been plotted at six equal intervals. After diffused damage evolution at the first two time steps, localization initiates from the third step itself. The fourth and fifth intervals display major amount of damage localization. The early initiation and propagation of localized damage can be attributed to the increased directional loading induced by large concentration gradients. Contrary to the intuitive understanding, some diffusive damage evolution is observed in the sixth interval. This apparent deviation from the regular behavior is explained by the fact that under large concentration gradients, only one end of the lattice structure is subjected to large

concentration induce load, whereas the other end experiences very little force. Thus early formation of localized damage has been observed. But, for the complete spanning crack to form, the crack front has to propagate through the entire lattice, including the portion that experiences very little concentration gradient induced load. Even after the first set of localized crack propagation, some diffused damage evolution occurs, before the stress concentration at the crack tip enforces the crack front to propagate through the region with less concentration gradient (see Fig 3.7(c)). In certain cases, under concentration gradient of $\delta = 0.9$, it is possible to experience two sets of diffused damage evolution and localization (see Fig 3.6(a)). The magnitude of load required for the second localization to occur, may exceed that experienced during the first localization. Such phenomenon of dual percolative damage propagation and localization under large diffusion gradients, have not been reported earlier.

All the damage localization analysis observed till date focuses only on the localization observed in the vertical direction. Damage localization along the horizontal direction was not analyzed because of the fact that the external load was applied uniformly along the x – direction. In the present study, the diffusion-induced load varies along the horizontal direction, which makes it important to investigate the localization phenomena along the x – direction as well. Figure 3.11(a), 3.11(b) and 3.11(c) shows the damage localization observed along horizontal direction under the three different loading gradients of $\delta = 0.1$, $\delta = 0.5$ and $\delta = 0.9$, respectively. The total number of broken bonds has been divided into six equal intervals and the damage profile along x – direction has been plotted at each of the intervals. Because of the concentration gradient,

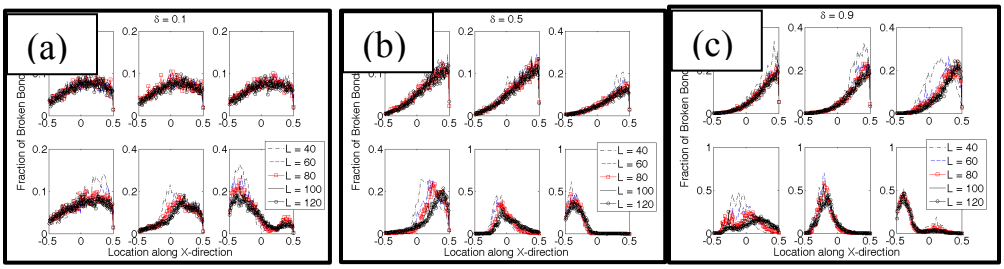

Fig: 3.11. *Localization of fracture along the horizontal direction is plotted given that higher gradient is applied on the right and lower on the left. The total time has been divided into six equal divisions. (a)* $\delta = 0.1$*, (b)* $\delta = 0.5$ *and (c)* $\delta = 0.9$*. For all the three cases, more damage evolve in the region where gradient is higher (right side of the lattice). Fracture also initiates in that region of high gradient. In the last two time division, propagation of fracture and development of the spanning crack occurs. Hence, more localization towards the left is observed (where loading is relatively less).*

diffusion-induced load is higher in the right hand side, and lower force is applied in the left side. As a result, when percolative damage evolution occurs, concentration of damage is higher in the right hand side and lower in the left hand side. This trend is observed in the initial few intervals for all the loading gradients where diffusive damage evolution occurs. When localized damage propagation occurs, a particular crack front travels from right end of the lattice to the left end. Thus during localized crack propagation, the general concept of "*wherever the load is large, enhanced damage occurs there*", is not applicable any more. The sixth interval of Fig 3.11(a) proves the hypothesis described above, where localized damage evolution occurs. Similarly in Fig 3.11(b) and 3.11(c), in the fifth and sixth time intervals, where localized damage evolution occurs, enhanced bond breaking has been observed in the left side, even though higher diffusion induced load acts on the right side. In most of the plots, collapse of the damage data along x – direction has been observed using the linear scaling law, which is given as $\langle \Delta p(x,L) \rangle = f\left((x - L/2)/L\right)$. For intercalation materials, smaller

values of concentration gradients would signify fracture propagation in a diffusive fashion, leading to formation of few crack fronts. However, large loading gradients give rise to extremely localized damage evolution with the formation of multiple crack fronts. These cracks can propagate in the subsequent loading cycles and give rise to a spanning crack. Analyzing this type of damage evolution along horizontal direction can shed light on the distribution of different materials that can be used to fabricate systems to have minimum damage when subjected to concentration gradient induced loads.

3.6 Surface roughness

The concept of surface roughness exponent was introduced to parameterize the spatial scaling behavior of self-affine crack surfaces. If the crack width is denoted by w and l signifies the window size, then for self-affine surfaces $w(l) \propto l^{\xi_{loc}}$, where ξ_{loc} is the roughness exponent $(0 < \xi_{loc} < 1)$. For large values of the window size, such that $l \approx L$, where L is the system size, the crack surface width $w(l)$ saturates to some value $W(L)$. The large-scale crack width also scales as $W(L) \propto L^{\xi_{glob}}$, where $\xi_{glob} > \xi_{loc}$ signifies the presence of anomalous scaling. The initial paradox of whether larger surface exponent corresponds to a rougher surface or smoother surface was clarified by Krim and Indekeu (see Ref. [170]). In smaller length scales, larger values of the roughness exponent signifies smooth surface; whereas, in large length scales values of $\xi_{glob} \approx 1$ corresponds to a rough surface. Under uniaxial tensile loading conditions, fracture surface roughness exponent for small as well as large length scales have been computed using the random fuse, random spring and random beam models [37, 58, 171,

172]. For brittle materials under uniaxial tensile load, a universal value of the surface roughness has been reported in several articles [168]. Scaling analysis of the roughness observed in yield surfaces of elasto-plastic materials has also been reported [37]. Some recent studies argue that even under tensile loading, anisotropy in material properties and extended correlations can lead to breakdown of the universal roughness exponent hypothesis [36]. In the current study, spanning cracks were developed in a triangular spring lattice network under diffusion-induced loads. The scaling of crack surface formed under diffusion-induced stress has not been studied yet. In this subsection, fracture surface roughness will be investigated for brittle disordered media subjected to loads generated by concentration gradients.

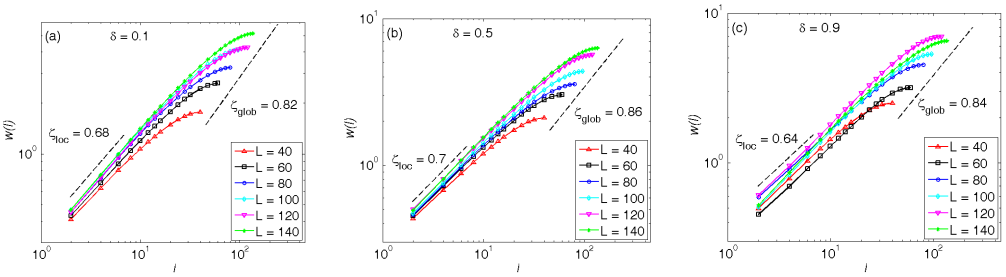

Fig: 3.12. *Roughness of the final crack is estimated using a moving window technique. (a) For* $\delta = 0.1$*, the local roughness exponent is obtained as 0.68 and the global roughness as 0.82. (b) For* $\delta = 0.5$*, the local roughness is 0.7 and global value is 0.86. (c) For* $\delta = 0.9$*, the local and global values of the roughness exponent is obtained as 0.64 and 0.84 respectively. Hence, the local roughness is around the approximate roughness exponent obtained using minimum energy principal which is 2/3.*

In the current simulations, once the lattice network fails, the spanning crack is identified that show overhangs in the crack profile. Before calculating the roughness, these overhangs and jumps were not removed from the profile. It is supposed to have some impact on the global roughness exponent of the fracture surface. The crack line is denoted as $h(x)$, where the values of $x \in [0, L]$ and $h(x)$ represents the local transverse

position of the crack-line at each x. For self-affine fracture surfaces, the local crack width is defined as,

$$w(l) = \left\langle \sum_{x=0}^{L} \left[h(x) - \frac{1}{l} \sum_{\xi=x}^{x+l} h(\xi) \right]^2 \right\rangle^{\frac{1}{2}} \tag{3.4}$$

The averaging is conducted as moving average within a single sample, and also over multiple realizations. The obtained crack profile is not periodic initially. It has been intentionally made periodic by shifting one of the two ends to accomplish the averaging scheme successfully. Figure 3.12(a), 3.12(b) and 3.12(c) shows the scaling of crack width $w(l)$ with respect to window size l for concentration gradient of $\delta = 0.1$, $\delta = 0.5$ and $\delta = 0.9$ respectively. For the smaller length scales, where $w(l) \propto l^{\xi_{loc}}$ relation is applicable, the values of ξ_{loc} were obtained as 0.66, 0.7 and 0.64 for $\delta = 0.1$, $\delta = 0.5$ and $\delta = 0.9$, respectively. But for large values of the window size, where $W(L) \propto L^{\xi_{glob}}$ relation is applicable, the value of ξ_{glob} were obtained as 0.82, 0.86 and 0.84 for $\delta = 0.1$, $\delta = 0.5$ and $\delta = 0.9$, respectively. No particular correlation has been observed between neither of the roughness exponents (ξ_{loc}, ξ_{glob}) and the concentration-loading gradient. This indicates that both the roughness exponents are independent of the applied diffusion induced load and behaves as a material property. The fact that the value of global roughness exponent is greater than the value of local roughness exponent $(\xi_{glob} > \xi_{loc})$ signifies anomalous scaling. The presence of jumps in the crack profile is attributed as the reason behind anomalous scaling (see Ref. [58]). Since bifurcation of

the crack front was allowed and coalescence of micro-cracks was accounted for, overhangs and jumps in the crack profile were induced.

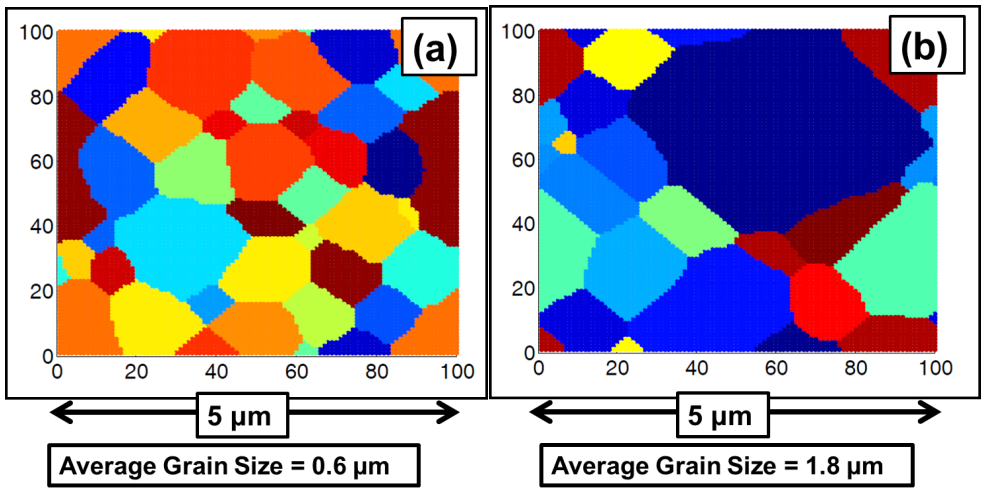

Fig: 3.13. *Computational reconstruction of grain/grain-boundary microstructure of a representative material. This microstructural image have been developed using the Potts model. Metropolis Monte-Carlo algorithm has been adopted to solve for the grain/grain-boundary microstructure evolution. (a) Average grain size is 0.6µm. (b) Average grain size is 1.8µm.*

3.7 Microstructural grain size effect

When observed from a lower length scale most of the materials display a polycrystalline microstructure which includes distinct grain and grain-boundary regions. Figure 3.13 represents the grain/grain-boundary microstructure of a material. Potts model was used to capture the microstructural evolution. Metropolis Monte Carlo based algorithm was adopted to solve the Potts model equations. Figure 3.13(a) shows a representative grain/grain-boundary microstructure which has an average grain size of 0.6µm. Whereas, Fig. 3.13(b) shows a microstructure with larger grain size of 1.8 µm. The two different grain sizes can be obtained by running the same Monte-Carlo simulation but for different amount of times. The simulation starts with a completely

random mixture. Over time the grain/grain-boundary microstructure evolves. At shorter amounts of time, smaller grain sizes are observed. Whereas, in simulations for longer time generates larger grain sizes. Analysis of damage evolution and fracture formation in polycrystalline materials has always attracted researchers for the last three decades [51, 57, 165, 171-173]. Different mathematical techniques have been adopted to capture nucleation and propagation of cracks in polycrystals, which includes the lattice spring method (see Ref. [51, 165, 171]), finite element method with cohesive zone elements (see Ref. [173]) and the extended finite element methods (see Ref. [172]). The common feature of all these techniques is the fact that an image of the polycrystalline microstructure is obtained first. For finite element based methodologies, grain interiors observed in the polycrystalline materials are meshed using finite elements. Zero thickness grain boundaries were assumed in these techniques [172, 174]. Cohesive zone elements were placed in between every two elements. Different fracture strength was assumed for cohesive elements depending on whether they lie in the grain interior or the grain boundary zone (see Ref. [173-175]). For the lattice spring based methodologies, image of the grain/grain-boundary microstructure has been mapped onto the uniformly distributed lattice springs [51, 176]. Finite or infinitesimal thickness of the grain boundary region can be implemented here. Depending on whether the spring lies within the grain interior or grain-boundary zone, different elastic modulus have been assigned (see Ref. [165, 171]).

Since the presence of grain/grain-boundary microstructure can have significant impact on damage evolution, the impact of grain size on the statistics of fracture will be

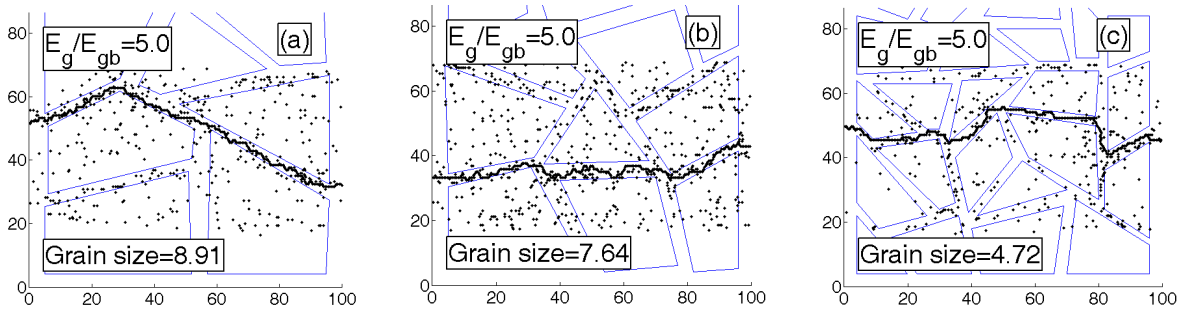

Fig: 3.14. *Three different grain/grain-boundary microstructures and fracture profile in each of them have been displayed. Volume fraction of the grain interior has been assumed to be almost constant for all the three microstructures. The ratio of elastic moduli at the grain interior and the grain boundary zone have been assumed be 5.0. The concentration gradient induced loading for this particular simulation is* $\delta = 0.1$. *(a) Average grain size is 8.91. (b) Average grain size is 7.64. (c) Average grain size is 4.72.*

discussed next. Figure 3.14 shows the three different polycrystalline microstructures considered in this analysis along with an example of damage and crack profile for each of the microstructures. Each microstructure has a different value of the average grain size, 8.91 for the first one (Fig. 3.14(a)), 7.64 for the second one (Fig. 3.14(b)) and 4.72 for the last one (Fig. 3.14(c)). The volume fraction of grain interior has been kept constant at 80% for all the three polycrystalline microstructures. A very important parameter that significantly impacts crack path is the ratio of the elastic modulus at the grain interior $\left(k_g\right)$ and the grain boundary $\left(k_{gb}\right)$ zone $\left(\rho = k_g / k_{gb}\right)$ [51]. The range of values of this ratio parameter used in the current research are $\rho = \left[1.5, 2.5, 5.0, 10.0\right]$. The fracture profile shown in Fig. 3.14 was generated by using $\rho = 5.0$. Another parameter that impacts the damage statistics significantly is the grain size $\left(L_c\right)$. Since the grains are not spherical in shape, defining the grain size is not very trivial. In this study, it has been assumed that $L_c = A / P$, where A signifies the area under the grain and P stands

for the grain perimeter. This nonconventional procedure of calculating the grain size gives a distribution of grain sizes in each of the polycrystalline microstructures. The average grain size were determined and reported in Fig. 3.14 as the size of grains for that particular microstructure. From SEM images of polycrystalline materials, it has been observed that thickness of the grain boundary region is negligible [48, 49, 176]. In this study we assume that the effect of grain boundary is not confined only at the boundary of the two grains. The mismatch in atomic arrangements penetrates within the grain interior as well resulting in a relatively thick zone which shows grain boundary like properties. This thick region has been termed as grain boundary affected zone (see Ref. [177]). In this article we recognize it simply as the grain boundary. Because of the existence of a thick grain boundary region, some of the lattice springs lie entirely on the grain-boundary (GB), and they are assigned properties of the GB region. Springs which fall completely on the grain interior (GI) display properties of the grain interior. Some lattice springs lie on the interface of the grain interior and the grain-boundary zone. Weighted averages of the corresponding properties (axial and transverse stiffness) have been assigned to these interfacial springs.

As mentioned earlier in the previous paragraph, the ratio of elastic stiffness in the grain interior over the grain boundary zone may significantly impact formation of the final spanning crack. Figure 3.15 shows a qualitative analysis of how the crack path changes with different values of the $\rho = k_g / k_{gb}$ ratio. The polycrystalline microstructure

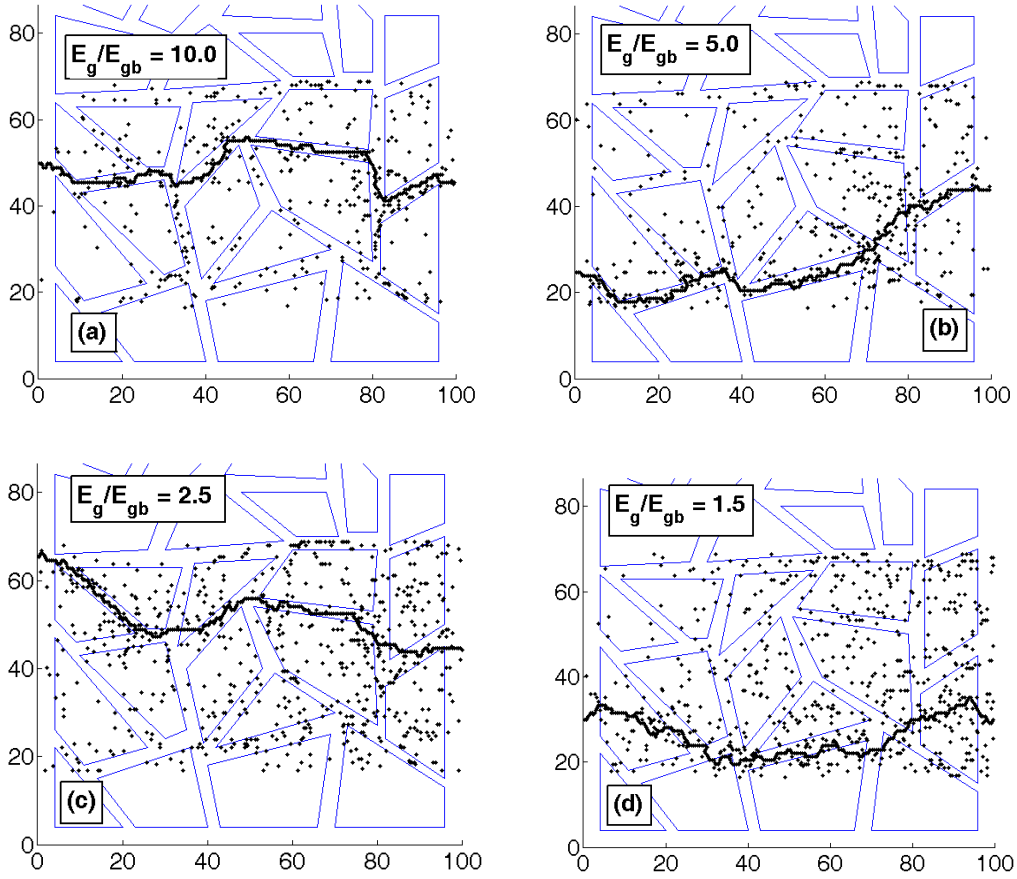

Fig: 3.15. *Distribution of broken bonds and the fracture profile on the microstructure with* $L_c = 4.72$. *The applied loading corresponds to* $\delta = 0.5$. *Different ratio of stiffness in the grain interior and the grain boundary region has been considered. (a) Stiffness ratio is 10.0. (b) Stiffness ratio is 5.0. (c) Stiffness ratio is 2.5. (d) Stiffness ratio is 1.5. For larger stiffness ratios the spanning crack entirely travels through the grain boundary region – intergranular fracture (a). For smaller stiffness ratios, the spanning crack can initiate as well as propagate through the grain interior – transgranular fracture (d).*

with average grain size of $L_c = 4.72$ and concentration loading gradient of $\delta = 0.5$ has been used in this analysis. Figures 3.15(a), 3.15(b), 3.15(c) and 3.15(d) correspond to $\rho = \left[10.0, 5.0, 2.5, 1.5\right]$ respectively. It is very well evident in Fig. 3.15(a) that for $\rho = 10.0$ the spanning crack propagates only through the grain boundary region. Some

damage evolution occurs within the grain interior, but the crack that develops is definitely an intergranular crack. As observed in Fig. 3.15(b) and 3.15(c), for $\rho = 5.0$ and $\rho = 2.5$, crack initiation and propagation happens mostly in the grain boundary region. But in some instances the propagating crack may penetrate into the grain interior if the fracture threshold inside the grain is favorable for fracture. Finally, in Fig. 3.15(d), the crack pattern for $\rho = 1.5$ cannot identify the difference between grain interior and grain boundary zone. It can initiate as well as propagate through both GI and GB regions. In these simulations with polycrystalline microstructure, the stiffness of the grain interior is kept constant. Elastic stiffness of the grain boundary zone has been determined based on the value of stiffness ratio $\rho\left(= k_g / k_{gb}\right)$. For large values of ρ, elastic stiffness in the grain boundary region is very small. Displacement of the lattice springs are given by $\vec{u} = \left[k\right]^{-1} \cdot \vec{f}$, where, $\vec{u}$ signifies displacement, $\left[k\right]$ is the stiffness matrix and $\vec{f}$ signifies externally applied diffusion induced load. Since for all the simulations, diffusion induced load does not change, $\vec{f} = const$. Smaller value of stiffness at the grain boundary region results in larger displacement in the intergranular domain. Energy in each spring is defined as $\psi = \left(1/2\right)\vec{f} \cdot \vec{u}$ or $\psi = \left(1/2\right)\vec{u} \cdot \left[k\right] \cdot \vec{u}$. Since energy is directly proportional to the square of displacement, large displacement in the GB gives rise to higher strain energy in the GB region. The fracture threshold $\left(\psi_t\right)$ is uniformly distributed in the grain interior and grain boundary zone. As a consequence, the springs residing in the grain boundary region has a higher propensity to fracture

when the stiffness ratio ρ is very high. Hence, intergranular cracks appear for large values of stiffness ratio. For smaller values of ρ, the elastic stiffness in GI and GB region are almost equal resulting in similar values of strain energy in both GI and GB zones. Inability of the propagating crack front to distinguish between GI and GB zones results in formation of transgranular cracks for smaller values of the stiffness ratio. Similar type of intergranular crack path with $\rho = 2.5$ and transgranular fracture with $\rho = 1.5$ were observed by Sridhar et al. [51] for anisotropic thermal expansion misfit strain induced fracture in polycrystalline materials.

Next, an effort will be made to find a correlation between stiffness ratio and damage evolution. Suppose the fraction of broken bonds in the grain interior and grain boundary zone is given by f_G and f_{GB}, respectively. We define a new parameter $f_{G/GB}\left(= f_G / f_{GB}\right)$ which can be used as a quantitative measure for the damage evolution in the grain interior with respect to that in the grain boundary zone. Since the volume fraction of GI is much larger than that of the GB zone, for $\rho = 1$ the value of $f_{G/GB} > 1$. This is attributed to the fact that when the elastic stiffness in the GI is equal to that of GB, there is equal probability of damage evolution in GI and GB region, and higher volume fraction of GI results in $f_G > f_{GB}$. Figure 3.16(a) shows a quantitative analysis of how $f_{G/GB}$ changes with stiffness ratio $\left(\rho\right)$ for different values of loading gradient $\delta = \left[0.1, 0.5, 0.9\right]$ and a constant grain size of $L_c = 4.72$. It is observed that for lower values of ρ, the value of $f_{G/GB} > 1$. As the value of ρ increases, $f_{G/GB}$ decreases and

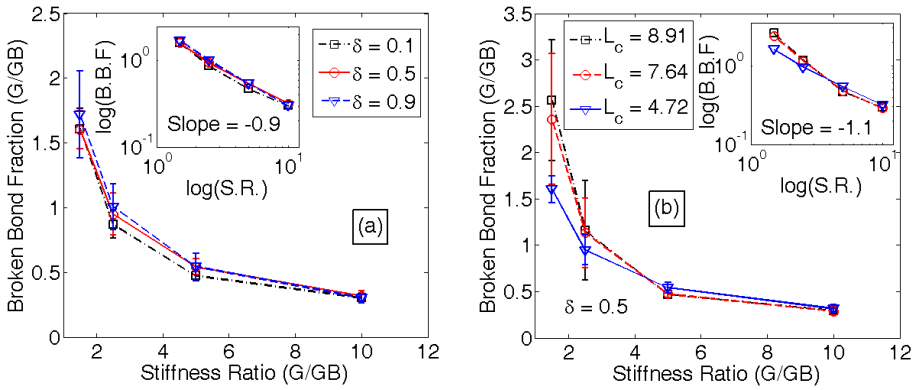

Fig: 3.16. *Variation in fraction of broken bonds with respect to stiffness ratio. (a) For different loading type, no significant change is observed. Inset shows that log – log plot of broken bond fraction vs. stiffness ratio gives a straight line with a slope approximately equal to -0.9. (b) Different values of the average grain size also have very little impact on the overall response. The log – log plot of broken bond fraction vs. stiffness ratio in the inset shows as approximately straight line with a slope -1.1. Hence, it can be concluded that the broken bond fraction and stiffness ratio are inversely proportional to each other.*

tends to saturate at a particular value. This observation exactly matches with the explanation provided in the previous paragraph that softer grain boundaries lead to enhanced damage in the grain boundary region. Data for all the three loading gradients also collapse on top of each other. $\log\left(f_{G/GB}\right)$ has been plotted with respect to $\log\left(\rho\right)$ in the inset of Fig. 3.16(a). A straight line signifies that a power law relation exist between the two parameters, which can be written as $f_{G/GB} \propto \rho^{-0.9}$. Similar analysis has been reported in Fig. 3.16(b), but for different grain sizes $L_c = \left[8.91, 7.64, 4.72\right]$ and constant loading gradient of $\delta = 0.5$. The data for $L_c = 8.91$ and $L_c = 7.64$ almost collapse on top of each other, but the data for $L_c = 4.72$ does not. This apparent mismatch can be attributed to the lack of sufficient number of statistical samples. Similar pattern of $f_{G/GB} > 1$ for small ρ and $f_{G/GB} \propto 0.5$ for large values of ρ have

been observed. In the inset of Fig. 3.16(b), $\log\left(f_{G/GB}\right)$ have been plotted with respect to $\log\left(\rho\right)$. A straight line with slope of -1.1 signifies a power law relation between $f_{G/GB}$ and stiffness ratio, which can be written as $f_{G/GB} \propto \rho^{-1.1}$. From the two slopes obtained in the inset of Fig. 3.16(a) and 3.16(b) it can be concluded that $f_{G/GB}$ varies inversely with the stiffness ratio, $f_{G/GB} \propto \rho^{-1}$. However, dependence of the power law exponent on the volume fraction of grain interior has not been investigated in this article.

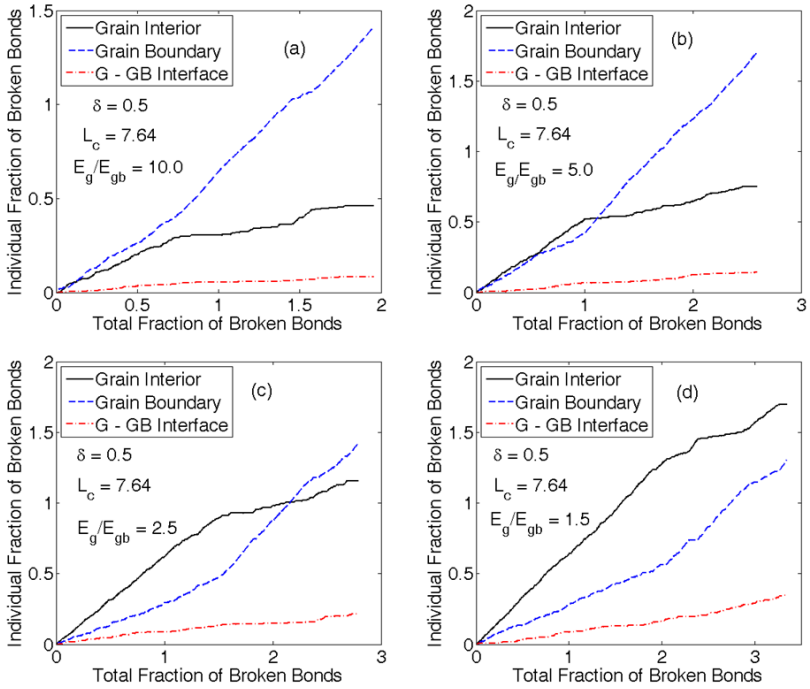

Fig: 3.17. *Evolution of damage in the grain interior (black line), grain boundary (blue dashed line) and grain – grain boundary interface (red dash-dot line) for a particular microstructure* $\left(L_c = 7.64\right)$*, particular loading* $\left(\delta = 0.5\right)$ *but different grain interior over grain boundary stiffness ratio. (a) Stiffness ratio = 10.0. (b) Stiffness ratio = 5.0. (c) Stiffness ratio = 2.5 and (d) Stiffness ratio = 1.5. As the stiffness ratio increases, evolution of damage becomes more localized in the grain boundary region. For all the stiffness ratios, a transition fraction of broken bonds is observed beyond which the rate of damage evolution in the grain boundary zone increases significantly.*

Evolution of damage with time inside the grain interior, grain boundary and the grain/grain-boundary interface has been reported in Fig. 3.17. The simulations were conducted on a polycrystalline microstructure with $L_c = 7.64$ and a loading gradient of $\delta = 0.5$. Figure 3.17(a), 3.17(b), 3.17(c) and 3.17(d) represents grain over grain-boundary stiffness ratio $\left(\rho = E_g / E_{gb}\right)$ of 10.0, 5.0, 2.5 and 1.5, respectively. Since the simulations are quasistatic in nature, no explicit time variables are present. The variable "total fraction of broken bonds" resembles closest to time in the current simulations. Thus in all the four plots of Fig. 3.17, the variable "total fraction of broken bonds" have been used along the abscissa to represent time. Figure 3.17(a) shows that for stiffness ratio $\rho = 10.0$, fraction of damage in the GB region is larger than that in GI from the beginning of the simulation. In Fig. 3.17(b), for $\rho = 5.0$, initially almost equal amount of damage evolves in the GI and GB. Towards the end of the simulation, major crack propagation occurs in the grain boundary region. For $\rho = 2.5$, shown in Fig. 3.17(c), initially more damage evolution occurs in the GI. Towards the end of the simulation, when stress concentration driven localized crack propagation occurs, more damage evolves in the grain boundary region. Finally, for $\rho = 1.5$, shown in Fig. 3.17(d), more damage is observed in the GI throughout the simulation. For all the four cases, very little damage is observed in the grain/grain-boundary interface zone (the red line close to the bottom of all the four plots). Another common feature observed in all the four plots is the change in slope of damage evolution in the GI and GB region. In the simulations without grain/grain-boundary microstructure, we observed the presence of two different

domain of damage evolution. In the first stage damage evolves in a diffusive manner, whereas, localized propagation of crack was observed in the second stage (see Fig. 3.7(a), 3.7(b) and 3.7(c)). Similarly, for lattice networks with GI/GB microstructure, evolution of damage occurs in two stages. The change in slope signifies transition from diffusive damage evolution to localized stress concentration driven crack propagation. Increase in the slope of GB damage and decrease in the slope of GI damage signifies that localized crack propagation occurs in the grain boundary region in the later part of the simulation.

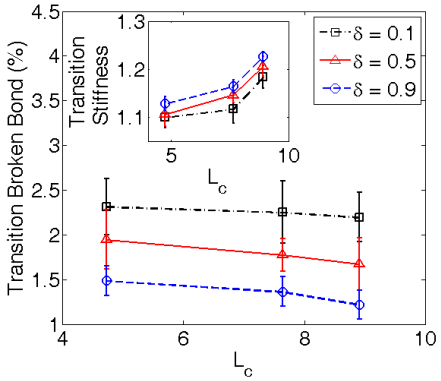

Fig: 3.18. *Similar to lattice networks without microstructures, lattice networks with microstructures show two distinct regions of stiffness reduction. The broken bond fraction and the stiffness at which the transition occurs depend on the grain size. This plot shows that the transition broken bond increases and the transition stiffness decreases (inset) with decreasing grain size. Since more broken bonds correspond to larger reduction of stiffness, it is self-explanatory that if transition broken bond increases for smaller grain size, the transition stiffness will decrease. More uniform loading* $(\delta = 0.1)$ *leads to diffusive fracture evolution for longer time than loading with high gradients* $(\delta = 0.9)$.

Evolution of damage occurs in two stages for lattice networks with polycrystalline microstructures. The first stage corresponds to bond breaking in a percolative manner. In the second stage, stress concentration driven localized crack

propagation occurs. Grain size of the polycrystals should have an impact on the point where this transition from diffusive damage evolution to localized fracture propagation occurs. Figure 3.18 shows that the fraction of broken bonds at transition decreases with increasing grain size. More number of broken bonds signifies reduced stiffness of the lattice network. Thus with increasing grain size, transition between the two fracture mechanisms should occur at a higher stiffness. The inset of Fig. 3.18 shows how transition stiffness increases with increasing grain size. Both the transition broken bond and transition stiffness were plotted for three different values of the concentration loading gradients $\delta = \left[0.1, 0.5, 0.9\right]$. Since grain interiors are stronger than the grain boundary zone, it is always easier for the damage to evolve in the GB region. In the second stage where stress concentration driven crack propagation occurs, existence of a straight path through the grain boundary region should be favorable for the early initiation of localized crack propagation. Microstructure with large grain size provides such straight paths through the grain boundary region (see Fig. 3.14(a)), which eventually accelerates the transition to localized crack propagation. On the other hand, microstructure with small grain size contains tortuous grain boundary region (see Fig. 3.14(c)). Non-existence of a straight pathway through the GB region delays the onset of localized crack propagation in materials with small grain sizes.

In polycrystalline microstructures as long as the damage evolution occurs in a percolative manner, the diffusion induced force required to break the subsequent spring, increases. With the onset of localized crack propagation, the required diffusion induced force to create the spanning crack, decreases significantly. This phenomenon for

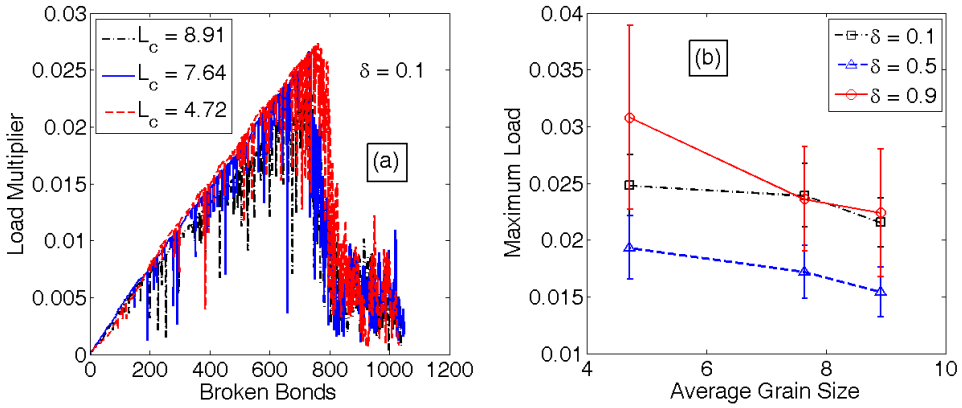

Fig: 3.19. *Change in the values of the load multiplier with grain size has been characterized here. (a) Evolution of the load multiplier with broken bond fraction for three different grain sizes. Loading gradient of* $\delta = 0.1$ *has been considered here. (b) Maximum value of the load multiplier increases with decreasing average grain size. Magnitude of the maximum load multiplier does not have a fixed trend with changing values of the loading gradient parameter,* δ *.*

polycrystalline microstructure with three different grain sizes has been shown in Fig. 3.19(a), under concentration induced loading gradient of $\delta = 0.1$. Diffusion induced load observed at the end of percolative damage propagation, is the maximum load that a lattice network, with polycrystalline microstructure, can sustain before rupture. The maximum load a microstructure can sustain signifies its strength. Figure 3.19(a) clearly shows that, as the grain size decreases, strength of polycrystalline microstructure increases. To understand the relation more clearly, Fig. 3.19(b) plots this maximum load with respect to grain size for different values of the loading gradient $\delta = [0.1, 0.5, 0.9]$. Increase in strength of polycrystals with decreasing grain size have been observed for all the values of δ. However, in the current simulations of lattice spring networks with polycrystalline microstructure, presence of dislocations was not taken into consideration. Thus, the reason behind increasing strength with decreasing grain size is worth investigating. It was mentioned in the previous paragraph that microstructures with large

grain size show straight pathways through the grain-boundary region (see Fig. 3.14). On the other hand, small grain size leads to a relatively tortuous pathway through the GB. During stress concentration driven localized crack propagation, the crack front does not experience a huge number of obstacles in microstructures with larger grain sizes. This leads to a smaller value of strength. Whereas, the microstructures with small grain size hinder the propagation of crack fronts and forces it to have an extremely tortuous pathway. More diffusion induced force is required for the crack front to overcome the obstacles and sustain a tortuous pathway in microstructures with small grain sizes. This leads to higher values of strength.

3.8 Conclusion

Intercalation materials play a major role as the host for different species (lithium or hydrogen) which are responsible for converting chemical energy to more useful forms of electrical or mechanical energy. Transport of intercalating species within the host material happens through diffusion process. Concentration gradient of the diffusing chemical species induces significant amount of diffusion induced stress within the host materials which can lead to fragmentation and loss of durability. A random lattice spring (RLSM) based network model have been implemented in this article to analyze the scaling properties of diffusion induced fracture. The average fraction of broken bonds follows a power law distribution with total number of elements, and the power law exponent $\left(n = -0.27\right)$ signifies correlated percolation phenomena. Total number of broken bonds that lie on the final crack line was observed to have a power law relation with the system size. An exponent of $n = 1.04$ was calculated, which signifies almost

straight crack paths with very little tortuosity. These scaling laws are also independent of the loading gradient (δ). At the beginning of the simulation, no localization of damage was observed within the lattice spring network. Towards the end of the simulation, when stress concentration driven fracture propagation occurred, significant localization was observed. The global and local roughness exponents of the crack line was obtained as $\xi_{loc} = 0.66$ and $\xi_{glob} = 0.84$. Presence of overhangs and jumps in the crack profile was attributed as the reason behind the existence of anomalous scaling.

In a disordered media, damage induced by the diffusion of intercalating materials evolves in two stages. In the first stage, the material disorder dominates and damage develops gradually in a random percolative fashion. Increase in diffusion induced force is required for damage to evolve within the material. In the second stage of damage evolution, stress concentration dominates over the material disorder. Localized crack propagation happens within the lattice network due to stress concentration effect. The diffusion induced load observed at the end of the percolative damage evolution phase is usually equal to the maximum load that the lattice network can sustain. Number of broken bonds observed at the peak load follows a power law relation with system size. The exponent has a value of $n = -0.36$ which signifies the existence of percolation scaling or uncorrelated damage propagation till the peak load is observed. In the second stage, during localized crack propagation, the value of diffusion induced force required is much smaller than the peak load observed at the end of percolative damage propagation. Similar to evolution of damage, reduction in stiffness also occur in two phases. During percolative damage evolution, stiffness decreases at a very slow rate,

which is also independent of the loading gradient (δ). In the second phase of localized fracture propagation, stiffness decreases drastically and becomes zero very quickly. The rate of stiffness reduction depends on the concentration loading gradient (δ). A lattice network with zero stiffness signifies complete rupture. Both the transition broken bond fraction and transition stiffness follows power law relation with the system size.

Grain/grain-boundary microstructures of polycrystals impact the evolution of damage and nucleation of cracks within a lattice spring network. Stiffness ratio of the grain interior over the grain boundary region controls the crack pathway. For $(k_g / k_{gb}) \approx 1.0$, the crack follows a transgranular pathway. Whereas, for $(k_g / k_{gb}) >> 1.0$ leads to intergranular fracture patterns. Capturing intergranular fracture was possible using the XFEM technique by controlling the toughness of the grain boundary region [172]. Similar type of transition between transgranular and intergranular fracture simply by changing the stiffness ratio was reported earlier [51, 176]. Temperature gradient induced load was considered in that study. Grain size in the polycrystalline microstructure also affects damage evolution. Microstructures with large grain size provide straight pathways through the grain-boundary region for easy propagation of localized crack fronts. On the other hand, polycrystals with smaller sized grains contain a very tortuous grain-boundary pathway. Propagation of a localized crack front becomes relatively difficult because of the hindrance provided by the tortuous pathway. As a result, higher strength of the lattice network was observed for smaller grain sizes. No

scaling analysis of the toughness with respect to the grain size has been reported in this article.

While predicting the elastic field, the discrete lattice spring model adopted in this study shows certain differences from the continuum based analysis. The elastic field at the crack tip is always singular according to continuum analysis. However, realistically the singularity in strain energy at the crack tip is relaxed by some dissipative means, such as plasticity. Atomic level discreteness of solids also sometime contributes to relaxation of the singular elastic field. The discrete lattice spring model adopted here introduces an explicit microstructural length scale, which stabilizes the governing equations and removes the singularity in the elastic field observed at the crack tip. The stress field predicted by the lattice spring model very close to the crack tip is a function of the size of each spring. Hence, the fracture strength predicted by this discrete lattice spring model may not quantitatively correspond to that observed experimentally. The current work is devoted to analyzing the scaling of different damage parameters and transition between diffusive and localized fracture propagation. The purpose of the present study is not to predict the accurate fracture strength of a disordered media under diffusion induced load. Thus the qualitative comparisons and trends predicted by the lattice spring models are still applicable. Correlation between the discreteness associated with the computational model and the discreteness corresponding to the grain size effect also arise a question. In the current study, size of each grain is assumed to be significantly larger than the size of lattice springs. Hence, the discreteness of the computational model should have very little effect on the qualitative trends observed in

the micro-cracking behavior of lattice networks with grain/grain-boundary microstructure. However, the inherent discreteness of the system renders quantitative comparison of the grain size effect obtained from simulations with that observed in experiments, meaningless.

CHAPTER IV

A MECHANO-ELECTROCHEMICAL PREDICTIVE MODEL FOR ACOUSTIC EMISSION RESPONSE IN INTERCALATION ELECTRODES*

An efficient way to characterize the amount of mechanical degradation in solid materials is through the acoustic emission. In the following chapter a computational scheme has been developed to predict the acoustic emission spectra observed in lithium ion battery active particles due to diffusion induced stress.

4.1 Computational analysis

A mechano-electrochemically coupled stochastic methodology, shown schematically in Fig. 4.1, has been developed to capture diffusion induced stress, damage evolution and corresponding acoustic emission characteristics in the lithium-ion battery electrode. In the current work, we restrict our attention to a representative circular active particle. The coupled formalism includes a *dynamic lattice spring model* which solves the transient momentum balance equation to capture the *dynamic damage evolution* based on the stress field resulting from the underlying lithium intercalation induced concentration field. In the previous work, a *quasistatic* lattice spring model was presented (see [85, 178]) to study the diffusion induced damage in intercalating active particles representative of LIB electrodes. The details of the present stochastic formalism are furnished below.

*Printed with permission from "Mechano-electrochemical model: Acoustic emission" by P. Barai and P. Mukherjee (2014) J. Elec. Soc. 161 F3123 – F3136 by Copyright 2014 ECS – The Electrochemical Soc.

Time dependent Fick's second law, along with a constant lithium ion flux boundary condition, is solved for the concentration field inside the single particle. Constant lithium ion flux is used as the boundary condition.

$$\frac{\partial c}{\partial t} = \nabla \cdot \left(D \cdot \nabla c \right) \tag{4.1}$$

$$D \frac{\partial c}{\partial n} = -\frac{I}{SF} \tag{4.2}$$

Here, $c = c(x, y, t)$ means the lithium ion concentration at a particular point (x, y) and at the time t, ∇ signifies the gradient operator, D is the diffusivity, n is the outer normal from the particle surface, I is the applied constant current on the particle surface applied during galvanostatic operation, S is the available surface area in the entire electrode and F signifies the Faraday's constant. The diffusion equation (Eq. (4.1)) is solved on a circular domain that represents the cross section of a representative spherical single particle. Finite volume method is used to solve the time dependent equation and obtain the ion concentration profile. Backward Euler time integration scheme is employed, which is unconditionally stable. Concentration gradients have been obtained by subtracting the average concentration from the local concentration. Volume averaging scheme has been adopted to estimate the mean value of concentration within the active particle.

The dynamic lattice spring method captures the mechanical degradation observed within the circular particle due to intercalation-induced stress. In this regard, the time dependent momentum balance equation is solved to capture the displacement, velocity and acceleration of the nodes in the lattice spring network superimposed on top of the

single particle. The finite element discretization of the wave equation (or the momentum balance equation), which takes into consideration the effect of damping, has been provided below:

$$[M]\{\ddot{U}\}+[C]\{\dot{U}\}+[K]\{U\}=\{F\} \tag{4.3}$$

Here, $[M]$ is the mass matrix, $[C]$ represents the damping matrix, $[K]$ signifies the stiffness matrix, $\{\ddot{U}\}$ is the acceleration vector, $\{\dot{U}\}$ signifies the velocity vector, $\{U\}$ stands for the displacement vector and $\{F\}$ represents the body force vector. To restrict the rigid body modes of translation and rotation, two points were selected inside the particle (close to the center) and they were fixed completely. The global stiffness ($[K]$), damping ($[C]$) and mass ($[M]$) matrix have been obtained by properly assembling over the local stiffness ($[k_l]$), damping ($[c_l]$) and mass ($[m_l]$) matrix, respectively. While converting from local coordinate system to global coordinate system, proper multiplication with the transformation matrix ($[T_l]$) has been conducted. For the mechanics solve, the entire continuum has been discretized using a point collocation of springs. Unlike regular trusses, the springs adopted in this study displays axial as well as shear resistance against deformation. This mesh configuration has been used quiet extensively in discrete element method (DEM) to characterize the behavior of solid continua. Details about the stiffness, damping and mass matrix are provided below. The values of displacement, velocity and acceleration have been obtained by solving Eq. (4.3). The computational methodology adopted to solve the time dependent momentum balance equation is also given below.

Estimation of the diffusion of lithium ions induced displacement in a critical aspect. The outcome from the computational technique depends significantly on how the concentration gradient is being coupled with the mechanical response. The diffusion induced displacement is calculated as, $\{u_d\} = \{-\Delta u_d \quad 0 \quad \Delta u_d \quad 0\}$, and Δu_d is defined as,

$$\Delta u_d = \omega \cdot \Delta c \cdot l \tag{4.4}$$

Here, ω is the diffusion expansion coefficient (unit m^3 / mol), Δc is the concentration gradient (unit mol / m^3) and l is the length of each spring element (unit m). The term diffusion expansion coefficient can be defined as the amount of expansion (or contraction) experienced when one mole of lithium ion intercalates (or de-intercalates) within an active particle of unit volume. The concentration gradient Δc at each node is estimated as the difference between the local concentration and the average concentration value $\left(\Delta c(x,t) = c(x,t) - c_{avg}(t)\right)$. The local concentration profile $\left(c(x,t)\right)$ is obtained by solving the time dependent diffusion equation given by Eq. (4.1) and (4.2). The average concentration profile is obtained by taking the volume average over the entire particle $\left(c_{avg}(t) = \frac{1}{V}\int_V c(x,t)\,dV\right)$. In the current simulation, the stress free concentration profile has not been adopted as the reference value. Usually, a particle subjected to uniformly distributed concentration (without any gradient in the concentration profile) experiences only dilatational strain and expands uniformly without the generation of stress. For both phase separating and non-phase transforming materials,

stress generates only when there exists concentration gradient. Thus, to capture the effect of concentration gradient on the generation of diffusion induced stress; the average concentration has been adopted as the reference value. For uniformly distributed concentration profile, amount of stress obtained based on this methodology is zero, which is also consistent with the experimental observations.

Once the values of displacement, velocity and acceleration at each node have been evaluated (using the technique described below), the next step is to calculate the elastic strain energy stored in each spring.

$$\psi = \frac{1}{2}\vec{F}_g \cdot \vec{u}_g \tag{4.5}$$

Here, ψ is the elastic strain energy stored in each spring, $\vec{F}_g$ is the global force vector and $\vec{u}_g$ is the global displacement vector for a particular spring. If the energy in a spring exceeds its rupture threshold $(\psi > \psi_t)$, the spring is assumed to be broken and subsequently removed from the lattice spring network in an irreversible fashion. The rupture energy threshold (ψ_t) is a randomly distributed parameter, which follows a uniform distribution around a particular mean value (ψ_{mean}). The adopted failure criterion is a local breaking mechanism. However, this local criterion of damage evolution has already been utilized in the literature. For example, Alava et al.[30] and Zapperi et al.[44] have employed similar failure criterion to simulate fracture in disordered media. Following their methodology, the current breaking criterion has been developed. In the current work, a local breaking threshold has been adopted to be

consistent with the energy requirement of the material being investigated. But how this compares with the global energy balance within the context of lattice spring model has not been explicitly tested yet, and is left as a future exercise. In the present simulations, the mean value of energy threshold is assumed to be same as that of graphite, $2J/m^2$. The actual value of the rupture energy threshold (ψ_t) ranges between $1J/m^2$ and $3J/m^2$ according to a uniform distribution. When a lattice spring is removed from the lattice network, its contribution into both the stiffness and damping matrix is subtracted. Since the mass is not lost, the mass matrix is kept unchanged.

The effect of concentration on the mechanical response is very obvious through the Eq. (4.4). But the effect of mechanical degradation on the diffusion process has not been taken into account. Under no fracture condition the diffusivity of a material remains constant at the pristine value. With the introduction of mechanical damage the local diffusivity of a material decreases. Based on this physical understanding a methodology was described in Barai and Mukherjee (see Fig. 3 in Ref. [85]) to reduce the value of diffusivity by a constant factor (α) in the control volume wherever the fracture occurs. The new effective diffusivity (D_e) would be represented as,

$$D_e = \alpha D \tag{4.6}$$

A schematic representation of the control volume adopted in the current simulation is provided in Fig. 4.1(a). Mapping of the lattice spring network on top of the control volume has also been shown in Fig. 4.1(a). Figure 4.1(b) demonstrates a schematic representation of the spring – damper system used in the dynamic lattice spring model.

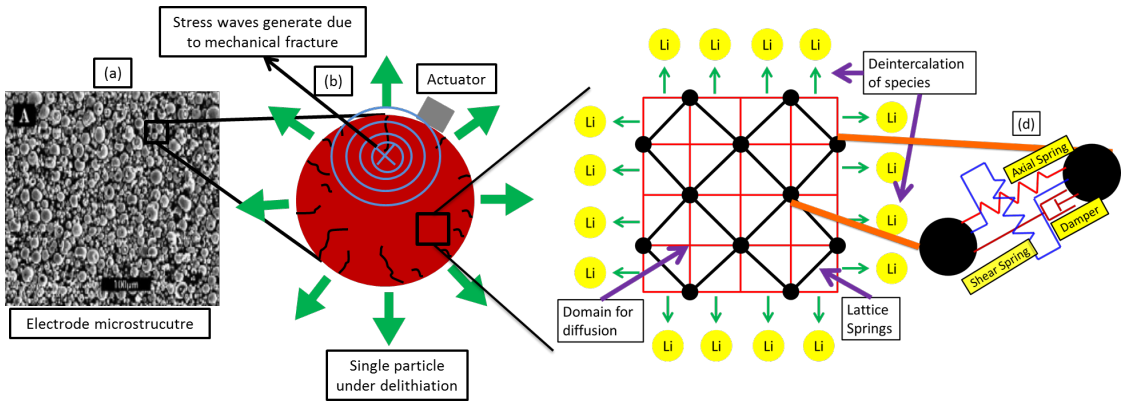

Fig: 4.1. *(a) SEM image of a typical composite electrode microstructure. (b) Schematic demonstration of delithiation, peripheral crack formation, acoustic wave propagation and detection of stress waves by an actuator. (c) Schematic illustration of the Dynamic lattice spring model (LSM) to capture the evolution of crack. The domain of LSM is depicted using the black color and it lies on top of the domain of diffusion. (d) Distribution of springs (axial and transverse) and dampers between two nodes is demonstrated.*

4.2 Details of the computational technique

The local stiffness matrix for each spring is calculated as,

$$[k_l] = \begin{bmatrix} k_n & 0 & -k_n & 0 \\ 0 & k_s & 0 & -k_s \\ -k_n & 0 & k_n & 0 \\ 0 & -k_s & 0 & k_s \end{bmatrix} \tag{4.7}$$

Where, k_n signifies axial stiffness and k_s represents the shear resistance of the spring against deformation. The exact value of the axial and shear spring stiffness (k_n, k_s) have been obtained from the Young's modulus (E) and shear modulus (G) according to the procedure described in Zhao et al (see [151]). The local damping matrix is written as,

$$[c_l] = \begin{bmatrix} c_n & 0 & -c_n & 0 \\ 0 & 0 & 0 & 0 \\ -c_n & 0 & c_n & 0 \\ 0 & 0 & 0 & 0 \end{bmatrix} \tag{4.8}$$

Here, c_n represents the damping coefficient along the axial direction. No damping parameter has been assumed along the transverse direction. Only a diagonal mass matrix has been taken into account to simplify the problem being solved. The local mass matrix usually takes the form,

$$\left[m_l\right] = \begin{bmatrix} m & 0 & 0 & 0 \\ 0 & m & 0 & 0 \\ 0 & 0 & m & 0 \\ 0 & 0 & 0 & m \end{bmatrix} \tag{4.9}$$

Here, m signifies the 50% mass of the entire spring. Since the local mass matrix is equivalent to a scalar multiplied by an identity matrix, while transforming it from local to global coordinate system, no multiplication with the transformation matrix is required. For all the three mass, damping and stiffness matrices, conversion from local to global form can be conducted by assembling the local matrices for all the springs using the procedure provided below (see [156]),

$$\left[K\right] = \prod_{\substack{all\ the \\ elements}} \left[T_l\right]^T \cdot \left[k_l\right] \cdot \left[T_l\right] \tag{4.10}$$

Diffusion of lithium ions creates concentration gradient, which results in generation of stress in the particle. This concentration gradient induced force on each of the particles has been estimated using the following relation:

$$\left\{F\right\} = \prod_{\substack{all\ the \\ elements}} \left[T_l\right]^T \cdot \left[k_l\right] \cdot \left\{u_d\right\} \tag{4.11}$$

To solve for displacement, velocity and acceleration at each time step, the Newmark's method of time integration scheme have been adopted. The average

acceleration method (under Newmark group of algorithms), which leads to unconditional stability have been adopted as the numerical technique for conducting the time integration (see [179]). The basis of this numerical scheme is that the displacement and velocity of the next time step can be written as a linear combination of the displacement, velocity and acceleration of the current or the next time step. Here we will follow the convention that "i"-th time step signifies the current time step and "i+1"-th time step signifies the next iteration.

$$\dot{u}_{i+1} = \dot{u}_i + (1-\gamma)\cdot(\Delta t)\cdot\ddot{u}_i + \gamma\cdot(\Delta t)\cdot\ddot{u}_{i+1} \tag{4.12}$$

$$u_{i+1} = u_i + (\Delta t)\cdot\dot{u}_i + \left(\frac{1}{2}-\beta\right)\cdot(\Delta t)^2\cdot\ddot{u}_i + \beta\cdot(\Delta t)^2\cdot\ddot{u}_{i+1} \tag{4.13}$$

Here, β and γ are two parameters which varies depending on the algorithm being used and Δt signifies the time increment at each step. The main governing equation that has to be solved is given in Eq. (4.3). For the next (i+1) time step, the equation can be written in a modified form,

$$M\ddot{u}_{i+1} + C\dot{u}_{i+1} + Ku_{i+1} = F_{i+1} \tag{4.14}$$

Substituting Eq. (4.12) and (4.13) into Eq. (4.14),

$$\ddot{u}_{i+1} = \frac{1}{\beta\cdot(\Delta t)^2}\cdot(u_{i+1}-u_i) - \frac{1}{\beta\cdot\Delta t}\cdot\dot{u}_i - \left(\frac{1}{2\beta}-1\right)\cdot\ddot{u}_i \tag{4.15}$$

Substituting Eq. (4.15) into Eq. (4.12) gives,

$$\dot{u}_{i+1} = \frac{\gamma}{\beta\cdot\Delta t}\cdot(u_{i+1}-u_i) + \left(1-\frac{\gamma}{\beta}\right)\cdot\dot{u}_i + \left(1-\frac{\gamma}{2\beta}\right)\cdot(\Delta t)\cdot\ddot{u}_i \tag{4.16}$$

Substituting Eq. (4.15) and Eq. (4.16) into the governing differential equation (Eq. (4.14)),

$$\left[\frac{M}{\beta(\Delta t)^2}+\frac{C\gamma}{\beta(\Delta t)}+K\right]\cdot u_{i+1}=F_{i+1}+\left(\frac{M}{\beta(\Delta t)^2}+\frac{C\gamma}{\beta\Delta t}\right)\cdot u_i+\left(\frac{M}{\beta(\Delta t)}-C\left(1-\frac{\gamma}{\beta}\right)\right)\cdot \dot{u}_i+\left(M\left(\frac{1}{2\beta}-1\right)-C(\Delta t)\left(1-\frac{\gamma}{2\beta}\right)\right)\cdot \ddot{u}_i \tag{4.17}$$

Eq. (4.17) can be written in a simplified form,

$$\hat{K}_{i+1}\cdot u_{i+1}=\hat{F}_{i+1} \tag{4.18}$$

By solving Eq. (4.18) using the LU decomposition method, u_{i+1} is obtained. The value of u_{i+1} is substituted back into Eq. (4.16) and Eq. (4.15) to have the values of $\dot{u}_{i+1}$ and $\ddot{u}_{i+1}$, respectively.

Table 4.1. Material parameters used to simulate acoustic emission response in the active particle. These properties correspond to that of "graphite" (adopted from Grantab and Shenoy, *JES* 2011 [17]).

Name	Material parameters
Diffusion coefficient (D)	$3.9\text{x}10^{-14}$ m^2/s
Expansion coefficient (ω)	$1.14\text{x}10^{-6}$ m^3/mol
Young's modulus (E)	70.57 GPa
Shear modulus (G)	27.63 GPa
Mean fracture threshold energy (ψ_{mean})	2 J/m^2
Density	2200 kg/m^3
Maximum Li ion concentration $(c_{\max})$	31833 mol/m^3
Operating temperature (T)	298 K

4.3 Numerical experiments

Using the computational methodology described in the previous section, some simulations were run to clearly elucidate the acoustic emission response observed in realistic experiments. The material parameters used in the simulations have been provided in Table: 4.1. The adopted properties correspond to that of graphite anode particles (adopted from Grantab and Shenoy, JES 2011)[17]. Active particles present inside the lithium ion battery electrode can be random in shape and size. In the present study, for consistency purpose, the particles have been assumed to be spherical in shape. In this work, a representative single electrode particle has been simulated and the corresponding acoustic response of the spherical active particle has been predicted. The out-of-plane scenario follows the plane strain assumption. Here the displacement along the out-of-plane direction is assumed to be zero $(u_z = 0)$. A two-dimensional circular cross-section has been adopted in this study for the demonstration of the acoustic emission prediction capability. Time dependent Fick's second law (Eq. (4.1)) and time dependent equilibrium equation (Eq. (4.3)) have been solved sequentially to obtain the acoustic emission response due to the diffusion of Li ions and rupture of the lattice springs. A particular value of the time step increment was selected as $\Delta t = 1s$. Unless mentioned otherwise, a particle of radius 10μm has been adopted in all the simulations. At the beginning of simulation constant concentration profile was assumed throughout the particle. The initial displacement, velocity and acceleration of all the nodes were considered to be zero. At the first step, constant out-flux of lithium ions were applied at the external boundary of the particle. Change in concentration gradient was calculated by

solving the time dependent diffusion equation by using a finite volume based solver. Backward Euler time integration has been adopted because of its unconditional stability. The average Li ion concentration of the entire particle was calculated by using a volume average technique. Concentration gradients at each control volume were estimated by subtracting the average concentration from the local concentration value. By mapping the mesh for the dynamic lattice spring method on top of the control volumes for the concentration profile, concentration gradient values for each of the nodes in the dynamic lattice spring model were obtained. Concentration gradient in each element was estimated by taking the average of the two adjacent nodes. Based on this value of the concentration gradient, the diffusion-induced force in each spring was calculated. The equilibrium displacement, velocity and acceleration were calculated by solving the dynamic momentum balance equation using the average acceleration method. The reason behind adopting the average acceleration method has been its ability to display unconditional stability irrespective of the time step used in the computation.

Once the equilibrium displacement, velocity and acceleration have been calculated, strain energy stored in each spring was estimated. If this elastic strain energy exceeded the fracture threshold, it was assumed to be broken and was irreversibly removed from the lattice network. Removal of a spring from the network was accomplished by subtracting its contribution from the network stiffness matrix. Similar to the stiffness matrix, contribution of the spring into the damping matrix was also removed. When a microcrack develops, the mass of the system does not change. Thus no modification was conducted in the mass matrix during removal of a spring from the

network. At each time step, multiple springs broke and were subsequently removed from the network if the concentration gradient was sufficiently large. Only one spring was removed from the network during each solve. Thus, to break multiple springs in a single time step, several solves were conducted. The network was allowed to mechanically re-equilibrate before calculating for the next iteration step. Breaking of bonds was continued until the concentration gradient required for the next bond to break became larger than that obtained by solving the diffusion equation. In the mechanics solve, small strain small displacement assumptions were used. When the displacement in the system is calculated under the total amount of externally applied load, the formulation is known as the total formulation. On the contrary, if the external load is applied in an incremental fashion and in each time step only the incremental displacement due to the incremental load is estimated, the methodology is known as an incremental formulation. For linear elastic materials, total as well as the incremental formulation provides the same response if the externally applied load is linear. In the current simulation, the criterion for breaking the springs depends on the total energy. Hence, a total formulation was preferred over an incremental one to be more consistent with the bond-breaking algorithm. To reduce the computational time, spring elements outside the circular particle were completely removed from the network. As a particular spring broke, its impact on the local diffusivity was also taken into account. Physically speaking, formation of a microcrack restricts the transportation of Li ions by increasing the tortuosity of the diffusion pathway. Thus the value of the local diffusivity gets reduced, which has been taken into consideration by reducing the diffusion coefficient of the

control volumes located around the broken bond by a constant factor $(\alpha = 0.55)$ (see Eq. (4.6)). Part of the strain energy released due to the rupture of a spring got converted into the kinetic energy of nodes. The dampers located around the broken spring dissipated some other part of the energy. Since the fracture energy is a randomly distributed parameter, 10 samples were considered with different values of the fracture threshold for each data point. Mean and range of the uniform distribution were kept same for all the different samples. While plotting the total amount of broken springs, average of all these ten samples were considered. The error bars signify one sigma standard deviation of these ten samples.

4.4 Results and discussion

The impact of energy release due to fracture formation on the stress wave propagation is illustrated in Fig. 4.2. Acoustic emission spectra capture the waves that propagate through the material and hits the actuator placed on the surface of the particle. Stress waves can generate because of increase in concentration gradient induced loading as well as rupture of a spring element (see [66, 69]). Thus it is important to quantify the magnitude of different types of stress waves that propagate through the media and hits the actuator. To accomplish this goal, two simulations were conducted on a single particle under 3C rate of discharge with and without rupture of spring elements. The results (shown in Fig. 4.2) clearly demonstrate that, the magnitude of stress waves due to the initiation of out-flux of lithium ions are in the order of 10^{-3}. On the other hand, the stress waves that generate due to the rupture of the spring elements display a magnitude of around 10^{-1}. Two orders of magnitude difference signifies that the stress waves due to

the initiation of the delithiation process would negligibly affect the acoustic emission spectra. Stress waves due to the energy released after the rupture of bonds significantly dominates over the other forms of waves. Thus the actuator detects only the energy from initiation, nucleation and propagation of microcracks. Every other signal almost gets filtered out because of their negligibly small amplitude.

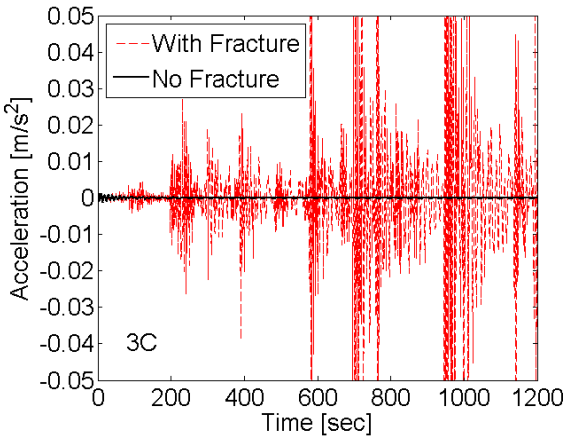

Fig: 4.2. *Acoustic emission spectra with (red) and without (black) microcrack evolution. The stress waves that generate because of the diffusion induced loading only has a very small magnitude as compared to the stress waves due to the energy released from microcrack formation. A particle of radius 10μm has been considered for this simulation.*

When a fully lithiated particle is delithiated, a state of tension occurs on the particle surface relative to the core, and surface fracture may occur. On the other hand, as lithium gets added to an empty active particle, a volume expansion is generally observed. As a result the material near the particle surface tries to expand as its lithium content is increased. The delithiated material near the core resists this expansion. As a result, the surface material contracts and the core material experiences tension (see [14, 144]). Microcrack generation and propagation happens only under tensile load. As a result, it is expected that mechanical damage will occur along the periphery during

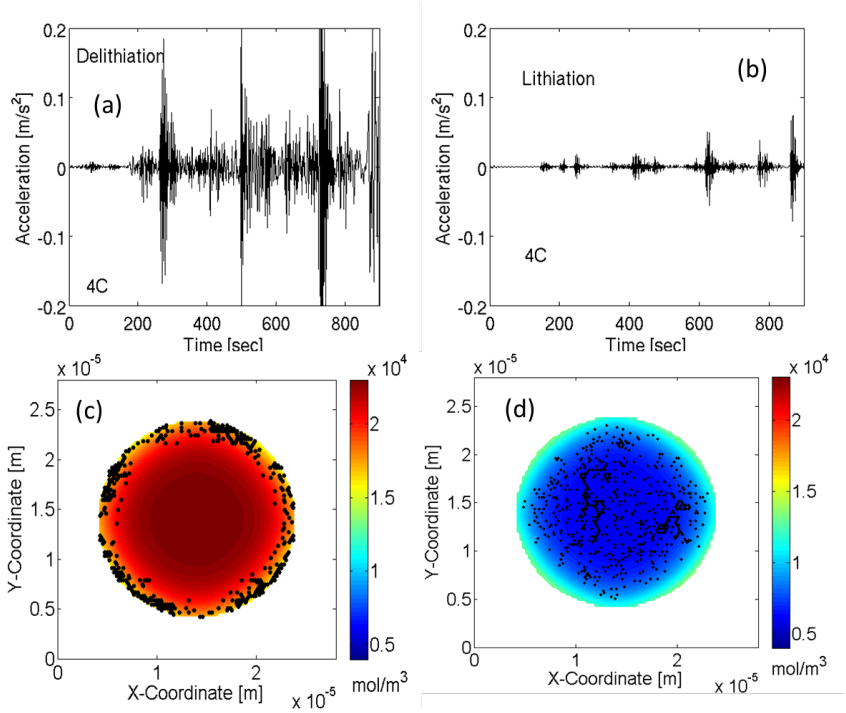

Fig: 4.3. *Difference in emission spectra and fracture contour during delithiation and lithiation. (a) Acoustic emission during delithiation at 4C. (b) Acoustic emission during lithiation at 4C. (c) Concentration contour and fracture profile during delithiation at 4C. (d) Concentration contour and fracture profile during lithiation at 4C. Particles of radius 10μm have been considered for this simulation.*

delithiation and in the central portion during lithiation (see [22]). A volumetric average of the lithium ion concentration is adopted as the equilibrium ion concentration (see [29]). Since the average concentration is not the arithmetic mean of the maximum and minimum concentrations observed within the particle, magnitude of tensile stress that acts on the particle during delithiation is higher than the magnitude of tension during lithiation. As a result more mechanical degradation is observed during delithiation as compared to that during the lithiation process (see [16, 25]). A comparison between the amount of mechanical damage observed during delithiation and lithiation process at 4C and the corresponding acoustic emission spectra have been demonstrated in Fig. 4.3. Severe mechanical damage evolves during the delithiation process (see Fig. 4.3(c)).

Relatively less mechanical damage has been observed for the lithiation process (see Fig. 4.3(d)). Since more number of springs break during the delithiation process under the action of higher concentration gradient and subsequently larger tensile load, larger amount of energy is released. This significantly increases the kinetic energy of the nodes. A strong acoustic emission response is observed with multiple peaks and some of the signals have very large amplitude (see Fig. 4.3(a)). On the other hand, during lithiation, smaller amount of mechanical damage releases less strain energy and the acoustic emission spectra is not very strong (see Fig. 4.3(b)). Corresponding to different localized damages under lithiation, some energy release occurs which shows up as peaks in the acoustic emission spectra. But their magnitude is smaller than that observed during the delithiation process. Moreover, during lithiation, damage evolves in the center of the particle. The actuators that detect the acoustic emission signal are placed along the surface of the particle. Because of the inherent energy dissipation of the active material due to damping, some of the stress waves get completely dissipated before reaching the surface. This results in even smaller amplitude of stress waves, and subsequently acoustic activity during the lithiation process. During delithiation, fracture evolution close to the periphery results in early detection of released strain energy by the actuators located on the surface, before significant dissipation of the stress waves. As a result, stronger acoustic activity is observed during the delithiation process.

The amount of mechanical degradation is characterized as fraction of broken springs in the DLSM framework [85]. This provides a local depiction of the effect of microcrack formation and propagation. However, experimentally it is quite difficult to

locally probe and measure how many microcracks develop. When a microcrack forms, the material releases strain energy that travels through the media as a stress wave. Detection of this propagating stress wave at the particle surface by an actuator gives the measure of mechanical damage within a material. Since energy is released whenever a microscopic crack is formed, the cumulative energy released should give us a measure of the total amount of mechanical degradation. The exact amount of mechanical degradation is given by the fraction of broken springs. To check how well the measurement of cumulative energy corresponds to the total number of broken springs, a comparative analysis is conducted in Fig. 4.4. Amount of mechanical stress is directly proportional to the concentration gradient. Higher stress gives rise to enhanced mechanical damage. For a fixed particle size, concentration gradient is inversely proportional to the diffusion coefficient. As a result, higher diffusivity would result in low concentration gradient, small mechanical stress and less damage. Cumulative strain

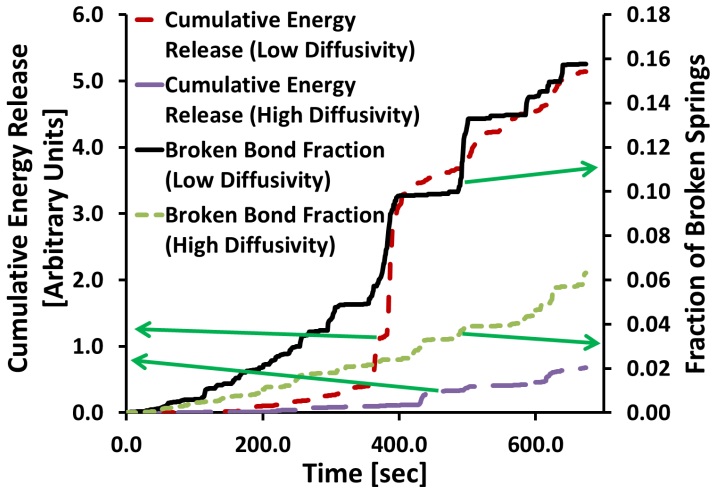

Fig: 4.4. *Demonstration of equivalence between damage evolution (fraction of broken springs) and cumulative energy released during delithiation process. At low values of diffusivity, enhanced microcrack formation is observed, which leads to more energy release. Opposite pattern is observed at high values of diffusivity. A particle of radius 10μm has been considered in this simulation.*

energy released due to microcrack formation will be smaller for particles with high diffusivity. On the other hand, particles with low diffusion coefficient give rise to higher concentration gradient. Subsequently larger mechanical degradation followed by enhanced release of strain energy is observed. Cumulative release of energy as well as the fraction of broken springs should be larger for low diffusivity than the case with high diffusivity. The same phenomena as described have been reported in Fig. 4.4. A particle of radius 10μm is subjected to delithiation at 6C. The two different diffusivities considered in this simulation are $3.9 \times 10^{-14} m^2/s$ (the lower value) and $7.8 \times 10^{-14} m^2/s$ (the higher value, which is double of the lower one). The lower value of diffusivity adopted in this simulation corresponds to that usually observed in graphite at room temperature. According to the Arrhenius relation, 10K rise in temperature, approximately doubles the diffusivity. Since the higher diffusivity is double in magnitude of the lower one, it corresponds to the diffusivity of graphite at elevated temperatures. One thing should be noted is the fact that the actuator is placed at one point in the surface of the particle. If a microcrack develops far away from the actuator, the stress wave might get completely dissipated before reaching the sensor. As a result, this microcrack located far away from the device will never be detected by the emission spectra. This discrepancy does not exist while calculating the fraction of broken elements. Thus a quantitative comparison between the energy release and fraction of broken springs is not possible. However, good qualitative measure can be achieved which are usually sufficient for practical purposes.

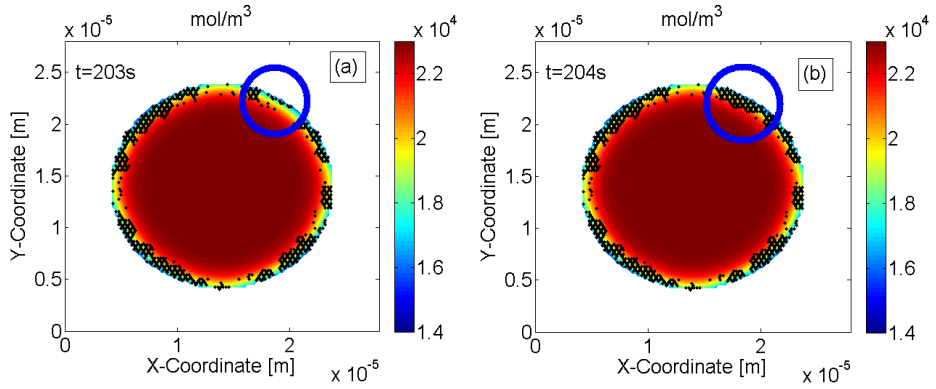

Fig: 4.5. *Demonstration of the avalanche phenomenon. (a) Fracture profile after 203s. (b) Fracture profile after 204s. The blue circle highlights a bunch of bonds which broke in just one time step. This is typically known as the avalanche phenomenon, where one strong bond holds a bunch of weak bonds around it. As soon as this strong bond breaks, all the weak bond also experience rupture, which is usually followed by enhanced acoustic activity. The particle size considered in this simulation is 10μm.*

As shown in Fig. 4.4, damage evolution over time often experience jumps in the fraction of broken springs (two such phenomena occurred at 400 seconds and 500 seconds, approximately). Why these types of jumps in the fracture profile occur has been a matter of concern. These jumps in damage evolution are known as “avalanches” (see [30, 44]). To demonstrate the occurrence of the avalanche phenomenon, Fig. 4.5 shows the formation of a bunch of broken elements in a very short period of time (1 second) in a circular particle during delithiation at a rate of 8C. What happens inside the lattice structure can shed some light onto the physical mechanism of the avalanche phenomenon. Since the fracture thresholds of the springs are randomly distributed, some springs are stronger than the others. It may happen that a strong spring holds a bunch of weak elements surrounding itself from rupture. Eventually, with increasing external load, the strong spring breaks at a point. Immediately, all the weak elements located around the strong one experiences rupture. This phenomenon of breaking a bunch of bonds in a very short period of time is characterized as an avalanche. In Fig 4.5(a) a

portion has been highlighted with a blue circle where less damage is present at the time $t = 203s$. In Fig 4.5(b) the same highlighted region experiences significant mechanical degradation at the time $t = 204s$. This sudden increment in mechanical degradation in a very short period of time corresponds to the avalanche phenomenon. Such sudden rise in damage occurrence result in jumps in the evolution of fraction of broken elements as well as the evolution of cumulative energy release curves.

To check whether the predictions of damage evolution and cumulative energy release obtained from the dynamic lattice spring method is consistent with the experimentally observed response, a comparison has been conducted in Fig. 4.6 with the damage evolution patterns reported in Woodford *et al.* (2012), which has also been obtained using acoustic emission [79]. The parameters of $LiCoO_2$ used to run the simulation is provided in Table: 4.2. In the experimental result, even

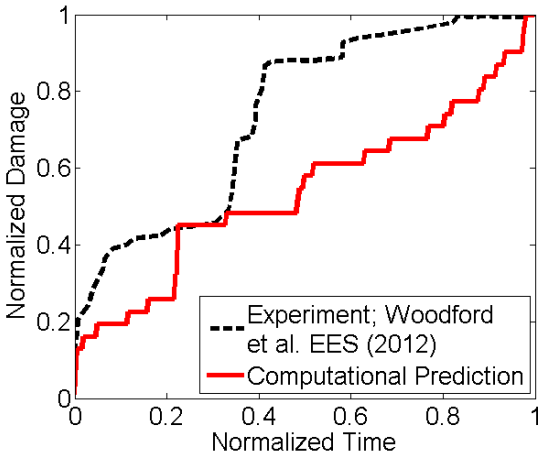

Fig: 4.6. *Qualitative comparison of acoustic emission response as observed in experiments and that predicted from the theory presented in the present article. The developed model is capable of predicting the jumps in damage evolution that corresponds to the avalanche phenomenon. The particle simulated in this case has a radius of 10μm.*

Table 4.2. Material parameters used to run the simulation of fracture and acoustic emission in $LiCoO_2$ active particle. This data set was used in the comparison with experimental results.

Name	Material parameters
Diffusion coefficient (D)	1.0×10^{-14} m^2/s [157]
Expansion coefficient (ω)	9.85×10^{-7} m^3/mol [21]
Young's modulus (E)	375 GPa [14]
Shear modulus (G)	124 GPa [180]
Mean fracture threshold energy (ψ_{mean})	1 J/m^2 [14]
Density	5060 kg/m^3 [181]
Maximum Li ion concentration $(c_{\max})$	51410 mol/m^3 [157]
Operating temperature (T)	298 K

though the fracture happens at a very low rate, it is evident that the crack forms and propagates due to the development of large concentration gradient between the two phases of $LiCoO_2$. In the current methodology, evolution of damage is governed by concentration gradient only. Even though, formation of the concentration gradient happens through different mechanisms in experiment and simulation, they should show similar acoustic energy release that only depends on the amount of mechanical damage and not how the damage is happening. Thus, the comparison of the acoustic emission spectra between these two cases is a preliminary attempt toward a more rigorous validation, which is left as a future exercise. However, evolution of damage depends significantly on the presence of pre-existing manufacturing flaws within the material. For different samples of the same material, during damage evolution amount of energy released through acoustic emission can be significantly different. The effect of preexisting flaws has been taken into consideration by varying the fracture energy according to a uniform distribution of random numbers. Due to the presence of these

randomly generated preexisting flaws, microcrack formation and fracture of active particles become random phenomena. Since damage evolution is a relatively random process, exact correlation between the two curves is almost impossible to attain. But, some of the experimentally observed features, such as the avalanche phenomenon have been characterized successfully. Jump in fraction of broken springs are observed at the beginning of the delithiation process. In the experimental analysis little damage evolution has been observed in the second half of the delithiation. But, for the computational prediction, damage continues to evolve till the end of the delithiation process. This can be attributed to the fact that in the lattice network used in DLSM, there were potentially more weak linkages where damage could evolve. A good qualitative comparison with the experimental result establishes the accuracy of the developed DLSM and this method can be used for predicting experimentally observed acoustic emission response.

It has been reported that larger mechanical degradation is observed under high C-rate conditions and low C-rates result in small amount of broken elements for non-phase transforming materials, such as, graphite and silicon (see [14, 27, 63, 65, 84]). For phase transforming cathode materials, fracture may appear at lower rates of operation as well (see [12, 13]). In the current research article, the main focus is to describe a computational methodology that can predict the experimentally observed acoustic emission spectra during the fracture of active electrode particles. The present methodology takes into consideration only the concentration gradient induced by the lithium diffusion phenomena. This methodology will be extended to phase transforming

materials as a part of future work, in which case the formation of cracks even at low rate operations (observed in cathode particles) can be captured. To estimate the total amount of mechanical degradation, an experimentalist measures the cumulative strain energy that releases during operation. The question is how well the cumulative energy released reflects the total amount of microcrack formation. To answer this question, a study have been conducted where a particle was delithiated at different C-rates and the corresponding fraction of broken springs (see Fig. 4.7(a)) as well as subsequent release of strain energy have been plotted (see Fig. 4.7(b)). As shown in Fig. 4.7(a), higher C-rate (6C and 8C) results in enhanced damage evolution. Smaller fraction of bonds broke for low C-rate applications (1C and 2C). As expected, damage evolution for 3C and 4C lies in between the two. Figure 4.7(b) shows a cumulative measure of the corresponding release of strain energy. Large amount of strain energy release has been detected under high C-rate conditions. Under low C-rates of 1C and 2C, strain energy released is minimal and can be neglected. For applications under intermediate C-rates of 3C and 4C, cumulative strain energy curves lie in between. Similar to the fraction of broken springs, total energy for 3C is less than that observed for 4C. Two apparent discrepancies in the acoustic emission response must be pointed out. In the figures 4.7(a) and 4.7(b), four curves in two pairs, “A”-“B” and “C”-“D”, have been separately demarcated to demonstrate the pair of apparent mismatch that can potentially occur in acoustic emission response. The fraction of broken elements under (see Fig. 4.7(a)) delithiation at 8C (denoted by “A”, solid red line) predominantly lies above the fraction of broken springs observed under delithiation at 6C (denoted by “B”, dash-dot red line). But in the

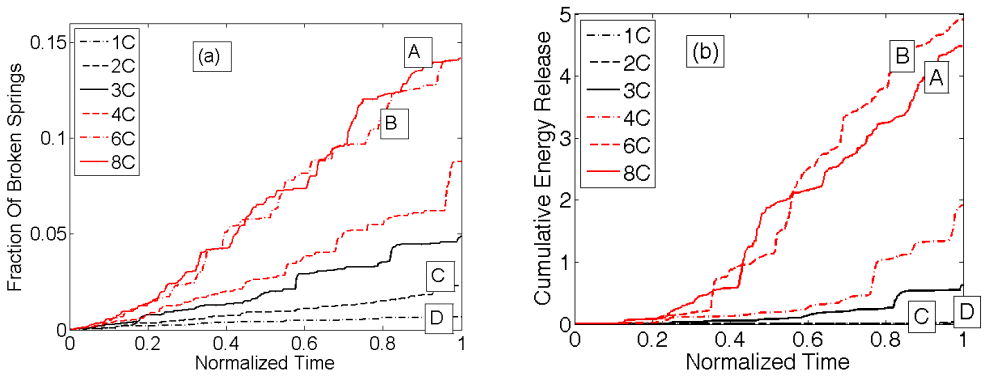

Fig: 4.7. *(a) Damage bonds observed at different C-rates have been plotted with respected to a normalized time scale. (b) Cumulative energy release at the same C-rates has been plotted with respect to the same normalized time scale. Even though during delithiation at 6C and 8C produces almost same amount of broken springs, the cumulative energy response suggests that higher damage evolution occurred at 6C. For 1C and 2C around 1% and 2.5% springs broke. But the cumulative energy release suggests that almost zero damage evolution occurred at 1C and 2C. Acoustic emission spectra may give rise to this type of minor discrepancies in the final result. The particles simulated in this case were assumed to have a radius of 10μm.*

cumulative measure of released strain energy (see Fig. 4.7(b)), the curve for 6C ("B") lies significantly above the line for 8C ("A"). This may mislead the experimentalist to have a conclusion that under 6C more damage is observed than 8C, which is not correct. The first potential reason why this type of discrepancy may be occurring is the fact that under 6C the particle is delithiated for 675 seconds, which is longer than that for 8C, where the particle gets delithiated for 450 seconds. To calculate the cumulative energy curve, integration is done over time. For 6C the released strain energy gets integrated over a longer time interval, resulting in potentially larger cumulative energy release. This discrepancy may be avoided by using multiple actuators placed at different locations of the particle. The cumulative energy released may be estimated by taking average of the energy measured by all the sensors. The second discrepancy is the amount of damage observed under low C-rate conditions 1C and 2C (denoted by "C" and "D").

Even though Fig. 4.7(a) shows that there is around 1%-2% broken springs under 1C ("D") and 2C ("C") rates of discharge, Fig. 4.7(b) signifies that the cumulative energy release is negligible for both the curves "C" and "D". To an experimentalist conducting the acoustic emission experiment, this may give a wrong impression that under delithiation at 1C and 2C, negligible amount of mechanical degradation occurs. However, in reality, delithiation at the rate of 2C (curve "C"), results in approximately 2.5% mechanical degradation. This is definitely not negligible.

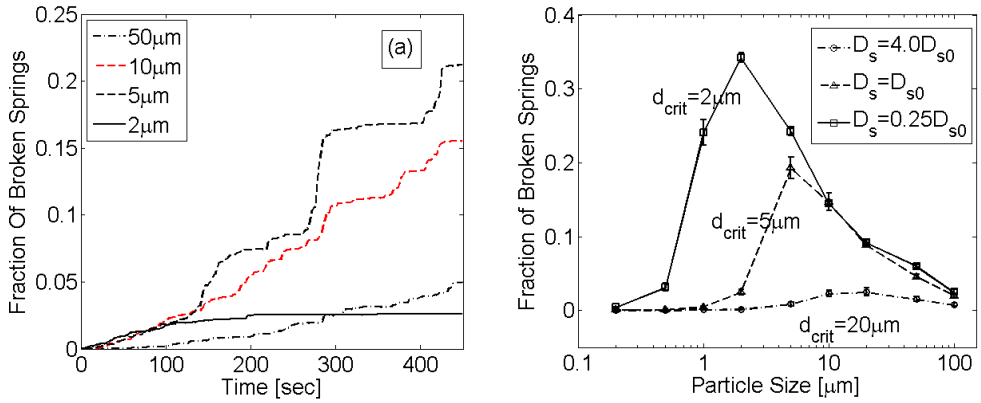

Fig: 4.8. *Effect of particle size on damage has been demonstrated here. (a) For relatively smaller particles with size 5μm and below, decreasing the particle size results in reduction of the fraction of broken springs. On the contrary, if the particle size is increased beyond the critical size of 5μm, reduced fraction of broken elements have been observed. This happens because of the fact that for large particles, there was not sufficient time for full concentration gradient to develop in the entire particle. Total amount of damage for the larger particles (10μm) can be higher, but maximum fraction of broken springs was observed for 5μm sized particles. Thus, it can be concluded that there exist a critical particle size at which maximum fraction of mechanical damage evolves. (b) Variation of the critical particle size* (d_{crit}) *with diffusivity has been demonstrated in this figure. It can be observed that the critical particle size also correlates with the value of diffusivity. The error bars signify one sigma standard deviation of ten different samples taken into consideration while plotting each point.*

It is well known that particle size impacts the evolution of mechanical degradation in active particles. It has been reported in earlier literatures that reducing the

particle size results in reduction of microcrack formation (see [18, 20]). Particle size is a measure of the diffusion length of an object. For higher diffusion length, larger concentration gradient is observed. This gives rise to enhanced mechanical stress and subsequently more damage evolution. Smaller particle size resulted in small diffusion length, low concentration gradient, less tensile stress generation and reduced crack formation. But for extremely large particles, the concentration gradient cannot evolve completely inside the entire particle within the amount of time allowed for delithiation to occur. This gives rise to reduced fraction of broken springs for extremely large particles. Figure 4.8(a) demonstrates this phenomenon and demarcates the existence of a critical particle size at which the observed fraction of broken elements is a maximum. As the particle size decreases from 50μm to 10μm and finally to 5μm, the fraction of broken bond increases. This increase in fractional damage with decreasing particle size occurs because; in large particles only a small portion close to the periphery experiences the concentration gradient. As the particle size gets smaller the entire particle can experience the concentration gradient in the provided amount of time, which leads to enhanced stress generation and subsequently, rupture of a larger fraction of lattice springs. As the particle size decreases to 2μm the amount of mechanical degradation decreases because of the reduction in diffusion length and generation of smaller concentration gradients. Thus from Fig 4.8(a) it can be concluded that the critical particle size $\left(d_{crit}\right)$ at which the maximum amount of broken springs evolve is around 5μm. Figure 4.8(b) shows the variation in fractional damage at the end of the delithiation process for different particle size and under different values of diffusivity of the material. As the diffusivity increases,

the critical particle size also increases. For an enhanced value of the material diffusivity $\left(D_s = 4.0D_{s0}\right)$, the critical particle size increases to $\left(d_{crit} = 20\mu m\right)$. Higher diffusivity also results in reduced concentration gradient, and subsequently less mechanical degradation. Smaller values of the diffusion coefficient $\left(D_s = 0.25D_{s0}\right)$ result in smaller values of critical particle size $\left(d_{crit} = 2\mu m\right)$. Smaller diffusivity results in larger concentration gradient and subsequently enhanced mechanical degradation. Extremely small standard deviation in the data set signifies the certainty and stability of the observed result (10 different samples were considered in this study).

Elastic stiffness of materials has significant influence on the amount of deformation it experiences as well as the strain energy stored inside the material under a certain amount of deformation (see [15]). In the present study, rupture of a spring in lattice spring systems is characterized by the amount of elastic strain energy stored in that spring element. If the energy stored in that element exceeds the fracture threshold energy, the spring is assumed to be broken. As a result, parameters, which impact the amount of strain energy stored in a lattice spring element, have the ability to affect the microcrack formation to a large extent. Since elastic modulus of a material directly affects the strain energy, variation in the value of E can affect the fracture formation, energy release and subsequently the acoustic emission spectra. Figure 4.9 demonstrates the effect of different values of the elastic stiffness on the cumulative energy release rate (Fig. 4.9(a)), acoustic emission spectra (Fig. 4.9(b)), fraction of broken springs (Fig. 4.9(c)) and a relation between amounts of damage evolution with stiffness ratio (Fig. 4.9(d)). In the computational scheme adopted in this research, the material is subjected

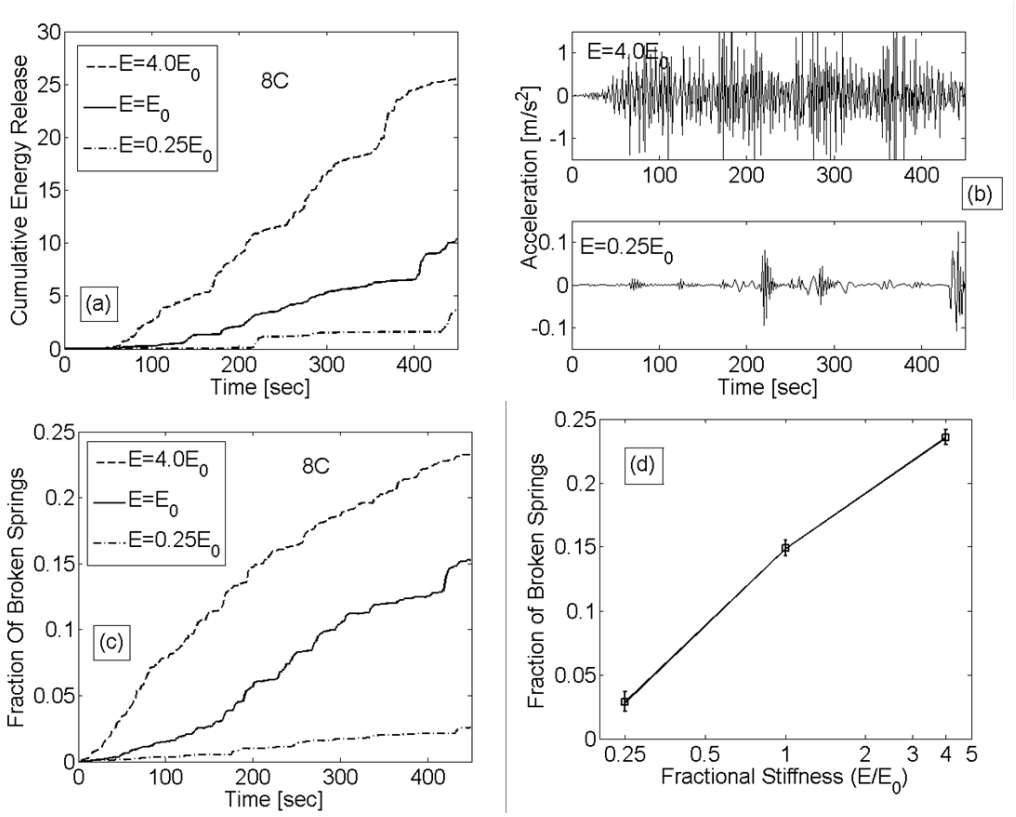

Fig: 4.9. *Effect of elastic modulus on damage evolution has been demonstrated here. Enhanced micro-cracking is observed for the higher values of the elastic modulus. (a) Cumulative energy release due to fracture evolution at 8C. (b) Acoustic emission spectra observed for very high and very low values of elastic stiffness. (c) Evolution of the fraction mechanical damage with time for three different values of the elastic modulus. (d) Total amount of microcrack observed at different elastic stiffness for multiple samples. Small standard deviation suggests that damage evolution for different stiffness is well defined. A particle of radius 10μm was assumed for this particular set of simulations. The error bars correspond to one sigma standard deviation obtained over ten samples. The plotted data points signify the mean value of the data set.*

to a constant amount of concentration gradient induced deformation. If the stiffness of the material is large, it leads to generation of higher elastic strain energy. Since the fracture threshold remains the same, enhanced strain energy would result in larger number of broken elements in the network. Increased number of broken springs release more strain energy, which gets reflected as enhanced acoustic emission activity in the spectra. Similarly, as shown in Fig. 4.9(a), the cumulative energy released is much

higher for the case of high stiffness and much lower for the relatively softer material with lower stiffness. The corresponding acoustic emission spectra for both high and low stiffness case are shown in Fig. 4.9(b). Because of more broken elements and larger energy release, the spectrum at $E = 4.0E_0$ has multiple peaks with high amplitude. Whereas, due to less number of broken springs, the emission spectra observed under low stiffness $\left(E = 0.25E_0\right)$ does not show many peaks and the amplitude of the peaks are also smaller. Figure 4.9(c) demonstrates the evolution of fraction of broken springs with time. Similar to the result observed in cumulative energy release, under high stiffness $\left(E = 4.0E_0\right)$ more than 20% broken springs are observed. For regular stiffness $\left(E = E_0\right)$ around 15% of the bonds break. For lower values of stiffness $\left(E = 0.25E_0\right)$ only 2.5% of the total bonds experiences rupture phenomena. For all the elastic stiffness related results reported above, the particle was delithiated at a rate of 8C. Finally in Fig 4.9(d), an attempt has been made to characterize the variation of damage evolution with stiffness ratio $\left(E/E_0\right)$. An almost straight line is observed when the "fraction of broken elements $\left(fbb\right)$" was plotted with respect to the stiffness ratio $\left(E/E_0\right)$ on a logarithmic scale. Thus a relation similar to "$fbb \propto \log\left(E/E_0\right)$" can be assumed to exist, at least within the range of stiffness ratio considered in the current simulation. According to the knowledge of the authors, no earlier work exists where an effort has been made to correlate the evolution of damage in materials with different stiffness under the same loading condition. Extremely small standard deviation obtained from the 10 samples considered in this study, signifies the stability of the response. The proportionality constant may be

a function of C-rate or diffusivity. In reality, most of the intercalation materials show concentration dependent elastic stiffness. For graphite, with increasing lithium ion concentration, the elastic stiffness increases (see [27]). For silicon, increasing lithium ion concentration reduces the elastic modulus (see [29]). Thus with continuing delithiation, increase in damage evolution would follow different trends for graphite and silicon type materials.

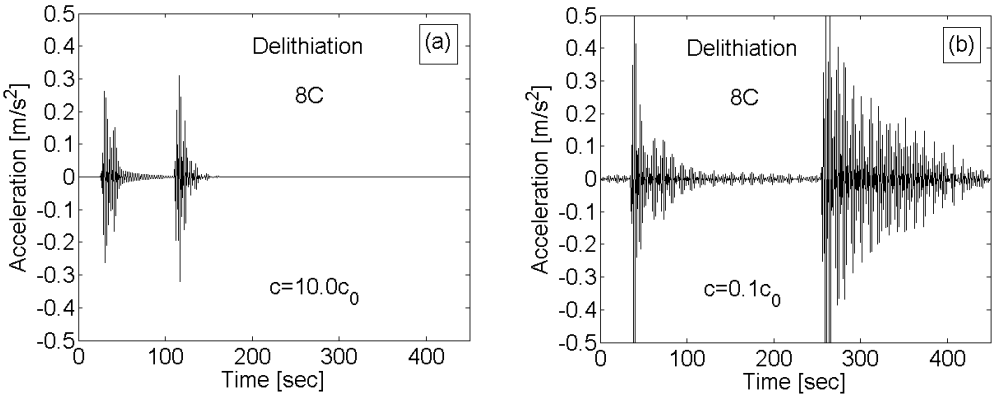

Fig: 4.10. *Effect of damping parameter on the amount of energy released has been demonstrated here. (a) High values of damping leads to reduced energy release and quick dissipation of the stress waves. (b) Low damping parameter enhances the energy release and the stress waves take much longer to dissipate completely. The particle simulated in this case has a radius of 10μm.*

The damping parameter is responsible for controlling how the elastic strain energy released due to formation of microcracks would dissipate (see [66, 179]). A small value of damping parameter would signify that the released energy would propagate through the material for a long distance without getting dissipated. Larger value of the damping parameter signifies that the elastic strain energy released due to rupture of a spring cannot propagate for a long distance and gets dissipated relatively quickly. The damping parameter of a material can be estimated through the vibrational response under impact loading. A good measure of the damping coefficient of a material is the

relaxation time associate with that specimen. Amount of time required to dissipate the energy imparted by an impact load is associated with the relaxation time of that particular material. Smaller relaxation time corresponds to higher values of damping, whereas, large values of relaxation time signifies small damping coefficient. In Fig 4.10(a) and 4.10(b), to demonstrate the effect of different damping parameters, four springs close to the boundary of the lattice spring network were preselected and assigned very low fracture threshold energy. All the other springs were assigned extremely high threshold values such that they never rupture. Two different damping parameters, one very high $\left(c = 10.0c_0\right)$ and another very low $\left(c = 0.1c_0\right)$, were selected for the two different simulations of delithiation under a C-rate of 8C. In the current simulation, the value of c_0 has been adopted as 1.0N-s/m. Figure 4.10(a) shows that for a higher value of the damping parameter $\left(c = 10.0c_0\right)$, small amplitude of signal is detected in the emission spectra. Also the released energy gets dissipated relatively quickly. On the other hand, as shown in Fig 4.10(b), for smaller values of the damping coefficient $\left(c = 0.1c_0\right)$, signals of much larger amplitude were observed in the acoustic emission spectra. Due to low damping coefficient, the released energy took longer time to dissipate as well. Since the entire delithiation process was conducted at 8C, the simulation for both the cases was run till 450 seconds. Important point to be noted is the fact that for higher damping coefficient, all the bonds broke within 120 seconds. But for the smaller damping coefficient, all the bonds broke after 250 seconds. This signifies that there may be a potential of resisting crack formation in materials with lower values

of the damping coefficient. According to the authors' knowledge, there does not exist any research article where the damping coefficient of lithium ion battery electrode active particle has been investigated. Hence, optimization of the viscosity of active particles will be considered as a future extension of the current research work.

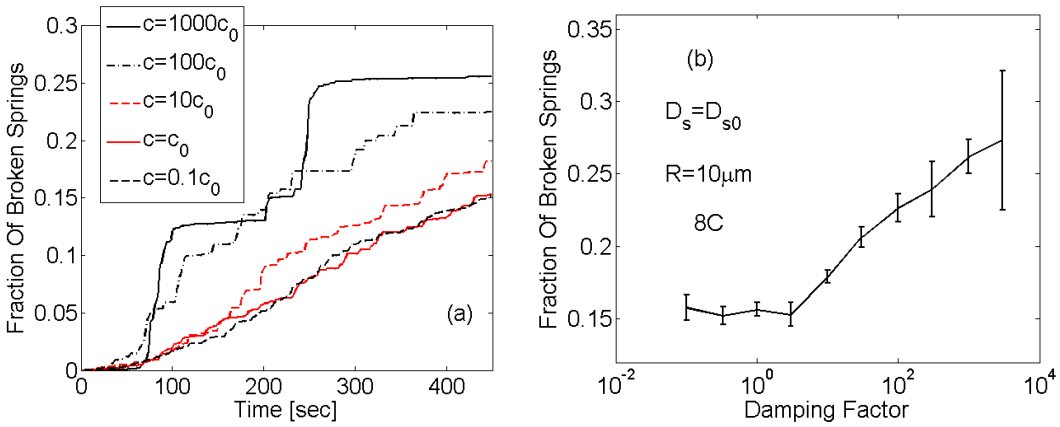

Fig: 4.11. *Effect of damping parameter on the amount of microcrack formation has been depicted here. (a) For large values of the damping parameter, damage evolution happens through big avalanche phenomena. For smaller damping parameters, microcracks develop at a uniform rate. (b) Reducing the damping parameter from a large value decreases the amount of damage. But for small values of damping, mechanical damage saturates at a particular value. Ten different samples were generated for each data point and the mean value has been plotted. The error bars correspond to one sigma standard deviation of all the samples.*

To investigate more on the matter whether smaller damping coefficient results in less mechanical degradation or not, some simulations of delithiation at 8C were conducted on a single particle with radius $R = 10\mu m$. Different damping coefficients were assumed for each of the samples. Figure 4.11(a) shows the evolution of fraction of broken springs under different damping parameters. Very large value of the damping coefficient results in excessively huge amounts of mechanical damage. As the damping parameter decreases, less amount of microcracks are developed. Another interesting thing that can be observed in Fig. 4.11(a) is the fact that under large values of damping

coefficient, damage evolves in a step wise fashion. These steps in broken bond evolution were observed because of the presence of avalanche phenomenon. As the damping parameter got reduced, increase in the fraction of broken elements became more continuous. To analyze how much the fraction of broken springs varies as the damping coefficient is reduced, Fig. 4.11(b) plots the amount of mechanical damage with respect to the ratio of the damping parameters $\left(c/c_0\right)$. As the value of the damping parameter ratio reduces from 3000.0 to 3.0, the amount of mechanical damage also decreases linearly. For further reduction of the ratio of damping parameter $\left(c/c_0\right)$ from 3.0 to 0.1, not much change in the fraction of broken springs was observed. While generating the plot in Fig. 4.11(b), average of 10 samples for each of the cases were taken into consideration. Relatively small standard deviation signifies the certainty of this analysis. For applications in realistic battery active particles, it is desirable to use materials with smaller values of the damping coefficient to reduce the evolution of mechanical degradation.

Only single delithiation of the active particles have been analyzed till now. But in realistic battery applications, all the active particles are delithiated – lithiated for multiple cycles (see [63, 64]). Since during delithiation fracture evolves in the peripheral region and during lithiation fracture evolves in the central portion of the active particles, subsequent cycles of delithiation – lithiation may have the potential to increase the mechanical degradation uncontrollably. Such cyclic loading – unloading behavior may result in fatigue crack propagation within the materials, which can eventually cause the active particles to rupture completely. In previous computational analysis conducted by

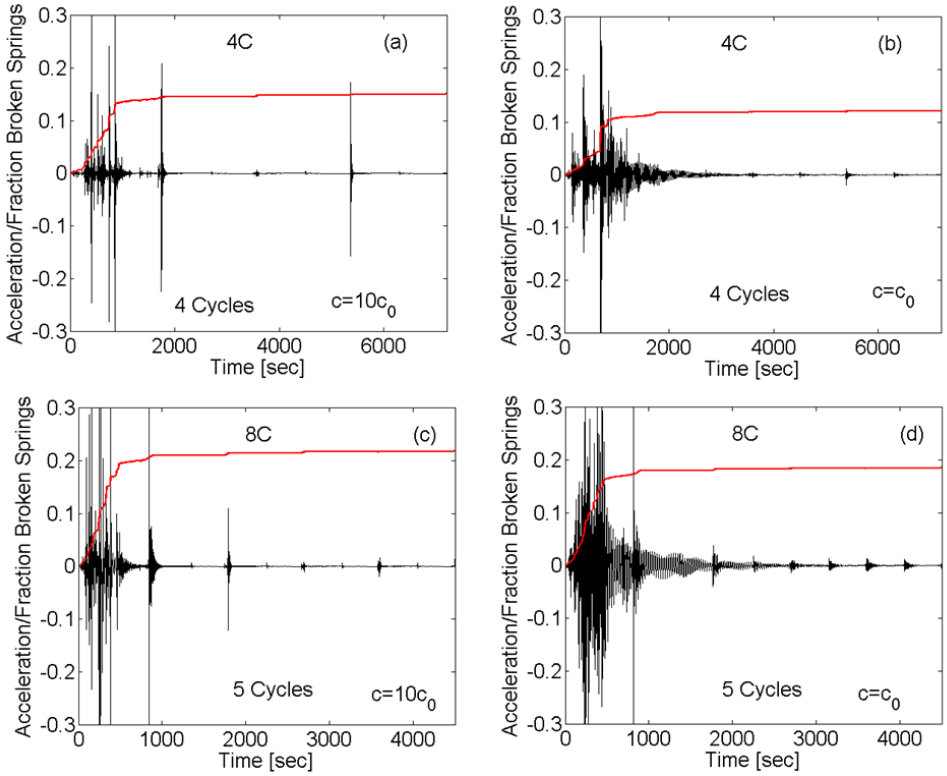

Fig: 4.12. *Depiction of damage evolution and energy released for different damping factors under different C-rate operating conditions. (a) High damping under low C-rate of 4C. (b) Low damping with cycles conducted at 4C. (c) High damping with operation at high c-rate of 8C. (d) Low damping along with 8C operating condition. For larger values of damping parameter, even though energy decays faster, magnitude of the peaks are larger than the low damping case. Particles of radius 10μm have been assumed in these set of simulations.*

the authors indicates that for the brittle active particles under consideration, fatigue crack propagation does not occur [85, 178]. However, the absence of crack prolongation via fatigue mechanism can be attributed as a consequence of the brittle lattice spring methodology adopted to study the fracture behavior. During delithiation – lithiation process at a particular C-rate, the maximum amount of load that acts on the system does not change from cycle to cycle. To accommodate that fixed amount of load, a certain amount of strain energy release must occur. The excessive strain energy that the system

cannot sustain, gets released in the first 1 to 2 delithiation – lithiation cycles through the formation of microscopic cracks. For subsequent cycles, no extra strain energy release is required to sustain the maximum amount of load. As a result, very little or no damage evolution occurs within the active particles after the second or third delithiation – lithiation cycles. This behavior of saturation in damage evolution has been successfully captured by the dynamic lattice spring model under operation at both the rates of 4C and 8C. The acoustic emission spectra for two different damping parameters have been reported in Fig 5.12 under both 4C and 8C operation. Figure 4.12(a) shows the acoustic emission spectra (black line) and the cumulative fraction of broken springs (red line) for four cycles under 4C and a large value of the damping parameter $\left(c = 10.0c_0\right)$. Similarly, Fig 4.12(b) shows the same emission spectra and cumulative fraction of broken elements for a smaller value of the damping parameter. Figures 4.12(c) and 4.12(d) represents the damage evolution subjected to five delithiation – lithiation cycles under 8C for large and small values of the damping coefficient, respectively. At higher C-rates definitely larger amount of mechanical degradation is observed (10%-15% at 4C as compared to around 20% at 8C). Higher damping coefficient also resulted in larger amount of microcrack formation for cycling at both 4C and 8C. The emission spectra at higher damping coefficients showed signals of larger amplitude, but they dissipated much earlier than their counterpart observed with lower values of the damping coefficient. Saturation in damage evolution have been observed in all the four conditions after two delithiation – lithiation cycles.

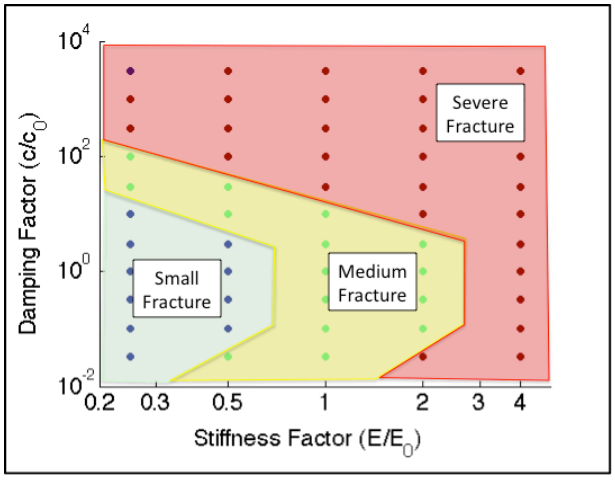

Fig: 4.13. *Damping vs. stiffness phase map showing the damage (fracture) regimes. Lower values of stiffness and damping factors may be favorable from the mechanical degradation perspective.*

The values of elastic stiffness and damping parameter for different materials span over a large range. Materials used as active particles in the battery electrodes can be susceptible to mechanical degradation. Large amount of mechanical damage can eventually lead to site loss as well as total energy of the cell may get reduced. In this article, it has been reported in Fig. 4.9 and Fig. 4.11 that increasing the magnitude of elastic stiffness as well as damping coefficient may result in enhanced microcrack formation. The aim here is to elucidate on that direction and devise a range of elastic modulus and damping coefficient for which less mechanical degradation would occur. Figure 4.13 shows a comparative description of how much mechanical damage evolves for a certain range of damping coefficients and another range of elastic stiffness. All the simulations were conducted for a particle size of $10\,\mu m$ and delithiation at a rate of 8C. Logarithmic scale has been used to represent the large variation in the elastic stiffness and damping factor being considered in this study. It has been observed that smaller values of elastic stiffness and damping coefficient results in less mechanical degradation.

Since the simulation was conducted under a very high rate (8C), and realistic battery particles seldom experience such high rates of delithiation, the cutoff between “small fracture” and “medium” fracture has been taken as 10% fraction of broken elements, which is a bit towards the higher side. The limit between “medium fracture” and “severe fracture” was taken to be 17.5% fraction of broken springs. For the usual high 4C or 5C operations observed in realistic battery active particles, these upper limits of small and medium amount of mechanical damage would become “6%-7%” and “10%-12%” fraction of broken springs, respectively. To reduce the amount of mechanical degradation, materials with high stiffness and high damping coefficient must be avoided as electrode active particles. The elastic modulus of some active particles, such as graphite, increases with increasing amount of lithium ion concentration. Enhanced mechanical damage is possible in the graphite anode under high values of stiffness. To reduce the microcrack formation, it is advised to keep the bulk SOC of graphite anodes at a lower level. But for silicon, the elastic stiffness decreases with increasing lithium ion concentration. Consequently, higher values of SOC would result in reduced mechanical degradation in Si anode particles. The concept of enhanced energy dissipation under high damping and less dissipation for the case of low damping coefficient, can be used in conjunction with the phase map to predict the nature of the acoustic emission spectra.

4.5 Convergence analysis

To establish the applicability of the developed computational scheme for scientific computation, it is very important to clearly demonstrate the mesh size independence and the time step convergence of the adopted methodology. The test that

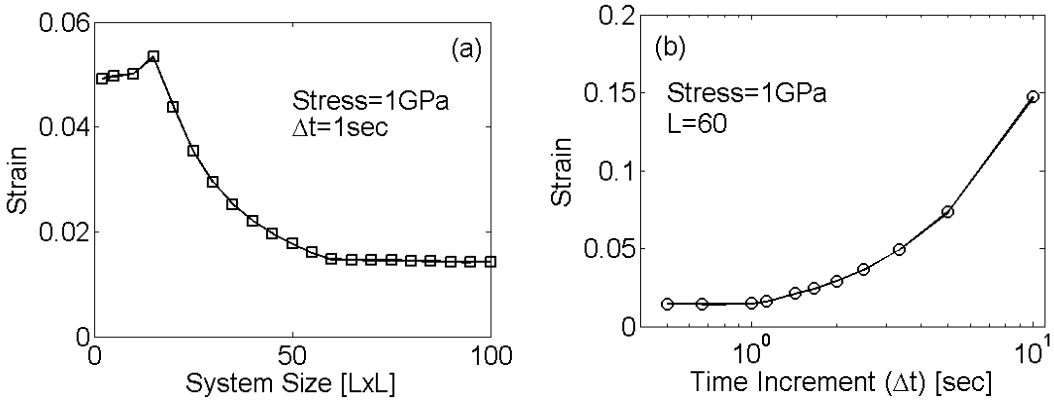

Fig: 4.14. *(a) Demonstration of mesh size independence for the adopted computational methodology. Strain observed in systems of different size has been reported under externally applied constant stress of 1GPa. For systems with size greater than 60x60, the observed amount of strain does not change. (b) Convergence analysis for different time steps. The value of strain observed in a 60x60 system under different amount of time increment have been plotted when subjected to a stress of 1GPa. The amount of strain for time steps smaller than 1sec does not change significantly.*

was conducted to examine the convergence behavior will be explained next: A square spring lattice network of size LxL was considered as the system being studied. The bottom of the network was fixed. Uniform stress of 1GPa was applied at the top. The stress was ramped up to the maximum value over 10 seconds. The time increment taken into consideration is denoted by Δt. The strain response after the first 10 seconds has been reported. For the mesh-size independence study, a time increment $\Delta t = 1s$ has been used. The system size L has been increased from 2 to 100. Figure 4.14(a) demonstrates that the strain obtained from the systems of size LxL=[65x65] or greater does not change significantly. In the present study, systems of size L=60 has been adopted, which lies sufficiently close to the range of converged domain sizes. A lattice spring network of size L=60 is also computationally benign and takes reasonably small amount of time to complete the entire simulation procedure. To demonstrate the convergence in time step,

Fig. 4.14(b) plots the amount of strain observed for a lattice spring network of size L=60 but for different values of Δt. As the time increment decreases, the strain response converges to a particular value. For time steps below $\Delta t = 1s$, the calculated strain does not change significantly. Hence, a time step of $\Delta t = 1s$ has been adopted in the current simulation. Newmark's average acceleration method has been adopted for the time integration, which corresponds to $\gamma = 1/2$ and $\beta = 1/4$. The average acceleration technique is also unconditionally stable. Hence for any time increment, stability of the computational scheme is ensured.

4.6 Conclusion

A computational methodology has been developed that can predict the concentration gradient induced fracture in a lithium ion battery electrode active particle and capture the corresponding acoustic emission response. The dynamic momentum balance equation has been solved on a lattice spring network, which estimates the formation and nucleation of microcracks. Rupture of a spring results in release of the elastic strain energy stored in that particular spring element. This energy travels through the network in the form of a stress wave and gets detected by the actuator placed on the surface of the particle. Recognition of this stress wave corresponds to the acoustic emission spectra observed in realistic battery active materials.

When constant lithium ion flux is applied on the boundary of the active particle kept at a fully rest condition, some stress waves develop within the material because of the concentration gradient induced impact. Amplitude of these reflected stress waves are two orders of magnitude smaller than those which develop due to the evolution of

microcracks. The magnitude of energy released during lithiation is smaller than the magnitude of energy released during delithiation. The cumulative energy released during acoustic emission provides a very good approximation of the total amount of mechanical degradation. Energy released is usually proportional to the cumulative fraction of broken elements, which is again linearly related to the applied C-rate. A critical particle size has been observed at which maximum fraction of mechanical degradation occurs. This critical particle size scales linearly with the diffusivity of the active particle. When the electrode active particle is subjected to multiple lithiation – delithiation cycles, saturation of mechanical damage as well as acoustic activity has been observed after the first couple of cycles.

The relevant mechanical parameters (e.g., Young's modulus, damping coefficient) can also affect the acoustic emission response of an active particle. With increasing elastic stiffness, enhanced mechanical degradation is observed. Softer materials result in reduced damage and very little acoustic activity is detected. Similarly, larger values of the damping coefficient can give rise to increased mechanical degradation. As the damping coefficient is reduced, below a particular value no further reduction in mechanical damage is observed. Higher damping coefficients also result in early dissipation of the released elastic energy. Finally, a phase map of damping factor vs. ratio of elastic stiffness has been constructed which can provide design guidelines regarding the choice of the most favorable mechanical property combination that could lead to minimum amount of mechanical degradation in the active particles.

CHAPTER V

REDUCED ORDER MODELING OF MECHANICAL DEGREDATION INDUCED PERFORMANCE DECAY IN LITHIUM ION BATTERY POROUS ELECTRODES*

5.1 Computational methodology

A realistic LIB involves two electrodes separated by a porous separator [4]. The actual microstructure of the electrodes involves four different phases; active materials, binders, conductive additives, and electrolyte [119]. The separator itself is a porous membrane through which electrolyte can flow freely. Detailed modeling of all these different phases accurately is a very complicated task and most of the time impossible to achieve due to the lack of computational resources. To capture all the relevant physics without modeling all the different phases, a homogenization technique has been developed to characterize the behavior of the electrodes as a bulk material. The different physical phenomena that go on inside the electrode (such as diffusion and migration of ions, maintaining electro-neutrality at each point throughout the cell) have been taken into consideration. This homogenized model is known as the "porous electrode theory." It was first developed by Newman and Tobias (see [103]) and later updated by Newman and Tiedemann (see [104]) for battery-specific applications. Figure 5.1 shows schematic diagram of a cell that is usually adopted in porous electrode theory. This porous electrode theory was implemented to different battery systems. A brief overview is

*Reprinted with permission from "Reduced order modeling of mechanical degradation induced performance decay in lithium-ion battery porous electrodes" by P. Barai *et al.*
(2015) J. Elec. Soc. 162 A1751 – A1771 by Copyright 2015 ECS – The Electrochemical Society.

provided below, which is specifically applicable to LIBs (see [4]). Texts below shows how the nonlinear Butler-Volmer equations have been linearized using the Taylor series expansion. The proposed reduced order model is developed to specifically capture the effect of mechanical damage evolution, which is integrated into the "porous electrode theory" based cell sandwich model for Li-ion cells by Newman and co-workers [103-107]. This reduced order model aims to characterize the amount of mechanical degradation as a function of Amp-hour throughput (Ahtp), C-rate and particle size which is discussed in the following sections.

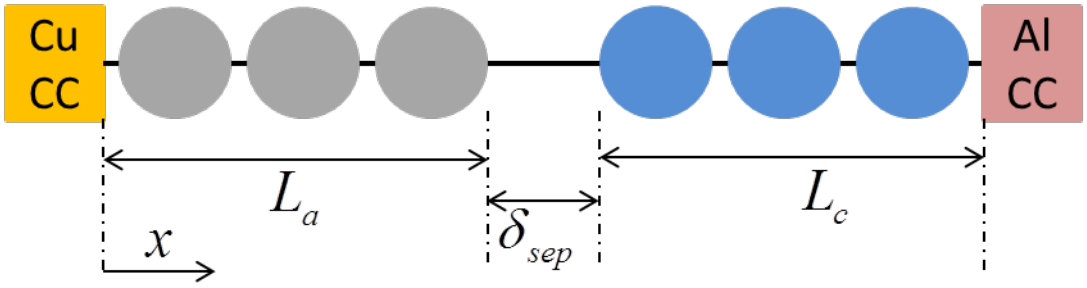

Fig: 5.1. *Schematic representation of the porous electrode theory for modeling of 1D+1D Li transport in a Li-ion cell.*

5.1.1 Relation between microcrack density and diffusivity

A reduced order model has been developed to estimate the amount of microcrack formation under certain C-rate operating conditions and for particular particle sizes $\left(R_s\right)$. A simplified expression for microcrack density (or fraction of broken bonds, f_{bb}) as a function of amp-hour-throughput (Ahtp) can be written as,

$$f_{bb} = f\left(C_{rate}, R_s, Ahtp\right) = A_{\max}\left(1-\exp\left(-m_{rate}\cdot Ahtp\right)\right) \tag{5.1}$$

along with $A_{\max} = f_1\left(C_{rate}, R_s\right)$ and $m_{rate} = f_2\left(C_{rate}, R_s\right)$ (5.2)

Here $A_{\max}$ signifies the maximum amount of damage that can occur in an active particle and m_{rate} stands for the rate at which damage evolution occurs. Both the $A_{\max}$ and m_{rate} parameters are functions of $C-rate$ and particle size $\left(R_s\right)$. More detailed expression of the maximum damage and rate of damage will be provided in sub-section 5.2.1 of the Results and Discussion section. It has been argued in Barai and Mukherjee [85] that formation of a microcrack increases the tortuosity of the diffusion pathway resulting in reduced diffusivity of the active particle. An expression for effective diffusivity has been developed to correlate the microcrack density with the diffusivity of the active particle, which is given as,

$$D_s^{eff} = D_s\left(1-f_{bb}\right)^{\gamma} \tag{5.3}$$

where D_s denotes the solid phase diffusivity in the anode active materials without any mechanical degradation. The solid phase diffusivity $\left(D_s\right)$ (also referred to Eq. (5.4) and (5.5)) is replaced by the expression of effective diffusivity as obtained from Eq. (5.3). It has been demonstrated that reducing the local diffusivity of the active particle could capture the effect of mechanical degradation on the diffusion of lithium species [85]. The simulation of diffusion inside active particles and mechanical degradation has been conducted in a circular 2D domain. For different particle sizes and different C-rates, certain values of surface concentration were obtained from the 2D simulations taking into account the effect of microcracks. For the same particle sizes and C-rates, 1D simulations were conducted with constant values of diffusivity that can generate the same surface concentration as that obtained from the 2D simulations. The diffusivity

value for the 1D simulations has been obtained from Eq. (5.3). Estimation of the exponent γ has been conducted by comparing the surface concentrations from 1D and 2D analyses. More elaborate explanation behind the exact value of the exponent (γ)will be provided towards the end of sub-section 5.2.1 of the Results and Discussion section.

In the computational analysis, fraction of broken bonds or microcrack density (f_{bb}) is defined as the ratio of broken elements over total number of elements. Here elements refer to a computational entity and does not have any experimentally observable counterpart. Thus, the term f_{bb} turns out to be a dimensionless number. Based on dimensional analysis, the term $A_{\max}$ turns out to be dimensionless. Whereas, the term m_{rate} must maintain the dimension of $(Ahtp)^{-1}$ to achieve dimensional equality within the exponent. However, the two defining terms $(A_{\max}, m_{rate})$ used in the reduced order model does not have any direct experimentally measurable counterparts. Acoustic emission is a methodology to measure the extent of mechanical degradation in solid materials. Cumulative strain energy release measured form acoustic emission experiments is equivalent to the damage profile observed in the present context [63, 182]. Hence, an experimental counterpart of the maximum amount of mechanical degradation parameter $(A_{\max})$ is the maximum cumulative strain energy release observed from acoustic emission experiments. Saturation in the strain energy release has been reported in several experimental articles [63, 64, 182], which is equivalent to the saturation in evolution of microcrack density observed by the authors [178].

Most of the reduced order models are derived from systematic reduction of governing differential equations. But if the phenomenon under consideration cannot be characterized by a governing differential equation, then based on the trend, phenomenological models can be developed to capture the variation [10]. In the present context, evolution of microcrack density cannot be captured using any differential equation. It is possible to develop reduced order models for stress generation, but fracture formation is rather a stochastic process because material heterogeneity is also involved there [30]. Due to the lack of governing equations, it is important to have phenomenological models for predicting damage evolution. Usually empirical models are mathematical expressions that are developed entirely based on data. No physical significance exists behind particular mathematical expressions. However, in the present context, the saturation phenomenon in mechanical degradation can be explained from the strain energy release perspective [85, 178]. Under externally applied load, evolution of mechanical degradation happens to release the excessive strain energy that the system cannot sustain. During lithiation – delithiation process, the same amount of diffusion induced load acts on the system. The strain energy release required for sustaining the concentration gradient induced load is achieved within the first few discharge – charge cycles. As a result, during subsequent lithiation – delithiation process, extra strain energy release is not required. This leads to saturation in the amount of mechanical degradation. Here, an inherent assumption is that the lithiation – delithiation process occurs at a constant rate. The maximum amount of mechanical degradation depends on the particle size and C-rate of operation, through the magnitude of concentration

gradient term. Thus there exists some form of physical significance behind the equations adopted in this study. To calculate the amount of microcrack formation, the governing differential equations are not being solved in details. As a result, the physics based mathematical representation of damage evolution can be described as a reduced order model of a complicated phenomenon.

5.1.2 Porous electrode theory

Figure 5.1 shows schematic diagram of a cell that is usually adopted in porous electrode theory. According to this homogenized model, two different phases are considered in each electrode, the active particles and the electrolyte. The separator acts as a medium through which only the electrolyte diffuses. The electrons cannot pass through the polymeric separator. The active particles are considered as spherical particles, and lithium diffusion within them are modeled using Fick's law of diffusion with a flux prescribed boundary condition on the surface.

$$\frac{\partial c_s}{\partial t} = \frac{D_s}{r^2}\left(\frac{\partial}{\partial r}\left(r^2 \frac{\partial c_s}{\partial r}\right)\right) \tag{5.4}$$

$$\text{along with,} \quad \left.\frac{\partial c_s}{\partial r}\right|_{r=0} = 0 \quad \text{and} \quad \left.\frac{\partial c_s}{\partial r}\right|_{r=R_s} = \frac{-j}{D_s F} \tag{5.5}$$

Here, c_s is the concentration of lithium atoms within the solid phase, D_s signifies the diffusivity of lithium within the solid, and j is the reaction current density that flows at the solid electrolyte interface. The expression for the reaction current density is obtained from the Butler- Volmer equation, which is also written as,

$$j = j_0 \cdot \left(\exp\left(\frac{\alpha_a F}{RT} \cdot \eta \right) - \exp\left(-\frac{\alpha_c F}{RT} \cdot \eta \right) \right) \tag{5.6}$$

Where j is the reaction current density, j_0 signifies the exchange current density, α_a and α_c are the anodic and cathodic transfer coefficients of electrode reaction, respectively, F signifies the Faraday constant, R represents the universal gas constant, and T corresponds to the temperature at which the reaction occurs. For the simulations conducted in the present article, the temperature has been kept fixed at room temperature or 298K. The overpotential in the anode and cathode are denoted by η and defined by the expression,

$$\eta = \phi_s - \phi_e - U \tag{5.7}$$

Where ϕ_s signifies the solid phase potential, ϕ_e denotes the electrolyte phase potential, and finally, U signifies the open circuit potential within the electrodes.

Similar to the solid phase, diffusion of lithium ions also occurs within the electrolyte phase. Usually the diffusivity of lithium ions within the electrolyte is much faster than that observed within the solid phase. Accumulation of lithium ions within the electrolyte due to the reaction current acts as a source term.

$$\frac{\partial\left(\varepsilon c_e\right)}{\partial t} = D_e^{eff} \frac{\partial^2 c_e}{\partial x^2} + a_s \left(\frac{1 - t_+}{F} \right) \cdot j \tag{5.8}$$

$$\text{with,} \quad \left. \frac{\partial c_e}{\partial x} \right|_{x=0,L} = 0 \tag{5.9}$$

Here, $L = L_a + L_c + \delta_{sep}$ and ε signifies the porosity. Also, c_e represents the concentration of lithium ions within the electrolyte, $D_e^{eff}\left(= D_e \varepsilon^{1.5}\right)$ represents effective

diffusivity of lithium ions within the electrolyte in terms of the actual diffusivity and the porosity of the medium, a_s is the active surface area per unit volume, and t_+ represents the transference number corresponding to lithium ions. Transference number signifies the fraction of current that is carried by the lithium ions. That fraction of lithium ions within the electrolyte does not accumulate and simply migrate from one electrode to the other. As a result, that fraction is deducted from the total amount of lithium ions that gets released during the flow of reaction current.

Electro-neutrality is a necessary condition to be satisfied at every point within the electrochemical cell. Thus, quasistatic charge conservation must occur within both the solid phase as well as the electrolyte phase of the cell. Electric potential within the solid phase follows Ohm's law,

$$\sigma^{eff} \frac{\partial^2 \phi_s}{\partial x^2} = a_s j \tag{5.10}$$

$$\text{along with,} \quad \sigma^{eff} \left.\frac{\partial \phi_s}{\partial x}\right|_{x=L,0} = \pm \frac{I}{A} \quad \text{and} \quad \left.\frac{\partial \phi_s}{\partial x}\right|_{\substack{electrode \\ separator \\ \text{int}erface}} = 0 \tag{5.11}$$

Here, $\sigma^{eff} \left(= \sigma(1-\varepsilon)^{1.5}\right)$ is the effective conductivity written as a function of real conductivity and porosity, ϕ_s is the solid phase potential, I signifies the applied current, and A represents the area at the electrode current collector interface. Similarly charge conservation within the electrolyte gives,

$$\kappa^{eff} \frac{\partial^2 \phi_e}{\partial x^2} + \kappa_d^{eff} \frac{\partial^2 c_e}{\partial x^2} = -a_s j \tag{5.12}$$

$$\text{along with,} \quad \left.\frac{\partial \phi_e}{\partial x}\right|_{x=0,L} = 0 \quad \text{and} \quad \left(\kappa^{eff} \frac{\partial^2 \phi_e}{\partial x^2} + \kappa_d^{eff} \frac{\partial^2 c_e}{\partial x^2} \right)\Bigg|_{\substack{electrolyte \\ separator \\ interface}} = 0 \tag{5.13}$$

Here, the electrolyte potential is denoted by ϕ_e. The effective electrolyte conductivity written as $\kappa^{eff} \left(= \kappa \varepsilon^{1.5}\right)$ in terms of the real electrolyte conductivity $\left(\kappa\right)$ and the porosity of the electrode $\left(\varepsilon\right)$. $\kappa_d^{eff} \left(= \kappa_d \varepsilon^{1.5}\right)$ is the diffusivity of the charged particles, which transport through the electrolyte via diffusion mechanism. While calculating conservation of charge within the electrolyte, the contribution from both the charge transport via Ohm's law and the diffusion of charged particles must be taken into consideration. As a result, there exist two terms in the left hand side (LHS) of the governing equation provided in Eq. (5.12). At the active particle-electrolyte interface, lithium ions are consumed as they react with the electron and diffuse inside the active particles as lithium atoms. Thus, the reaction current acts as a sink term at the electrode electrolyte interface. The conductivity of the electrolyte $\left(\kappa\right)$ and the conductivity of charged particles $\left(\kappa_d\right)$ are not independent parameters. It depends on the diffusivity of the electrolyte phase $\left(D_e\right)$ and the initial electrolyte concentration $\left(c_{e,init}\right)$.

$$\kappa = \frac{z^2 F^2 D_e c_{e,init}}{RT} \qquad \text{and} \qquad \kappa_d = zFD_e \tag{5.14}$$

Cell voltage is determined by calculating the difference between the solid phase potential at the positive and the negative electrodes. The drop in cell voltage due to the internal resistance $\left(R_{cell}\right)$ should also be incorporated.

$$V = \phi_{\substack{s,positive \\ electrode}}\left(x = L\right) - \phi_{\substack{s,negetive \\ electrode}}\left(x = 0\right) \tag{5.15}$$

5.1.3 Numerical procedure

The entire computational methodology adopted in the present context can be divided into several smaller components. Firstly, diffusion of lithium inside a circular cross section of a spherical particle have been solved using the time dependent Fick's law. The concentration gradient inside the active particles give rise to diffusion induced stress (DIS). Secondly, generation of DIS can lead to formation of microcracks, which can be captured by solving the momentum balance equation. Nucleation and propagation of microcracks produce spanning cracks. Details of the computational methodology used to obtain the spanning cracks have been described by the authors in earlier articles [85, 178]. A brief description of the same computational technique will be provided below. Time dependent diffusion equation is solved using the finite volume method on a 2D square grid. Constant flux boundary condition is applied on the surface of the circular active particle. Two dimensional lattice spring methods have been used to capture the microcrack formation within the active particles. The main essence of this methodology is that the entire mass of the continuum can be assumed to be discretized within uniformly distributed nodes. Each of the nodes is connected by spring elements. This spring elements display axial as well as shear resistance. Under externally applied diffusion induced load, these lattice spring elements deform to maintain equilibrium within the structure. This gives rise to evolution of strain energy within each of the springs. If the energy stored in an element exceeds its fracture threshold, it is assumed to be broken and irreversibly removed from the network of lattice springs. Subsequent

rupture of adjacent spring elements due to diffusion induced stress can give rise to formation of spanning cracks within the active particles. The variable "fraction of broken bonds" $\left(f_{bb}\right)$ is defined as the ratio of number of broken springs over the total number of springs that exist within the domain.

Formation of a microcrack hinders the diffusion pathway of active particles, and increases the tortuosity within the material [85]. This is taken into account within the 2D diffusion solve by modifying the diffusivity parameter only at the point where mechanical degradation occurred. Such modification of the local diffusivity resulted in higher values of concentration gradient within the active particles. Surface concentration decreases much faster during the delithiation process due to formation of microcracks. Consequently, reduction in effective capacity is observed due to increased mass transport resistance.

To solve for this capacity fade due to mechanical degradation in the anode active particles, the effective solid phase diffusivity has been extracted from Eq. (5.1) and (5.3). The values of diffusion coefficient in individual active particles under different amounts of microcrack density have been estimated. After that, it is implemented within the 1D computational framework for electrode level analysis (Eq. (5.4)). Because the evolution of voltage and capacity within an electrode is a transient process, the governing differential equations (Eq. (5.4), (5.21), (5.22) and (5.23)) are solved in an incremental fashion by taking small steps over the time variable. At each time steps, the increment in microcrack density for every particle in the negative electrode is estimated according to the following rate equation:

$$\frac{df_{bb}}{d\left(Ahtp\right)} = m_{rate} \cdot \left(A_{\max} - f_{bb}\right) \tag{5.16}$$

Eq. (5.16) has been obtained by taking the first derivative of Eq. (5.1) with respect to the independent variable $Ahtp$. In a small time increment, the incremental amp-hour-throughput $\left(Ahtp\right)$ is also small. Thus, the total amount of microcrack density after a small time increment can be obtained as:

$$f_{bb}\left(Ahtp\right) = f_{bb}\left(Ahtp_0\right) + \left.\frac{df_{bb}}{d\left(Ahtp\right)}\right|_{Ahtp_0} \cdot \Delta Ahtp \tag{5.17}$$

Here, $Ahtp$ is the amp-hour-throughput at the end of the current step, $Ahtp_0$ is the amp-hour-throughput at the end of the previous step, and $\Delta Ahtp$ is the incremental amp-hour-throughput. The effective diffusivity under this modified amount of microcrack density has been estimated from Eq. (5.3), and fed into Eq. (5.4) of the 1D coupled-electrode level model. Reduction in solid phase diffusivity increases the resistance due to mass transport and results in an effective capacity fade of the lithium ion cell. The capacity fade due to reduction in solid phase diffusivity becomes more prominent under high C-rate operating conditions.

The governing differential equations described above have been discretized along the thickness direction of the electrode. All three different regions of the anode, separator, and cathode have been taken into consideration. There exist four unknown variables at each node of the computational domain, which are given as follows, (i) solid phase concentration on the surface of the active particles $\left(c_{s,s} = c_s\left(r = R\right)\right)$, (ii)

electrolyte phase concentration (c_e), (iii) solid phase potential (ϕ_s), and (iv) electrolyte phase potential (ϕ_e). The electrolyte concentration, solid potential, and the electrolyte potential have been solved in a coupled fashion using the governing differential equations, Eq. (5.8), (5.10), and (5.12). Solution of the solid phase concentration was conducted separately (Eq. (5.4)). All the terms in Eq. (5.8), (5.10), and (5.12) except the reaction current density (j) are linear in nature. A Taylor series expansion has been introduced to linearize the nonlinear component of the reaction current density (j), which is a function of solid phase potential (ϕ_s), electrolyte potential (ϕ_e), and solid phase surface concentration $(c_{s,s})$. Because the solid phase concentration has been computed separately, the reaction current density has not been linearized with respect to the $c_{s,s}$ term. The Taylor series expansion of the reaction current density gives,

$$j(\phi_s,\phi_e) = j(\phi_{s,0},\phi_{e,0}) + \left.\frac{\partial j}{\partial \phi_s}\right|_{\phi_s=\phi_{s,0}} \cdot (\phi_s - \phi_{s,0}) + \left.\frac{\partial j}{\partial \phi_e}\right|_{\phi_e=\phi_{e,0}} \cdot (\phi_e - \phi_{e,0}) \tag{5.18}$$

Here, ϕ_s and ϕ_e are the current values of solid and electrolyte potential, which are unknown and being solved for. $\phi_{s,0}$ and $\phi_{e,0}$ are the values of solid and electrolyte phase potential at the previous time step, which is known. Derivative of the reaction current density with respect to the solid and electrolyte phase potential can be written as,

$$\frac{\partial j}{\partial \phi_s} = \frac{\partial j}{\partial \eta}\cdot\frac{\partial \eta}{\partial \phi_s} = \frac{\partial j}{\partial \eta} \quad \text{and} \quad \frac{\partial j}{\partial \phi_e} = \frac{\partial j}{\partial \eta}\cdot\frac{\partial \eta}{\partial \phi_e} = -\frac{\partial j}{\partial \eta} \tag{5.19}$$

Please see Eq. (5.7) for an expression of η as a function of ϕ_s and ϕ_e. The derivative of reaction current density with respect to the overpotential is provided in Eq. (5.20):

$$\frac{\partial j}{\partial \eta} = j_0 \cdot \left(\frac{\alpha_a F}{RT} \exp\left(\frac{\alpha_a F}{RT} \eta \right) + \frac{\alpha_c F}{RT} \exp\left(-\frac{\alpha_c F}{RT} \eta \right) \right) \tag{5.20}$$

Substituting Eq. (5.18), (5.19), and (5.20) into Eq. (5.8), (5.10), and (5.12), linearized versions of the governing differential equations have been obtained as follows:

$$\begin{aligned} &\varepsilon \frac{\partial c_e}{\partial t} - D_e^{eff} \frac{\partial^2 c_e}{\partial x^2} - a_s \left(\frac{1-t_+}{F} \right) \cdot \left(\left. \frac{\partial j}{\partial \phi_s} \right|_{\phi_s = \phi_{s,0}} \cdot \phi_s + \left. \frac{\partial j}{\partial \phi_e} \right|_{\phi_e = \phi_{e,0}} \cdot \phi_e \right) \\ &\quad = a_s \left(\frac{1-t_+}{F} \right) \cdot \left(j\left(\phi_{s,0}, \phi_{e,0} \right) - \left. \frac{\partial j}{\partial \phi_s} \right|_{\phi_s = \phi_{s,0}} \cdot \phi_{s,0} - \left. \frac{\partial j}{\partial \phi_e} \right|_{\phi_e = \phi_{e,0}} \cdot \phi_{e,0} \right) \end{aligned} \tag{5.21}$$

$$\begin{aligned} &\sigma^{eff} \frac{\partial^2 \phi_s}{\partial x^2} - a_s \left(\left. \frac{\partial j}{\partial \phi_s} \right|_{\phi_s = \phi_{s,0}} \cdot \phi_s + \left. \frac{\partial j}{\partial \phi_e} \right|_{\phi_e = \phi_{e,0}} \cdot \phi_e \right) = \\ &\quad a_s \left(j\left(\phi_{s,0}, \phi_{e,0} \right) - \left. \frac{\partial j}{\partial \phi_s} \right|_{\phi_s = \phi_{s,0}} \cdot \phi_{s,0} - \left. \frac{\partial j}{\partial \phi_e} \right|_{\phi_e = \phi_{e,0}} \cdot \phi_{e,0} \right) \end{aligned} \tag{5.22}$$

$$\begin{aligned} &\kappa^{eff} \frac{\partial^2 \phi_e}{\partial x^2} + \kappa_d^{eff} \frac{\partial^2 c_e}{\partial x^2} + a_s \left(\left. \frac{\partial j}{\partial \phi_s} \right|_{\phi_s = \phi_{s,0}} \cdot \phi_s + \left. \frac{\partial j}{\partial \phi_e} \right|_{\phi_e = \phi_{e,0}} \cdot \phi_e \right) = \\ &\quad - a_s \left(j\left(\phi_{s,0}, \phi_{e,0} \right) - \left. \frac{\partial j}{\partial \phi_s} \right|_{\phi_s = \phi_{s,0}} \cdot \phi_{s,0} - \left. \frac{\partial j}{\partial \phi_e} \right|_{\phi_e = \phi_{e,0}} \cdot \phi_{e,0} \right) \end{aligned} \tag{5.23}$$

Discretizing the linear equations Eq. (5.21), (5.22), and (5.23) by using a finite difference scheme, the coupled matrix for solid and electrolyte potential and electrolyte concentration are obtained.

For the single discharge simulations, the initial state of charge (SOC) is assumed to be 0.9 in the negative electrode and 0.35 in the positive electrode. These values of

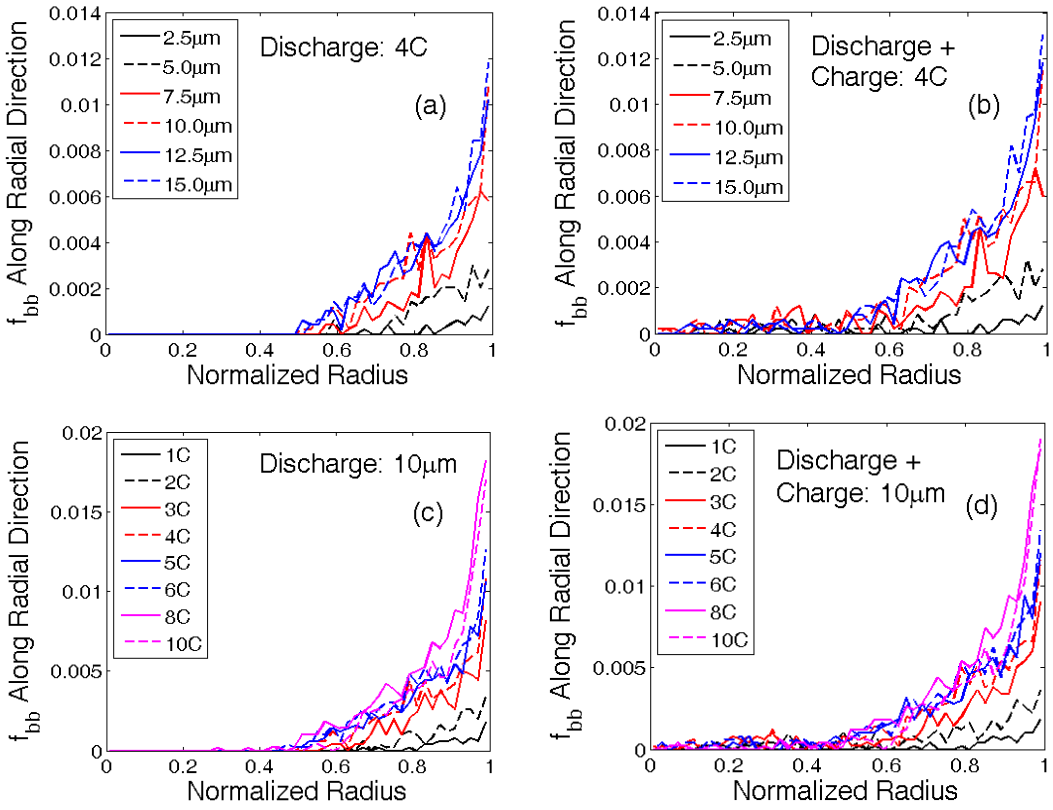

Fig: 5.2. *Fraction of broken bonds along the radial direction showing evolution of damage during discharge and charge processes. (a) After discharge at 4C (delithiation), for all the particle sizes, microcracks predominantly develop near the particle surface. (b) Subsequent constant-current-constant-voltage charge process at 4C (lithiation) creates some microcracks close to the center. (c) Discharge at multiple C-rates for a particle size of 10μm, also shows damage predominantly located near particle surface. (d) CCCV charge after the discharge process causes some microcrack evolution close to the center, but compared to the peripheral region it is insignificant. Thus, majority of the damage evoltuion occurs close to the surface of the particle.*

SOC resulted in an initial voltage of approximately 4.3V. The lower cut-off voltage for lithium ion cells has been assumed to be 2.4V for hard-carbon based anodes. For analyzing cycling performance, the lithium ion battery is assumed to be in a discharged state. It is charged to an upper voltage limit of 4.2V at a very slow rate (0.05C). Discharge-charge cycles are conducted on these electrodes to estimate the cycling performance of an LIB under different design (particle size) and operating conditions

(C-rate). The parameters used in the simulations are listed in Table 5.1. Evolution of mechanical degradation within single active particles and different particles located at different portions of the electrode are elaborated in the Results and Discussion section.

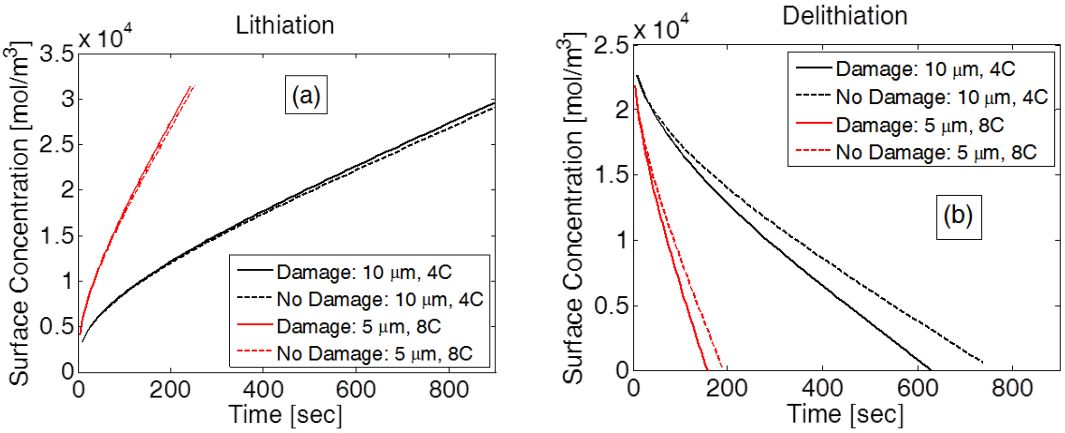

Fig: 5.3. *Variation in surace concentration due to the effect of damage during (a) Lithiation and (b) Delithiation. Two different design and operating conditions were considered: i) Particle size 10μm and operation at 4C, and ii) Particle size 5μm and operation at 8C. (a) For both the operating conditions, during lithiation, damage evolution occurs at the center. It does not affect the surface concentration significantly. (b) During delithiation, peripheral damage evolution affects the surface concentration more significantly. Most of the electrochemical reactions are governed by the surface concentration only. Damage evolution close to the surface during delithiation will be modeled.*

5.2 Results and discussion

LIBs are manufactured in factories in a discharged state [43]. They are then charged in a controlled environment and at a low C-rate (C/20). According to some of the previous works by the authors, no mechanical damage evolution occurs during lithiation or delithiation under low rate operations [85, 178]. Most of the microcrack evolution occurs during and after the first discharge process. Additionally, mechanical degradation has only been observed during high C-rate operations. The formation of microcracks along the radial direction plays a major role in determining its impact on

cell performance. Figure 5.2 and figure 5.3 discusses about the evolution of microcrack density in a 2D circular cross section of a spherical particle. Effect of mechanical degradation on diffusion process has been taken into account by decreasing the local effective diffusivity due to increased tortuosity of the diffusion pathway. This modification in diffusivity due to microcrack formation has been incorporated within the 2D model. The computational model adopted for this 2D analysis has been described in detail in a previous article (see [85]). Diffusion process in a circular cross section can also be simulated in a simplified fashion by solving for concentration only along the radial direction. This will be referred to as 1D model in the following sub-section (5.2.1). Usage of a constant value of effective diffusivity can help us to capture the reduction in local diffusion coefficient due to microcrack formation. Diffusion of lithium species within the solid active particles is captured using this technique (also provided in Eq. (5.4)). Effect of mechanical degradation in solid phase is taken into account by expressing the value of effective diffusivity $\left(D_s^{eff}\right)$ as a function of microcrack density $\left(f_{bb}\right)$ (see Eq. (5.3)). Point to be noted, this analysis is not the 1D Newman type porous electrode theory. Results of the 1D porous electrode theory will be discussed from sub-section 5.2.2 onwards.

In Figure 5.2, microcrack density $\left(f_{bb}\right)$ along the radial direction of a graphite anode has been plotted with respect to the normalized radius after the first discharge and the subsequent charge process. Figure 5.2(a) demonstrates the distribution of f_{bb} along the radial direction after constant current discharge at 4C for different particle sizes

(2.5μm – 15.0μm). Similarly, Figure 5.2(c) shows the microcrack density for a 10.0μm particle after constant current discharge under a wide range of C-rates (1C – 10C). In both of the abovementioned cases, delithiation occurs during the discharge process. The first delithiation gives rise to significant amounts of damage evolution close to the periphery of the active particles. No damage is observed near the center of the active particles during the first discharge process.

Table: 5.1. List of parameters used to solve the one dimensional lithium-ion battery model. All the parameters shown below have been adopted from Gu and Wang (see [67]) and Guo et al. (see [108]).

Name	Units	Anode	Separator	Cathode
Length $\left(L_a, \delta_{sep}, L_c\right)$	m	130e-6	26e-6	130e-6
Porosity $\left(\varepsilon\right)$	--	0.357	0.41	0.444
Solid conductivity $\left(\sigma\right)$	S/m	100	--	3.8
Electrolyte diffusivity $\left(D_e\right)$	m^2/s	7.5e-11	7.5e-11	7.5e-11
Solid diffusivity $\left(D_s\right)$	m^2/s	3.9e-14	--	1.0e-13
Particle radius $\left(R_s\right)$	m	12.5e-6	--	8.5e-6
Temperature $\left(T\right)$	K	298.15	298.15	298.15
Initial electrolyte concentration $\left(c_{e,init}\right)$	mol/m^3	2000	2000	2000
Transference number $\left(t_+\right)$	--	0.363	--	0.363

Figure 5.2(b) demonstrates the microcrack density along the radial direction after constant current (CC) discharge and constant current constant voltage (CCCV) charge at 4C for different graphite particle sizes (2.5 μm – 15.0 μm). Similarly, Figure 5.2(d) gives an example of microcrack density along the radial direction for a 10.0-μm graphite particle after CC discharge and CCCV charge at a wide range of C-rates (1C – 10C). During the charge process, lithiation occurs within the anode active particles. Formation of tensile stress close to the center of the particle gives rise to mechanical degradation at the center during the lithiation process. In Figures 5.2(b) and 5.2(d), minor microcrack evolution can be observed close to the center of the graphite active particle after the charge process. However, microcrack density after the first discharge-charge process along the periphery of the graphite active particle is much greater than the mechanical damage at the center. Because the mechanical degradation at the central portion of the active particle during lithiation is minor, monitoring only the peripheral damage evolution during delithiation should be sufficient for successfully capturing the effect of microcrack density on the effective diffusivity of the anode active particles.

The results reported in Figure 5.3 show the extremely minor impact of central damage evolution on the surface concentration of the active particles as compared to that of the peripheral damage evolution. This supports the hypothesis made with regard to Figure 5.2, namely monitoring damage evolution along the periphery of the active particle should be sufficient to capture the impact of microcrack density on the diffusivity of the active particles. Two different particle sizes (5μm and 10μm) operating at two different C-rates (4C and 8C) are taken into consideration for analyzing the

impact of microcrack density on surface concentration. In Figure 5.3(a), surface concentrations during lithiation for a 10μm particle operating under 4C (black line) and another 5μm particle operating at 8C (red line) are reported. Surface concentrations with and without taking damage evolution into consideration are represented by the solid and dashed lines, respectively. During lithiation, damage evolution occurs at the center of the active particle. Extremely small differences between the surface concentration with and without damage evolution lead to the conclusion that microcrack formation at the center of the active particles does not impact the surface concentration significantly during the lithiation process.

However, during the delithiation process, damage evolution occurs close to the peripheral region of the active particles. In Figure 5.3(b), for both the 10μm particle operating at 4C (black line) and the 5μm particle operating at 8C (red line), the surface concentrations without damage (dashed line) is significantly larger than the surface concentration with damage (solid line). Thus, microcrack evolution during delithiation has a significant impact on the surface concentrations of the active particles. To estimate the open-circuit-potential, only the surface concentrations of the solid active particles have been used. As a result, from the electrochemical perspective, only the surface concentration of the active particles has an impact on the behavior of the LIB. Microcrack formation at the center of the active particle during lithiation has an insignificant impact on the surface concentration. Thus, it is unnecessary to track the evolution of microcrack density during the lithiation process. Capturing the evolution of damage along the periphery of the active particles that occurs during the delithiation

process is sufficient for tracking the change in surface concentration and, subsequently, the behavior of the LIB.

It should be noted that, the delithiation process, which corresponds to discharge, is conducted under constant current (CC) condition. However, the lithiation phenomena corresponding to the charge process, is conducted under constant current constant voltage (CCCV) condition. As a result, during operation at 4C, it is possible to reach only 800s during the delithiation process, whereas, simulation can be conducted till 900s during the charge process.

5.2.1 Development of a reduced order model

According to the authors, evolution of microcrack density occurs toward the beginning of the delithiation process [85, 178]. Eventually, the amount of microcrack formation reaches a state of saturation, and no further increase in mechanical degradation is observed during subsequent discharge-charge cycles. Thus, an exponential increase in damage evolution followed by saturation can be successfully captured by Eq. (5.1) provided in the Methodology section. The maximum amount of damage $\left(A_{\max}\right)$ and the rate of damage evolution $\left(m_{rate}\right)$ depend on the particle size $\left(R_s\right)$ and the C-rate at which the simulation is being conducted. The purpose of reduced order modeling is to develop an analytical expression that can approximately predict the microcrack density $\left(f_{bb}\right)$ under certain particle size and C-rate operating condition. Following Eq. (5.1) and (1*a*), the unfinished task is to estimate an analytical representation of $A_{\max}$ and m_{rate} as a function of particle size and C-rate. Evolution of microcracks has been simulated for six different particle sizes, R_s = [2.5μm, 5.0μm,

7.5μm, 10.0μm, 12.5μm, and 15.0μm], and eight different C-rates [1C, 2C, 3C, 4C, 5C, 6C, 8C and 10C], for each of the particles. Individual values of $A_{\max}$ and m_{rate} were estimated for microcrack evolution in each of the simulations. Two analytical expressions have been developed that can capture the variation in $A_{\max}$ and m_{rate} for various particle sizes and C-rates, which are also provided below,

$$A_{\max}\left(R_s, C_{rate}\right) = -0.5902 + \frac{0.7173 + 0.0027 \cdot R_s + \left(-0.15/R_s\right)}{1 + \left|\left(0.0223 \cdot C_{rate}\right) - \left(0.2115 + \left(-0.002\right) \cdot R_s\right)\right|} \tag{5.24}$$

and,

$$m_{rate}\left(R_s, C_{rate}\right) = 1.9572 + \left(1 + \left(-0.2058\right) \cdot C_{rate} + \frac{22.5694}{C_{rate}} + \frac{\left(-21.7787\right)}{\left(C_{rate}\right)^2}\right) \cdot \left(1 + \frac{\left(-7.6826\right)}{R_s} + \frac{19.8345}{R_s^2} + \left(-0.0544\right) \cdot R_s\right) \tag{5.25}$$

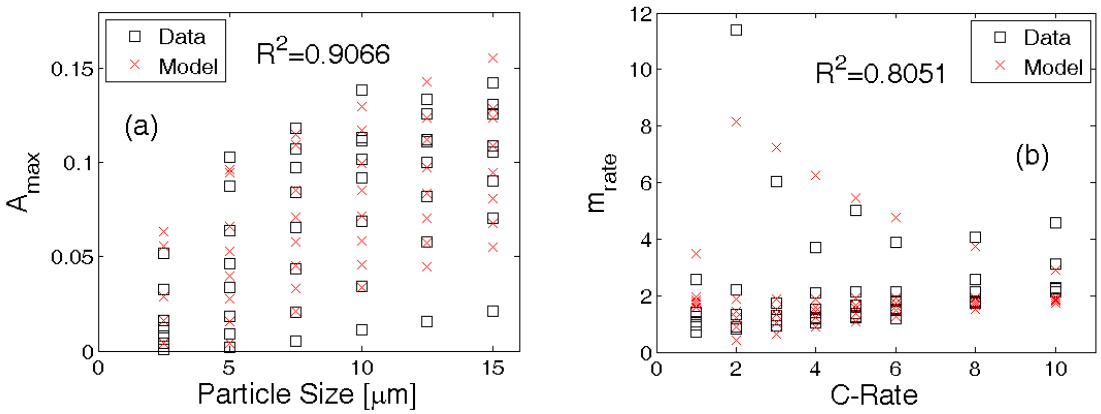

Fig: 5.4. *Reduced order model fits for $A_{\max}$ and m_{rate} parameters in Eq. 5.24 and Eq. 5.25 as functions of C-rate and particle size. (a) The maximum amount of damage $\left(A_{\max}\right)$ for different particle sizes and C-rates can be captured till an R^2 value of 0.9066 using the analytical expression provided in Eq. 5(a). (b) The rate of damage evolution $\left(m_{rate}\right)$ can be predicted by the analytical expression given in Eq. 5(b) with an accuracy of R^2 equal to 0.8051.*

where, R_s represents particle size and C_{rate} signifies how fast the active particles are delithiated and lithiated. Figure 5.4(a) demonstrates that Eq. (5.24) can estimate the

values of $A_{\max}$ with R^2 accuracy equal to 0.9066. Similarly, as depicted in Figure 5.4(b), Eq. (5.25) can predict the values of m_{rate} with R^2 accuracy equal to 0.8051. The different parameters used in Eq. (5.24) and (5.25) are obtained using the "nlinfit" function embedded in MATLAB. These analytical expressions given in Eq. (5.24) and (5.25) along with Eq. (5.1) constitute the reduced order model for predicting microcrack density inside active particles. The R^2 value for $A_{\max}$ is 0.9, which is definitely good for prediction purposes. However the R^2 value of m_{rate} is only 0.8 that is not sufficiently good for prognosis purpose. Since the maximum value of mechanical degradation depends on $A_{\max}$, and m_{rate} just dictates how quickly/slowly the maximum value is reached, not very accurate prediction for m_{rate} can still be applied for prediction purposes. The inaccuracy introduced by R^2 value of 0.8 for the m_{rate} parameter, will have minor impact on the final prognosis. This reduced order model is applicable to active particles of different size and operating at different C-rates but maintained at a fixed room temperature $\left(T = 25^0 C\right)$ condition. Reduced order models of microcrack density applicable to different operating temperatures were not investigated in this study and will be reported as part of a separate article. Because of the usage of the reduced order model (ROM), the mechanical equilibrium equation and subsequent crack formation is not being solved at each time step. Hence the time required for running the simulation decreases significantly (by two orders of magnitude).

Once an approximate expression for the evolution of microcrack density is established, it is important to characterize how the mechanical degradation affects the

solid phase diffusivity of the active particles. In earlier articles, it was argued by the authors that formation of a microcrack hinders the diffusion pathway of lithium [85, 139, 178]. In the presence of a microcrack, the ions take a more tortuous pathway to traverse from one point to another, which eventually results in reduction of the diffusivity of the active particles. To capture this deterioration in the diffusion coefficient due to evolution of microcracks, an analytical expression is suggested in Eq. (5.3). The only unknown term in the right hand side of that equation is the exponent γ. In the 2D simulations reported here, the impact of local microcrack formation on the diffusion of lithium species is taken into consideration by decreasing the local diffusivity. Thus, the effect of increased tortuosity is incorporated within the 2D simulations. The concentration gradient obtained from the 2D simulation incorporates the effect of microcrack formation within itself. In Figure 5.5, the symbols denote the concentration gradient at the end of single delithiation process for different particles operating at various C-rates obtained from the 2D simulations.

1D simulations are also conducted with different values of effective diffusivity that can predict the concentration gradient obtained from the 2D simulations. The effective diffusivities used in the 1D simulations were evaluated using Eq. (5.3). The main purpose of this exercise is to estimate a value of the exponent γ that can most accurately predict the values of the concentration gradient obtained from the 2D simulations. In Figure 5.5, the lines denote values of concentration gradients as estimated by the 1D simulation. Figures 5.5(a), 5.5(b) and 5.5(c) report the comparison between the concentration gradients obtained from 2D and 1D simulations for $\gamma = 5.0$,

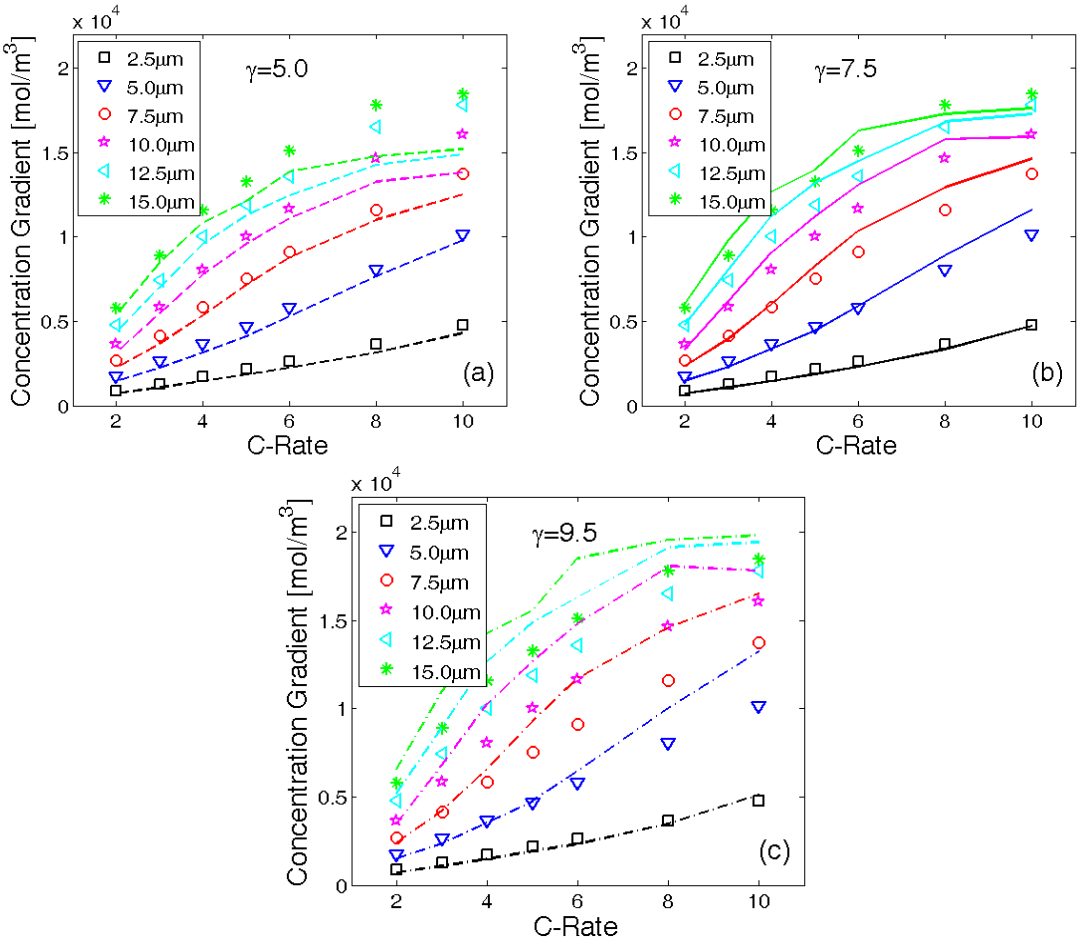

Fig: 5.5. *Estimation of the parameter* γ *in Eq. (5.3). For different C-rate and different particle size, the concentration gradient at the end of the simulation for 1D (lines) and 2D (symbols) analysis has been compared. (a)* $\gamma = 5.0$ *underestimates the concentration gradient for large particles under high C-rate operating conditions. (b)* $\gamma = 7.5$ *estimates the concentration gradient for all particle sizes at all C-rate in a relatively accurate fashion. (c)* $\gamma = 9.5$ *significantly overestimates the concentration gradient for most of the particle sizes at high C-rate operation. Thus* $\gamma = 7.5$ *is the most accurate approximation and will be adopted in the subsequent studies.*

$\gamma = 7.5$ and $\gamma = 9.5$, respectively. As can be observed in Figure 5.5(a) that the 1D simulation with $\gamma = 5.0$ significantly under-predicts the concentration gradient for large particles. On the contrary, Figure 5.5(c) clearly shows that $\gamma = 9.5$ over-predicts the concentration gradient for large particle sizes operating at high C-rate conditions. The

best correlation between the concentration gradients from the 1D and 2D simulations can be obtained with $\gamma = 7.5$, also depicted in Figure 5.5(b). Usage of least square based fitting methodology would definitely be mathematically more accurate. However, it does not render any physical understanding of how variation of the parameters changes the effective diffusivity value. As a result, relatively more brute force type methodology have been adopted to calculate the exact value of exponent γ. It can be concluded that, to correlate the effect of microcrack density between 2D and 1D simulations, an optimum estimate of the exponent γ is 7.5. However, the active particles observed inside the LIB electrodes are spherical in shape and definitely require 3D consideration. To extend the estimate of exponent γ from 2D to 3D applications, it is raised by a factor of $3/2$. Thus, for 3D applications, the optimum value of the exponent will be $\gamma_{3D} = 3/2 \cdot \gamma = 11.25$. For all the subsequent applications, the optimum value of γ in 3D will be used (unless otherwise mentioned).

5.2.2 Effect of coupling mechanical degradation into 1D electrode level model

All the simulations and analysis reported until now were conducted on a single active particle. The theory behind the 2D single particle simulations can be found in a previous article by the same authors [85]. A realistic electrode consists of several spherical particles. The electrolyte concentration and electrolyte potential also change along the thickness of the electrode, which becomes more prominent under high C-rate conditions. As observed by the authors (see [85, 178]) as well as other researchers (see [6, 29, 183]), larger diffusion-induced stress acts on the active particles under higher C-

rates. Large diffusion-induced stress has the potential to induce enhanced amounts of mechanical degradation. Different C-rates affect the lithium flux within the active particles. Flux of lithium in or out of the active particle changes along the thickness of the electrode. To capture the variations in applied lithium flux, or in other words the C-rate, it is very important to solve the coupled 1D mass and charge transport equations (Eq. (5.4), (5.8), (5.10) and (5.12)).

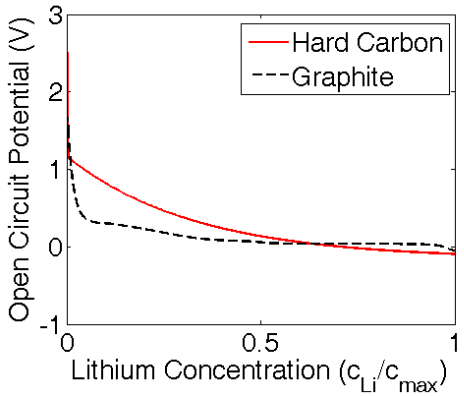

Fig: 5.6. *Comparison between the open circuit potential of hard carbon and graphite. The mathematical expression of OCP for hard carbon is taken from Gu and Wang (see Ref. [67]), and the OCP for graphite is adopted from Srinivasan, 2004 (see Ref. [184]). The OCP profile for hard carbon shows a higher slope. Whereas, the OCP profile for graphite is more flat in nature and gives rise to a relatively flat performance curve.*

Performance of a lithium-ion cell depends on the open circuit potential of the active materials used in the electrode. Lithium nickel manganese cobalt oxide ($LiNiMnCoO_2$), also known as NMC, has been used as the cathode material. The expression of open-circuit-potential (OCP) for NMC has been adopted from Awarke et al. [88]. Because damage evolution inside anode is being analyzed here, two different OCP curves have been taken into consideration, which correspond to two different anode materials (hard carbon and graphite). The OCP of hard-carbon has been adopted from Gu and Wang (see [67]), whereas the OCP for graphite has been adopted from

Srinivasan and Newman (see [184]). Comparative reproduction of the OCP profiles for hard-carbon and graphite has been reported in Figure 5.6. Graphite shows a much flatter open circuit potential than hard carbon. As a result, the reaction current density at the anode shows a much higher gradient for graphite as compared to hard-carbon. For computational simplicity, the OCP for hard carbon has been adopted for the full charge-discharge simulations. The drive cycle simulations are conducted using both the OCP profiles (graphite and hard carbon). A comparative analysis, of which material leads to reduced mechanical degradation under drive cycle conditions, is presented below.

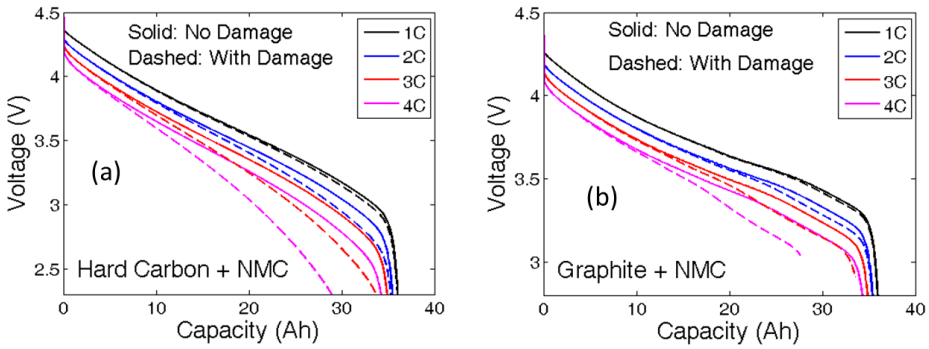

Fig: 5.7. *Comparison of the performance curves with and without mechanical degradation at different C-rate operation conditions. (a) "Hard carbon + NMC" chemistry have been used here. (b) "Graphite + NMC" chemistry have been used in these simulations. For both the chemistries, effect of mechanical degradation on cell performance is only significant for high C-rate operations. The performance curve for "Graphite + NMC" at 4C with mechanical degradation (case (b)) stops abruptly, because of the fact that severe mechanical degradation causes the local concentration to become zero.*

A comparison between the open circuit potential curves for graphite and hard carbon is shown in Figure 5.6. For hard carbon, the OCP decreases gradually with increasing lithium content. Whereas, for graphite the OCP curve remains more or less constant for a wide range of lithium concentration, and suddenly drops as the concentration reaches very close to the maximum value. This is reflected in the voltage

profile as well, which is shown in Figure 5.7. Voltage profiles for hard-carbon anode and NMC cathode is shown in Figure 5.7(a) at multiple C-rates (solid line). Difference in performance curve due to mechanical degradation is also clearly demonstrated there (dashed line). Similar performance curves for graphite anode and NMC cathode at multiple C-rates have been demonstrated in Figure 5.7(b). The solid line corresponds to the performance without mechanical degradation, whereas, the dashed line signifies the impact of mechanical degradation on cell performance. For both hard-carbon and graphite, enhanced mechanical degradation happens at high C-rate (3C and 4C). As a result, the impact of mechanical damage on performance curve is also more sever at high rate operating conditions. For graphite anode and NMC cathode, the voltage vs. capacity curve with mechanical damage at 4C stops much earlier before reaching the lower cutoff voltage, which is set at 2.8V for graphite (see Figure 5.7(b)). At 4C, due to enhanced mechanical degradation, diffusivity of the solid active particles decreases rapidly. Reduction in diffusivity causes the surface concentration to decrease extremely quickly and it becomes zero at certain points within the anode. The current computational procedure is incapable of handling constant concentration boundary condition at the surface of the active particles. The simulation is stopped as soon as the surface concentration of the active particle becomes zero.

The linearized governing differential equations given in Eq. (5.4), (5.21), (5.22), and (5.23) have been discretized using the finite-difference method and solved by implementing it in MATLAB. Coupling between these governing differential equations has been conducted through the nonlinear Butler-Volmer equation provided in Eq. (5.6).

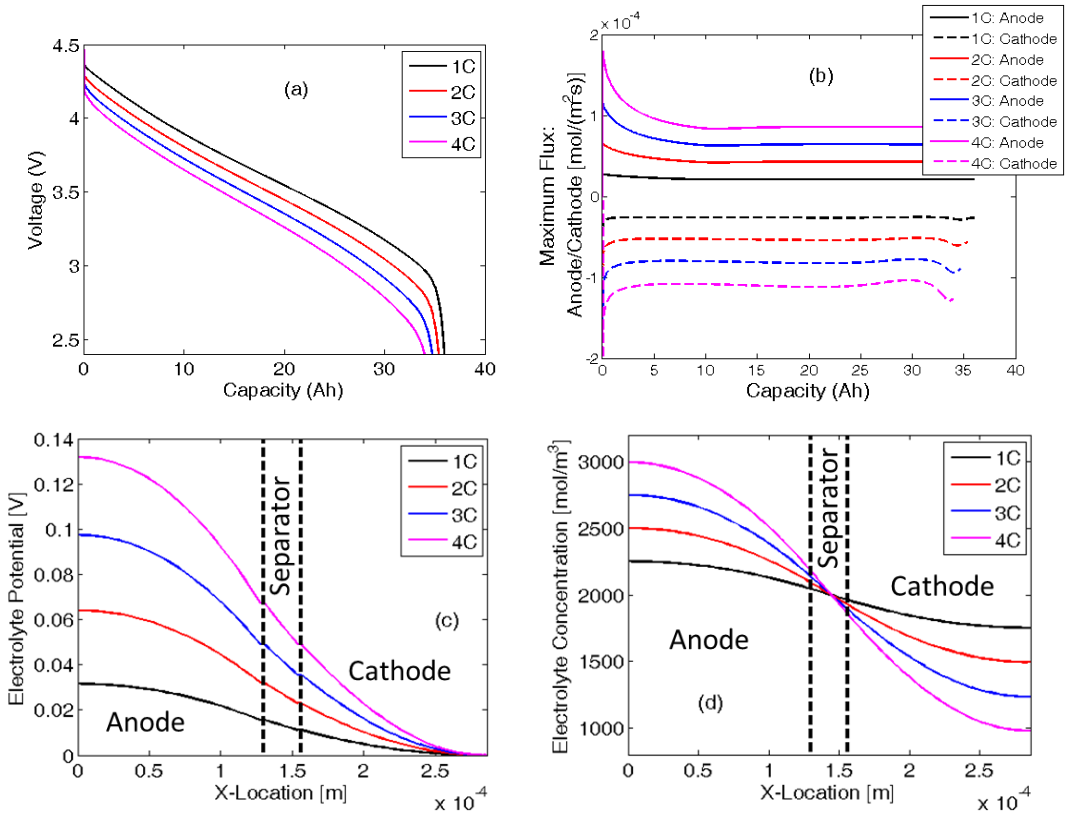

Fig: 5.8. *Variation in electrochemical quantities during the first discharge process for "NMC + Hard Carbon" under different C-rate operation. (a) Voltage vs. capacity plots at different C-rates reveals that increasing the C-rate results in reduction in effective capacity of the cell. (b) Maximum flux in anode and cathode with respect to the discharged capacity. Higher C-rate results in larger magnitude of ion flux. (c) Variation in electrolyte potential across the electrode at the end of the discharge process, (d) Variation in electrolyte concentration across the electrode at the end of the discharge process.*

The parameters used to solve these coupled differential equations are provided in Table 5.1. The voltage vs. capacity performance curve during the first constant current discharge process obtained by solving the 1D electrode level model is demonstrated in Figure 5.8(a). Here, hard-carbon has been used as the anode active material and NMC as the cathode active material. Four different C-rates are taken into consideration. Higher values of C-rate resulted in reduced capacity due to enhanced kinetic and mass transport limitations. The maximum amount of lithium flux observed in the anode and cathode

during the first CC discharge at different C-rates is reported in Figure 5.8(b). In the present analysis, during the discharge process, the current is assumed to be positive. Outflux of lithium is assumed to have a positive sign, and the influx is signified by a negative value of the flux variable. During the discharge process, lithium species move out of the negative graphite electrode and enter the cathode. According to the convention followed in this research, during the discharge process, the anode experiences a positive flux of lithium, and negative flux is observed inside the cathode. As depicted in Figure 5.8(b), the lithium flux in both the anode and cathode increases with the increase in applied C-rate. It can also be concluded from Figure 5.8(b) that the magnitude of the maximum lithium flux in both the anode and cathode is highest at the beginning of the discharge process. It eventually reduces and saturates at a particular value. Towards the end of the discharge process, maximum flux at the cathode experiences some fluctuation. The maximum lithium flux traverses along the thickness of the electrode during the discharge process, which is not shown in Figure 5.8(b).

During the first discharge process, the variation in the electrolyte potential and the electrolyte concentration plays a major role in determining the performance of the LIB. Figure 5.8(c) demonstrates the distribution of the electrolyte potential at the end of the first discharge state along the thickness of the entire electrode. Increasing the C-rate at which the cell is being operated results in an increased electrolyte potential at the negative electrode. The electrolyte potential is kept fixed at zero at the positive electrode-current collector interface (see boundary condition Eq. (5.13)). Similarly, variations in the electrolyte concentration along the thickness of the electrode at the end

of the discharge process are displayed in Figure 5.8(d). The portion inside the vertical dashed line signifies the region that lies inside the separator. The initial concentration inside the electrolyte is assumed to be 2,000 mol/m^3. During the discharge process, inside the anode the lithium atoms come out of the solid active particles and enter the electrolyte. Within the cathode, the lithium atoms travel from the electrolyte into the solid active particles. During discharge, transport of lithium ions from anode to cathode through the separator happens via the diffusion and migration process. Due to diffusion-induced limitations, at a high C-rate (4C), a significant amount of lithium ions is depleted from the cathode electrolyte. It is important to note that, during discharge lithium ion concentration in the anode may reach values as high as 3M. There are chances of salt precipitation within the electrolyte, which can lead to loss of cyclable lithium and subsequently capacity fade. Also variation in lithium ion concentration may impact the conductivity within the electrolyte. Hence, an appropriate value of the initial concentration of lithium salt within the electrolyte should be considered. Proper care must be taken while charging or discharging an LIB at very high C-rates to prevent situations where lithium ions are completely deleted from the electrolyte. Mechanical degradation within the solid active particles is not taken into consideration in any of the simulation results reported in Figure 5.8(a)–(d).

To establish the validity of the developed computational model, voltage vs. capacity performance curves predicted by the simulation is compared with experimentally observed results. Such a comparison between the performance curves obtained at 1C and 3C are shown in Figure 5.9. The experimentally observed voltage vs.

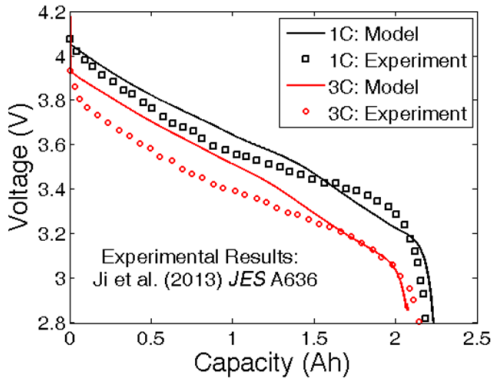

Fig: 5.9. *Comparison of performance curve obtained from computational model with experimental results. The experimental results were obtained from Ji et al JES A636 (2013) (see Figure 2 in [109]). Minor differences between the experimental result and the computational prediction can be attributed to the difference in the OCP curves. The computational predictions have been made using graphite as anode and NMC as cathode active material.*

capacity plots have been adopted form Figure 2 in Ji et al. (*JES* 2013) [109]. Even though the comparison is not one on top of the other, they match quiet well in a qualitative sense. Graphite anode and NMC cathode has been used in both experiment and simulation. But the OCP curves for NMC and graphite used in computational analysis are not the same as reported in the experimental article. Isothermal condition has not been maintained in the experimentally observed result. Whereas, the simulations are conducted under isothermal operating conditions at T=25^{0}C. The change in temperature for 1C is not significant, as reported in the experimental results. For operation at 3C, almost 20^{0}C increase in temperature is observed. The increased capacity for the cell at 3C can be attributed to this increase in internal temperature. Difference in the overall voltage profile can be due to the mismatch in OCP curves for both the anode and cathode materials. Also in the present computational analysis, electrolyte conductivity (κ) has been assumed to be constant, and not dependent on lithium ion

concentration. In a realistic electrolyte, conductivity changes strongly as a function of lithium ion content. The difference between the experimentally observed and simulated voltage curve can also be attributed to this parametric discrepancy. In the present simulations dependence of electrolyte conductivity on the lithium ion concentration has not been incorporated.

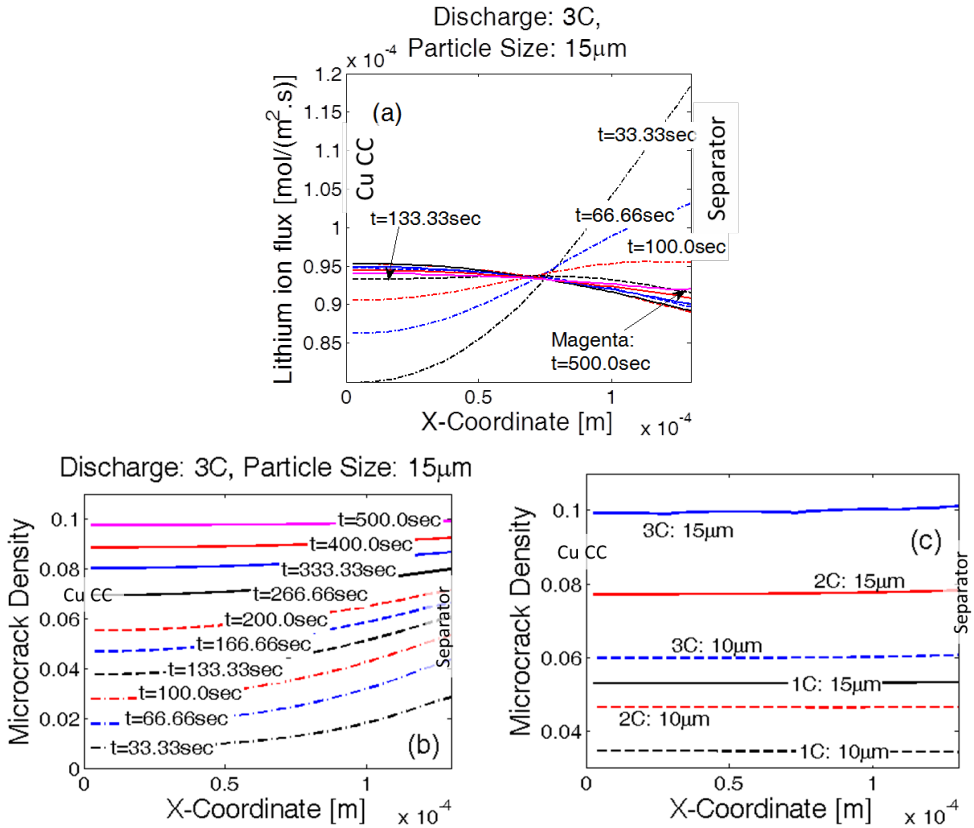

Fig: 5.10. *Evolution of damage along the thickness of the anode electrode, hard-carbon graphite active material. (a) For 15μm sized anode active particles and discharge at 3C, evolution of lithium flux along the thickness of the electrode over time. The location of maximum reaction current density shifts over time along the thickness direction. (b) For a particular discharge at 3C and for particle size of 15μm, damage evolution over time. Overall damage increases with time. Initially, microcracks evolve predominantly in particles near the separator. Towards the end more damage evolves at the current collector, and the final profile looks almost flat. (c) Uniform distribution of final damage profile for discharge at three different C-rates (1C, 2C and 3C) and two different particle sizes (10μm and 15μm).*

For solid active particles where transport of lithium species can be reasonably approximated by the diffusion process, delithiation gives rise to tensile stress and evolution of microcrack density along the peripheral region. During the lithiation process, microcrack evolution takes place close to the center of the active particles. The analytical expressions in Eq. (5.1), (5.24), and (5.25) estimate the amount of microcrack density during delithiation for wide range of C-rates (1C – 10C) and particle sizes (2.5 μm – 15.0 μm). This relation is derived based on mechanical damage evolution only within the graphite active particles during the delithiation process. At the time of discharge, the graphite active particles within the anode experience delithiation. Hence, the analytical expression derived for microcrack evolution can be applicable to the anode active particles during the discharge process. For the current study, the cathode particles are assumed to be free of mechanical degradation. According to Eq. (5.3), diffusivity of the solid active phase decreases due to evolution of mechanical damage. Figure 5.10 demonstrates the distribution of mechanical degradation along the thickness of the negative electrode at the end of the first discharge process. Capacity fade due to increasing microcrack density has been analyzed in Figure 5.11. Strictly speaking, there should be a feedback of cell performance and capacity fade on the mechanical degradation. Based on some earlier investigations conducted by the authors, impact of capacity fade on further mechanical degradation is negligible (see [85]). Because of this minor feedback effect, while deriving the reduced order model, only the impact of mechanical degradation on change in solid-state diffusivity has been taken into consideration. Point to be noted here is that, microcrack formation happens due to

formation of concentration gradient within the active particles during operation. Effect of further microcrack formation due to performance decay has been neglected here.

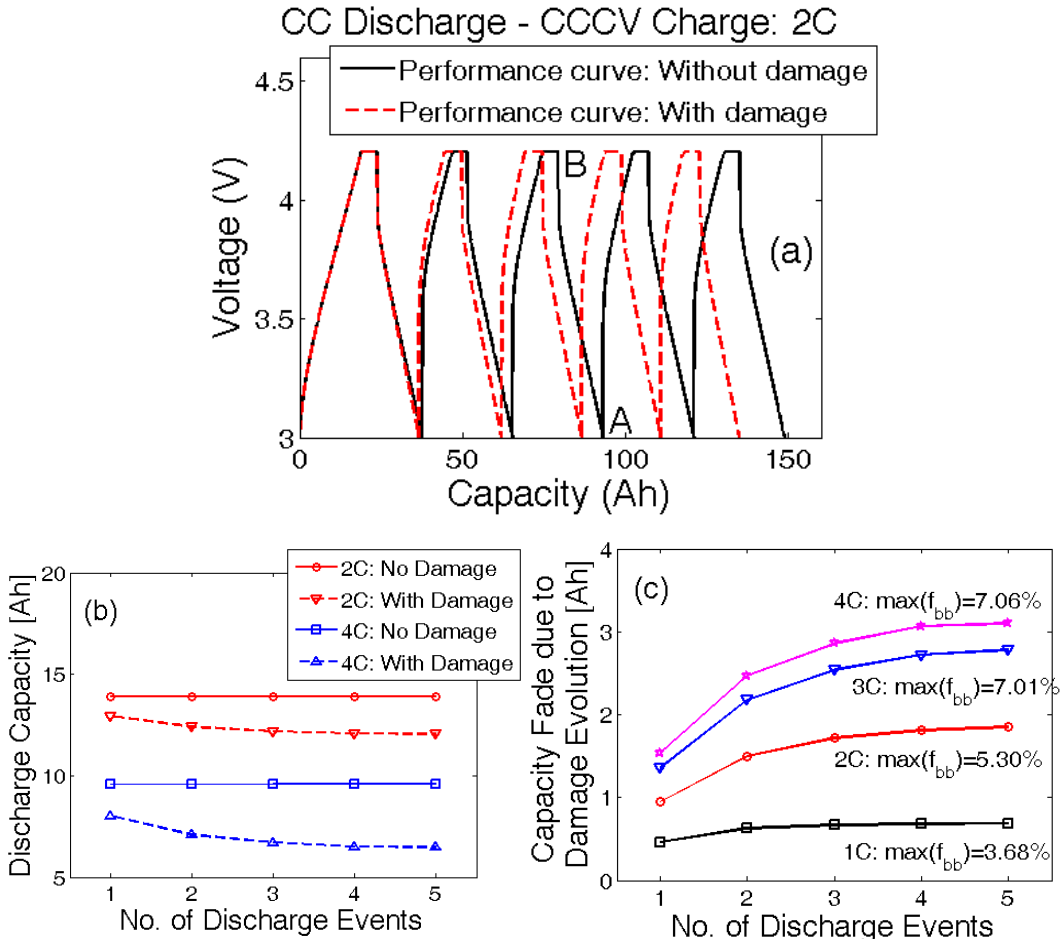

Fig: 5.11. *Capacity fade due to mechanical damage evolution over multiple cycles. (a) Evolution of voltage vs. capacity for five 2C CC discharge and 2C CCCV charge cycles, with and without damage evolution. (b) Discharge capacity at 2C (red line) and 4C (blue line). Difference between the capacity with (dotted line) and without (solid line) damage evolution is defined as the capacity fade. (c) Capacity fade over multiple cycles for different C-rates. Higher C-rates result in larger fraction of broken bonds and eventually more capacity fade.*

Under uniform distribution of particle sizes, the flux of lithium atoms experienced by the active particles determines the amount of diffusion-induced stress and subsequently the evolution of mechanical degradation. The location where

maximum lithium flux is observed, experiences the largest extent of microcrack density. Thus, it is very important to have a prior knowledge of the location of the maximum reaction current density to properly understand the evolution of microcrack density along the thickness of the electrode. Figure 5.10(a) demonstrates the variations in lithium flux along the thickness of anode during CC discharge at 3C containing active particles with a radius of 15 μm. Towards the beginning of the discharge simulation, at time t = 33.33 sec, a significantly large reaction current density and lithium flux are observed close to the separator. The lithium flux observed close to the current collector is significantly smaller than the value observed at the separator. With increasing time, the lithium flux close to the separator decreases and the flux at the current collector increases. At around t = 133.0 sec, the lithium atom flux at the current collector and the separator becomes almost equal. Close to the end of the discharge process, at t = 500.0 sec, the active particles close to the current collector experience slightly higher lithium flux than the particles located close to the separator. Thus, during the discharge process, there is a shift in the maximum reaction front from the separator to the current collector over time.

Because of the variation in the reaction current density over time, mechanical degradation also evolves accordingly along the thickness of the electrode. Figure 5.10(b) depicts how the microcrack density increases during CC discharge process at 3C in an anode containing uniformly distributed active particles with a radius of 15 μm. Initially, at t = 33.33 sec, active particles close to the separator experience the maximum amount of lithium flux, which results in enhanced damage evolution near the separator. A similar pattern of higher microcrack density close to the separator and less damage near the

current collector are observed until t = 166.66 sec. Then, due to the shift of the reaction current front towards the current collector, enhanced mechanical degradation is observed inside the active particles close to the current collector. Finally, close to the end of the discharge process, at t = 500.0sec, almost uniform microcrack density is observed from the separator to the current collector. Distribution of mechanical damage at the end of the first discharge process is reported along the thickness of the negative electrode in Figure 5.10(c) for two different particle sizes (10.0 μm and 15.0 μm) and three different C-rates (1C, 2C, and 3C). Less damage evolution is observed for smaller particles operating under low C-rate conditions. Larger particles operating at high C-rates display enhanced microcrack density. However, for all the particle sizes and all the operating conditions, damage evolution is very much uniform along the thickness of the electrode (from separator to current collector). This uniformity in microcrack density appears due to shifting of the maximum reaction current front from the separator to the current collector during the constant current discharge process.

To analyze the impact of microcrack density on the overall performance of the LIB electrode, multiple charge discharge cycles were conducted taking into consideration the effect of mechanical degradation on diffusivity of anode active particles. A correlation between the solid phase diffusivity of the anode active particles and microcrack density can be obtained from Eq. (5.3). Figure 5.11(a) demonstrates five charge-discharge cycles with (red dashed line) and without (black solid line) taking the damage evolution in the anode active particles into consideration. To maintain consistency in the capacity values, the battery is charged first from a very low state-of-

charge condition in a CCCV fashion until a maximum voltage of 4.2V is reached. Incorporation of mechanical degradation of the anode active particles results in reduction of effective solid phase diffusivity, and subsequently the resistance due to ion transport increases. Hence, a reduction in effective capacity is observed due to the evolution of microcracks inside the active particles. Capacity during a discharge process is estimated by subtracting the Ahtp at the beginning of discharge from the Ahtp at the end of the discharge process. Referring to Figure 5.11(a), to estimate the discharge capacity without damage during the third cycle, Ahtp at point B is subtracted from the Ahtp at point A.

Figure 5.11(b) demonstrates the discharge capacity while operating at 2C and 4C during five subsequent charge-discharge cycles. If the evolution of mechanical degradation in anode active particles is not taken into consideration, the capacity values during all five discharge phenomena are exactly the same. Capacity at 4C discharge (blue solid line) is less than that observed at 2C (red solid line) due to the rise in kinetic and transport resistance at higher rates of operation. If mechanical degradation is taken into account, the discharge capacity keeps decreasing as the battery is cycled more and more (dashed line). Capacity fade during operation at 4C is much greater than that observed at 2C because at higher rates enhanced mechanical degradation occurs. A higher fraction of microcrack density $\left(f_{bb}\right)$ results in smaller values of effective diffusivity of the anode active particles. Reduced diffusivity increases the transport resistance and subsequently enhances the capacity fade. Hence, the capacity fade due to

mechanical degradation observed at higher rates of operation are much larger than that experienced at low C-rates.

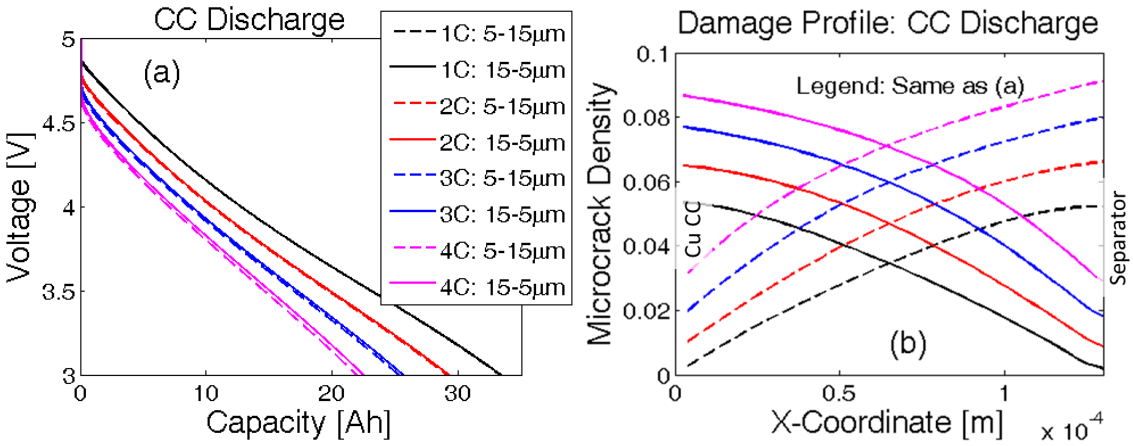

Fig: 5.12. *Instead of having a uniform particle size, a gradient in particle size distribution may have a different impact on the damage profile and capacity of the electrode. Two different particle size distributions have been investigated: i) Linearly increasing particle size from 5μm at the current collector to 15μm at the separator, and ii) Linearly decreasing particle size from 15μm at the current collector to 5μm at the separator. a) Voltage vs. capacity performance curves during the first discharge at four different C-rates. Capacity is same for both the particle size distributions at low C-rate operations (1C and 2C). For high C-rate operations (4C), smaller particles close to the separator (case (ii)) leads to slightly larger capacity (around 0.54Ah). (b) Damage profile for both the particle size distributions after the first discharge process.*

Capacity fade due to only the mechanical degradation can be estimated by obtaining the difference between capacity without and with damage. The extent of capacity fade solely due to mechanical degradation is reported in Figure 5.11(c). Maximum amount of damage at four different C-rates are also reported. Operation at lower values of C-rate (1C or 2C) gives rise to less damage and subsequently smaller capacity fade. However, a larger extent of damage and enhanced capacity fade are observed for high rate (3C and 4C) operations. Irrespective of the rate of operation, capacity fade tends to saturate at a certain limit. For smaller rates of operation, the capacity fade saturates much earlier than the batteries operating at higher C-rates. The

maximum capacity fade also increases with an increasing rate of operation. All the simulations reported in Figure 5.11 used a particle radius of 10.0 μm in the anode. Extremely close values of microcrack density observed at 3C and 4C lead to the conclusion that the particle has almost reached the maximum amount of damage it will ever experience during CCCV charge–CC discharge cycles.

Instead of having a constant particle size along the thickness of the negative electrode, implementation of a gradient in particle size from the current collector to the separator (ascending or descending) may impact the evolution of microcrack density and subsequently capacity fade of the LIB. The two different particle size distributions taken into consideration are as follows: i) linearly increasing particle size from 5 μm at the current collector to 15 μm at the separator, and ii) linearly decreasing particle size from 15 μm at the current collector to 5 μm at the separator. While using different particle size distributions, the total volume of the electrode and the volume fraction of solid active material have been kept constant. For changing particle radius, the electroactive surface area changes accordingly, which is taken into account by modifying the specific surface area parameter $\left(a_s\right)$. Since the total amount of active material dictates the overall capacity of the electrode, maintaining a fixed volume fraction of the solid phase ensures consistency of capacity. The cathode and anode parameters used in the simulations have been adopted from existing literature and listed in Tables 5.1. Here, "N" refers to the variables/parameters corresponding to the negative electrode, "P" refers to those relevant to the positive electrode. Figure 5.12(a) depicts a comparative analysis of voltage vs. capacity performance curve for the two different particle size distributions.

The solid line corresponds to the case where particle size decreases from current collector to separator. The dashed line signifies the other particle size distribution of smaller particles close to the current collector and larger particles close to the separator. The performance curves at lower C-rates (1C and 2C) show insignificant difference between the two particle size distributions. At higher values of the C-rate, the case with descending particle size from current collector to separator displays slightly larger capacity than its counterpart. For example, at 4C the particle size distribution with 5.0-μm particles close to the current collector and 15.0 μm particles at separator [case (i)] shows 0.4-Ah lower capacity than the particle size distribution with 15.0 μm particles at the current collector and 5.0-μm particles near the separator [case (ii)].

When the variation in particle size in the negative electrode is taken into account, evolution of mechanical degradation inside the active particles of anode deserves investigation. Figure 5.12(b) demonstrates the damage profile after the first discharge for two different particle size distributions: i) 5.0-μm particles close to the current collector and 15.0-μm particles at the separator (denoted by dashed lines), and ii) 15.0-μm particles at current collector and 5.0-μm particles close to the separator (denoted by solid lines). Because larger particles experience enhanced mechanical degradation for both types of particle size distributions, a greater amount of microcrack density is observed wherever there exist large-sized particles. Thus, for case (i), enhanced mechanical damage occurs close to the separator. Similarly, for case (ii), evolution of higher amounts of microcrack density appears close to the current collector. It is evident from Figure 5.12(b) that the extent of damage evolution is independent of the location of the

particle. For example, particles with a radius 15.0 μm experience around 9% microcrack densities at the end of the first discharge at 4C, irrespective of whether it is located near the separator or the current collector. Similar behavior can be observed for other particle sizes operating at other C-rate conditions as well. This saturation in mechanical degradation happens because the maximum reaction front shifts from the separator to the current collector during the discharge process.

LIBs are usually operated in multiple charge-discharge cycles. Thus, it is important to investigate the evolution of microcrack density and capacity fade due to particle size distribution inside the anode. For the cycling analysis smaller magnitude of particle size distributions are taken into consideration: i) linearly increasing particle size from 2.5 μm at the current collector to 12.5 μm at the separator (denoted by black lines), and ii) linearly decreasing particle size from 12.5 μm at the current collector to 2.5 μm at

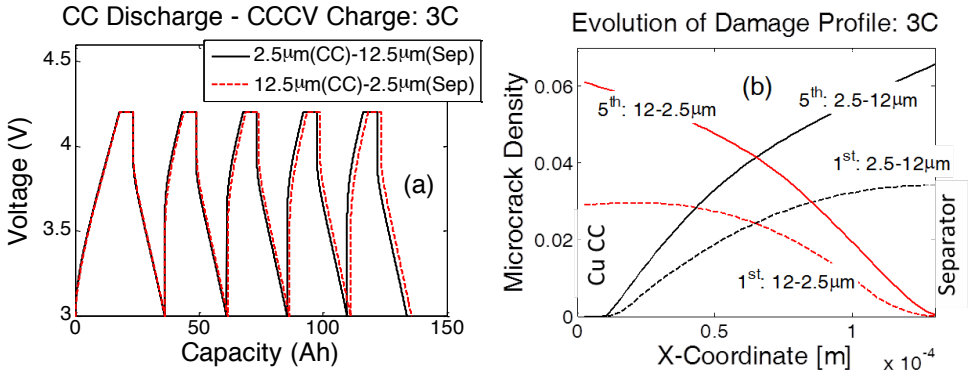

Fig: 5.13. *For cycling analysis, the two different ranges of particle sizes have been taken into consideration: i) Linearly increasing particle size from 2.5μm at the current collector to 12.5μm at the separator, and ii) Linearly decreasing particle size from 12.5μm at the current collector to 2.5μm at the separator. (a) Voltage vs. capacity curves for five CCCV charge – CC discharge cycles at 3C. After the fifth discharge at 3C, smaller particle sizes close to the separator (case (ii)) experience 0.23Ah extra capacity than large particles close to the separator (case (i)). (b) Increase in damage after five cycles at 3C. From the first to the fifth discharge cycle, the microcrack density almost doubled for large sized particles.*

the separator (denoted by red lines). For the cycling analysis, the cell is initially charged in a CCCV fashion from a very low SOC to 4.2V. Then, the LIB is operated under CC discharge–CCCV charge conditions for five subsequent cycles. The voltage vs. capacity performance curve for operation at 3C is shown in Figure 5.13(a) for both particle size distributions. The two curves almost overlap, indicating a minor difference in capacity fade observed by the two different particle size distributions. A closer look at the discharge curves for the fifth cycle shows that the particle size distribution with 2.5-μm particles close to the separator [case (ii)] leads to a capacity 0.23 Ah larger than case (i), which contains 12.5-μm particles close to the separator.

When a distribution of particle size is used, evolution of microcrack density inside the anode active particles during multiple cycles deserves investigation. Two different particle size distributions considered in this study are same as that reported in the previous paragraph; the first one involves 2.5 μm–12.5 μm particles with increasing size and the other one consists of 12.5 μm–2.5 μm particles with decreasing size from the current collector to the separator. Figure 5.13(b) demonstrates the extent of microcrack density at the end of the first and the fifth discharge process for both particle size distributions. Irrespective of the location of the particles, larger particles experience higher microcrack density. Equivalently, less mechanical degradation is observed in smaller particles. Damage observed in the active particles after the fifth discharge is almost double of what occurred in the first discharge process. The extent of microcrack density after the first discharge process reported in Figure 5.12(b) is much greater than that observed in Figure 5.13(b). This difference appears because for the single discharge

experiments, the lithium ion cells are discharged from a voltage of 4.75 V to a lower cutoff limit of 3.0 V. In contrast, during the charge-discharge cycles, at the time of the first discharge the lithium ion cells are discharged from 4.2 V to 3.0 V. Because the lithium ion cell operates in a smaller voltage range in the second case, the anode active particles experience the delithiation process for shorter amount of time. Thus, the extent of mechanical degradation is much smaller after the first discharge for multiple charge-discharge cycles.

Solid-state diffusivity depends on the local lithium concentration (i.e. SOC) . In the present study, diffusivity is assumed to be a linear function of the local lithium concentration.

$$D\left(c_s\right) = D_0 \cdot \left(1 - k_d \cdot \frac{c_s}{c_{s,\max}}\right) \tag{5.26}$$

Here, $D\left(c_s\right)$ is the concentration dependent diffusivity, D_0 is the diffusivity under zero lithium concentration, k_d is a parameter which controls how quickly the diffusivity drops with increasing concentration, c_s and $c_{s,\max}$ corresponds to the local and maximum lithium concentration, respectively. From physical considerations, for single phase materials, the value of diffusivity cannot be negative, which signifies that the magnitude of k_d will always lie between zero and one $\left(0 < k_d < 1\right)$. For the present analysis $k_d = 0.5$ has been assumed.

The effect of concentration dependent diffusivity on the performance curve has been demonstrated in Figure 5.14 for graphite anode material for two different C-rates

(1C and 3C). At higher rates of operation concentration gradient within the active particle is much larger. As a result, at 3C, concentration dependent diffusivity leads to enhanced mass transport resistance and subsequently smaller effective capacity of the cell. Addition of mechanical degradation on top of the concentration dependent diffusivity results in further increase of mass transport resistance (as shown in Figure 5.14). At low C-rate operation, small amount of microcrack formation shows little impact on the performance curve. However, at high C-rate enhanced mechanical degradation indeed affects the cell performance by increasing the mass transport resistance. Reduction in effective capacity at 3C due to mechanical degradation is evident in the red dash-dot curve of Figure 5.14.

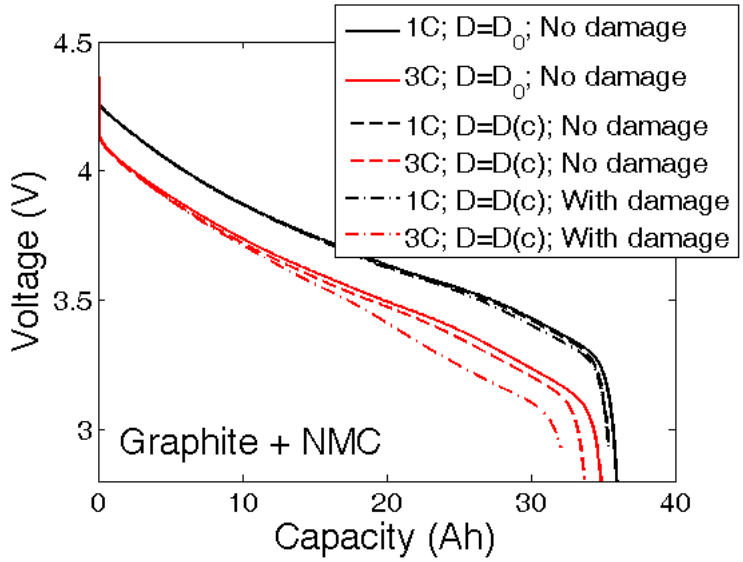

Fig: 5.14. *Performance curves for "Graphite + NMC" at two different C-rates. The solid line corresponds to the case where diffusivity is kept constant. The dash-dash line corresponds to the performance curve when diffusivity is a function of concentration. The dash-dot line signifies performance when mechanical degradation is taken into consideration. At low C-rate operation, mechanical degradation has minimal impact on overall cell performance. At high C-rate operations (3C), enhanced microcrack formation impacts the performance curve significantly.*

Most of the electrode properties used in this analysis correspond to slightly old spinel type cathode chemistries. The electrodes are assumed to be thicker $\left(L_a = L_c = 130\mu m\right)$ with higher porosity $\left(\varepsilon_a = 0.357, \varepsilon_c = 0.444\right)$ for electrolyte transport. At present, NMC or NCA based cathode chemistries are used under the condition of thinner electrode and smaller amounts of porosity for electrolyte movement. Mostly cells used in HEVs and PHEVs have a thinner electrode for high power requirements. Some simulations have been conducted to demonstrate the applicability of the developed method for thinner electrodes $\left(L_a = L_c = 80\mu m\right)$ with reduced porosity for electrolyte transport $\left(\varepsilon_a = 0.264, \varepsilon_c = 0.281\right)$. The voltage vs. capacity plots for the first discharge are reported in Figure 5.15(a). Damage profiles along the thickness of the negative electrode at the end of the discharge process are reported in Figure 5.15(b). NMC and graphite have been used as the active cathode and anode materials, respectively. Two different particle size distributions have been considered: (i) Decreasing particle size of 15μm close to the current collector to 5μm at the separator, and (ii) Increasing particle size of 5μm close to the current collector to 15μm at the separator. At lower rates of operation, such as 1C, the maximum amount of mechanical degradation is around 6% observed within the largest particles of size 15μm (see Figure 5.15(b)). Capacity for both the increasing and decreasing particle size distributions are almost the same at 1C (see Figure 5.15(a)). However, at higher rates of operation, such as 3C, two different particle size distribution leads to completely different damage profiles. For the increasing particle size distribution, microcrack density increases monotonically from the current collector to the separator (red solid line in Figure

5.15(b)). At 3C for the decreasing particle size distributions, as depicted by the red dashed line in Figure 5.15(b), microcrack density drops initially from the current collector towards the middle of the electrode. Extremely close to the separator, where 5μm sized active particles reside, the density of microcracks increase. Thus, for the decreasing particle size distribution, there exist a minimum in microcrack density somewhere in the middle of the electrode. Effective capacity of the decreasing particle size distribution is marginally larger than its increasing counterpart at high C-rate operations (red dashed and solid lines in Figure 5.15(a)). Voltage vs. capacity curve at 3C ends even before reaching the lower cutoff voltage of 3.0V. This happens due to enhanced mechanical degradation within the anode active particles close to the separator, concentration profile reaches negative values much before discharging till 3.0V. More detailed analysis of the 3D electrode microstructure must be conducted to fully understand the exact effect of thin electrodes with three or four particles along the thickness.

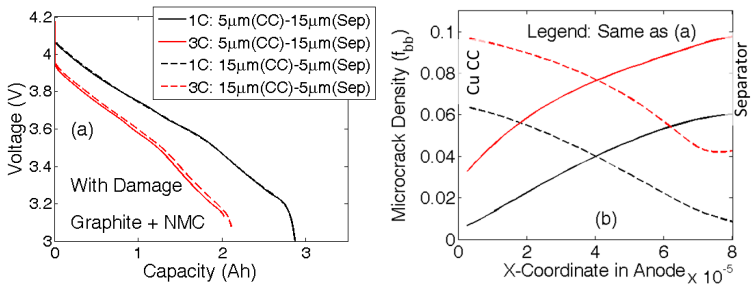

Fig: 5.15. *Analysis of performance curves and microcrack profiles for thin electrodes and small values of porosity. Two different particle size distributions are considered: (i) Increasing particle size of 5μm close to the current collector to 15μm at the separator. (ii) Decreasing particle size of 15μm close to the current collector to 5μm near the separator. (a) Voltage vs. capacity performance curves at two different C-rates (1C and 3C) and both the increasing and decreasing particle size distributions. (b) Profile of microcrack density for 1C and 3C under increasing and decreasing particle size distributions.*

5.2.3 Effect of mechanical degradation on drive cycles

Until now, all the simulations are conducted under the assumption that during operation the lithium ion cells experience complete discharge and then complete charge at a constant C-rate, and the discharge-charge cycle goes on. However, in a realistic drive cycle, the lithium ion cells rarely experience complete discharge at a constant rate. Under drive-cycle operation, discharge-charge pulses occur depending on the driving conditions. Figures 5.16(a) and 5.16(b) included here, demonstrate the C-rate experienced by LIBs in hybrid electric vehicles (HEV) and plugin-hybrid-electric-vehicles (PHEV), respectively. Positive C-rates correspond to discharging, and negative C-rates signify charging. HEVs operate mostly in a charge sustaining (CS) mode and experience equal amounts of discharge and charge pulses. The discharge-charge pulses are extremely strong and range between -10C and 20C. On the other hand, PHEVs can operate in both charge sustaining (CS) and charge depleting (CD) modes. The C-rate profile demonstrated in Figure 5.16(b) corresponds to a PHEV operating under CD condition. There exist both discharge and charge pulses in CD operations. PHEVs experience much milder discharge-charge pulses, which range between -3.5C and 6C.

Evolution of mechanical degradation under HEV and PHEV drive cycle conditions for different particle sizes is reported in Figure 5.17(a) and 5.17(b), respectively. Two different open circuit potential (OCP) profiles are used inside the anode: i) hard-carbon, and ii) graphite. The OCP of a hard-carbon anode shows a steep profile (see Figure 5.6). Thus, the reaction current density within the negative electrode remains flatter during the discharge process. In contrast, graphite has an extremely flat

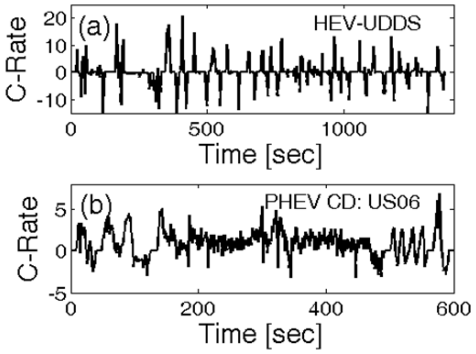

Fig: 5.16. *C-rate vs. time profiles for two different vehicles under different drive cycle conditions. (a) C-rate vs. time curve for a HEV under UDDS driving conditions. (b) C-rate vs. time curve for a PHEV operating under charge depleting (CD) US06 driving conditions.*

OCP profile. This leads to a large gradient in the reaction current density inside the anode. In the graphite anode, the active particles close to the separator experience significantly large reaction current density than those located near the current collector. Thus, mechanical degradation should be much larger near the separator for graphite than for hard-carbon materials. This trend is more prominent in Figure 5.17(b), where the hard-carbon chemistry shows a relatively flat damage profile (solid line) whereas under graphite chemistry, a steeper damage profile is observed (dashed line) while traveling from the current collector to the separator.

In both Figures 5.17(a) and 5.17(b), a lower microcrack density is observed close to the current collector, and larger microcracks appear near the separator for all the different particle sizes considered. Under drive cycle operating conditions, the lithium ion cells experience high C-rates in multiple pulses. As shown in Figure 5.10(a), at the beginning of the discharge process, a maximum reaction current is experienced close to the separator. As the discharge process continued, the maximum reaction current front shifted towards the current collector. In drive cycles, because the C-rates act in pulses,

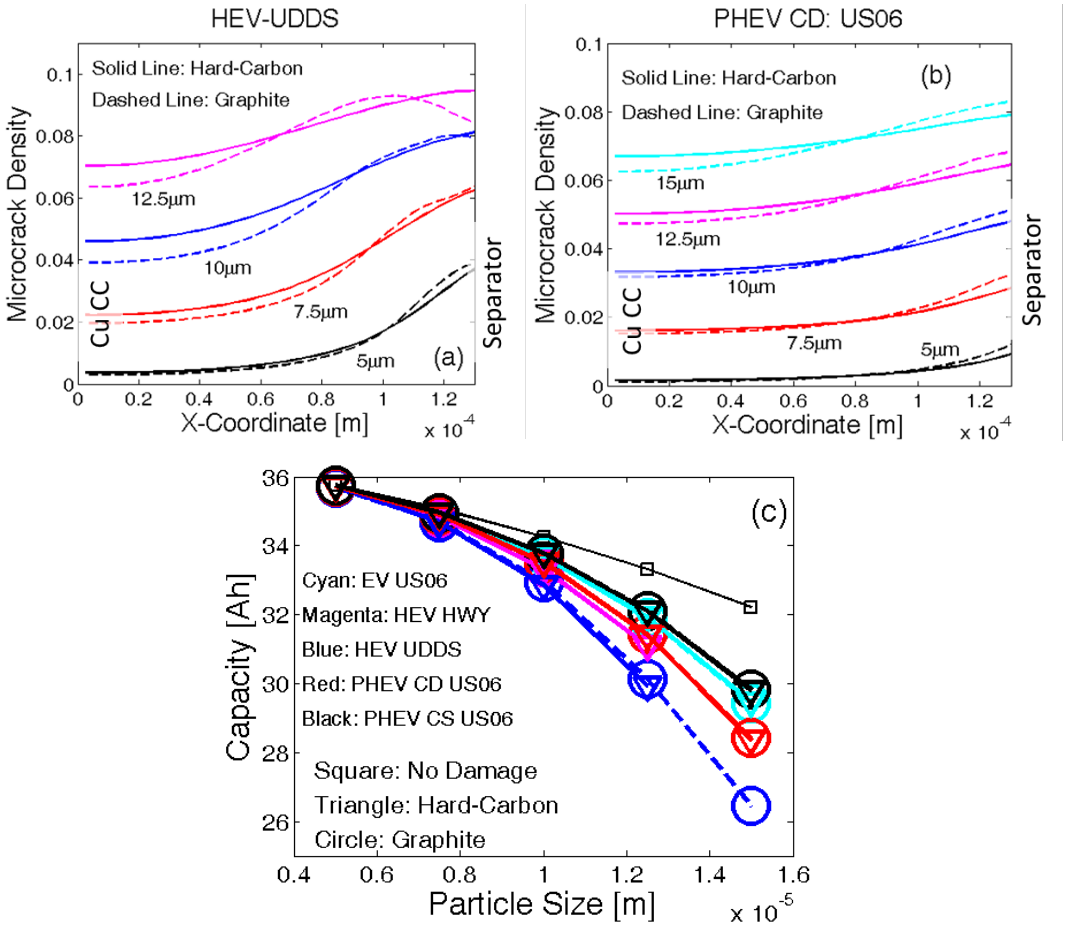

Fig: 5.17. *Investigation of damage evolution and capacity fade for different drive cycle operating conditions. Two representative drive cycle operating conditions are shown in Figure 5.16(a) and 5.16(b). (a) Final damage profile at different particle sizes for the HEV subjected to driving conditions shown in Figure 5.16(a). (b) Final damage profile at different particle sizes for the PHEV subjected to driving conditions shown in Figure 5.16(b). In both (a) and (b), enhanced damage evolution is observed close to the separator (right side) as compared to the current collector (left side of the figure). (e) Capacity fade observed in various particle sizes after operating under different drive cycle conditions. Particle sizes less than 10µm do not experience significant capacity fade due to damage evolution. Most severe capacity fade is observed for the largest particle size of 15µm.*

the maximum reaction current only acts close to the separator; it never gets the opportunity to shift towards the current collector. As a result, in drive cycle scenarios, the maximum reaction current front confines itself near the separator only. Thus, a significant gradient in mechanical degradation is observed while between the current

collector and the separator. This observation is applicable to both the hard-carbon and graphite chemistries. Because the HEV vehicles experience a much larger magnitude of C-rates [-10C to 20C, see Figure 5.16(a)], the mechanical degradation reported in Figure 5.17(a) shows a large gradient along the thickness of the electrode. For example, under HEV drive conditions, 7.5-μm particles experience only 2% microcrack density near the current collector whereas, near the separator, the mechanical degradation can be as high as 6%. The PHEVs operate under less severe C-rate conditions. Figure 5.17(b) demonstrates that for the same 7.5-μm particles, under PHEV driving conditions only 1.8% damage evolves close to the current collector, which increases to 3% microcrack density near the separator. Hence, HEV operating conditions are relatively more detrimental for the LIBs from a mechanical degradation perspective.

For 12.5-μm particles, some irregularity in the usual pattern of highest microcrack density close to the separator is observed in Figure 5.17(a). The microcrack density drops below the maximum value for the active particles located extremely close to the separator. It was argued in earlier articles (see [178]) that for extremely large active particles under very high C-rate operations, the concentration gradient confines itself very much close to the surface of the particles and cannot penetrate into the interior. Thus, the mechanical degradation is also observed close to the peripheral region only, which results in a reduction in microcrack density. Figure 5.17(a) reports the evolution of microcrack density under HEV drive cycles, where the C-rates can be as high as 20C, being applied in multiple pulses of very short duration. Under such large magnitude of C-rates, the reaction current density close to the separator will be

extremely high. For the 12.5-μm particles, the lithium concentration will mostly be confined extremely close to the surface of the particle. Due to a lack of penetration of the concentration gradient, reduced evolution of microcrack density is observed in 12.5-μm particles under HEV operating conditions at locations extremely close to the separator.

It has already been argued that the OCP profile for graphite is more flat than hard-carbon. This leads to formation of higher gradient in reaction current density along the thickness of the graphite anode. Also, as observed in Figure 5.17(b), mechanical degradation for graphite is slightly larger than that observed for hard-carbon. According to the OCP profile, due to higher gradient in reaction current density, mechanical degradation in graphite should be significantly larger than hard-carbon. However, the small difference in microcrack formation can be attributed to the fact that the mechanical degradation reaches a peak value with increasing reaction current density. Further increase in reaction current density results in reduction of microcrack density. This maximum value of microcrack density is observed due to the fact that under extremely high reaction current density, the lithium concentration gradient cannot penetrate significantly within the solid active particles. Lithium concentration remains confined close to the particle surface, resulting in reduced mechanical degradation at extremely high rates of operation. Because of the existence of a maximum amount of microcrack formation, the difference in mechanical degradation is minimal for hard-carbon and graphite anode materials.

Evolution of microcrack density inside the active particles during the drive cycles is definitely not sufficient to characterize the impact of mechanical degradation on the

performance of LIBs. Analysis of capacity fade due to the evolution of microcrack density deserves elaboration to complete the investigation process. A computational reference performance test (RPT) has been defined to characterize the amount of capacity fade under certain drive cycle conditions for different particle sizes. According to this computational RPT, the lithium ion cells are discharged at 1C from a high SOC, $x_p = 0.2$ and $x_n = 0.9$, which corresponds to a voltage usually greater than 4.5V. The CC discharge process is continued until the lower cutoff voltage limit of 3.0 V is reached. The Ahtp during the entire discharge process is reported as the capacity of the cell. Distribution of microcrack density that occurred during the drive cycle was kept constant while conducting the computational RPT test. Reduced diffusivity due to the formation of microcracks increases the resistance due to mass transport and eventually results in deterioration of the effective capacity. For different particle sizes, the net discharge capacities are reported in Figure 5.17(c). The small squares signify the magnitude of the discharge capacity without the presence of any mechanical degradation. Five different drive cycles are considered: i) an EV under US06 driving conditions (denoted by cyan lines), ii) an HEV operating on highway (magenta lines), iii) an HEV operating under Urban Dynamometer Driving Schedule (UDDS) driving conditions (blue lines), iv) a PHEV operating in CD mode on US06 (denoted by red lines), and v) a PHEV operating in CS mode (denoted by the thick black line). Both the anode chemistries of hard carbon (denoted by triangles) and graphite (denoted by big circles) have been investigated. Among all the drive cycles, the HEVs operating in UDDS driving conditions experience the maximum amount of capacity fade, solely due

to mechanical degradation. In contrast, EVs and PHEVs operate in a less severe fashion from the capacity fade perspective. Particle size also impacts the amount of capacity fade during drive cycle operations. As can be observed in Figure 5.17(c), lithium ion cells with particles less than 10.0 μm do not experience any severe capacity fade even under the HEV driving conditions. However, particles larger than 10.0μm indeed experience severe capacity fade under HEV operating conditions. For example, HEVs operating under UDDS driving conditions, experience 10% capacity fade for 12.5-μm particles and approximately 16% capacity fade for particles with radius around 15.0μm. From this analysis, it is clearly evident that usage of particles smaller than 10.0μm is beneficial for drive cycle applications.

Capacity fade due to mechanical degradation while using hard-carbon anode or graphite anode is approximately the same. But from their OCP curves, graphite is supposed to have significantly higher gradient in reaction current density along the thickness of the active particles, which would give rise to enhanced mechanical degradation. Slightly larger microcrack formation for graphite than hard-carbon anode material has already been demonstrated in Figure 5.17(a) and 5.17(b). The capacity-fade reported in Figure 5.17(c) is estimated using the computational RPT technique, where the cell is discharged at a rate of 1C. At such low rates of operation, minor spatial variation in mechanical degradation along the thickness of the electrode, does not affect the overall cell resistance. As a result, capacity-fade for both graphite and hard-carbon is almost the same. However, the overall mechanical degradation has a significant impact on the effective capacity of the electrode. It has been demonstrated in Figure 5.17(c) that

large particles experience more severe mechanical degradation and subsequently higher capacity fade, which conclusion is applicable to both the anode chemistries.

Instead of using a constant particle size throughout the thickness of the negative electrode, the impact of a gradient in particle size from the current collector to the separator on the mechanical degradation and subsequently the capacity of the lithium ion cell are worth investigating. Two different particle size distributions have been considered here: i) linearly increasing particles size from 5.0 μm close to the current collector to 15.0 μm at the separator, and ii) linearly decreasing particle size from 15.0 μm at the current collector to 5.0 μm close to the separator. Damage profiles at the end of drive cycles observed in four different types of vehicles (EV, HEV, PHEV-CD and PHEV-CS) and for two different anode chemistries (hard-carbon and graphite) are shown in Figures 5.18(a) and (b). The extent of microcrack density for increasing (5–15 μm) particle size [case (i)] is shown in Figure 5.18(a). Larger particle sizes and higher reaction current densities close to the separator significantly enhanced mechanical degradation in the active particles that are located near the separator. The magnitude of the microcrack density close to the separator can be as high as 10% under the most severe HEV operating conditions. Smaller active particles located close to the current collector rarely experience high reaction current density, and the damage evolution within them is significantly low.

The damage profile for decreasing active particle sizes from 15 μm at the current collector to 5 μm at the separator is depicted in Figure 5.18(b) at the end of four different drive cycles. Evolution of microcrack density under both hard-carbon (denoted by a

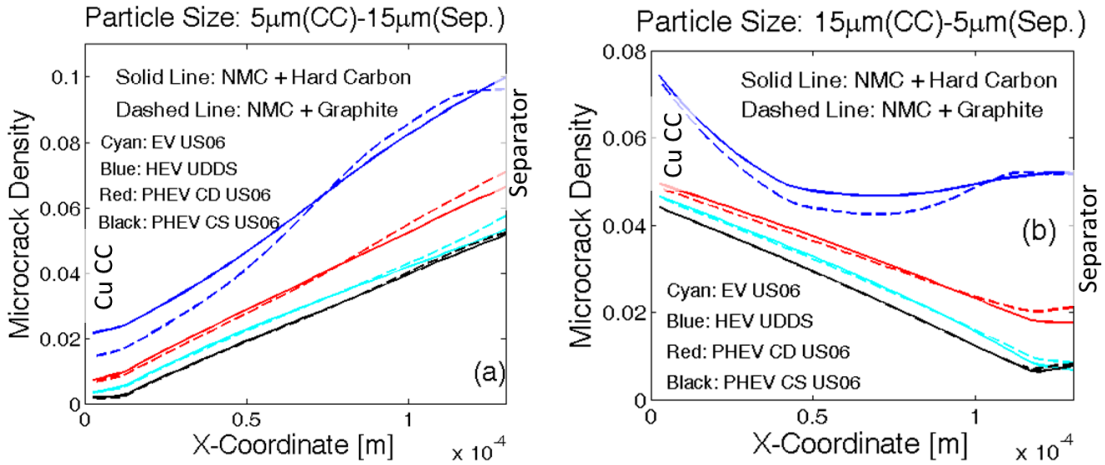

Fig: 5.18. *Instead of using uniform particle size, usage of a gradient in particle size would result in a different damage profile. Two different particle size distributions were considered: a) Linearly increasing particle size from 5μm at the current collector to 15μm at the separator, and b) Linearly decreasing particle size from 15μm at the current collector to 5μm at the separator. Four different drive cycles have been investigated for both the particle size distributions. For the drive cycles, larger rate of reaction is observed close to the separator. Thus, large particle size close to the separator leads to increased damage evolution as compared to the other case with small particle size close to the separator. Capacity analysis at 1C rate of discharge revealed that the particle size distribution with smaller particles close to the separator is capable of retaining larger amount of capacity (see Table: 5.2).*

solid line) and graphite (denoted by a dashed line) chemistries of the anode was investigated, and the damage profiles for both of them are very close to each other. It was argued earlier that under drive cycle conditions, current is extracted in pulses, and the maximum reaction front is confined to the region very close to the separator. Thus, maximum damage should happen to the particles near the separator only. However, for the decreasing particle size distribution with the smallest particles located close to the separator, less damage should occur near the separator region. Thus, for this particular case of decreasing particle size operating under drive cycle conditions, there exist competitions with regard to where the minimum amount of damage should occur. Figure 5.18(b) clearly demonstrates that the amount of damage is not the minimum extremely

close to the separator even though the smallest particles reside there. Due to the extremely high reaction current density, microcrack density evolves to a larger extent near the separator. Hence, the minimum amount of damage occurs somewhere at the interior of the negative electrode. The exact location of the minimum microcrack density depends on the drive cycle under which the battery is being operated. For example, HEVs operating under UDDS driving conditions (blue line) will experience the minimum damage somewhere close to the center of the electrode. However, for other PHEV and EV driving conditions, the minimum damage occurs near the separator somewhere at the interior of the electrode (see the red, cyan, and black lines). The active particles adjacent to the separator still experience higher microcrack density due to enhanced reaction current density. The maximum amount of damage is observed wherever the largest particles reside. For the particular case under investigation, the largest particles (15 μm) are located near the current collector. As a result, the maximum amount of damage is observed close to the current collector itself.

Table: 5.2 (a). Capacity after different drive cycle operations for two particle size distributions with "NMC + Hard Carbon" chemistry.

Name of Drive Cycle	5μm - 15μm	15μm - 5μm
No damage	34.13 Ah	34.18 Ah
Leaf, US06	33.33 Ah	33.48 Ah
HEV, HWY	32.86 Ah	33.07 Ah
HEV, UDDS	32.14 Ah	32.9 Ah
PHEV, CD, US06	33.07 Ah	33.36 Ah
PHEV, CS, US06	33.40 Ah	33.56 Ah

Table: 5.2 (b). Capacity after different drive cycle operations for two particle size distributions with "NMC + Graphite" chemistry.

Name of Drive Cycle	5μm - 15μm	15μm - 5μm
No damage	34.13 Ah	34.18 Ah
Leaf, US06	33.31 Ah	33.49 Ah
HEV, HWY	-	33.13 Ah
HEV, UDDS	32.19 Ah	32.98 Ah
PHEV, CD, US06	33.02 Ah	33.39 Ah
PHEV, CS, US06	33.39 Ah	33.56 Ah

Some knowledge about the extent of mechanical degradation is important to estimate the durability of the active particles. However, the real impact of the mechanical degradation is reflected in analyzing the capacity fade after operation under different drive cycle conditions. Computational RPT tests were conducted on both distributions of particle sizes [linearly increasing from 5 μm to 15 μm (denoted as case (i)), and linearly decreasing from 15 μm to 5μm (represented as case (ii))] after operating under five different drive cycles. The capacities obtained from the computational RPT are shown in Tables 5.2(a) and 5.2(b) for the two anode chemistries of hard-carbon and graphite, respectively. For case (ii), where 5-μm sized particles reside close to the separator, under no mechanical degradation, this distribution shows a higher magnitude of capacity (0.05 Ah larger) than its counterpart that contains 15-μm sized particles (case (i)) near the separator. Under the most severe HEV operating conditions, the particle size distribution with decreasing particle size (current collector to separator) shows 0.75 Ah larger capacity than its counterpart with increasing particle

size. This difference in capacity fade will be even more under high C-rate operations. Utilization of graphite chemistry leads to more capacity fade than that observed for hard-carbon anodes. Thus, particle size distributions with large particles close to the separator should be avoided from the perspective of mechanical degradation. Similarly, capacity fade is less severe for those distributions that contain smaller particles close to the separator.

5.3 Conclusion

A reduced order model has been developed to characterize the amount of mechanical degradation in single active particles for different particle sizes during operation under different C-rates. The reduced order model involves two different parameters, a) maximum extent of damage evolution (denoted by $A_{\max}$), and b) rate of damage evolution (denoted as m_{rate}). Evolution of microcrack density on the outer surface of the active particles impacts the surface concentration significantly. Mechanical degradation close to the center of the active particles shows a minor impact on the surface concentration. For electrochemical purposes, only the surface concentration of the active particles affects the other reactions. While developing the reduced order model, only the formation of microcracks near the particle surface during delithiation is taken into consideration. An expression of effective diffusivity has also been developed to incorporate the impact of microcrack density on the diffusivity of the active particles.

A 1D multiphysics computational framework has also been developed that can solve for the evolution of potential and concentration in a coupled fashion along the

thickness of the electrodes and the separator. Coupling between the concentration and the potential terms have been accomplished via the extremely nonlinear Butler-Volmer equation. A Taylor-series expansion has been implemented to linearize the nonlinear terms. The impact of mechanical degradation in the anode has been incorporated within the 1D electrode-level model via reduction in effective diffusivity of the solid active particles. For uniform particle sizes along the thickness of the negative electrode, under CC discharge and CCCV charge conditions mechanical damage evolves in a uniform fashion throughout the thickness of the electrode. This happens because during the discharge process, the maximum reaction current front travels along the thickness of the electrode. At the beginning of the discharge process, the maximum reaction current density is observed close to the separator; with time it shifts towards the current collector, resulting in uniform evolution of microcrack density. Evolution of microcracks on the active particles does not result in lithium loss, but increases the resistance due to transport limitations. Capacity fade due to microcrack evolution is larger for high C-rate operations. If a particle size distribution is used within the electrode, it is beneficial to place the smaller particles close to the separator and larger particles near the current collector.

If a LIB is operating under drive cycle conditions, the discharge and charge currents act as strong pulses. Due to short duration of the pulse, the maximum reaction current density front cannot move along the thickness of the electrode and remains confined close to the separator only. Thus, significantly large mechanical degradation is observed within active particles close to the separator while operating under drive cycle

conditions. Particles close to the current collector experience a smaller magnitude of reaction current density, and subsequently a reduced extent of mechanical degradation is observed there. As a result, it is always beneficial to use a distribution of particles with smaller particles close to the separator for drive cycle operations. However, for HEV applications with graphite anode active materials, due to excessively high reaction current density, maximum amount of mechanical degradation can occur somewhere in the middle of the electrode. Also, under drive cycle scenarios, the majority of the capacity fade due to microcrack formation is observed in particles greater than 10 μm in radius. Thus, it is also suggested to use anode active particles less than 10 μm in size for drive cycle applications. In this way, the impact of mechanical degradation of active particles on cell performance can be mitigated to a significant extent.

CHAPTER VI

MECHANO-ELECTROCHEMICAL STOCHASTIC ANALYSIS OF DAMAGE EVOLUTION IN HIGH-CAPACITY ELECTRODES FOR ENERGY STORAGE*

High capacity anode materials such as silicon (Si), tin (Sn) and/or germanium (Ge) experiences significant amount of volume expansion during lithium insertion through some form of alloying reaction. Usage of high specific-capacity anode materials within lithium ion batteries is desired because of achieving large energy density. However, these alloying anode materials experience significant fracture due to the evolution of large concentration gradient (at the two phase interface) and high volume expansion (at the particle surface) induced load. A computational methodology has been developed that can capture both the modes of mechanical degradation.

6.1 Computational methodology

In a realistic lithium ion battery electrode, both cathode and anode consists of multiple phases, separated by a porous polymeric separator [3]. Diffusion and migration of lithium ions occur from anode to cathode during the discharge process. Transport of lithium ions occur in the opposite direction (cathode to anode) during the charge process. Lithium ions combine with electrons at the active particle – electrolyte interface, and get stored within the solid active materials as lithium atoms [4]. Lithium transport inside the solid phase occur via either single-phase or two-phase diffusion process according

*Under preparation: "Mechano-electrochemical stochastics of damage evolution in high-capacity electrodes for energy storage" by P. Barai and P. P. Mukherjee (for submission)

to whatever is more feasible based on thermodynamics [121]. For example, graphite and hard-carbon based anode active materials store lithium ions through single-phase diffusion process [29]. Lithium iron phosphate ($LiFePO_4$) and lithium cobalt oxide ($LiCoO_2$) based cathode active particles display transport of lithium via multi-phase diffusion process [185, 186]. Inside high capacity anode materials, such as, silicon (Si) and tin (Sn), diffusion of lithium occurs through the formation of multiple phases within the active particle [42, 121, 187].

In the present article, transport of lithium within high capacity anode materials, volume expansion due to large amount of lithium insertion and finally, microcrack formation due to concentration gradient and large volume expansion have been modeled. To maintain simplicity of the computational framework, transport of lithium inside the anode active material has been assumed to occur via a two-phase diffusion process [139]. Fick's law of diffusion is only applicable to single phase diffusion process. In high capacity anode materials, two-phase diffusion is modeled by solving the Cahn-Hilliard equation, which is provided below [139, 188]:

$$\frac{\partial \hat{c}_s}{\partial t} = \nabla \cdot M_{Li}\left(\hat{c}_s\right)\nabla\left\{c_{s,\max}RT\left[\omega\left(1-2\hat{c}_s\right)+\ln\frac{\hat{c}_s}{1-\hat{c}_s}\right]-\kappa\nabla^2\hat{c}_s\right\} \tag{6.1}$$

$$\left.\frac{\partial \hat{c}_s}{\partial r}\right|_{r=0} = 0 \tag{6.2}$$

$$M_{Li}\left(\hat{c}_s\right)\nabla\left\{c_{s,\max}RT\left[\omega\left(1-2\hat{c}_s\right)+\ln\frac{\hat{c}_s}{1-\hat{c}_s}\right]-\kappa\nabla^2\hat{c}_s\right\}\Bigg|_{r=1} = \frac{I_{applied}}{SF} \tag{6.3}$$

Here, $\hat{c}_s$ is the non-dimensional concentration variable that is defined as, $\hat{c}_s = \frac{c_s}{c_{s,\max}}$, where c_s signifies the molar concentration of lithium within the active material and $c_{s,\max}$ corresponds to the maximum amount of lithium that can be stored within the active particles. M_{Li} is the concentration dependent mobility of lithium within the solid phase that is defined as, $M_{Li} = \frac{D_{Li}}{c_{s,\max} RT}\left(\hat{c}_s\left(1-\hat{c}_s\right)\right)$, where, D_{Li} corresponds to the diffusivity of lithium, R is the universal gas constant and T signifies the temperature in Kelvin units. Also, ω is a non-dimensional parameter, which physically signifies the enthalpy of mixing, and mathematically produces the double well in the free energy functional. The parameter κ takes into account the contribution to the free energy at the phase boundary due to large concentration gradient at the two-phase interface. From the expression provided in Eq. (6.1), it is clear that the equation is a fourth order equation. To simplify the problem, Eq. (6.1) has been divided into two second order equations, and both the equations are solved in a fully-coupled fashion [188]. Since the particles are assumed to be spherical in shape, lithium concentration only along the radial direction is solved. From the boundary condition given in Eq. (6.2), at the center of the active particle, symmetry boundary condition is applied. Constant flux boundary condition is applied at the particle surface, magnitude of which depends on the applied current (also shown in Eq. (6.2)). Details of how this complicated fourth order transient differential equation is solved have been provided below.

While solving for the diffusion of lithium within solid spherical active particles, variation in concentration only along the radial direction is taken into consideration [188]. Lithium concentration along the azimuthal directions is assumed to be symmetric. Thus the fourth order governing differential equation can be simplified into two second order governing differential equations along the radial direction [188]:

$$\frac{\partial \hat{c}_s}{\partial t} = \frac{1}{r^2}\frac{\partial}{\partial r}\left(M_{Li} r^2 \frac{\partial \mu}{\partial r} \right) \tag{6.4}$$

$$\mu = c_{s,\max} RT \left[\ln\left(\frac{\hat{c}_s}{1-\hat{c}_s} \right) + \omega\left(1-2\hat{c}_s\right) \right] - \frac{\kappa}{r^2}\frac{\partial}{\partial r}\left(r^2 \frac{\partial \hat{c}_s}{\partial r} \right) \tag{6.5}$$

The second boundary condition on the surface of the particle also simplifies to:

$$-M_{Li} \left. \frac{\partial \mu}{\partial r} \right|_{r=1} = \frac{I_{applied}}{SF} \tag{6.6}$$

Backward Euler time integration is implemented for integrating Eq. (6.4) over time [139]. The governing differential equation is solved using finite difference scheme. The second order terms are discretized using central differencing scheme because of higher accuracy. In the discretization process, n signifies the time step, k stands for the iteration number and i corresponds to the spatial steps. $n-th$ time step is the previous known time step and $(n+1)-th$ time step is the unknown that we are solving for. The previous iteration is denoted as $k-th$ iteration and the present iteration is represented by $(k+1)-th$. The final discretized expression for both Eq. (6.4) and (A2) are written as:

$$\hat{c}_{s,i}^{n+1} - \mu_{i+1}\left\{\frac{\Delta t\cdot\left(M_{Li,i+1}^{n+1,k} - M_{Li,i-1}^{n+1,k}\right)}{4\left(\Delta r\right)^2} + M_i^{n+1,k}\cdot\left(\frac{\Delta t}{2\left(\Delta r\right)r_i} + \frac{\Delta t}{\left(\Delta r\right)^2}\right)\right\} + \mu_i\left\{M_{Li,i}^{n+1,k}\cdot\frac{2\Delta t}{\left(\Delta r\right)^2}\right\}$$
$$- \mu_{i-1}\left\{-\frac{\Delta t\cdot\left(M_{i+1}^{n+1,k} - M_{i-1}^{n+1,k}\right)}{4\left(\Delta r\right)^2} + M_{Li,i}^{n+1,k}\cdot\left(-\frac{\Delta t}{2\left(\Delta r\right)r_i} + \frac{\Delta t}{\left(\Delta r\right)^2}\right)\right\} = \hat{c}_{s,i}^{n} \tag{6.7}$$

$$\mu_i + \hat{c}_{s,i+1}^{n+1}\left\{\frac{\kappa}{2r_i\left(\Delta r\right)} + \frac{\kappa}{\left(\Delta r\right)^2}\right\} + \hat{c}_{s,i}^{n+1}\left\{2\omega c_{s,\max}RT - \frac{2\kappa}{\left(\Delta r\right)^2}\right\} +$$
$$\hat{c}_{s,i-1}^{n+1}\left\{-\frac{\kappa}{2r_i\left(\Delta r\right)} + \frac{\kappa}{\left(\Delta r\right)^2}\right\} = c_{s,\max}RT\left\{\ln\frac{\hat{c}_{s,i}^{n+1,k}}{1-\hat{c}_{s,i}^{n+1,k}} + \omega\right\} \tag{6.8}$$

Implementation of the boundary condition is conducted as follows:

$$c_{s,1}^{n+1} = c_{s,2}^{n+1} \qquad \text{at } r = 0 \tag{6.9}$$

$$\mu_{Nr+1} - \mu_{Nr} = -\frac{I_{applied}}{SFM_{Li,Nr+1}^{n+1,k}} \qquad \text{at } r = 1 \tag{6.10}$$

Here, the mobility term is defined as:

$$M_{Li,i}^{n+1,k} = \frac{D_{Li}}{c_{s,\max}RT}\hat{c}_{s,i}^{n+1,k}\left(1-\hat{c}_{s,i}^{n+1,k}\right) \tag{6.11}$$

Both the discretized Eq. (6.7) and (6.8) along with the boundary conditions (6.9) and (6.10) are solved in a fully coupled fashion to obtain the evolution of lithium concentration along the radial direction.

Another important point to be noted here is the fact that effect of mechanical volume expansion has not been accounted for in the two-phase diffusion process [142]. The main aim of this article is to capture the mechanical degradation in terms of crack formation and propagation under concentration gradient and large volume expansion induced load. Effect of mechanical degradation on the diffusion process is expected to

impact the overall concentration gradient as well as successive crack propagation, but to a relatively minor extent. Also, change in cell performance due to larger volume expansion and degradation is not being investigated here. Hence, neglecting the effect of mechanical deformation on lithium diffusion is justified. Solution of two-phase diffusion process coupled with large volume expansion will be reported in a future article.

The main purpose of this article is to capture the evolution of mechanical degradation within high capacity anode active materials during lithiation-delithiation process. A lattice spring based computational methodology was developed by the authors earlier to capture the formation of microcracks in low volume expansion anode materials (such as, graphite) [85, 139, 178]. A new lattice spring based methodology has been developed to incorporate the effect of large volume expansion observed in high capacity anode materials (such as, Si and Sn). Two different types of external load acts on the high capacity anode materials [147]: a) Large concentration gradient at the two phase interface, and, b) Excessive volume expansion due to severe lithium insertion. A combination of these two types of diffusion induced stress results in formation and propagation of spanning cracks within Si and Sn anode active particles. While solving this problem, large displacement and large strain of the active particle has been assumed [189]. An updated lagrangian based lattice spring methodology has been developed that can predict the large volume expansion and fracture, simultaneously. The governing differential equation adopted to solve this problem is [189]:

$$\int_{{}^{t}V} {}_{t}^{t+\Delta t}S_{ij}\,\delta\,{}_{t}^{t+\Delta t}\varepsilon_{ij}\,d\,{}^{t}V - \int_{{}^{t}A} {}_{t}^{t+\Delta t}F_{i}\,\delta\,{}_{t}^{t+\Delta t}u_{i}\,d\,{}^{t}A = {}^{t+\Delta t}R \tag{6.12}$$

Here, ${}^{t}V$ and ${}^{t}A$ corresponds to the volume at the previous equilibrium configuration, ${}^{t+\Delta t}_{t}S_{ij}$ is the 2nd Piola-Kirchhoff stress tensor, ${}^{t+\Delta t}_{t}\varepsilon_{ij}$ is the Green-Lagrange strain tensor, ${}^{t+\Delta t}_{t}F_{i}$ is the externally applied force, ${}^{t+\Delta t}_{t}u_{i}$ is the displacement and ${}^{t+\Delta t}R$ is the residual. On the LHS, the first term indicates the internal energy and the second term signifies the energy due to externally applied forces. In the present problem, there is no externally applied force and the entire load comes from concentration gradient induced body force. We try to minimize the residual term under any externally applied loading conditions. Minimizing the residual indicates that all the external forces should be balanced by internal forces. The Green-Lagrange strain tensor is written in an expanded form as [190]:

$$ {}^{t+\Delta t}_{t}\varepsilon_{ij} = \frac{1}{2}\left(\frac{\partial\, {}_{t}u_{i}}{\partial x_{j}} + \frac{\partial\, {}_{t}u_{i}}{\partial x_{j}} + \frac{\partial\, {}_{t}u_{k}}{\partial x_{i}} \frac{\partial\, {}_{t}u_{k}}{\partial x_{j}} \right) \tag{6.13} $$

Here, summation over repeated exponent is implied. ${}_{t}u_{i}$ signifies the incremental displacement from time step t to $t+\Delta t$ and x_{j} corresponds to the spatial location. For the updated lagrangian lattice spring model being investigated here, the strain-displacement kinematic relations and stress-strain constitutive relations should be modified such that they are applicable to one-dimensional spring elements. To constraint the rotational rigid body mode, some shear resistance has also been added to each of the springs. However, only small strain assumption is used along the transverse direction. Large strain is allowed to occur only along the axial direction. Details of how to

incorporate the strain-displacement and stress-strain relations into the governing differential equation and construct the stiffness matrix will be discussed below.

In this article mechanical degradation along the cross section of a spherical particle has been investigated. Hence, mechanical deformation occurs in a 2D plane. Displacement in both "x" and "y" direction should be taken into consideration. The lattice springs are 1D element, but they can be oriented in any direction to take into consideration the effect of 2D geometry. Displacement of these elements along both "x" and "y" directions will be taken into account. In a local coordinate frame, suppose "x" signifies the local axial direction and "y" signifies the local transverse direction, which is also perpendicular to the local axis. Since the aim of the solution process is to minimize the residual, or make the residual zero, the governing equation can be modified for the lattice spring elements and written as [189]:

$$\int_{{}^{t}V}\left[{}^{t+\Delta t}_{t}S_{xx}\cdot\delta\frac{1}{2}\left(\frac{\partial_{t}u}{\partial x}+\frac{\partial_{t}u}{\partial x}+\left(\frac{\partial_{t}u}{\partial x}\right)^{2}+\left(\frac{\partial_{t}v}{\partial x}\right)^{2}\right)+{}^{t+\Delta t}_{t}S_{xy}\cdot\delta\frac{1}{2}\left(\frac{\partial_{t}v}{\partial x}\right)\right]d{}^{t}V=0 \qquad (6.14)$$

The equation given above only takes into account the axial stress $\left({}^{t+\Delta t}_{t}S_{xx}\right)$ and shear stress $\left({}^{t+\Delta t}_{t}S_{xy}\right)$ due to the transverse displacements. Here, x denotes the local axial direction, ${}_{t}u$ signifies the axial displacement and ${}_{t}v$ corresponds to the displacement along the transverse direction. All the displacements are incremental in nature. Applying the variation over all the displacement terms:

$$\int_{{}^{t}V}\left[{}^{t+\Delta t}_{t}S_{xx}\cdot\left(\frac{\partial\delta_{t}u}{\partial x}+\left(\frac{\partial_{t}u}{\partial x}\frac{\partial\delta_{t}u}{\partial x}\right)+\left(\frac{\partial_{t}v}{\partial x}\frac{\partial\delta_{t}v}{\partial x}\right)\right)+\frac{1}{2}{}^{t+\Delta t}_{t}S_{xy}\cdot\left(\frac{\partial\delta_{t}v}{\partial x}\right)\right]d{}^{t}V=0 \qquad (6.15)$$

Separating out the linear and the nonlinear components, the equation mentioned above can be written in a vector/matrix form as:

$$\int_{{}^{t}V}\begin{bmatrix} {}^{t+\Delta t}_{\ t}S_{xx} & \frac{1}{2}\,{}^{t+\Delta t}_{\ t}S_{xy} \end{bmatrix}\begin{bmatrix} \frac{\partial \delta_{\ t} u}{\partial x} \\ \frac{\partial \delta_{\ t} v}{\partial x} \end{bmatrix} d\,{}^{t}V + \int_{{}^{t}V} {}^{t+\Delta t}_{\ t}S_{xx}\begin{bmatrix} \frac{\partial_{\ t} u}{\partial x} & \frac{\partial_{\ t} v}{\partial x} \end{bmatrix}\begin{bmatrix} \frac{\partial \delta_{\ t} u}{\partial x} \\ \frac{\partial \delta_{\ t} v}{\partial x} \end{bmatrix} d\,{}^{t}V = 0 \tag{6.16}$$

The first integral on the left hand side gives rise to the linear stiffness matrix and the second integral forms the nonlinear component of the stiffness matrix. Derivatives of the axial displacement $\left(u\right)$ and the transverse displacement $\left(v\right)$ along the axial direction can be written as [190]:

$$\frac{\partial_{\ t} u}{\partial x} = \frac{{}_{t}u_2 - {}_{t}u_1}{l} \qquad \text{and} \qquad \frac{\partial_{\ t} v}{\partial x} = \frac{{}_{t}v_2 - {}_{t}v_1}{l} \tag{6.17}$$

Here, ${}_{t}u_1$ and ${}_{t}u_2$ are the axial displacement of node 1 and 2, ${}_{t}v_1$ and ${}_{t}v_2$ are the transverse displacement of node 1 and 2, and l is the current length of the lattice spring element. The local displacements can be written in terms of global displacement components using the coordinate transformation matrix:

$$\vec{u} = \left[T\right]\cdot\vec{U} \tag{6.18}$$

Here, $\vec{u}$ is the local displacement vector and $\vec{U}$ corresponds to the global displacement vector. The rotation matrix $\left(\left[T\right]\right)$ mentioned in the previous equation can be written in terms of the angle $\left(\theta\right)$ the element makes with the x-axis of the global reference frame:

$$[T]=\begin{bmatrix} \cos\theta & \sin\theta & 0 & 0 \\ -\sin\theta & \cos\theta & 0 & 0 \\ 0 & 0 & \cos\theta & \sin\theta \\ 0 & 0 & -\sin\theta & \cos\theta \end{bmatrix} \tag{6.19}$$

Since the rotation matrix $[T]$ is orthogonal in nature, multiplication of $[T]$ with its transpose gives rise to an identity matrix. Hence, the nonlinear term in Eq. (6.16) does not show any dependence on the rotational configuration of the spring element.

The axial and shear strains are written in terms of the axial displacement $(u_a = \Delta l)$ and shear displacement $(u_t = {}_t v_2 - {}_t v_1)$ as:

$${}^{t+\Delta t}_{t}\varepsilon_{xx} = \frac{u_a}{l} + \frac{1}{2}\left[\left(\frac{u_a}{l}\right)^2 + \left(\frac{u_t}{l}\right)^2\right] \qquad \text{and} \qquad {}^{t+\Delta t}_{t}\varepsilon_{xy} = \frac{1}{2}\frac{u_t}{l} \tag{6.20}$$

Here, the magnitude of Δl is obtained from Eq. (6.24) given in the main text. However, in Eq. (6.24), while calculating the total length, the most updated x and y coordinates are used. In Eq. (6.21), to obtain the normal component of the 2nd Piola-Kirchhoff stress, the axial strain is multiplied with the Young's modulus. In that expression, complete nonlinear form of the axial strain is taken into consideration. However, in Eq. (6.16), to maintain linearity of the first integral in the left hand side (which also gives rise to the linear component of the stiffness matrix), the nonlinear components in the axial strain term is neglected. This does not affect the overall solution because during the residual calculation, correct expression of the normal strain is being used [189]. Minor modification in the stiffness matrix makes the convergence of the final solution slightly slower.

The constitutive relation plays a major role in determining the amount of mechanical deformation as well as degradation of the active particles. Material specific properties should be taken into consideration while developing constitutive relations applicable to different high capacity anode materials. For example, silicon (Si) deforms elastically till rupture for both the non-lithiated crystalline as well as lithiated amorphous phases. However, deformation of tin (Sn) in the non-lithiated crystalline phase occurs as a ductile process, whereas, brittle deformation is observed for the lithiated amorphous phase. In the present article, results of two-phase diffusion and successive mechanical degradation will be generated for a Si anode active particle. Hence, only linear elastic relation between second Piola-Kirchhoff stress and Green-Lagrange strain along the axial direction is taken into consideration [189, 190]:

$$ {}^{t+\Delta t}_{t}S_{11} = E \cdot {}^{t+\Delta t}_{t}\varepsilon_{11} \tag{6.21} $$

Here, "11" corresponds to the local "xx" or axial direction and E signifies Young's modulus along the axial direction, which displays different magnitude for the crystalline and amorphous phase. Presence of plastic flow during lithiation within the Si active particles has been reported in some literature, but detailed investigation of those cases is out of the scope of this article.

Depending on the free energy functional and the magnitude of the enthalpy of mixing term (ω), which is already incorporated within Eq. (6.1), there exist two levels of concentration where minimum energy is observed [139]. The lower concentration level $(\hat{c}_s = 0.128)$ signifies lithium poor phase, whereas, the higher magnitude of

concentration $\left(\hat{c}_s = 0.872\right)$ corresponds to lithium rich phase. Since each of the lithium poor and rich phases belong to equilibrium configurations, as soon as lithium poor or lithium rich phase gets generated, it can be assumed to be a stress free configuration. Initially the entire active particle is assumed to be in the lithium poor phase, which is free from internal stresses. Lithiation is supposed to occur as constant influx of lithium ions through the surface of the spherical active particle. As soon as the surface of the active particle reaches the lithium rich phase, it becomes free from any internal stresses (because the lithium rich phase is an equilibrium configuration). Under subsequent lithiation, the two-phase front moves inward and pushes the lithium rich phase along the outer direction [139]. Inward traversal of the two phase front results in high volume expansion, and subsequent outward movement of the lithiated phase generates tensile stress near the surface [147]. The lithium poor phase adjacent to the lithium rich phase experiences severe tension due to large concentration gradient associated with the two-phase boundary [14].

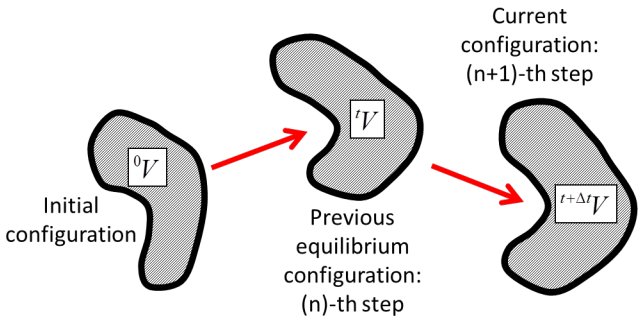

$$u^{total} = u^{elastic} + u^{chemical} \qquad \varepsilon^{total} \neq \varepsilon^{elastic} + \varepsilon^{chemical}$$

Fig: 6.1. *Schematic diagram of the updated lagrangian framework adopted in this study to incorporate the large volume expansion within the lattice spring network. Instead of strain, additive decomposition of the displacements has been adopted here.*

The next important aspect that should be discussed is the incorporation of concentration induced stress and subsequent deformation. In the present context, transport of lithium and mechanical deformation has been solved in an incremental fashion [189]. The equilibrium concentration of the lithium poor phase and the lithium rich phase are assumed to be the stress free configurations. Insertion of lithium results in additional concentration induced strain [139, 147]. Under a small time increment, at a particular point the change in concentration can be given as $\Delta\hat{c}_s$. If the volume expansion coefficient is defined as Ω and $l_{elastic}$ is the length of the spring element only due to elastic deformation, then the total length can be described as [190]:

$$l_{elastic} + \left(l_{elastic} \cdot \Delta\hat{c}_s \cdot \Omega \cdot c_{s,\max} \right) = l_{total} \tag{6.22}$$

$$\therefore \; l_{elastic} = \frac{l_{total}}{1 + \left(\Delta\hat{c}_s \cdot \Omega \cdot c_{s,\max} \right)} \tag{6.23}$$

For small deformation problems, the elastic length $l_{elastic}$ for the second term in the left hand side of Eq. (6.22) can be assumed to be equal to the initial length. However, for the case where large volume expansion is involved, the elastic length becomes significantly different from the initial one. A schematic representation of the different configurations is provided in Figure 6.1. A methodology to calculate the elastic length is derived in Eq. (6.23). Axial deformation which gives rise to internal stress can be estimated as [189]:

$$\Delta l = l_{elastic} - L \tag{6.24}$$

Here, Δl signifies the change in length and L corresponds to the spring length at the previous equilibrium configuration. Diffusion of lithium ion inside the active particle is a

transient process. Thus a time dependent equation has been solved in Eq. (6.1). But the mechanical equilibrium can be achieved as soon as slight change in lithium concentration occurs [18]. Hence the quasistatic mechanical equilibrium equation has been solved in Eq. (6.12), and any dependence on the time variable is neglected.

Along with estimation of large volume expansion, evolution of microcrack within the active particle is also another important aspect of this article. A lattice spring based methodology was developed by the authors to capture the damage propagation in low volume expansion anode materials. In the present context, similar energy based criterion has been developed to capture the formation and propagation of microcracks within high capacity anode active particles. Since the concentration gradient and high volume expansion induced load is applied in an incremental sense, the energy in each lattice spring element is also calculated in an additive fashion. If the strain energy for a particular spring element $\left("e"\right)$ at the current time step $\left(n+1\right)$ is denoted as ψ_e^{n+1}, it can be written in terms of the strain energy after the previous equilibrium step $\left(\psi_e^n\right)$ as [85]:

$$\psi_e^{n+1} = \psi_e^n + \frac{1}{2}\Delta\vec{f}\cdot\Delta\vec{u} \tag{6.25}$$

Here, $\Delta\vec{f}$ and $\Delta\vec{u}$ corresponds to the incremental internal force and displacement of the lattice spring element, respectively. If the energy in a particular spring exceeds its fracture threshold $\left(\psi_e^{n+1} > \psi_{e,t}\right)$, the spring is assumed broken and irreversibly removed from the lattice spring network. For the subsequent load increments, the effect of the broken element is entirely removed from the stiffness matrix. The load that was being carried by the broken element gets distributed among the neighboring lattice springs,

which eventually gives rise to the stress concentration effect around the tip of a spanning crack. Subsequent rupture of elements from the lattice spring network gives rise to the evolution of microcrack and eventually nucleation of these microcracks results in the formation of spanning cracks [139, 178]. Demonstration of crack formation and propagation during the lithiation process will be provided later in the Results and Discussion section. Comparison with experimentally observed results will also be discussed there.

6.2 Numerical procedure

After calculating the concentration profile, it is applied on top of a Si active particle. Response of the particle against the diffusion induced load is analyzed. The Si active particles are modeled using the modified lattice spring elements. It successfully takes into account the large deformation experienced by high capacity anode materials. The size of the lattice spring network used to model a single active particle should be large enough to successfully capture the continuum behavior of the material. Extremely small size of the lattice spring network renders wrong results. Increasing the size of the network will indeed produce more accurate results. But the computational time required to conduct the analysis will increase significantly for very large lattice-spring systems. Thus an optimum size of the lattice spring network must be identified that will give a reasonably accurate result under acceptable amount of computational time. Figure 6.2 demonstrates an analysis showing the effect of increasing lattice-spring system size on the ratio of final particle radius over initial particle radius at the end of lithiation process. The partial molar volume assumed in this particular analysis is $\Omega \cdot c_{s,\max} = 0.6$. The

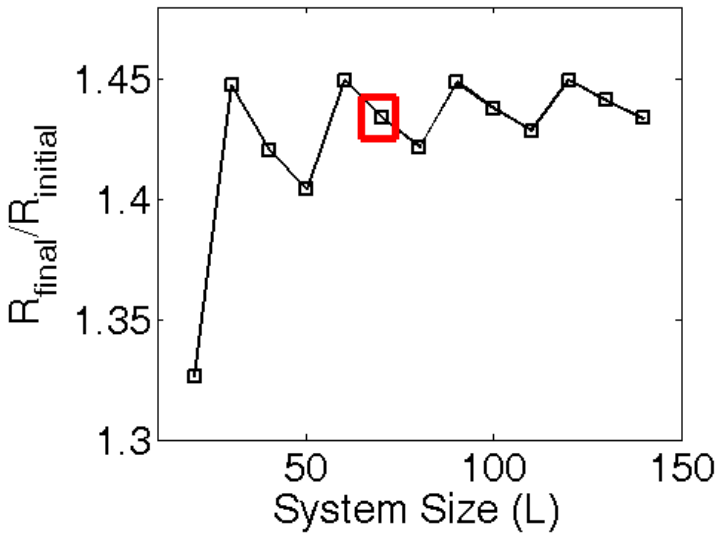

Fig: 6.2. *Evaluation of the system size dependence for the triangular mesh adopted in this study under large deformation conditions.* $\Omega \cdot c_{\max} = 0.6$ *and initial particle radius* $R_{initial} = 1.0 \mu m$ *have been adopted for this analysis. It is evident that deformation experienced by a particle tends to converge to a particular value with increasing system size. To keep the computational expense within reasonable limits,* $L = 70$ *has been considered for all the simulations reported in this article.*

initial particle radius considered for this study is $R_{initial} = 0.5 \mu m$. No mechanical degradation has been considered in this analysis of system size independence. It is evident from Figure 6.2 that with increasing system size, the ratio $R_{final} / R_{initial}$ converges to a particular value. However, for lattice spring systems of size $L = 90$ or greater, the computational expense to construct and solve the stiffness matrix for a single particle becomes excessively large. Thus $L \geq 90$ is not suitable for simulation of mechanical degradation within active particles. The ratio of final over initial radius for $L = 70$ resides close to the final converged solution, which is highlighted using a red box in Figure 6.2. The computational time requirement is also not excessively large for a

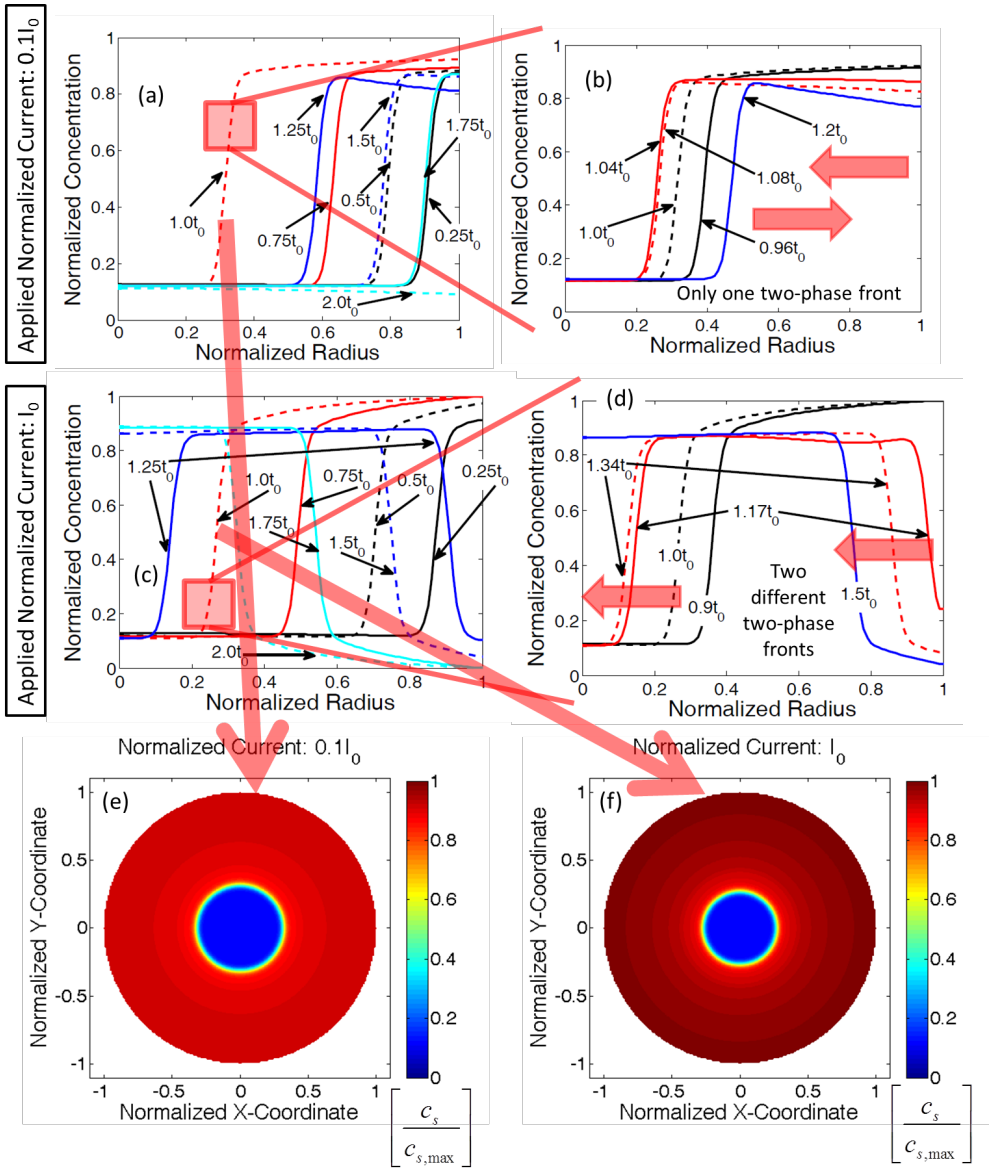

Fig: 6.3. *Evolution of concentration profile within silicon (Si) active particles. Lithiation happens between normalized time* 0.0 *and* $1.0t_0$. t_0 *is the normalized time at which lithiation completes. Delithiation occurs between* $1.0t_0$ *and* $2.0t_0$. *(a) Evolution of concentration profile and the two-phase front under low rates of current. (b) A zoomed in view of the movement of phase front close to* t_0 *under low rates of current. (c) Evolution of concentration profile and the two-phase front under high rates of current. (d) A zoomed in view of the movement of the phase front close to* t_0 *under high rates of current. (e) Contour plot of concentration profile under low rates of current at the end of lithiation process. (f) Contour plot of concentration profile under high rates of current at the end of lithiation process.*

70×70 lattice-spring network. Hence, all the computational analysis of mechanical degradation that will be conducted in the subsequent sections of this article will use $L = 70$ as the size of the lattice-spring network. The list of parameters used for the final simulation is also provided in Table: 6.1.

6.3 Results and discussion

The computational methodology developed above has been applied to analyze the two-phase transport of lithium ions within Si active particles (from Eq. (6.1)). Subsequent mechanical degradation during lithiation-delithiation phenomena has also been investigated (from Eq. (6.12)-(6.24)). The mechanical and transport properties of silicon (Si) is provided in Table: 6.1. All the properties have been inherited from existing articles that analyzed the mechanical properties [191], fracture strength [192] and transport phenomena within silicon active particles [139, 193].

In these particular simulations, transport of lithium happens within the active particles in a two-phase diffusion process. The concentration gradient at the two-phase interface applies some diffusion-induced load on the active particles, but that load is not sufficient for creating significant amount of mechanical degradation in Si anodes [42]. As lithiation continues, the two-phase interface moves inward and due to extremely high volume expansion, pushes the lithium rich surface of the active particle along the radially outward direction. Outward movement of the lithium rich phase induces tensile stress on the particle surface, which leads to initiation of crack fronts [147]. Hence, evolution of concentration gradient followed by large volume expansion acts as the loading factor and mechanical degradation is the effect. To correctly understand the

microcrack formation, it is necessary to properly realize how the concentration of lithium changes within the Si active particle.

Figure 6.3 shows the variation in lithium concentration within spherical silicon active particle during lithiation and successive delithiation process. Figure 6.3(a) and 6.3(b) demonstrates the evolution of lithium concentration under a relatively slow $\left(0.1I_0\right)$ rate of externally applied current. Radius of the active particle considered in this simulation is around 100nm. Under constant flux prescribed boundary condition, the concentration at the particle surface increases from lithium poor phase to lithium rich phase. The two phase front that gets generated moves inward along the radial direction during subsequent lithiation process. Figure 6.3(a) depicts that from time $0.0\cdot t_0$ to $1.0\cdot t_0$, the lithiation phenomenon occurs. From time $1.0\cdot t_0$ to $2.0\cdot t_0$, the delithiation process takes place. Under low rates of current, a single two-phase front develops, which moves inward during the lithiation process and comes out at the time of delithiation. A more detailed description of what happens close to the time $1.0\cdot t_0$ where transition from lithiation to delithiation occurs is portrayed in Figure 6.3(b). The time range between $0.96\cdot t_0$ and $1.2\cdot t_0$ have been emphasized here. As shown in Figure 6.3(b), even though the lithiation process stops at $1.0\cdot t_0$ (black dashed line in Figure 6.3(b)), the two-phase front moves inward till $1.04\cdot t_0$ (red solid line in Figure 6.3(b)). It should be noted that delithiation occurs during the time interval of $1.0\cdot t_0$ and $1.04\cdot t_0$ from the surface of the active particle. Then at $1.08\cdot t_0$ (red dashed line), the two-phase front changes its direction of movement and starts to traverse outward. Subsequent delithiation from the

surface of the active particle causes the two-phase front to move along the radially outward direction. The lithium concentration at the particle surface can deplete significantly with respect to the equilibrium concentration of the lithium rich phase (solid blue line that corresponds to $1.2 \cdot t_0$) during the delithiation process. However, the particle surface still remains in the lithium rich phase.

Figure 6.3(c) and 6.3(d) demonstrates how the lithium ion concentration changes inside a spherical silicon active particle of radius 100nm during fast lithiation and delithiation phenomena. The magnitude of applied normalized current is I_0 for the fast charge-discharge process. Similar to Figure 6.3(a), in Figure 6.3(c) lithiation occurs till a normalized time of $1.0 \cdot t_0$ (red dashed line), and after that delithiation occurs till $2.0 \cdot t_0$ (cyan dashed line). Under constant influx of lithium ions, surface concentration increases quickly and becomes equal to the lithium rich phase. Because of fast influx of lithium ions, and relatively slower movement of the two-phase front along the radial direction, the surface concentration eventually reaches the maximum concentration (red solid line in Figure 6.3(c) that corresponds to time $0.75 \cdot t_0$). Similarly, at the end of delithiation, the concentration at the surface of the active particle is the minimum concentration, which is smaller than the concentration of the lithium poor phase (see cyan dashed line in Figure 6.3(c)). Figure 6.3(d) demonstrates the generation of two different two-phase fronts that move along the same direction when lithiation ends and delithiation begins. At the end of lithiation process (black dashed line in Figure 6.3(d)), there exist only one two-phase front. With the initiation of fast delithiation process, the surface concentration

drops very quickly and becomes equal to the lithium poor phase at around $1.17 \cdot t_0$ (solid red line in Figure 6.3(d)). As a result, two different two-phase fronts get developed (at time $1.34 \cdot t_0$): one close to the center, and the other close to the surface of the active particle (see red dashed line in Figure 6.3(d)). The two-phase front close to the center reaches the center of the active particle and vanishes. The two-phase front near the surface of the active particle moves inward with subsequent delithiation process (blue solid line).

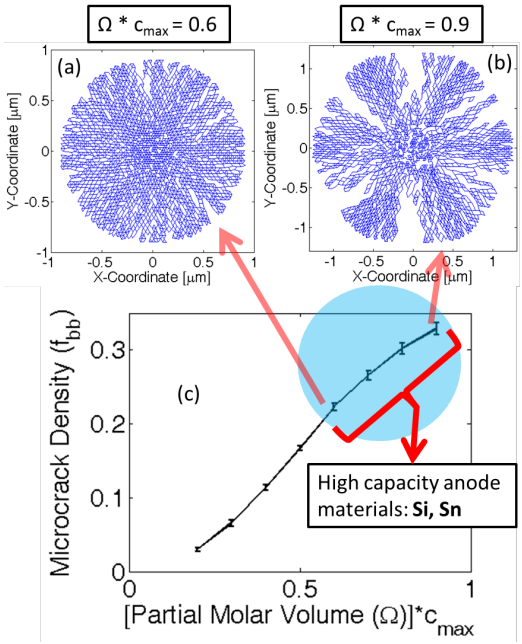

Fig: 6.4. *Evolution of microcracks under different magnitude of partial molar volume of the lithiated phase. Initial particle size has been assumed to be 1μm. (a) Expansion and damage evolution within an active particle where* $\Omega \cdot c_{\max} = 0.6$. *(b) Expansion and damage evolution inside active particles with* $\Omega \cdot c_{\max} = 0.9$. *(c) Amount of mechanical degradation during lithiation under different values of partial molar volume. Higher magnitude of* $\Omega \cdot c_{\max}$ *leads to large amounts of microcrack density. Silicon (Si) and Tin (Sn) type high capacity anode materials lie within the blue circular region. However, the simulations have been conducted for Si only. Si and Sn have different concentration dependence for mechanical properties. Ten samples have been considered to generate the error-bar within the figure.*

Figures 6.3(e) and 6.3(f) shows the contour plots of normalized lithium concentration under low and high rates of current, respectively. The displayed concentration profile corresponds to the time at the end of the lithiation process $\left(t = 1.0 \cdot t_0\right)$. The color bar signifies magnitude of normalized lithium concentration. Since the contour plots are generated at the end of the lithiation process, significant portion of the active particle close to the surface is in lithium rich phase. A small amount of active particle close to the center is still in lithium poor phase at the end of the lithiation process. For lithiation-delithiation at lower rates of current, the two-phase front never reaches the center of the active particle. Hence, the center of the active particle always remains in the lithium poor phase at the time of delithiation (also depicted in Figure 6.3(a)). However, for lithiation-delithiation at higher rates of current, the two-phase front indeed reaches the center of the active particle. Hence, the lithium poor phase at the end of the lithiation process (blue region in Figure 6.3(f)) eventually becomes lithium rich sometime during the delithiation phenomena (also shown in Figure 6.3(c)). The existence of a sharp two-phase interface is also evident from Figures 6.3(e) and 6.3(f).

The two different types of lithiation-delithiation mechanism described in Figures 6.3(a) and 6.3(c) leads to completely different amount of mechanical degradation within the active particles. Inward and outward movement of the same two-phase front demonstrated in Figure 6.3(a) and 6.3(b) induces mechanical degradation only during the lithiation process. Since no new concentration gradient develops or extra volume expansion occurs during the delithiation process, chances of further mechanical

degradation are minimal [147]. However, under fast lithiation-delithiation phenomena, two different two-phase fronts develop, which has the potential to produce severe mechanical degradation during delithiation process as well (shown in Figure 6.3(c) and 6.3(d)). Formation of the second two-phase front at the time of delithiation close to the surface of the active particle induces severe concentration gradient induced load. This causes the crack fronts to propagate significantly that opened up during the lithiation process [194]. Since severe mechanical degradation can occur during the fast lithiation-delithiation process (shown in Figure 6.3(c) and 6.3(d)), microcrack formation will be investigated under these types of concentration gradient in the subsequent sections.

The concentration profile and operating condition that applies the maximum amount of load has been identified. Next, it will be applied on a Si active particle to estimate the amount of mechanical degradation under diffusion-induced stress. Amount of mechanical degradation during lithiation under different magnitudes of partial molar volume of the lithiated phase has been investigated in Figure 6.4. By multiplying the partial molar volume of the lithiated phase with the maximum lithium concentration $\left(\Omega \cdot c_{\max}\right)$, a non-dimensional number has been developed. In Figure 6.4(c), the microcrack density, also known as the fraction of broken elements $\left(f_{bb}\right)$, has been plotted with respect to the non-dimensional partial molar volume of the lithiated phase. The dependent variable, microcrack density (or fraction of broken elements), has been defined as the ratio of number of broken springs over the total number of spring elements within the network [85]. It is evident form Figure 6.4(c) that with increasing magnitude of the partial molar volume, the total amount of microcrack density during

lithiation increases. Figure 6.4(a) and 6.4(b) demonstrates the fracture profile after the lithiation process for non-dimensional partial molar volume of magnitude 0.6 and 0.9, respectively. As discussed earlier, transport of lithium inside silicon active particles happen via two-phase diffusion process. Large magnitude of partial molar volume of the lithiated phase applies two different types of loads: a) Concentration gradient induced load at the two-phase interface, and b) High volume expansion induced tensile load at the particle surface, which increases as the two-phase front moves inward (see [147]). The concentration gradient induced load at the two-phase interface is relatively smaller in magnitude, and gives rise to minor generation of microcracks. None of this microscopic damage nucleates into spanning cracks. However, the magnitude of tensile load at the particle surface due to large volume expansion has the potential to create spanning cracks. Higher the magnitude of partial molar volume, the outer lithium rich phase moves more towards the radially outer direction. Tensile stress on the particle surface gets generated solely by the outward movement of the lithium rich phase. Hence, higher magnitude of partial molar volume produces enhanced tension followed by crack formation and propagation at the surface of the active particle. Figure 6.4(b) clearly demonstrates that for $\Omega \cdot c_{\max} = 0.9$, significantly higher radially propagating cracks are developed as compared to $\Omega \cdot c_{\max} = 0.6$, as shown in Figure 6.4(a). For silicon, the magnitude of non-dimensional partial molar volume lies around 0.7 or 0.8 (shown using a blue circle in Figure 6.4(c)), which leads to severe mechanical degradation after the first lithiation process. The error bar shown in Figure 6.4(c) has been obtained by averaging over ten different samples.

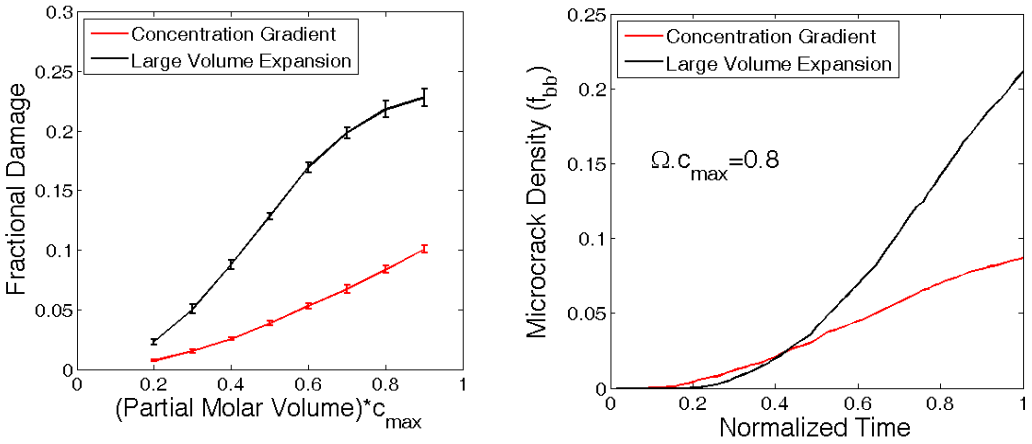

Fig: 6.5. *Comparison between microcrack evolution due to concentration gradient effect and large volume expansion effect. The entire analysis conducted here corresponds to initial particle diameter of* $D_{initial} = 1.0\mu m$. *(a) Mechanical degradation at the end of lithiation process due to different mechanisms. Red line shows concentration gradient induced damage evolution. Black line denotes mechanical degradation occurring because of large volume expansion. (b) Comparison between time evolutions of both the degradation mechanisms for a particle with* $\left(\Omega \cdot c_{\max}\right) = 0.8$. *Towards the end of lithiation, mechanical degradation due to large volume expansion is significantly greater than microcrack evolution from concentration gradient.*

It has already been discussed in the last paragraph that there exist two different mechanisms of microcrack formation: a) Concentration gradient induced load, and b) Large volume expansion induced load (also see [119]). Since it is established that larger magnitude of partial molar volume lead to enhanced mechanical degradation [139], it is important to understand which mechanism produces more microcracks. A comparative analysis of mechanical degradation due to both the mechanisms has been demonstrated in Figure 6.5(a). With increasing partial molar volume of the lithiated phase, damage due to each of the mechanisms increase monotonically. But the overall magnitude of degradation due to concentration gradient (red line) is significantly smaller than the mechanical damage because of large volume expansion (black line). The ratio of

concentration gradient induced microcrack over large volume expansion driven microcrack remains almost constant for all the values of the partial molar volume. Similar to Figure 6.4(c), ten different samples have been considered to generate the error bars shown in Figure 6.5(a).

Time evolution of mechanical degradation during lithiation from both the mechanisms has been depicted in Figure 6.5(b). The initial diameter of the active particle considered in this simulation is 1μm, and the non-dimensional partial molar volume is $\Omega \cdot c_{\max} = 0.8$. The lithiation process is assumed to end at normalized time 1.0. Initially the entire active particle exists in a lithium poor phase. During lithiation, concentration of the particle surface increases and becomes equivalent to the lithium rich phase. Negligible mechanical degradation is observed during this time interval when the two-phase front gets developed. With subsequent lithiation, the two-phase front starts to propagate inward, which induces severe concentration gradient induced tensile load on the lithium poor phase. Hence, the concentration gradient induced mechanical damage evolution starts earlier during the lithiation process. This is well reflected in Figure 6.5(b), where at normalized time 0.2, microcrack formation from concentration gradient (red line) is larger in magnitude than volume expansion induced damage (black line). As lithiation progresses, the lithium rich phase is pushed outward along the radial direction. Magnitude of this tensile stress due to outward expansion is significantly larger than its concentration gradient induced counterpart, and it increases very quickly as more lithiation occurs. As a result, severe mechanical degradation near the particle surface starts to occur from normalized time 0.25. Around normalized time of 0.45, mechanical

degradation due to large volume expansion becomes larger in magnitude than concentration gradient induced damage. Significantly higher tensile stress at the particle surface leads to rapid increase in volume expansion induced damage evolution. At the end of lithiation process, the ratio of volume expansion induced damage over concentration gradient induced degradation approximately equals to 2.5. Thus it can be concluded that for phase separating and high capacity anode materials, majority of the mechanical degradation happens due to large volume expansion of the active particles.

All the simulation results shown till now correspond to only the lithiation process. Delithiation after the lithiation phenomena indeed applies some amount of concentration gradient induced load. As shown in Figure 6.3(c) and 6.3(d), a new two-phase front develops close to the surface at the time of delithiation, where the lithium poor phase resides close to the particle surface. As delithiation continues, this new two-phase front moves inward which gives rise to tension within the lithium poor phase located close to the surface of the particle. Tension induced by concentration gradient is smaller in magnitude than the tensile stresses due to large volume expansion. As a result, during delithiation, new crack fronts do not develop. However, the surface cracks that developed during the lithiation process propagate radially during the delithiation phenomena. Figures 6.6(a) and 6.6(b) shows the damage profiles for an active particle of size 1μm after the lithiation and successive delithiation process, respectively. The partial molar volume considered in this simulation has a magnitude of $\Omega \cdot c_{\max} = 0.7$. It is clear from Figure 6.6(b) that after the delithiation process, the particle gets fragmented into multiple smaller particles. The smaller interconnection at the center of the particle

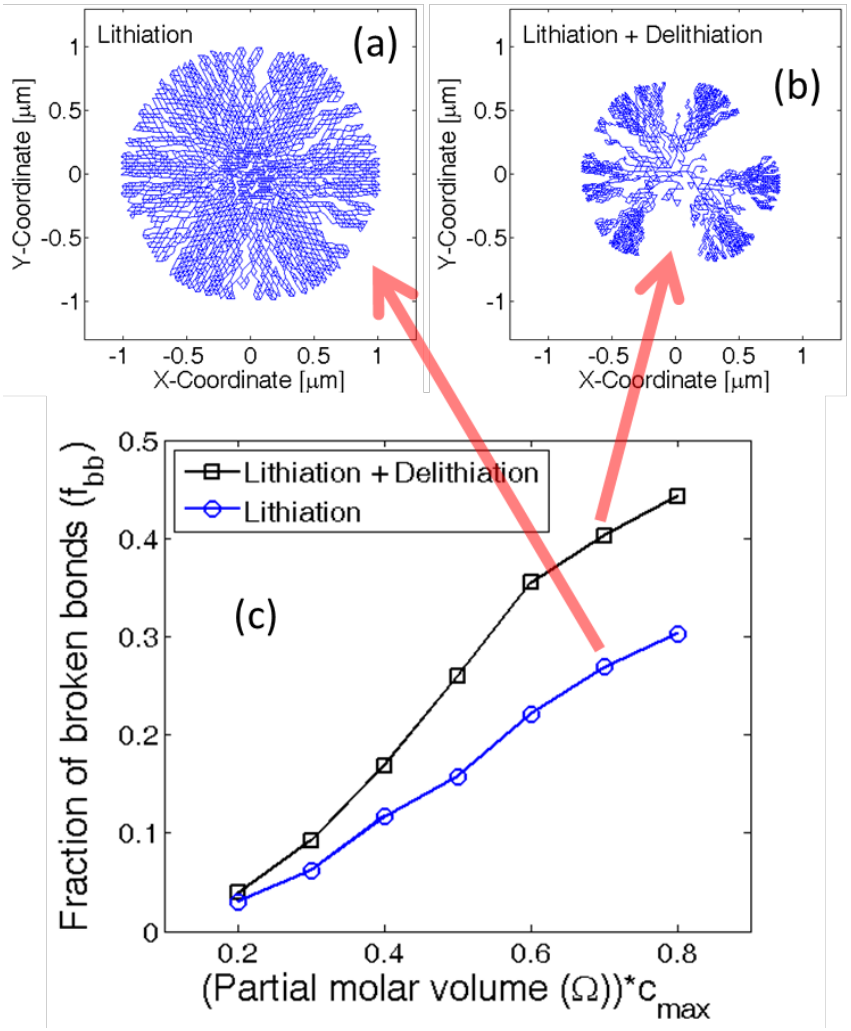

Fig: 6.6. *Microcrack evolution at the end of lithiation and delithiation process. The entire analysis has been conducted for a particle of initial diameter* $D_{initial} = 1\mu m$. *(a) Damage profile observed within an active particle after lithiation for which* $\Omega \cdot c_{\max} = 0.7$. *(b) Damage profile inside the same active particle where* $\Omega \cdot c_{\max} = 0.7$ *after successive lithiation and delithiation process. Only one cycle has been conducted here. (c) Microcrack density observed within active particles with different magnitudes of partial molar volume* $\left(\Omega \cdot c_{\max}\right)$. *In this particular analysis subsequent lithiation and delithiation occurred. A comparative observation clearly states that majority of the microcrack evolution occurs during the lithiation process.*

vanishes after few more lithiation-delithiation processes. Figure 6.6(c) depicts the total amount of mechanical degradation after the first lithiation (blue circles) and successive delithiation (black squares) process. Only single sample has been considered to generate

these plots. By comparing Figures 6.6(a) and 6.6(b), it looks like severe damage occurred during the delithiation phenomenon. However, from Figure 6.6(c) it is very clear that significantly more microcrack evolution occurs during the lithiation process. Delithiation experiences more crack propagation and particle fragmentation. Since during the delithiation process, some of the crack fronts open-up significantly, it gives a false impression of enhanced mechanical degradation.

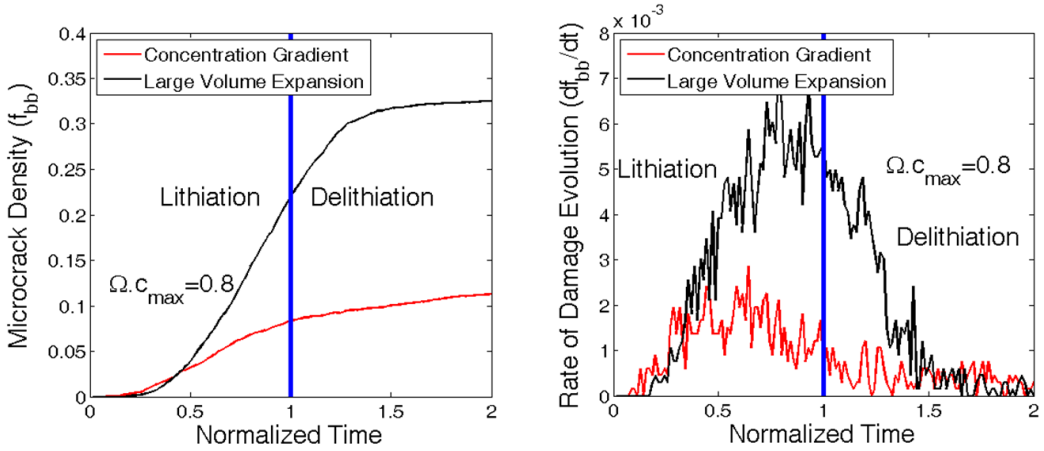

Fig: 6.7. *Comparison between damage evolution due to two different mechanisms. For this analysis a particle diameter of* $D_0 = 1\mu m$ *has been assumed. In the normalized time scale, time from 0 to 1 corresponds to the lithiation process. Whereas delithiation occurs between time 1 to 2 in the normalized scale. For this particular analysis, the particle displays* $\Omega \cdot c_{\max} = 0.8$. *(a) Comparison between damage evolution due to concentration gradient effect and microcrack formation because of high volume expansion. (b) Rate of damage evolution due to each of the two mechanisms. From both the figures, it is evident that microcrack evolution within high capacity materials is mostly governed by the volume expansion phenomenon.*

Time evolution of concentration gradient induced and high volume expansion driven mechanical degradation is demonstrated in Figure 6.7(a). Successive lithiation and delithiation occurred within an active particle of initial diameter 1μm. The magnitude of non-dimensional partial molar volume is assumed to be $\Omega \cdot c_{\max} = 0.8$.

Lithiation occurs between normalized time 0 to 1 and delithiation occurs within 1 and 2. The blue vertical line in both Figures 6.7(a) and 6.7(b) differentiates between the lithiation and delithiation process. During the delithiation process, concentration gradient induced load controls the formation of microcracks [194]. At the beginning of the delithiation process, significant amount of mechanical degradation due to large volume expansion is definitely counter-intuitive (see Figure 6.7(a)). This particular phenomenon can be explained from Figure 6.3(d). Even after the end of lithiation, the two-phase front corresponding to the lithiation process keeps on moving inward and vanishes at the center of the active particle. A separate two-phase front corresponding to the delithiation process initiates at the particle surface and moves inward. The lithium rich phase arrives at the center of the active particle at around normalized time 1.25. Due to this inward movement of the lithium rich phase, the outer layer gets pushed along radially outward direction. This results in generation of tensile stress within the lithium rich phase, and subsequently mechanical degradation due to high volume expansion. Once the lithium rich phase reaches the center, volume expansion induced damage almost saturates (black line). Concentration gradient induced degradation keeps on increasing due to inward movement of the two-phase front that belongs to the delithiation process (red line).

Figure 6.7(b) depicts the rate of microcrack formation by the two different mechanisms during lithiation and successive delithiation process. Rate of mechanical degradation due to large volume expansion is at a maximum at the end of the lithiation process. At the beginning of the lithiation process, till normalized time 0.3, rate of concentration gradient induced damage (red line) is larger than volume expansion

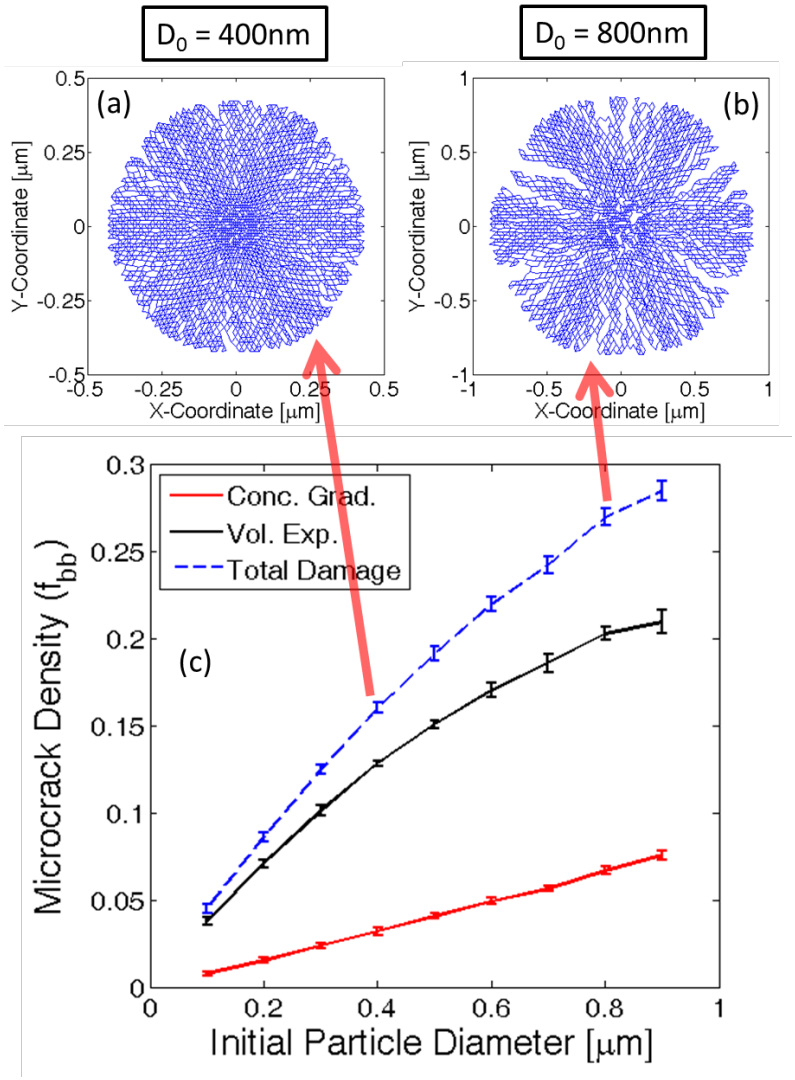

Fig: 6.8. *Microcrack density at the end of first lithiation process for different particle sizes. The material under consideration displays* $\Omega \cdot c_{\max} = 0.8$. *(a) Damage profile observed within an active particle of initial diameter* $D_{initial} = 400nm$. *(b) Damage profile observed within a larger active particle of diameter* $D_{initial} = 800nm$. *(c) Total amount of microcrack density after the first lithiation process for different particle sizes (denoted by blue dashed line). Damage evolution due to large volume expansion (black line) and concentration gradient induced load (red line) have also been displayed. The error-bars have been generated by averaging over ten samples.*

induced degradation (black line). The overall rate of concentration gradient induced degradation is much smaller than that observed due to volume expansion. The same trend is observed even at the beginning of the delithiation process. However, the rate of

volume expansion induced degradation decreases as the delithiation proceeds. During delithiation, formation of the lithium poor phase close to the particle surface leads to contraction. This eventually reduces the possibility of microcrack formation due to high volume expansion. Towards the end of the delithiation process, almost negligible mechanical degradation occurs due to high volume expansion. However, a small magnitude of concentration gradient induced damage can still be observed even towards the end of delithiation phenomenon. Hence, from Figures 6.7(a) and 6.7(b) it can be concluded that concentration gradient induced damage can be observed throughout the lithiation-delithiation process, but the magnitude is extremely small. Whereas, large volume expansion induced degradation occurs at the second half of lithiation and beginning of delithiation process, but in a significantly larger amount.

Till now it has been well established that variation in partial molar volume of the lithiated phase induces different amounts of mechanical degradation within the active particles. Similarly, variation in particle size should also give rise to different magnitude of microcrack density for a particular value of the partial molar volume. In this manuscript, all the analysis of particle size dependence has been conducted for $\Omega \cdot c_{\max} = 0.8$. Figure 6.8 explains the evolution of mechanical degradation during lithiation for different particle sizes. Damage profiles at the end of lithiation process for two different particles of initial diameter $400nm$ and $800nm$ are shown in Figures 6.8(a) and 6.8(b), respectively. At the end of lithiation process, larger particles experience enhanced mechanical degradation. Several spanning cracks can be observed in the $800nm$ sized active particle that travels along the radial direction. Relatively

fewer cracks generate inside the $400nm$ sized particle at the end of lithiation. More rigorous analysis of how microcrack density changes with particle size is demonstrated in Figure 6.8(c). Increase in particle size leads to more severe mechanical degradation of the active materials. The blue dashed line in Figure 6.8(c) corresponds to the total amount of mechanical degradation. The black solid line signifies microcrack formation due to large volume expansion. Whereas the red solid line corresponds to damage evolution under concentration gradient induced load. As observed in Figure 6.8(c), concentration gradient induced damage for active particles with different diameter are significantly smaller than volume expansion induced degradation. For each representative data point, the error bars are generated by averaging over ten different samples.

Damage due to large volume expansion occurs because of the outward movement of lithium-rich phase. For large particles, the lithium rich phase close to the surface moves along the radial direction by a larger extent. This eventually produces enhanced tensile stress and subsequently more mechanical degradation close to the surface of the larger active particles. Concentration gradient induced load is not significant and cannot give rise to severe spanning cracks during the lithiation process. With decreasing particle size the concentration gradient induced tensile load also reduces, which eventually leads to reduction in microcrack formation. Hence, damage due to both large volume expansion and concentration gradient induced load decreases with reduction in particle size.

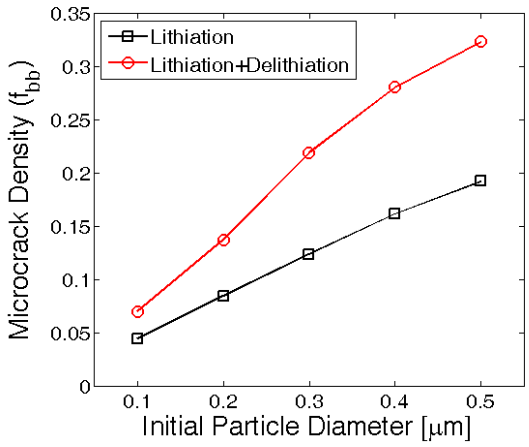

Fig: 6.9. *Total amount of microcrack density for active particles of different size under lithiation and successive delithiation process. Smaller active particles of initial diameter 200 or 300 nm, which experience very little mechanical degradation during the lithiation process, can undergo severe crack opening and propagation during the delithiation process.*

During operation, lithium ion batteries are subjected to multiple charge discharge cycles. Hence, the active materials located within the electrode experiences several lithiation-delithiation cycles. Mechanical degradation due to only the lithiation process has been investigated till now. If a battery is discharged after the first charge process, the anode active materials experience delithiation right after the completion of lithiation process. Variation in concentration gradient can be assumed to follow the pattern provided in Figure 6.3(c). Evolution of microcrack during delithiation must be investigated to correctly determine the particle size below which mechanical degradation can be neglected even under multiple lithiation-delithiation cycles. Figure 6.9 demonstrates the microcrack density after lithiation (black square) and successive delithiation (red circle) process. Particle sizes ranging from 100nm to 500nm has been analyzed here. After only the lithiation process, even particles as large as 300nm experiences only 12% mechanical degradation. However, successive delithiation process

significantly increases the total amount of microcrack formation. From Figure 6.9 it can be concluded that even particles of size 200nm experiences around 15% mechanical degradation after successive lithiation-delithiation process. Whereas, 300nm sized active particles experience around 22% mechanical degradation after the delithiation process. Microcrack density within particles of initial diameter 100nm only remains well below 10% even after the delithiation process. Which magnitude of microcrack density is safe and what should be considered as mechanically degraded, has not been analyzed yet. A rough estimate will be provided in the next paragraph along with the images of damage profile for different particle sizes.

While analyzing the mechanical degradation, it is assumed that lithiation-delithiation occurs only from the surface of the active particles. If a crack front connected to the surface opens up, electrolyte can flow through the opening which would allow influx or outflux of lithium to occur form regions other than the particle surface. Hence the computational analysis being conducted here would no longer be valid. Hence, an active particle can be characterized as damaged if one or multiple crack fronts open up during the entire lithiation-delithiation process. For certain intermediate particle sizes, no significant crack fronts develop during the lithiation process. But, during the first half of the delithiation process, some crack propagation and opening is observed. Again, towards the end of the delithiation process these crack fronts close because of contraction. This type of particle fracture can be characterized as minor degradation. Figure 6.10 demonstrates the damage profile as observed in four different particle sizes of initial diameter $D_0 = [100; 200; 300; 400] nm$ during successive lithiation

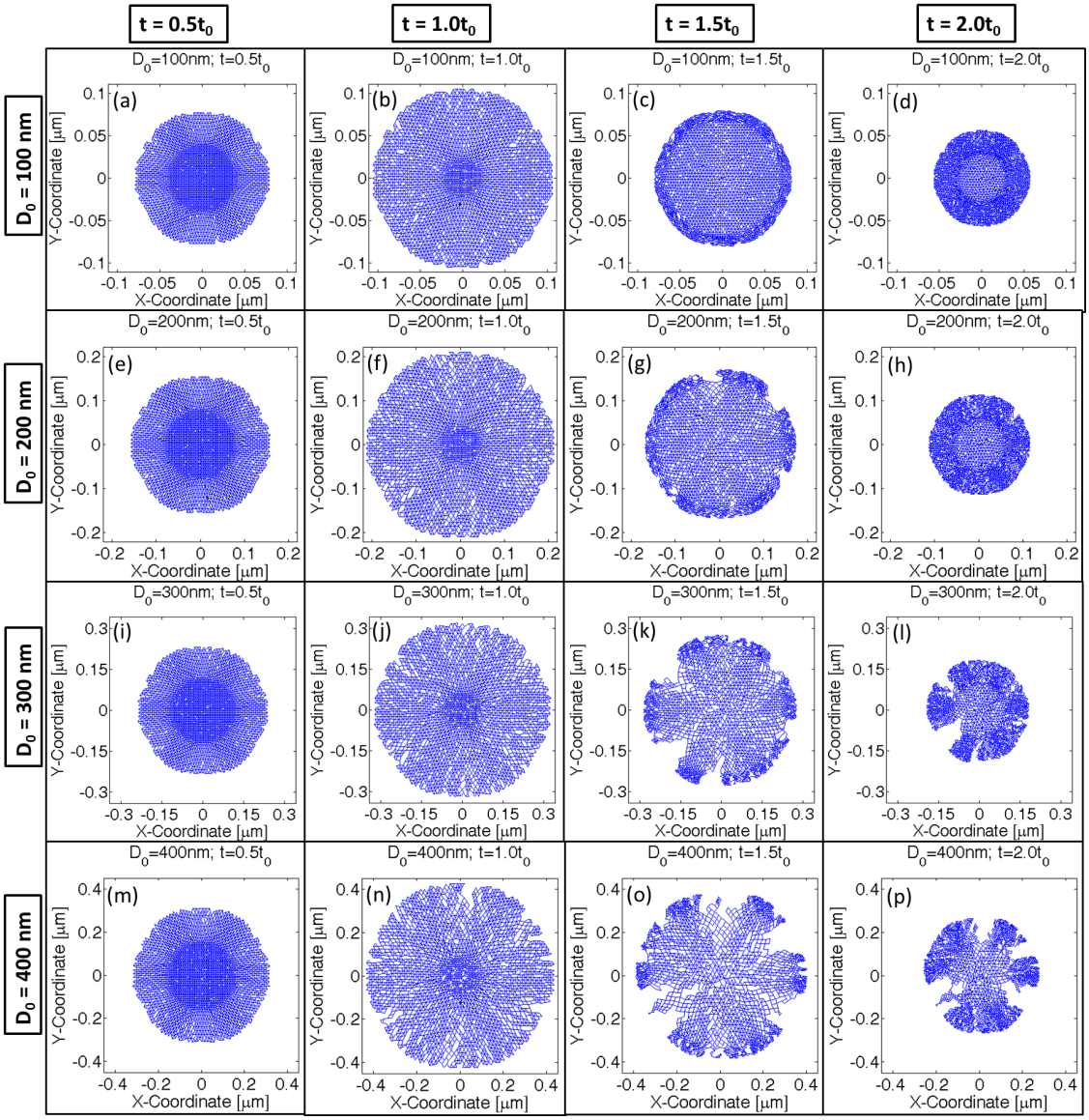

Fig: 6.10. *Crack formation within active particles of different size* $\left(D_0 = \left[100; 200; 300; 400\right] nm\right)$. *Time* $t = 1.0t_0$ *corresponds to the end of lithiation process for all the four different particle sizes analyzed here. Microcrack profiles at four different time instances have been plotted here: half way into the lithiation process, end of lithiation process, halfway into delithiation process, and end of delithiation process. (a–d) 100nm particle size, (e–h) 200nm particle size, (i–l) 300nm particle size and (m-p) 400nm sized particle have been plotted.*

and delithiation process. Damage profiles at four different time instance have been plotted for each of the particle sizes: a) Time $t = 0.5t_0$ which corresponds to midway

during lithiation, b) Time $t = 1.0t_0$ that signifies end of lithiation, c) Time $t = 1.5t_0$ which is halfway during the delithiation process, and finally, d) Time $t = 2.0t_0$ that corresponds to the end of delithiation process. The active particles of initial diameter $D_0 = 300nm$ experiences almost negligible degradation at the end of lithiation (see Figure 6.10(j)), which approximately equals 12% microcrack density (from Figure 6.9). But several crack fronts open up during the delithiation process (see Figure 6.10(l)), which renders Si active particles of size 300nm unsuitable for lithiation-delithiation cycles. This corresponds to around 22% microcrack density (as reported in Figure 6.9). Active particles of initial diameter 200nm are also not a good choice because minor degradation can be observed halfway into the delithiation process where some crack fronts open up (see Figure 6.10(g)). However, these crack fronts eventually close at the end of delithiation process (Figure 6.10(h)). But, they have the potential to grow during subsequent lithiation-delithiation cycles. Comparing with Figure 6.9, 200nm sized active particles experience around 14% microcrack density at the end of delithiation process. Only 100nm sized active particles did not experience any damage nucleation. Similar size dependence was also observed experimentally (see [119]). Hence, it can be concluded that microcrack density below 12% can be characterized as free from mechanical degradation. Minor fracture occurs when microcrack density lies within 12% and 18%. Anything above 18%-20% can be characterized as severe mechanical degradation, which leads to propagation and opening of multiple crack fronts.

The correlation between microcrack density and the amount of fracture propagation has been established in the previous paragraph. Next, it is important to

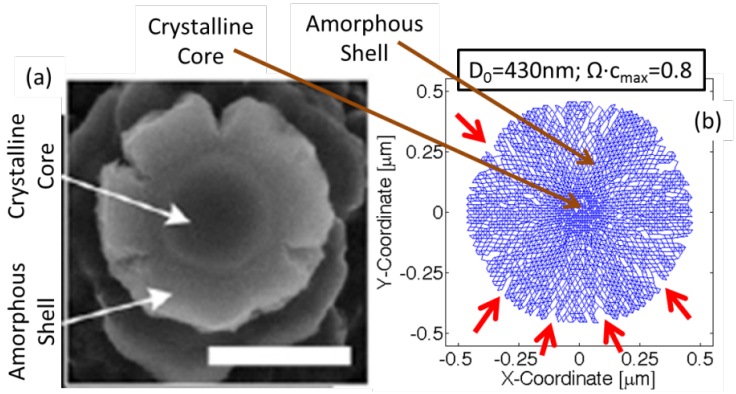

Fig: 6.11. *(a) SEM image of the cross-section of a Si nano-pillar which experienced mechanical degradation during lithiation (adopted from Lee et al., PNAS, (2012) 4080). Presence of surface cracks is evident from this image. (b) Crack formation on the surface of active particles as predicted by the developed lattice-spring based numerical technique. The red arrows show crack fronts that develop on the particle surface.*

understand how accurately the developed computational model can capture the experimentally observed damage evolution. In Figure 6.11, a visual comparison of experimentally observed and computationally predicted crack propagation, during the lithiation process is reported (see [42]). Figure 6.11(b) demonstrates the initiation of crack fronts close to the particle surface during the lithiation of a 430nm diameter silicon active particle. There exist significant amount of similarity between the experimentally observed features (shown in Figure 6.11(a)) and the computational predictions (in Figure 6.11(b)) in a qualitative sense. Such as, there exists a lithium rich amorphous phase near the surface and a lithium poor crystalline phase at the center of the active particle. Also, the cracks initiate close to the surface of the active particles during the lithiation process. This demonstrates the effectiveness of the developed scheme to capture the microcrack formation within high capacity anode materials. However, there still exist some discrepancies between the experiments and the computational predictions. Even though the initiation of the surface cracks during lithiation is equivalent to the experimental

results, the computationally predicted cracks do not open up as much as that observed in SEM images (see Figure 6.11(a)). Also, the computational analysis predicts the generation of multiple small crack fronts close to the particle surface. However, the experimental SEM image indicates the formation of a few crack fronts which tend to propagate along the radial direction. This discrepancy can be attributed to the distribution of the fracture threshold energy adopted in the present study. A uniform distribution of the threshold energy over a wide range has been taken into consideration here. This results in generation of small microcracks throughout the system. Thus significant amount of strain energy release occurs without the formation of large spanning cracks. Detailed analysis of the distribution of the threshold energy is out of the scope of this article, and will be considered as part of a future study.

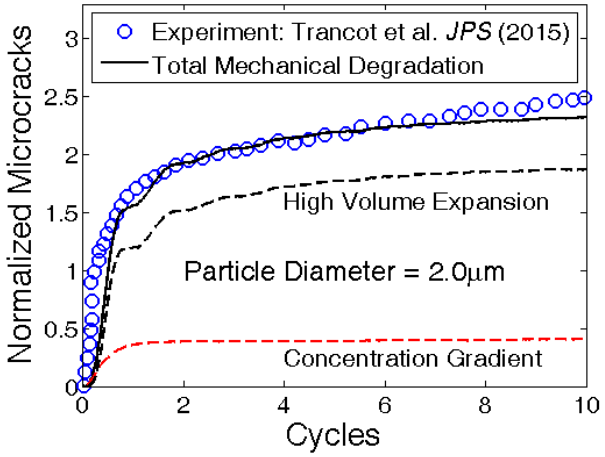

Fig: 6.12. *Qualitative comparison of mechanical degradation predicted by the developed model with experimentally observed acoustic emission response. Amount of mechanical degradation due to high volume expansion (black dashed line) and concentration gradient (red dashed line) induced loading has also been reported. Concentration gradient induced damage evolution almost saturates after the first cycle. However, mechanical degradation due to high volume expansion increases till the fifth or sixth cycle (though the increment is negligible as compared to the first cycle).*

Evolution of mechanical degradation within solid materials can be experimentally characterized by acoustic emission based techniques. Experimental characterization of fracture evolution within Si active particles during lithiation-delithiation cycles, have been reported in several research articles [63, 182]. The essence of acoustic emission based techniques lie behind the fact that during microcrack formation, some strain energy gets released. It propagates through the media as a stress wave and reaches the surface [178]. The stress wave is detected by an actuator located on the surface as a hit. Multiple hits in a very short period of time correspond to formation and propagation of spanning cracks. Total amount of mechanical degradation can be characterized by the cumulative summation of strain energy detected by the actuator. A similar acoustic emission based experimental procedure have been adopted by Trancot et al. to characterize the evolution of mechanical degradation within a 2μm sized Si active particle over 10 lithiation-delithiation cycles [182]. In the present study, similar lithiation-delithiation simulations have been conducted on a spherical active particle of initial diameter 2μm over 10 cycles. Figure 6.12 demonstrates the comparison between evolution of mechanical degradation extracted from simulations (black solid line) and the experimentally observed cumulative damage (blue circles). The cumulative acoustic activity is represented by the units of energy and microcrack density from simulations is characterized as a fraction. Hence, proper normalization of amount of damage should be conducted to achieve a successful qualitative comparison between computation and experiments. In the present context, damage evolution at the end of first lithiation process is assumed to have a magnitude of 1.0. Extremely good qualitative

correlations between the computational and experimental results demonstrate the robustness of the developed lattice-spring based methodology.

It has already been discussed that the evolution of microcrack within phase separating high capacity Si anode active particles occurs through two different mechanisms: a) concentration gradient induced loading, and b) tensile stress caused by high volume expansion. Figure 6.12 demonstrates the amount of damage evolution over 10 cycles due to each of the two mechanisms. Red dashed line indicates microcrack due to concentration gradient, and black dashed line corresponds to microcrack under high volume expansion. From Figure 6.12, it can be concluded that concentration gradient induced degradation occurs only in the first lithiation-delithiation cycle and saturates after that from the second cycle. However, damage evolution due to high volume expansion does not saturate after the first cycle. Majority of the mechanical degradation under large volume expansion occurs during the lithiation process (see [182]). Maximum amount of fracture formation due to volume expansion occurs in the first cycle (also reported in [63]). Significant amount of microcrack evolution can still be observed in the second, third and fourth lithiation process. Eventually from the fifth cycle onwards, large volume expansion induced microcrack formation also tends to saturate. This saturation in mechanical degradation is explained from the perspective of strain energy release requirement to sustain a certain amount of externally applied load. During each lithiation-delithiation cycles, the same amount of diffusion induced load is applied on the system. The total amount of strain energy release required to sustain that amount of load, occurs within the first four to five cycles. Strain energy release happens through the

formation of microcracks. Since, after four-five cycles, no more strain energy release is required to withstand the external load, the total amount of microcrack also saturates (also provided in [85]).

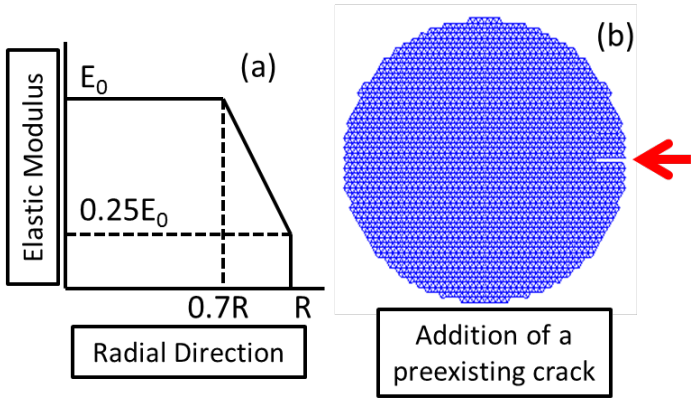

Fig: 6.13. *Two different methods have been proposed here that can be used to minimize the total amount of microcrack formation. (a) A novel "graded-by-elastic-modulus" design. Reduced elastic modulus of the active particle close to the surface is the main feature of this technique. (b) Addition of a thin pre-existing crack inside the particle. Length of the crack is supposed to impact the amount of strain energy release.*

After validating the developed computational procedure, it is important to investigate and propose some modifications that can reduce the overall microcrack formation. Mechanical degradation usually occurs to release the excessive strain energy stored within the system [85]. If it is somehow possible to reduce the total amount of strain energy stored within the system, overall mechanical degradation can be minimized. Two different procedures to reduce the overall stored strain energy have been elaborated in Figure 6.13. Since majority of the cracks initiate at the particle surface, reducing the elastic modulus close to the outer surface can result in smaller magnitude of strain energy. Based on this strategy, a new functionally graded material has been suggested in Figure 6.13(a). The elastic modulus decreases close to the particle surface according to the profile shown. From the center to a radius of 0.7R, the stiffness

remains equal to the pristine material. From 0.7R to R, the elastic modulus decreases linearly from the pristine amount to a value that is one-fourth in magnitude of the actual modulus. The second technique takes into consideration that pre-existing cracks help in reducing the total amount of stored strain energy [16]. The circular cross section of a spherical active particle that contains a pre-existing crack is shown in Figure 6.13(b). Depending on the length of the pre-existing crack, different magnitude of strain energy gets released. Effectiveness of these two mechanisms in terms of decreasing the total magnitude of microcrack formation during lithiation-delithiation cycles, will be discussed next.

Fractional microcrack density has been reported in Figure 6.14 for different length of pre-existing cracks $\left({}^{a}\!/_{D_0} = \left[0.0 : 0.05 : 0.5\right] \right)$ within the solid active particle. Here a denotes the pre-existing crack length and D_0 signifies the initial diameter of the active particle. For this particular analysis, $D_0 = 300nm$ and normalized partial molar volume $\Omega \cdot c_{\max} = 0.8$, has been assumed. It is expected that increasing length of the pre-existing crack should help in reducing the stored strain energy. Eventually this should result in decreased microcrack formation. Figures 6.14(a) and 6.14(b) shows the microcrack profile after successive lithiation-delithiation process for normalized pre-existing crack lengths of 0.2 and 0.4, respectively. For ${}^{a}\!/_{D_0} = 0.2$, the pre-existing crack does not propagate significantly. However, for normalized crack length of 0.4, the pre crack opens up and propagates significantly during the lithiation-delithiation process.

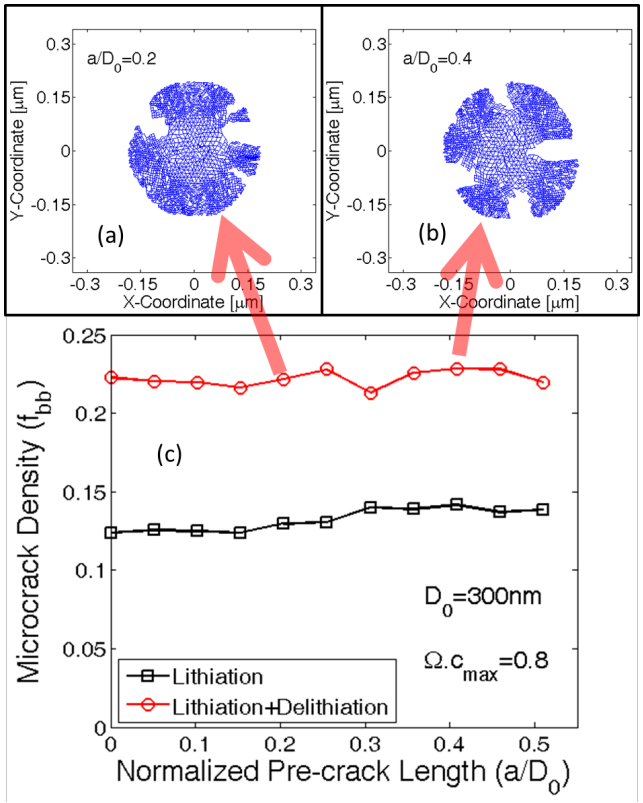

Fig: 6.14. *Analysis of how the presence of a preexisting crack impacts the microcrack formation in an active particle of initial diameter 300nm has been reported here. (a) For a normalized preexisting crack length of 0.2, none of the spanning crack fronts initiate from the initial imperfection. (b) For very large preexisting cracks of normalized length 0.4 or higher, stress concentration at the crack tip may overcome the disorder effect resulting in propagation of the initial imperfection. (c) Microcrack density at the end of lithiation and successive delithiation process inside various active particles containing different length of initial imperfections. Presence of preexisting crack does not have a significant impact on the overall microcrack formation.*

For relatively small cracks, the stress concentration at the crack tip is not sufficient to make them propagate along the radial direction.

It is also important to properly estimate the magnitude of microcrack density in order to determine the effectiveness of adding pre-cracks. Figure 6.14(c) demonstrates the magnitude of mechanical degradation experienced by active particles containing different size of the initial imperfection. The black square signifies fracture evolution till

the end of lithiation process. The red circles correspond to damage formation at the end of delithiation process, which occurred after the initial lithiation. It is evident from Figure 6.14(c) that incorporation of initial imperfection does not help in reducing the total amount of microcrack formation. To understand why incorporation of pre-existing cracks does not help in reduction of microcrack evolution, it should be properly realized that the distribution of fracture threshold is conducted in a random fashion. A pre-existing crack is assigned without taking into consideration the distribution of fracture threshold. During formation of the initial-imperfection, the lattice-spring elements that are removed from the network may not belong to the group of weak springs. Under externally applied diffusion induced load, the relatively weak lattice-spring elements experience rupture irrespective of their location. Unless the pre-existing crack is capable of removing some of the weak lattice-springs, introduction of an initial imperfection does not help in reducing the overall mechanical degradation.

Effectiveness of functionally graded materials in mitigating the problem of mechanical degradation will be investigated next. The type of functionally graded material considered here shows reduced elastic modulus close to the surface of the particle (also depicted in Figure 6.13(a)). A comparative demonstration of the amount of microcrack density for functionally graded and regular silicon material has been provided in Figure 6.15. Five different active particle sizes of initial diameter 100nm, 200nm, 300nm, 400nm and 500nm have been taken into consideration. All the particles are subjected to successive lithiation-delithiation procedure. In Figure 6.15, the blue dashed and solid lines with triangular symbols signify the magnitude of mechanical

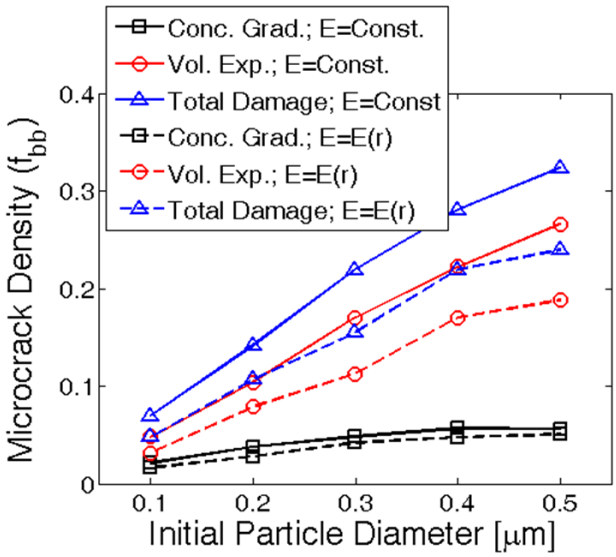

Fig: 6.15. *Comparison between the amount of mechanical degradation due to concentration gradient (square symbol) and volume expansion (circular symbol) induced load. The total damage is denoted by triangular symbols. The solid lines signify mechanical degradation under constant Young's modulus, whereas the dashed lines correspond to microcrack formation with reduced elasticity parameters. A comparative analysis shows that reduction in elastic modulus significantly decreases the volume expansion induced mechanical degradation (compare between the red solid and red dashed lines). As a result, the overall microcrack formation gets diminished significantly with graded elastic parameters (compare between the blue solid and the blue dashed line).*

degradation after the lithiation-delithiation procedure within the functionally graded Si and regular Si material, respectively. The dashed blue line lies well below the solid blue one. It is evident from Figure 6.15 that functionally graded materials are effective in reducing the mechanical degradation to some extent. Under externally applied load evolution of microcrack occurs to release the extra strain energy stored within the material. Total amount of strain energy depends on the elastic modulus of the system. Under a fixed amount of external load, reduction in elastic stiffness results in smaller magnitude of strain energy generation. Hence, the functionally graded material needs to

release less strain energy than the regular silicon material. As a result smaller magnitude of microcrack evolution happens for the material with reduced elastic modulus.

It is clearly demonstrated in the previous paragraphs that the usage of functionally graded silicon active materials significantly reduces the overall mechanical degradation. There exist two different mechanisms of microcrack formation: a) Concentration gradient induced, and b) High volume expansion induced. It is worth to investigate which mechanism is affected more due to the reduction in elastic modulus close to the surface of the active particle. Figure 6.15 demonstrates a comparative analysis of mechanical degradation due to both the mechanisms within regular (solid line) and functionally graded (dashed line) silicon active particles. The red circles signify damage due to large volume expansion and black squares correspond to damage under concentration gradient induced load. It is evident that reduction in elastic modulus close to the surface of the active particle decreases microcrack evolution due to both the mechanisms. For an active particle of initial diameter 300nm, rupture due to high volume expansion gets mitigated by approximately 7%. However, rupture under concentration gradient induced load decreases by only 1%. During expansion of the lithium rich phase, outer-most surface of the active particle experiences maximum amount of tensile load. Hence, large volume expansion induced fracture initiates at the particle surface and propagates along the radially inward direction. Whereas, concentration gradient induced load evolves throughout the particle. In the functionally graded Si, minimum elastic modulus occurs at the particle surface. Hence, reduction in strain energy reaches maximum near the surface of the functionally graded silicon active

particle. Fracture happens to release the excessive strain energy stored within the system. Since less strain energy gets developed within functionally graded materials near particle surface, smaller amount of it needs to be released. Hence, lesser magnitude of microcrack evolves near the particle surface. As a result, mechanical degradation under large volume expansion induced load decreases significantly. Since concentration gradient induced degradation develops uniformly throughout the particle, reduction in elastic modulus close to the surface marginally mitigates damage evolution under this mechanism. Hence, it can be concluded that, usage of functionally graded silicon active particles significantly reduces the large volume expansion induced mechanical degradation.

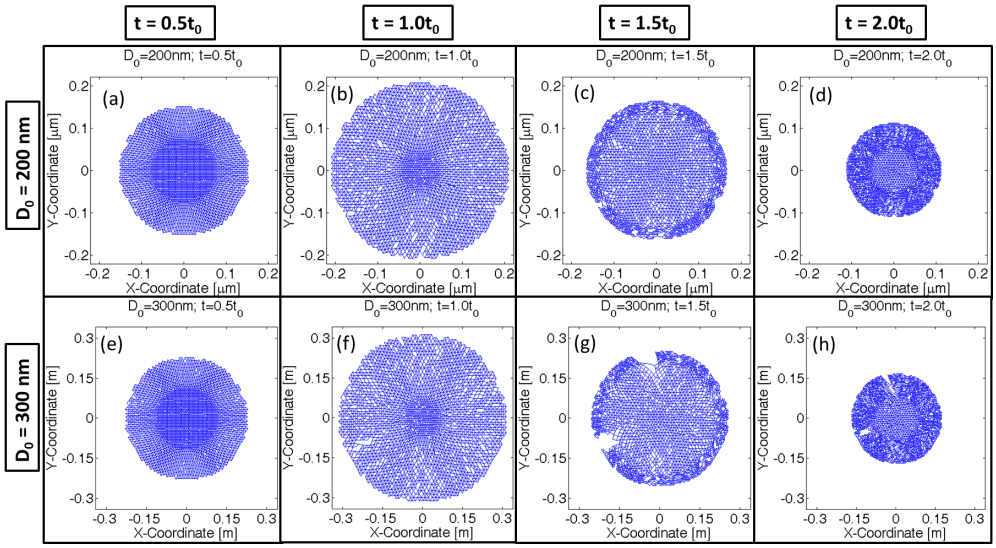

Fig: 6.16. *By applying the gradient in elastic modulus, reduction in mechanical degradation can be achieved. Time* $t = 1.0t_0$ *corresponds to end of lithiation process. Delithiation occurs between time* $1.0t_0$ *and* $2.0t_0$*. (a-d) Damage evolution within an active particle of initial diameter 200nm during lithiation and delithiation. (e-h) Damage evolution inside a 300nm diameter active particle during lithiation and delithiation. Application of gradient in elastic modulus almost mitigates spanning crack formation within 200nm sized active particles. Damage evolution in 300nm sized particles reduces significantly (compare with Figure. 6.10(i-l)).*

The next important thing is to characterize whether the reduction in mechanical degradation experienced by functionally graded silicon active particles are sufficient from a practical perspective. It was concluded from Figures 6.9 and 6.10 that regular silicon active particles of size 100nm and less do not experience any fracture. Silicon active particles of size 200nm and higher goes through some amount of rupture and spanning crack propagation. Using functionally graded silicon, it will be investigated whether it is possible to increase the maximum particle size limit of zero fracture. Figure 6.16 shows the damage profile experienced by 200nm and 300nm sized functionally graded silicon active particles during successive lithiation-delithiation procedure. The four snapshots of damage profiles are obtained at midway into the lithiation $\left(t = 0.5t_0\right)$, end of lithiation $\left(t = 1.0t_0\right)$, halfway into delithiation $\left(t = 1.5t_0\right)$ and end of delithiation process $\left(t = 2.0t_0\right)$. From Figure 6.16 and comparing it with the values obtained from Figure 6.15, particles of initial diameter 200nm show around 11% microcrack density at the end of delithiation. This corresponds to zero formation of spanning cracks with functionally graded silicon materials. Whereas 300nm sized particles that used to observe severe fracture with regular silicon material, experiences around 16% microcrack density with the functionally graded material. It is evident that 300nm sized particles show some crack opening during the first half of the delithiation process (see Figure 6.16(g)), but most of them close at the end of delithiation (Figure 6.16(h)). The lithiation process is almost free from spanning cracks for the 300nm sized active particles (Figure 6.16(f)). According to our definition (elaborated while explaining Figure 6.10), 300nm sized functionally graded silicon active particles belong to the

range of some fracture. This is also evident from 16% microcrack density. Hence, it can be concluded that using functionally graded silicon material, active particles of size 200nm and smaller can be characterized as zero damage materials during lithiation-delithiation cycles.

Finally, a phase map is provided in Figure 6.17 to demonstrate the different combinations of particle diameter and the partial molar volume that gives rise to different amounts of mechanical degradation. This study has been conducted for regular

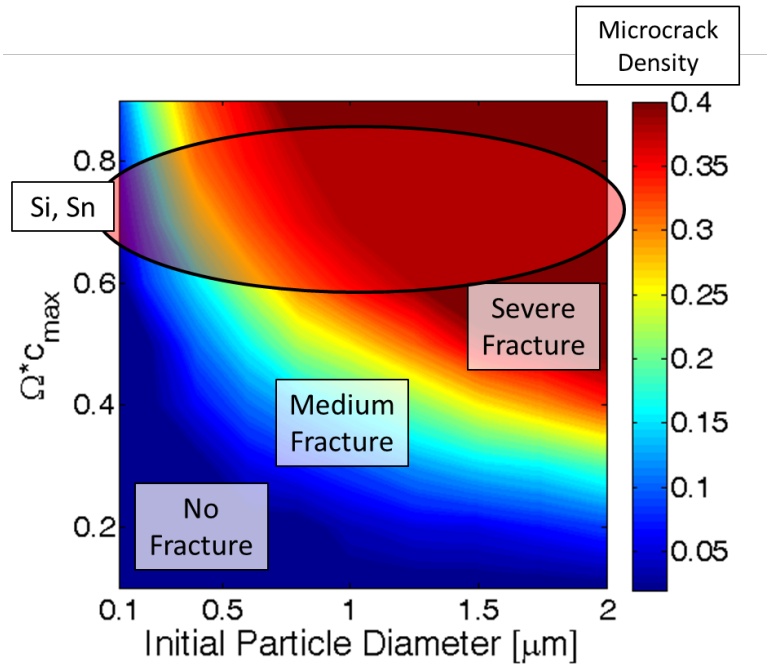

Fig: 6.17. *A phase map between particle size and partial molar volume to explain the amount of mechanical degradation observed during a single lithiation-delithiation cycle. The "colorbar" indicates amount of microcrack density. Three regions can be separately identified: a) If the amount of microcrack formation is less than 0.12, it can be characterized as "no fracture" region. b) If the total mechanical degradation is within 0.12 and 0.18, it can be categorized as medium fracture zone. Here, cracks open up during the lithiation process, but after complete delithiation, those crack fronts tries to close. c) Finally, if the microcrack density is greater than 0.18, severe mechanical degradation occurs, and spanning cracks are observable that also propagates. The portion where Si and Sn based anode active materials lie are shown using the red oval shaped object.*

silicon active particles with constant elastic modulus along the radial direction. The color bar signifies the microcrack density at the end of successive lithiation-delithiation procedure. Smaller sized particles (around 100nm) experience very little mechanical degradation even for very high partial molar volumes $\Omega \cdot c_{\max} = 0.9$. Whereas, the large sized particles, which has a diameter greater than 1μm, experiences severe fracture with partial molar volume as low as $\Omega \cdot c_{\max} = 0.5$. From Figure 6.17 it is evident that even for extremely large sized particles (around 5-10μm in diameter), there exists a certain magnitude of partial molar volume, around $\Omega \cdot c_{\max} = 0.3$, below which almost zero fracture is observed. However, the high capacity anode materials (such as, Si and Sn) shows partial molar volumes of magnitude 0.7 or 0.8 for the lithiated phase. Hence, the region of interest for the present analysis is highlighted in Figure 6.17 using the red oval shaped object. Particles of size 100nm or 150nm will be free from mechanical degradation (also supported experimentally [119]). Anything larger than that will experience fracture (demonstrated in Figures 6.9 and 6.10). This eventually leads to capacity fade due to the formation of solid electrolyte interface at the cracked surface. Hence, improved cyclic performance can be obtained for Si and Sn active particles of size 100nm or smaller. Usage of functionally graded materials (see Figure 6.13(a)) can increase the maximum particle size of zero fracture from 100nm to 200nm (demonstrated in Figures 6.15 and 6.16).

To validate the developed computational methodology with respect to a separate material (such as, Sn), the experimentally observed fracture within Sn active particles have been compared with the computational predictions (see [195]). The experimental

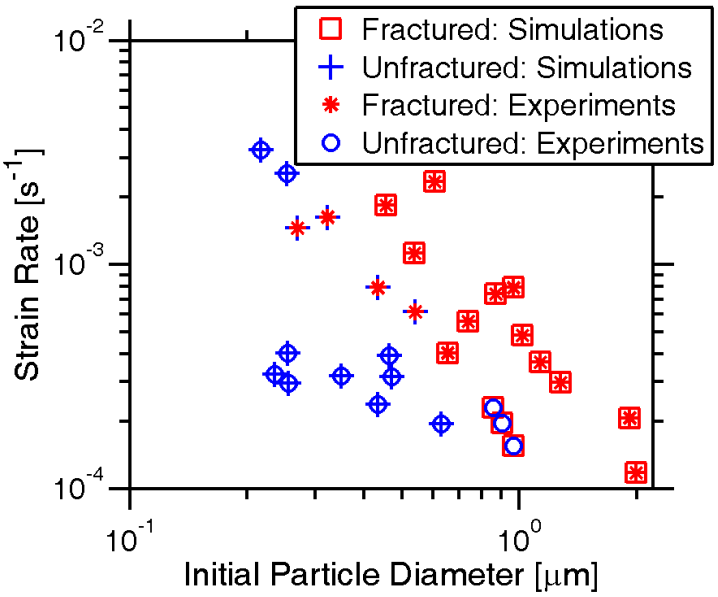

Fig: 6.18. *Comparison between the computationally predicted and experimentally observed fracture within the Sn active particles. For large particle sizes and high C-rate operations, the computational predictions correlate very well with experimentally observed phenomena. Similarly, computational predictions for medium and small particle sizes operating at relatively lower C-rates show extremely good correlation with experimental results. However, at some intermediate particle sizes and C-rates, discrepancies between the experimental and computational predictions exist.*

results were obtained from personal collaboration with Dr. Shen Dillon from UIUC (see [196]). Since the melting point of Sn is much lower than that of Si, creep deformation can become important during lithiation of Sn active particles at lower rates of operation. Since creep deformation can release some of the strain energy stored within the active particle through stress relaxation, less mechanical degradation is observed within Sn active particles at very low rates of operation (strain rate in the order of 10^{-4}/s). Figure 6.18 demonstrates a comparison of strain rate and particle size dependent fracture as obtained from experiments and computational simulations. For small sized active particles operating at lower strain rates, no fracture is ever observed and the computational results correlate very well with the experiments. Similarly, large particles

experiencing high strain rate fractures easily, this is similar for both simulations and experiments. However, particle size and strain rates that fall within the "*some/minor fracture*" regime, does not necessarily correlate well with the experimental results. This can be attributed to the nonexistence of a clear barrier between "*fractured*" and "*unfractured*" particles, in both the experimental and computational results.

6.4 Conclusion

High capacity materials, such as, silicon (Si) and tin (Sn) are strong candidates that can replace graphite as anode within next generation lithium ion batteries [121]. The cost of extremely high capacity in Si and Sn comes in the form of large volume expansion that leads to severe mechanical degradation [121]. Pulverization of the high capacity Si active particle leads to severe capacity fade due to SEI growth [11]. Particle isolation can lead to loss of active sites because of detachment from conductive additives. A computational methodology has been developed here that is capable of predicting the movement of two-phase fronts during the lithiation and delithiation process. At high C-rate operations or for large sized particles, during successive lithiation-delithiation process, two different two-phase fronts develop. For small active particles under low rate operation, the same two-phase front moves in during lithiation and comes out at the time of delithiation. Development of multiple two-phase fronts has the potential to generate enhanced amount of mechanical degradation. In the present study, lithiation-delithiation under high C-rate operation or within large sized particle is assumed, where two different multi-phase fronts get developed. Variation in the lithium

transport due to changes in volume of the active particle has not been taken into account in the present study, and will be investigated as part of a future article.

To capture the mechanical degradation due to two-phase transport of lithium within active particles, an updated lagrangian based lattice-spring methodology has been developed. The complete nonlinear strain displacement relation has been considered here [189]. Along with axial stiffness, shear resistance of the spring elements have also been taken into account. Larger magnitude of partial molar volume of the lithiated phase gives rise to not only higher concentration gradient induced load, but also larger tensile force under high volume expansion [147]. Hence, increased partial molar volume of the lithiated phase generates enhanced mechanical degradation [139]. Reducing the particle size significantly decreases the amount of microcrack density at the end of lithiation-delithiation process [119]. Silicon active particles of initial diameter 100nm and smaller, experience almost zero fracture during operation. A phase map has also been generated to demonstrate the amount of mechanical degradation that evolves during one lithiation-delithiation cycle. Various initial particle diameter and different partial molar volume of the lithiated phase has been considered while developing the phase diagram.

Fracture evolves to reduce the excessive strain energy stored within the material under externally applied loads [85]. If the material can be modified in such a way that less strain energy generates, smaller magnitude of mechanical degradation will also be observed. Two different techniques have been investigated that is capable of reducing the overall microcrack formation within silicon active particles. The first one involves introduction of a spanning crack at the surface of the particle (see Figure 6.13(b)). The

second technique deals with introduction of a functionally graded silicon active particle, which shows reduced elastic modulus close to the surface of the active particle (Figure 6.13(a)). It has been deduced that introduction of an external crack is not highly effective in reducing the overall microcrack density (see Figure 6.14). However, functionally graded silicon particles with reduced elastic modulus close to the surface is more effective in reducing the evolution of mechanical degradation (see Figures 6.15 and 6.16). Usage of functionally graded silicon can increase the maximum active particle size at which no fracture occurs from 100nm to 200nm (compare Figures 6.10(g) and 6.16(c)). Flow of electrolyte within the fractured portion of the electrode active particle has not been taken into account in the present study. Changes in lithium transport and microcrack formation due to presence of electrolyte within the cracked region will be considered as a future work.

Table: 6.1. List of parameters used in simulating silicon active particles.

Name of the parameter	Symbol	Units	Value
Diffusivity	D_{Li}	m^2 / s	2×10^{-12}
Maximum lithium concentration	$c_{s,\max}$	mol / m^3	29.52×10^{4}
Temperature	T	K	300
Non-dimensional enthalpy of mixing	ω	--	2.6
Gradient energy coefficient	κ	J / m	2.0×10^{-9}
Applied current	$I_{applied}$	A / m^2	44.183
Electrochemically active surface area	S	m^2	1.0
Young's modulus of the amorphous Li_xSi	E_a	GPa	45.0
Young's modulus of the crystalline Si	E_c	GPa	90.0
Shear modulus	G	GPa	20.0
Fracture threshold energy of amorphous Li_xSi	$\psi_{t,a}$	J / m^2	5.0
Fracture threshold energy of crystalline Si	$\psi_{t,c}$	J / m^2	10.0

CHAPTER VII

CONCLUSION AND FUTURE WORK

Due to the increased commercialization of lithium ion chemistry, it is desired to extend the lifetime of lithium ion batteries[86]. Significant amount of research is being conducted to characterize the reason behind the capacity fade and resistance growth experienced by the lithium ion batteries[197]. In the present thesis, impact of mechanical degradation of the capacity fade has been investigated. Different types of diffusion induced load and multiple anode active materials are considered here.

7.1. Conclusion

Graphite anode active particles experience mechanical degradation due to concentration gradient induced load. Within graphite, transport of lithium happens via a single phase diffusion process. During delithiation, shortage of lithium ions produces tensile stress close to the surface of the active particle. Compressive stress is observed at the center of the active particles. On the other hand, during lithiation, compression is observed at the particle surface and tension at the center. Depending on the type of force that acts on the graphite active particle, surface cracks develop at the time of delithiation and central microcracks evolve during lithiation process. Electrolyte can flow through the cracks which are connected to the surface of the active particle. However, in the present analysis it has been assumed that electrolyte cannot penetrate within the active particles because of the very small width of the spanning crack fronts. Presence of

microcracks is assumed to hinder the diffusion pathway for lithium. Since the lithium atoms cannot directly cross the voids produced by the microcracks, they take a tortuous pathway to go around the microscopic damages. This increased resistance to lithium diffusion is taken into consideration by lowering the local lithium diffusivity by a certain fraction. Hence the mass transport resistance of the cell increases significantly. Since more mechanical degradation is observed at higher rates of operation, capacity fade due to mass transport resistance is also large at high C-rates.

During lithiation-delithiation, graphite active particles does not experience significant change in volume. Models that capture small strain and small deformation of active particles are sufficient for graphite. In this model development the major focus has been to capture the evolution of microcracks within the material. A random lattice spring based computational methodology has been adopted to predict the evolution of mechanical degradation. Diffusion induced load is assumed to be directly proportional to the concentration gradient. An energy prescribed criterion has been implemented to capture the formation of microcracks. As soon as the strain energy within a lattice spring element exceeds its fracture threshold, it is assumed to be broken and irreversibly removed from the network. Multiple adjacent broken bonds form a spanning crack. The present analysis indicates that smaller active particles experience less mechanical degradation. Also, operation at low C-rate does not give rise to significant amount of microcracks. The effect of concentration dependent elastic modulus on microcrack formation has been investigated. It was revealed that constant values of elastic modulus can significantly underestimate the total amount of mechanical degradation. Due to

saturation in strain energy release, mechanical degradation in the form of brittle fragmentation stops after two or three delithiation-lithiation cycles. However, the effect of fatigue loading has not been considered in the present context.

Because of the high demand in electronic, automotive and grid energy storage industry, it has become necessary to increase the energy density of lithium ion batteries. One possibility is to use high energy density active materials (such as, Si, Sn, Ge) to construct the anode of the lithium ion battery. Lithium reacts with these high capacity anode materials through an alloying mechanism. Two different phases exist within the active material in a core-shell pattern. For Si active particles, during lithiation, the amorphous lithiated-Si shell exists close to the surface. The crystalline-Si core lies at the center. Large concentration gradient at the two phase interface induces significant amount of tensile stress at the lithium poor phase. Large volume expansion is also a major drawback of these high capacity anode materials. Tensile stress at the surface of the active particle due to the large volume expansion can produce significant spanning cracks. The two phase diffusion of lithium is captured by solving Cahn-Hilliard equation along the radial direction of the circular active particle. The rate of lithiation-delithiation and particle size governs the evolution of concentration within the active particles. If a single two phase front moves in during lithiation, and comes out at the time of delithiation, the overall mechanical degradation is relatively small. On the contrary, as observed during fast lithiation-delithiation process, if two different two-phase fronts develop within the active particles, significantly large microcrack formation can happen.

The random lattice spring method developed for small volume expansion graphite particles have been extended for capturing the fracture of Si active particles. Since large volume expansion occurs within Si active particles, the traditional lattice spring method needs to be modified to capture the large strain large deformation aspects. The complete nonlinear strain-displacement relation has been used to calculate the strain of the spring element along the axial direction. Multiplicative decomposition has been conducted to separate the elastic strain from the concentration induced strain. The results clearly indicate that, during lithiation, majority of the mechanical degradation happens from the surface of the active particle. At the two-phase interface, concentration gradient induced tensile load does not give rise to significant amount of microcracks. However, during delithiation, large tensile stress at the surface of the active particle results in significant propagation of the preexisting cracks. Active particles of diameter 100nm and smaller does not experience any mechanical degradation due to the concentration induced load. Usage of functionally graded Si with reduced elastic modulus close to the surface of the active particle has the potential to significantly mitigate the problem of microcrack formation. Addition of preexisting cracks is not effective in reducing the overall mechanical degradation within the active particles.

Increasing mechanical degradation within the active particles increases the mass transport resistance inside solid phase. This is captured as reduction in effective diffusivity of the solid active particle. A Bruggeman type power law relation has been proposed to estimate the decrease in solid phase diffusivity as a function of “fraction of broken elements”. Exact value of the power law exponent has been estimated by

comparing the concentration gradient predicted by the 2D model and that obtained from 1D models but using the effective diffusivity. A reduced order model has also been developed that can predict the evolution of microcrack formation as a function of particle size and C-rate. The ROM for mechanical degradation and the microcrack dependent effective diffusivity has been implemented on top of a porous electrode theory. Mechanical degradation in the graphite electrode has only been taken into consideration. The simulation result clearly indicates uniform mechanical degradation along the thickness of the negative electrode at the end of the discharge process. Enhanced evolution of microcrack has also been observed for operation at higher C-rates and for large sized active particles. Lithium ion batteries used in electric vehicle does not experience constant charge or discharge process. Constant current pulses of charge and discharge is observed by the lithium ion cell during drive cycle operation. Hybrid electric vehicles (HEVs) experience the strongest current pulses because of their very low capacity. Under drive cycle operation, active particles of radius 10μm and smaller, does not experience significant capacity fade from microcrack formation. However, active particles of radius 12.5μm or larger, can experience around 10% capacity fade due to mechanical degradation while operating only under drive cycle conditions. Impact of fracture on chemical degradation has not been investigated here.

Experimental characterization of crack formation within active particles can be conducted using the acoustic emission technique. Several acoustic emission based experimental studies indicate that fracture of active particles due to diffusion induced stress, saturates after four or five lithiation-delithiation cycles. The lattice spring method

applicable to small strain small displacement systems, has been updated to incorporate the effect of inertia and dependence on time. By solving the complete time dependent momentum balance equation, acoustic signature of graphite active particles has been obtained during microcrack formation. Large amount of strain energy release at the time of crack propagation produces oscillations of very high amplitude. Cumulative strain energy release calculated from the acoustic response provides a very good estimation of the total amount of mechanical degradation. Saturation in strain energy release after two or three cycles can be predicted from the computational simulations as well. Elastic stiffness and damping coefficient of the material shows huge impact on the overall acoustic response. A phase map has been developed that indicates the range of elastic modulus and damping coefficient which results in less microcrack formation within the active particles. The cumulative strain energy release profile contains multiple jumps, which indicates release of large amount of strain energy in a very short interval of time. These jumps are characterized as avalanches when large number of weak elements breaks over a very short period of time giving rise to significant amount of release in strain energy.

Approximating the brittle active material as a disordered media, evolution of microcracks and complete rupture of the lattice spring network under diffusion induced load has been analyzed. It has been observed that initially, as long as disorder of the media dominates, mechanical degradation increases in a random fashion. After sometime, once the effect of stress concentration dominates over the disorder effect, bunch of microcracks nucleate and forms a spanning crack. Much less diffusion induced

load is required for the propagation of this spanning crack. Based on the mechanism of damage evolution, the entire rupture process can be divided into two steps: a) Uniformly distributed microcrack formation with increasing diffusion induced load, and b) Stress concentration driven propagation of spanning cracks at a significantly lower diffusion induced load. Statistical analysis of number of broken elements, fracture strength and crack surface roughness indicates the presence of two step damage evolution. For a disordered media with grain/grain-boundary microstructure, reduced elastic modulus of grain-boundary causes the crack front to propagate only through the grain-boundary region. Disordered media with smaller grain size experience higher strength because of the hindrance provided by the tortuous pathway of the small grains on the propagating crack.

7.2. Future work

Almost all the work presented in this thesis can be extended to solve more complex problems. Other physical phenomena observed inside lithium ion batteries can be incorporated within these models to make it more generalized with minor extra effort. One major assumption while modeling diffusion and fracture within the low volume expansion graphite electrode particle is that electrolyte cannot flow through the cracks connected with the surface. However, in a realistic scenario, this is not strictly true. Electrolyte can easily flow through the surface crack front that has significantly large width. Hence the electrochemical reaction is not confined only at the surface. Lithium influx can also occur from the cracked region. This can significantly affect both the lithium ion concentration as well as crack propagation inside the active particles. During

lithiation-delithiation process, a cyclic load acts on top of the active particles. Hence mechanical degradation emanating from fatigue of the material must be taken into consideration. In the present analysis any such fatigue mechanism has not been taken into account. As a result, the crack evolution was observed to saturate after three-four cycles. Incorporating the effect of fatigue mechanics can significantly increase the chances of crack propagation over multiple charge-discharge cycles. Incorporation of flow of electrolyte within the cracked region and reduction of fracture threshold with increasing number of cycles can produce the long cracks usually observed within used graphite active particles.

For the small strain small displacement lattice spring model, the values of axial and shear stiffness of the spring elements have been estimated using an energy equivalence scheme. That technique may not be always applicable for networks with ruptured springs. Hence, calibration of the lattice spring model with respect to correct experimentally observed elastic modulus should be conducted to estimate the exact values of axial and shear stiffness of the springs. Estimation of the fracture threshold of each spring is also a big challenge. A magnitude of the fracture threshold can be estimated based on the cross-sectional area of the springs, but that does not necessarily correspond to the exact fracture threshold predicted by experiments. Proper calibration of the threshold energy should be conducted and how it is distributed around the mean value must be studied thoroughly. At present only uniform distribution is taken into consideration. Whether normal or exponential distributions of the fracture threshold energy capture the reality better, is another topic that can be pursued as a future task.

While modeling the diffusion of lithium within high capacity anode materials (such as, Si), the moving boundary has not been taken into consideration. The entire concentration gradient is calculated based on the initial configuration. However, with lithiation as the particle fractures and deforms, the lithium flux and concentration distribution changes, which has not been incorporated in the present context. Also, flow of electrolyte within the active particles has not been taken into account. A future work possibility is to add the effect of large deformation and flow of electrolyte in the surface cracks while solving for the concentration distribution inside the active particle. Addition of the effect of stress on lithium diffusion can also be a very useful extension of the present work.

The developed pseudo 2D model for estimating performance of lithium ion batteries uses a constant value for electrolyte conductivity. However, according to the concentrated solution theory, both conductivity and diffusivity of lithium within the electrolyte is a function of local lithium concentration. Usage of concentration dependent electrolyte conductivity is a must for more accurate prediction of performance. Under fast charge-discharge conditions, when the electrolyte becomes transport limited, existence of a diffusion layer must be taken into consideration. Butler-Volmer kinetics might not be applicable in such diffusion limited scenarios, and the existence of a diffusion layer must be taken into consideration. Updating the pseudo 2D model to incorporate the effect of diffusion layer under lower magnitude of lithium concentration can be a very good future work. Another possibility is to modify the pseudo 2D model into full scale 2D model for predicting performance of lithium ion

batteries. Irregular shape of the active particles can be successfully captured using the full scale 2D lithium ion battery model. Electrochemical isolation of active particles due to transport limitations can also be predicted using the 2D lithium ion battery model.

It has been estimated that total amount of mechanical degradation saturates after three or four cycles for both small volume expansion as well as large volume expansion materials. Direct impact of microcrack formation on the cell performance is well captured in the present study. However, solid electrolyte interface (SEI) can form on the cracked surface, which results in loss of cyclable lithium. Formation of the SEI layer causes capacity fade and impacts the total lifespan of the lithium ion battery. In the present research, reaction of electrolyte with the fresh electrode surface and formation of SEI is not taken into account. SEI formation, subsequent capacity fade and impact on battery life can also be an important extension of the present research.

The computational model developed to capture the acoustic response during crack propagation of low volume expansion active materials assumes constant value of elastic modulus for all lithium concentration level. Variation in the elastic stiffness with changing lithium concentration has been studied extensively. Hence the assumption of constant elastic modulus is far from the realistic scenario. Incorporation of concentration dependent elastic modulus is a necessary future extension that must be incorporated to use the acoustic emission model for further applications. Also the developed model only captures the acoustic signature due to fracture within the active particles. Acoustic emission emanating due to delamination between active particle-binder interfaces can also be estimated using the developed model after minor modification of the existing

model. Fast Fourier Transform can be utilized to differentiate between the acoustic response that generates from the fracture of active particle and that evolves due to delamination of particle-binder interface. Extension of the model to predict the acoustic signature of an entire lithium ion battery can be considered as a very useful future work. Estimation of the state of health (SOH) of the lithium ion cell in a non-invasive fashion is the main aim behind the usage of acoustic emission technique.

Finally, while calculating the fracture strength of different grain/grain-boundary microstructure a linear concentration gradient has been applied on top of the lattice spring network. Since diffusion of lithium happens at different rate inside the grain interior and the grain boundary region, uniform linear variation in concentration can never be achieved. Exact lithium ion concentration distribution must be estimated by solving the diffusion equation along with the effect of hydrostatic stress to correctly predict the crack propagation within the grain/grain-boundary microstructure. Only brittle fracture of the grain interior and grain boundary region has been modeled here. Incorporation of plastic deformation of the grain interior can definitely improve the quality of the solution and make it more close to that observed in experiments. Hence, there are chances of improving almost all the computational methodologies reported in the present thesis to make it more accurate and predict the experimental response correctly. New physics can also be added on top of the developed framework to capture different multi-physical phenomena.

REFERENCES

[1] K. Annamalai, I. K. Puri, and M. A. Jog, *Advanced thermodynamics engineering*: CRC Press, 2011.

[2] M. J. Moran, H. N. Shapiro, D. D. Boettner, and M. B. Bailey, *Fundamentals of engineering thermodynamics*. United States of America: John Wiley and Sons, 2011.

[3] M. Winter and R. J. Brodd, "What are batteries, fuel cells, and supercapacitors?," *Chemical Reviews,* vol. 104, pp. 4245-4269, Oct 2004.

[4] C. D. Rahn and C.-Y. Wang, *Battery systems engineering*: John Wiley and Sons, 2013.

[5] E. J. Cairns and P. Albertus, "Batteries for electric and hybrid-electric vehicles," *Annual Review of Chemical and Biomolecular Engineering, Vol 1,* vol. 1, pp. 299-320, 2010.

[6] J. Christensen, "Modeling diffusion-induced stress in Li-ion cells with porous electrodes," *Journal of the Electrochemical Society,* vol. 157, pp. A366-A380, 2010.

[7] J. Liu, J. W. Wang, X. D. Yan, X. F. Zhang, G. L. Yang, A. F. Jalbout*, et al.*, "Long-term cyclability of LiFePO4/carbon composite cathode material for lithium-ion battery applications," *Electrochimica Acta,* vol. 54, pp. 5656-5659, Oct 1 2009.

[8] A. J. Bard and L. R. Faulkner, *Electrochemical methods: Fundamentals and applications*: John Wiley and Sons, 2001.

[9] P. Arora, R. E. White, and M. Doyle, "Capacity fade mechanisms and side reactions in Lithium - Ion batteries," *Journal of The Electrochemical Society,* vol. 145, pp. 3647 - 3667, 1998.

[10] R. Narayanrao, M. M. Joglekar, and S. Inguva, "A phenomenological degradation model for cyclic aging of Lithium ion cell materials," *Journal of the Electrochemical Society,* vol. 160, pp. A125-A137, 2013.

[11] M. B. Pinson and M. Z. Bazant, "Theory of SEI formation in rechargeable batteries: Capacity fade, accelerated aging and lifetime prediction," *Journal of the Electrochemical Society,* vol. 160, pp. A243-A250, 2013.

[12] D. Y. Wang, X. D. Wu, Z. X. Wang, and L. Q. Chen, "Cracking causing cyclic instability of LiFePO4 cathode material," *Journal of Power Sources,* vol. 140, pp. 125-128, Jan 10 2005.

[13] H. F. Wang, Y. I. Jang, B. Y. Huang, D. R. Sadoway, and Y. T. Chiang, "TEM study of electrochemical cycling-induced damage and disorder in LiCoO2 cathodes for rechargeable lithium batteries," *Journal of the Electrochemical Society,* vol. 146, pp. 473-480, Feb 1999.

[14] T. K. Bhandakkar and H. Gao, "Cohesive modeling of crack nucleation under diffusion induced stresses in a thin strip: Implications on the critical size for flaw tolerant battery electrodes," *International Journal of Solids and Structures,* vol. 47, pp. 1424 - 1434, 2010.

[15] J. Lemaitre and J. L. Chaboche, *Mechanics of solid materials*: Cambridge University Press, 1990.

[16] W. H. Woodford, Y. M. Chiang, and W. C. Carter, ""Electrochemical shock" of intercalation electrodes: A fracture mechanics analysis," *Journal of the Electrochemical Society,* vol. 157, pp. A1052-A1059, 2010.

[17] R. Grantab and V. B. Shenoy, "Location- and orientation-dependent progressive crack propagation in cylindrical graphite electrode particles," *Journal of the Electrochemical Society,* vol. 158, pp. A948-A954, 2011.

[18] C. K. Chan, H. L. Peng, G. Liu, K. McIlwrath, X. F. Zhang, R. A. Huggins*, et al.*, "High-performance lithium battery anodes using silicon nanowires," *Nature Nanotechnology,* vol. 3, pp. 31-35, Jan 2008.

[19] Y.-T. Cheng and M. W. Verbrugee, "The influence of surface mechanics on diffusion induced stresses within spherical nanoparticles," *Journal of Applied Physics,* vol. 104, p. 083521, 2008.

[20] B. J. Dimitrijevic, K. E. Aifantis, and K. Hackl, "The influence of particle size and spacing on the fragmentation of nanocomposite anodes for Li batteries," *Journal of Power Sources,* vol. 206, pp. 343-348, May 15 2012.

[21] S. Renganathan, G. Sikha, S. Santhanagopalan, and R. E. White, "Theoretical analysis of stresses in a lithium ion cell," *Journal of the Electrochemical Society,* vol. 157, pp. A155 - A163, 2010.

[22] S. J. Harris, R. D. Deshpande, Y. Qi, I. Dutta, and Y. T. Cheng, "Mesopores inside electrode particles can change the Li-ion transport mechanism and

diffusion-induced stress," *Journal of Materials Research,* vol. 25, pp. 1433-1440, Aug 2010.

[23] F. Joho, B. Rykart, A. Blome, P. Novak, H. Wilhelm, and M. E. Spahr, "Relation between surface properties, pore structure and first cycle charge loss of graphite as negative electrode in lithium-ion batteries," *Journal of Power Sources,* vol. 97 - 98, pp. 78 - 82, 2001.

[24] Y.-T. Cheng and M. W. Verbrugee, "Diffusion-induced stress, interfacial charge transfer, and criteria for avoiding crack initiation of electrode particles.," *Journal of The Electrochemical Society,* vol. 157, pp. A508 - A516, 2010.

[25] R. E. Garcia, Y.-M. Chiang, W. C. Carter, P. Limthongkul, and C. M. Bishop, "Microstructure modeling and design of rechargeable Lithium-Ion batteries," *Journal of The Electrochemical Society,* vol. 152, pp. A255 - A263, 2005.

[26] S. Golmon, K. Maute, and M. L. Dunn, "Numerical modeling of electrochemical–mechanical interactions in lithium polymer batteries," *Computers and Structures,* vol. 87, pp. 1567 - 1579, 2009.

[27] R. Deshpande, Y. Qi, and Y. T. Cheng, "Effects of concentration-dependent elastic modulus on diffusion-induced stresses for battery applications," *Journal of the Electrochemical Society,* vol. 157, pp. A967-A971, 2010.

[28] V. B. Shenoy, P. Johari, and Y. Qi, "Elastic softening of amorphous and crystalline Li-Si phases with increasing Li concentrations: A first principles study," *Journal of Power Sources,* vol. 195, pp. 6825 - 6830, 2010.

[29] R. Deshpande, Y. T. Cheng, and M. W. Verbrugge, "Modeling diffusion-induced stress in nanowire electrode structures," *Journal of Power Sources,* vol. 195, pp. 5081-5088, Aug 1 2010.

[30] M. J. Alava, P. K. V. V. Nukalaz, and S. Zapperi, "Statistical models of fracture," *Advances in Physics,* vol. 55, pp. 349-476, May-Jun 2006.

[31] J. A. Astrom, "Statistical models of brittle fragmentation," *Advances in Physics,* vol. 55, pp. 247-278, May-Jun 2006.

[32] M. Zaiser, "Scale invariance in plastic flow of crystalline solids," *Advances in Physics,* vol. 55, pp. 185-245, Jan-Apr 2006.

[33] B. Lawn, *Fracture of brittle solids*. New York: Cambridge University Press, 1993.

[34] J. Nolting, "Disorder in solids (Ionic crystals and metals)," *Angewandte Chemie-International Edition,* vol. 9, pp. 489-&, 1970.

[35] A. S. Balankin, O. Susarrey, C. A. M. Santos, J. Patino, A. Yoguez, and E. I. Garcia, "Stress concentration and size effect in fracture of notched heterogeneous material," *Physical Review E,* vol. 83, Jan 18 2011.

[36] M. Ansari-Rad, S. M. V. Allaei, and M. Sahimi, "Nonuniversality of roughness exponent of quasistatic fracture surfaces," *Physical Review E,* vol. 85, Feb 15 2012.

[37] P. Barai, R. Sampath, P. K. V. V. Nukala, and S. Simunovic, "Scaling of surface roughness in perfectly plastic disordered media," *Physical Review E,* vol. 82, Nov 19 2010.

[38] G. A. Buxton and A. C. Balazs, "Lattice spring model of filled polymers and nanocomposites," *Journal of Chemical Physics,* vol. 117, pp. 7649-7658, Oct 22 2002.

[39] R. Deshpande, M. Verbrugge, Y. T. Cheng, J. Wang, and P. Liu, "Battery cycle life prediction with coupled chemical degradation and fatigue mechanics," *Journal of the Electrochemical Society,* vol. 159, pp. A1730-A1738, 2012.

[40] A. Etiemble, H. Idrissi, and L. Roue, "On the use of acoustic emission technique for in-situ monitoring of the pulverization of battery electrodes," in *30th European Conference on Acoustic Emission Testing & 7th International Conference on Acoustic Emission* University of Granada, 2012.

[41] T. Goldman, R. Harpaz, E. Bouchbinder, and J. Fineberg, "Intrinsic nonlinear scale governs oscillations in rapid fracture," *Physical Review Letters,* vol. 108, Mar 9 2012.

[42] S. W. Lee, M. T. McDowell, L. A. Berla, W. D. Nix, and Y. Cui, "Fracture of crystalline silicon nanopillars during electrochemical lithium insertion," *Proceedings of the National Academy of Sciences of the United States of America,* vol. 109, pp. 4080-4085, Mar 13 2012.

[43] L. Y. Liang, Y. Qi, F. Xue, S. Bhattacharya, S. J. Harris, and L. Q. Chen, "Nonlinear phase-field model for electrode-electrolyte interface evolution," *Physical Review E,* vol. 86, Nov 26 2012.

[44] P. K. V. V. Nukala, S. Zapperi, and S. Simunovic, "Statistical properties of fracture in a random spring model," *Physical Review E,* vol. 71, Jun 2005.

[45] C. B. Picallo, J. M. Lopez, S. Zapperi, and M. J. Alava, "From brittle to ductile fracture in disordered materials," *Physical Review Letters,* vol. 105, Oct 7 2010.

[46] T. D. Xu and L. Zheng, "The elastic modulus in the grain-boundary region of polycrystalline materials," *Philosophical Magazine Letters,* vol. 84, pp. 225-233, Apr 2004.

[47] G. Wang, A. Al-Ostaz, A. H. D. Cheng, and P. R. Mantena, "Hybrid lattice particle modeling: Theoretical considerations for a 2D elastic spring network for dynamic fracture simulations," *Computational Materials Science,* vol. 44, pp. 1126-1134, Feb 2009.

[48] Y. Ohya, Z. E. Nakagawa, and K. Hamano, "Grain-boundary microcracking due to thermal-expansion anisotropy in aluminum titanate ceramics," *Journal of the American Ceramic Society,* vol. 70, pp. C184-C186, Aug 1987.

[49] Y. Ohya and Z. Nakagawa, "Measurement of crack volume due to thermal expansion anisotropy in aluminium titanate ceramics," *Journal of Materials Science,* vol. 31, pp. 1555-1559, Mar 15 1996.

[50] S. W. Paulik, M. H. Zimmerman, K. T. Faber, and E. R. Fuller, "Residual stress in ceramics with large thermal expansion anisotropy," *Journal of Materials Research,* vol. 11, pp. 2795-2803, Nov 1996.

[51] N. Sridhar, W. H. Yang, D. J. Srolovitz, and E. R. Fuller, "Microstructural mechanics model of anisotropic-thermal-expansion-induced microcracking," *Journal of the American Ceramic Society,* vol. 77, pp. 1123-1138, May 1994.

[52] D. P. H. Hasselman and J. P. Singh, "Role of mixed-mode crack propagation in thermally shocked brittle materials," *Theoretical and Applied Fracture Mechanics,* vol. 2, pp. 59 - 65, 1984.

[53] H. A. Bahr, H. Balke, M. Kuna, and H. Liesk, "Fracture-analysis of a single edge cracked strip under thermal-shock," *Theoretical and Applied Fracture Mechanics,* vol. 8, pp. 33-39, Aug 1987.

[54] H. A. Bahr, G. Fischer, and H. J. Weiss, "Thermal-shock crack patterns explained by single and multiple crack propagation," *Journal of Materials Science,* vol. 21, pp. 2716 - 2720, 1986.

[55] H. A. Bahr, H. J. Weiss, H. G. Maschke, and F. Meissner, "Multiple crack-propagation in a strip caused by thermal-shock," *Theoretical and Applied Fracture Mechanics,* vol. 10, pp. 219-226, Dec 1988.

[56] L. Dearcangelis, S. Redner, and H. J. Herrmann, "A random fuse model for breaking processes," *Journal De Physique Lettres,* vol. 46, pp. L585-L590, 1985.

[57] A. Jagota and S. J. Bennison, "Spring-network and finite-element models for elasticity and fracture," *Lecture Notes in Physics,* vol. 437, pp. 186 - 201, 1994.

[58] P. K. V. V. Nukala, S. Zapperi, M. J. Alava, and S. Simunovic, "Crack roughness in the two-dimensional random threshold beam model," *Physical Review E,* vol. 78, Oct 2008.

[59] G. A. Buxton, C. M. Care, and D. J. Cleaver, "A lattice spring model of heterogeneous materials with plasticity," *Modelling and Simulation in Materials Science and Engineering,* vol. 9, pp. 485-497, Nov 2001.

[60] G. A. Buxton and A. C. Balazs, "Micromechanical simulation of the deformation and fracture of polymer blends," *Macromolecules,* vol. 38, pp. 488-500, Jan 25 2005.

[61] E. Schlangen and E. J. Garboczi, "Fracture simulations of concrete using lattice models: Computational aspects," *Engineering Fracture Mechanics,* vol. 57, pp. 319-332, May-Jun 1997.

[62] S. I. Heizler, D. A. Kessler, and H. Levine, "Propagating mode-I fracture in amorphous materials using the continuous random network model," *Physical Review E,* vol. 84, Aug 3 2011.

[63] S. Kalnaus, K. Rhodes, and C. Daniel, "A study of lithium ion intercalation induced fracture of silicon particles used as anode material in Li-ion battery," *Journal of Power Sources,* vol. 196, pp. 8116-8124, Oct 1 2011.

[64] T. Ohzuku, H. Tomura, and K. Sawai, "Monitoring of particle fracture by acoustic emission during charge and discharge of Li/MnO2 cells," *Journal of the Electrochemical Society,* vol. 144, pp. 3496-3500, Oct 1997.

[65] K. Rhodes, N. Dudney, E. Lara-Curzio, and C. Daniel, "Understanding the degradation of Silicon electrodes for Lithium-ion batteries using acoustic emission," *Journal of the Electrochemical Society,* vol. 157, pp. A1354-A1360, 2010.

[66] M. Huang, L. Jiang, P. K. Liaw, C. R. Brooks, R. Seeley, and D. L. Klarstrom, "Using acoustic emission in fatigue and fracture materials research," *JOM-e,* vol. 50, 1998.

[67] A. Garcimartin, A. Guarino, L. Bellon, and S. Ciliberto, "Statistical properties of fracture precursors," *Physical Review Letters,* vol. 79, pp. 3202-3205, Oct 27 1997.

[68] L. I. Salminen, A. I. Tolvanen, and M. J. Alava, "Acoustic emission from paper fracture," *Physical Review Letters,* vol. 89, Oct 28 2002.

[69] M. A. Hamstad, "A review - Acoustic-emission, a tool for composite-materials studies," *Experimental Mechanics,* vol. 26, pp. 7-13, Mar 1986.

[70] M. H. B.Nasseri, B. Thompson, A. Schubnel, and R. P. Young, "Acoustic emission monitoring of Mode I fracture toughness (CCNBD) test in Lac du Bonnet granite," in *The 40th U.S. Symposium on Rock Mechanics (USRMS)*, Anchorage, Alaska, 2005.

[71] W. Grosshandler and M. JAckson, "Acoustic emission of structural materials exposed to open flames," *Fire Safety Journal,* vol. 22, pp. 209 - 228, 1994.

[72] K. E. Aifantis, S. A. Hackney, and J. P. Dempsey, "Design criteria for nanostructured Li-ion batteries," *Journal of Power Sources,* vol. 165, pp. 874-879, Mar 20 2007.

[73] H. Heidary, A. R. Oskouei, and M. Ahmadi, "Mechanism detection of stress corrosion cracking by acoustic emission and effect of manufacturing process on AE signals," in *Acoustics*, Paris, 2008, pp. 2109 - 2114.

[74] M. Kalicka and T. Vogel, "Acoustic emission in structural health monitoring - corrosion detecting in post-tensioned girders," in *8th International PhD Symposium in Civil Engineering*, Kgs. Lyngby, Denmark, 2010.

[75] K. J. Rhodes, R. Meisner, M. Kirkham, N. Dudney, and C. Daniel, "In situ XRD of thin film Tin electrodes for Lithium ion batteries," *Journal of the Electrochemical Society,* vol. 159, pp. A294-A299, 2012.

[76] T. Fukushima, N. Kuwata, and J. Kawamura, "In-situ acoustic emission study of Sn anode in Li ion battery," in *The 17th International Meeting on Lithium Batteries*, Como, Italy, 2014.

[77] T. Matsuo, M. Uchida, and H. Cho, "Development of acoustic emission clustering method to detect degredation of lithium ion batteries," *Journal of Solid Mechanics and Materials Engineering,* vol. 5, pp. 678 - 689, 2011.

[78] C. Villevieille, M. Boinet, and L. Monconduit, "Direct evidence of morphological changes in conversion type electrodes in Li-ion battery by

acoustic emission," *Electrochemistry Communications,* vol. 12, pp. 1336 - 1339, 2010.

[79] W. H. Woodford, W. C. Carter, and Y. M. Chiang, "Design criteria for electrochemical shock resistant battery electrodes," *Energy & Environmental Science,* vol. 5, pp. 8014-8024, Jul 2012.

[80] W. H. Woodford, Y. M. Chiang, and W. C. Carter, "Electrochemical shock in ion-intercalation materials with limited solid-solubility," *Journal of the Electrochemical Society,* vol. 160, pp. A1286-A1292, 2013.

[81] R. Teti and D. Dornfeld, "Modeling and experimental analysis of acoustic emission from metal cutting," *Journal of Engineering for Industry,* vol. 111, pp. 229 - 237, 1989.

[82] M. Minozzi, G. Caldarelli, L. Pietronero, and S. Zapperi, "Dynamic fracture model for acoustic emission," *European Physical Journal B,* vol. 36, pp. 203-207, Nov 2003.

[83] M. Marder and X. M. Liu, "Instability in lattice fracture," *Physical Review Letters,* vol. 71, pp. 2417-2420, Oct 11 1993.

[84] X. H. Liu, L. Zhong, S. Huang, S. X. Mao, T. Zhu, and J. Y. Huang, "Size-dependent fracture of Silicon nanoparticles during lithiation," *Acs Nano,* vol. 6, pp. 1522-1531, Feb 2012.

[85] P. Barai and P. P. Mukherjee, "Stochastic analysis of diffusion induced damage in Lithium-ion battery electrodes," *Journal of the Electrochemical Society,* vol. 160, pp. A955-A967, 2013.

[86] J. M. Tarascon and M. Armand, "Issues and challenges facing rechargeable lithium batteries," *Nature,* vol. 414, pp. 359-367, Nov 15 2001.

[87] M. Zackrisson, L. Avellan, and J. Orlenius, "Life cycle assessment of lithium-ion batteries for plug-in hybrid electric vehicles - Critical issues," *Journal of Cleaner Production,* vol. 18, pp. 1519-1529, Oct 2010.

[88] A. Awarke, S. Pischinger, and J. Ogrzewalla, "Pseudo 3D modeling and analysis of the SEI growth distribution in large format Li-ion polymer pouch cells," *Journal of the Electrochemical Society,* vol. 160, pp. A172-A181, 2013.

[89] K. Smith, M. Earleywine, E. Wood, J. Neubauer, and A. Pesaran, "Comparison of plug-in hybrid electric vehicle battery life across geographies and drive cycles," presented at the 2012 SAE World Congress, Detroit, Michigan, 2012.

[90] V. Etacheri, R. Marom, R. Elazari, G. Salitra, and D. Aurbach, "Challenges in the development of advanced Li-ion batteries: a review," *Energy & Environmental Science,* vol. 4, pp. 3243-3262, Sep 2011.

[91] H. D. Yoo, E. Markevich, G. Salitra, D. Sharon, and D. Aurbach, "On the challenge of developing advanced technologies for electrochemical energy storage and conversion," *Materials Today,* vol. 17, pp. 110-121, Apr 2014.

[92] J. Christensen and J. Newman, "A mathematical model for the lithium-ion negative electrode solid electrolyte interphase," *Journal of the Electrochemical Society,* vol. 151, pp. A1977-A1988, 2004.

[93] G. Ning, B. Haran, and B. N. Popov, "Capacity fade study of lithium-ion batteries cycled at high discharge rates," *Journal of Power Sources,* vol. 117, pp. 160-169, May 15 2003.

[94] S. M. M. Alavi, M. F. Samadi, and M. Saif, "Plating mechanism detection in Lithium-ion batteries, by using a particle-filtering based estimation technique," *2013 American Control Conference (Acc),* pp. 4356-4361, 2013.

[95] M. Rashid and A. Gupta, "Mathematical model for combined effect of SEI formation and gas evolution in Li-ion batteries," *Ecs Electrochemistry Letters,* vol. 3, pp. A95-A98, 2014.

[96] H. Jannesari, M. D. Emami, and C. Ziegler, "Effect of electrolyte transport properties and variations in the morphological parameters on the variation of side reaction rate across the anode electrode and the aging of lithium ion batteries," *Journal of Power Sources,* vol. 196, pp. 9654-9664, Nov 15 2011.

[97] G. Ning, R. E. White, and B. N. Popov, "A generalized cycle life model of rechargeable Li-ion batteries," *Electrochimica Acta,* vol. 51, pp. 2012-2022, Feb 1 2006.

[98] H. J. Ploehn, P. Ramadass, and R. E. White, "Solvent diffusion model for aging of lithium-ion battery cells," *Journal of the Electrochemical Society,* vol. 151, pp. A456-A462, Mar 2004.

[99] G. Sikha, B. N. Popov, and R. E. White, "Effect of porosity on the capacity fade of a lithium-ion battery - Theory," *Journal of the Electrochemical Society,* vol. 151, pp. A1104-A1114, 2004.

[100] P. Arora, M. Doyle, and R. E. White, "Mathematical modeling of the lithium deposition overcharge reaction in lithium-ion batteries using carbon-based

negative electrodes," *Journal of the Electrochemical Society,* vol. 146, pp. 3543-3553, Oct 1999.

[101] R. D. Perkins, A. V. Randall, X. C. Zhang, and G. L. Plett, "Controls oriented reduced order modeling of lithium deposition on overcharge," *Journal of Power Sources,* vol. 209, pp. 318-325, Jul 1 2012.

[102] J. Christensen and J. Newman, "Stress generation and fracture in lithium insertion materials," *Journal of Solid State Electrochemistry,* vol. 10, pp. 293-319, May 2006.

[103] J. S. Neuman and C. W. Tobias, "Theoretical analysis of current distribution in porous electrodes," *Journal of The Electrochemical Society,* vol. 109, pp. 1183 - 1191, 1962.

[104] J. Newman and W. Tiedemann, "Porous-electrode theory with battery applications," *Aiche Journal,* vol. 21, pp. 25-41, 1975.

[105] M. Doyle, T. F. Fuller, and J. Newman, "Modeling of galvanostatic charge and discharge of the lithium polymer insertion cell," *Journal of the Electrochemical Society,* vol. 140, pp. 1526-1533, Jun 1993.

[106] M. Doyle and J. Newman, "The use of mathematical-modeling in the design of Lithium polymer battery systems," *Electrochimica Acta,* vol. 40, pp. 2191-2196, Oct 1995.

[107] M. Doyle, T. F. Fuller, and J. Newman, "The importance of the Lithium ion transference number in Lithium polymer cells," *Electrochimica Acta,* vol. 39, pp. 2073-2081, Sep 1994.

[108] M. Guo, G. H. Kim, and R. E. White, "A three-dimensional multi-physics model for a Li-ion battery," *Journal of Power Sources,* vol. 240, pp. 80-94, Oct 15 2013.

[109] Y. Ji, Y. C. Zhang, and C. Y. Wang, "Li-ion cell operation at low temperatures," *Journal of the Electrochemical Society,* vol. 160, pp. A636-A649, 2013.

[110] G. H. Kim, K. Smith, K. J. Lee, S. Santhanagopalan, and A. Pesaran, "Multi-domain modeling of Lithium-ion batteries encompassing multi-physics in varied length scales," *Journal of the Electrochemical Society,* vol. 158, pp. A955-A969, 2011.

[111] K. Takahashi and V. Srinivasan, "Examination of graphite particle cracking as a failure mode in Lithium-ion batteries: A model-experimental study," *Journal of The Electrochemical Society,* vol. 162, pp. A635 - A645, 2015.

[112] V. Ramadesigan, P. W. C. Northrop, S. De, S. Santhanagopalan, R. D. Braatz, and V. R. Subramanian, "Modeling and simulation of Lithium-ion batteries from a systems engineering perspective," *Journal of The Electrochemical Society,* vol. 159, pp. R31 - R45, 2012.

[113] A. A. Franco, "Multiscale modelling and numerical simulation of rechargeable lithium ion batteries: concepts, methods and challenges," *Rsc Advances,* vol. 3, pp. 13027-13058, 2013.

[114] L. Cai and R. E. White, "Reduction of model order based on proper orthogonal decomposition for Lithium-ion battery simulations," *Journal of the Electrochemical Society,* vol. 156, pp. A154-A161, 2009.

[115] S. K. Rahimian, S. Rayman, and R. E. White, "Extension of physics-based single particle model for higher charge-discharge rates," *Journal of Power Sources,* vol. 224, pp. 180-194, Feb 15 2013.

[116] K. A. Smith, C. D. Rahn, and C. Y. Wang, "Control oriented ID electrochemical model of lithium ion battery," *Energy Conversion and Management,* vol. 48, pp. 2565-2578, Sep 2007.

[117] K. Smith and C. Y. Wang, "Solid-state diffusion limitations on pulse operation of a lithium ion cell for hybrid electric vehicles," *Journal of Power Sources,* vol. 161, pp. 628-639, Oct 20 2006.

[118] K. Smith and C.-Y. Wang, "Solid-state diffusion limitations on pulse operation of a lithium ion cell for hybrid electric vehicles," *Journal of Power Sources,* vol. 161, pp. 628 - 639, 2006.

[119] R. Deshpande, M. Verbrugee, Y.-T. Cheng, J. Wang, and P. Liu, "Battery cycle life prediction with coupled chemical degradation and fatigue mechanics," *Journal of The Electrochemical Society,* vol. 159, pp. 1730 - 1738, 2012.

[120] A. Hoke, A. Brissette, K. Smith, A. Pratt, and D. Maksimovic, "Accounting for Lithium-ion battery degradation in electric vehicle charging optimization," *IEEE JOURNAL OF EMERGING AND SELECTED TOPICS IN POWER ELECTRONICS,* vol. 2, pp. 691 - 700, 2014.

[121] N. Nitta, F. X. Wu, J. T. Lee, and G. Yushin, "Li-ion battery materials: present and future," *Materials Today,* vol. 18, pp. 252-264, Jun 2015.

[122] J. R. Croy, A. Abouimrane, and Z. C. Zhang, "Next-generation lithium-ion batteries: The promise of near-term advancements," *Mrs Bulletin,* vol. 39, pp. 407-415, May 2014.

[123] J. R. Croy, D. Kim, M. Balasubramanian, K. Gallagher, S. H. Kang, and M. M. Thackeray, "Countering the Voltage Decay in High Capacity xLi(2)MnO(3)center dot(1-x)LiMO2 Electrodes (M=Mn, Ni, Co) for Li+-Ion Batteries," *Journal of the Electrochemical Society,* vol. 159, pp. A781-A790, 2012.

[124] K. G. Gallagher, J. R. Croy, M. Balasubramanian, M. Bettge, D. P. Abraham, A. K. Burrell*, et al.*, "Correlating hysteresis and voltage fade in lithium- and manganese-rich layered transition-metal oxide electrodes," *Electrochemistry Communications,* vol. 33, pp. 96-98, Aug 2013.

[125] U. Kasavajjula, C. S. Wang, and A. J. Appleby, "Nano- and bulk-silicon-based insertion anodes for lithium-ion secondary cells," *Journal of Power Sources,* vol. 163, pp. 1003-1039, Jan 1 2007.

[126] A. Kadota. (2009, 25th December). *Panasonic develops high-capacity Lithium-ion battery cells that can power laptops and electric vehicles*.

[127] B. Gao, S. Sinha, L. Fleming, and O. Zhou, "Alloy formation in nanostructured silicon," *Advanced Materials,* vol. 13, pp. 816-+, Jun 5 2001.

[128] M. Green, E. Fielder, B. Scrosati, M. Wachtler, and J. Serra Moreno, "Structured silicon anodes for lithium battery applications," *Electrochemical and Solid State Letters,* vol. 6, pp. A75-A79, May 2003.

[129] N. Dimov and M. Yoshio, "Towards creating reversible silicon-based composite anodes for lithium ion batteries," *Journal of Power Sources,* vol. 174, pp. 607-612, Dec 6 2007.

[130] W. R. Liu, M. H. Yang, H. C. Wu, S. M. Chiao, and N. L. Wu, "Enhanced cycle life of Si anode for Li-ion batteries by using modified elastomeric binder," *Electrochemical and Solid State Letters,* vol. 8, pp. A100-A103, 2005.

[131] D. M. Piper, J. J. Travis, M. Young, S. B. Son, S. C. Kim, K. H. Oh*, et al.*, "Reversible high-capacity Si nanocomposite anodes for Lithium-ion batteries enabled by molecular layer deposition," *Advanced Materials,* vol. 26, pp. 1596-1601, Mar 2014.

[132] W. Wang, Z. Favors, R. Ionescu, R. Ye, H. H. Bay, M. Ozkan*, et al.*, "Monodisperse porous Silicon spheres as anode materials for Lithium ion batteries," *Scientific Reports,* vol. 5, Mar 5 2015.

[133] P. Limthongkul, Y. I. Jang, N. J. Dudney, and Y. M. Chiang, "Electrochemically-driven solid-state amorphization in lithium-silicon alloys and implications for lithium storage," *Acta Materialia,* vol. 51, pp. 1103-1113, Feb 25 2003.

[134] M. Ebner, F. Geldmacher, F. Marone, M. Stampanoni, and V. Wood, "X-Ray tomography of porous, transition metal oxide based Lithium ion battery electrodes," *Advanced Energy Materials,* vol. 3, pp. 845-850, Jul 2013.

[135] J. Cho, "Porous Si anode materials for lithium rechargeable batteries," *Journal of Materials Chemistry,* vol. 20, pp. 4009-4014, 2010.

[136] S. D. Xun, X. Y. Song, V. Battaglia, and G. Liu, "Conductive polymer binder-enabled cycling of pure Tin nanoparticle composite anode electrodes for a Lithium-ion battery," *Journal of the Electrochemical Society,* vol. 160, pp. A849-A855, 2013.

[137] M. Kummer, J. P. Badillo, A. Schmitz, H. G. Bremes, M. Winter, C. Schulz*, et al.*, "Silicon/polyaniline nanocomposites as anode material for Lithium ion batteries," *Journal of the Electrochemical Society,* vol. 161, pp. A40-A45, 2014.

[138] G. Bucci, S. P. V. Nadimpalli, V. A. Sethuraman, A. F. Bower, and P. R. Guduru, "Measurement and modeling of the mechanical and electrochemical response of amorphous Si thin film electrodes during cyclic lithiation," *Journal of the Mechanics and Physics of Solids,* vol. 62, pp. 276-294, Jan 2014.

[139] C. F. Chen, P. Barai, and P. P. Mukherjee, "Diffusion induced damage and impedance response in Lithium-ion battery electrodes," *Journal of the Electrochemical Society,* vol. 161, pp. A2138-A2152, 2014.

[140] T. Song, J. L. Xia, J. H. Lee, D. H. Lee, M. S. Kwon, J. M. Choi*, et al.*, "Arrays of sealed Silicon nanotubes as anodes for Lithium ion batteries," *Nano Letters,* vol. 10, pp. 1710-1716, May 2010.

[141] S. K. Soni, B. W. Sheldon, X. C. Xiao, A. F. Bower, and M. W. Verbrugge, "Diffusion mediated lithiation stresses in Si thin film electrodes," *Journal of the Electrochemical Society,* vol. 159, pp. A1520-A1527, 2012.

[142] A. F. Bower, P. R. Guduru, and V. A. Sethuraman, "A finite strain model of stress, diffusion, plastic flow, and electrochemical reactions in a lithium-ion half-

cell," *Journal of the Mechanics and Physics of Solids,* vol. 59, pp. 804-828, Apr 2011.

[143] V. A. Sethuraman, M. J. Chon, M. Shimshak, V. Srinivasan, and P. R. Guduru, "In situ measurements of stress evolution in silicon thin films during electrochemical lithiation and delithiation," *Journal of Power Sources,* vol. 195, pp. 5062-5066, Aug 1 2010.

[144] T. K. Bhandakkar and H. Gao, "Cohesive modeling of crack nucleation in a cylindrical electrode under axisymmetric diffusion induced stresses," *International Journal of Solids and Structures,* vol. 48, pp. 2304 - 2309, 2011.

[145] M. E. Stournara, X. Xiao, Y. Qi, P. Johari, P. Lu, B. W. Sheldon*, et al.*, "Li segregation induces structure and strength changes at the amorphous Si/Cu interface," *Nano Letters,* vol. 13, pp. 4759 - 4768, 2013.

[146] M. E. Stournara, Y. Qi, and V. B. Shenoy, "From ab initio calculations to multiscale design of Si/C core−shell particles for Li-ion anodes," *Nano Letters,* vol. 14, pp. 2140 - 2149, 2014.

[147] S. Huang, F. Fan, J. Li, S. Zhang, and T. Zhu, "Stress generation during lithiation of high-capacity electrode particles in lithium ion batteries," *Acta Materialia,* vol. 61, pp. 4354-4364, Jul 2013.

[148] F. M. Wang, M. H. Yu, Y. J. Hsiao, Y. Tsai, B. J. Hwang, Y. Y. Wang*, et al.*, "Aging effects to solid electrolyte interface (SEI) membrane formation and the performance analysis of Lithium ion batteries," *International Journal of Electrochemical Science,* vol. 6, pp. 1014-1026, Apr 2011.

[149] I. Ryu, J. W. Choi, Y. Cui, and W. D. Nix, "Size-dependent fracture of Si nanowire battery anodes," *Journal of the Mechanics and Physics of Solids,* vol. 59, pp. 1717 - 1732, 2011.

[150] L. d. Arcangelis and S. Redner, "A random fuse model for breaking processes," *Journal de Physique Lettres,* vol. 46, pp. L585 - L590, 1985.

[151] G. F. Zhao, J. N. Fang, and J. Zhao, "A 3D distinct lattice spring model for elasticity and dynamic failure," *International Journal for Numerical and Analytical Methods in Geomechanics,* vol. 35, pp. 859-885, Jun 10 2011.

[152] M. Doyle, T. F. Fuller, and J. Newman, "Modeling of galvanostatic charge and discharge of the lithium polymer insertion cell," *Journal of The Electrochemical Society,* vol. 140, pp. 1526 - 1533, 1993.

[153] M. Doyle and J. Newman, "Analysis of capacity-rate data for lithium batteries using simplified models of the discharge process," *Journal of Applied Electrochemistry,* vol. 27, pp. 846 - 856, 1997.

[154] J. C. Simo and J. W. Ju, "Strain and stress based continuum damage models - I. Formulation," *International Journal of Solids and Structures,* vol. 23, pp. 821 - 840, 1987.

[155] R. D. Cook, D. S. Malkus, M. E. Plesha, and R. J. Witt, *Concepts and applications of finite element analysis*. Singapore: John Wiley and Sons, Inc., 2002.

[156] J. N. Reddy, *An introduction to the finite element method*. New Delhi: Tata McGraw-Hill Publishing Company Limited, 2003.

[157] M. Guo, G. Sikha, and R. E. White, "Single-particle model for a lithium-ion cell: Thermal behavior," *Journal of the Electrochemical Society,* vol. 158, pp. A122 - A132, 2011.

[158] M. A. Martin, "Modeling of transport in Li ion battery electrodes," Master of Science, Mechanical Engineering, Texas A&M University, May, 2012.

[159] S. Liu, "An analytical solution to Li/Li+ insertion into a porous electrode," *Solid State Ionics,* vol. 177, pp. 53 - 58, 2006.

[160] P. P. Mukherjee, S. Pannala, and J. A. Turner, "Modeling and simulation of battery systems," in *Handbook of Battery Materials, Second Edition*, C. Daniel and J. O. Besenhard, Eds., ed: Wiley-VCH Verlag GmbH & Co., 2011.

[161] V. Ramadesigan, V. Boovaragavan, J. C. P. Jr., and V. R. Subramanian, "Efficient reformulation of solid-phase diffusion in physics-based Lithium-ion battery models," *Journal of The Electrochemical Society,* vol. 157, pp. A854 - A860, 2010.

[162] V. R. Subramanian, V. D. Diwakar, and D. Tapriyal, "Efficient macro-micro scale coupled modeling of batteries," *Journal of The Electrochemical Society,* vol. 152, pp. A2002 - A2008, 2005.

[163] V. R. Subramanian and R. E. White, "New separation of variables method for composite electrodes with galvanostatic boundary conditions," *Journal of Power Sources,* vol. 96, pp. 385 - 395, 2001.

[164] C. Y. Wang, W. B. Gu, and B. Y. Liaw, "Micro-macroscopic coupled modeling of batteries and fuel cells : I. model development," *Journal of The Electrochemical Society,* vol. 145, pp. 3407 - 3417, 1998.

[165] M. Ostoja-Starzewski, "Lattice models in micromechanics," *Applied Mechanics Review,* vol. 55, pp. 35 - 60, 2002.

[166] L. Y. Beaulieu, K. W. Eberman, R. L. Turner, L. J. Krause, and J. R. Dahn, "Colossal reversible volume changes in Lithium alloys," *Electrochemical and Solid State Letters,* vol. 4, pp. A137 - A140, 2001.

[167] Y.-T. Cheng and M. W. Verbrugee, "Evolution of stress within a spherical insertion electrode particle under potentiostatic and galvanostatic operation," *Journal of Power Sources,* vol. 190, pp. 453 - 460, 2009.

[168] A. Hansen and J. Schmittbuhl, "Origin of the universal roughness exponent of brittle fracture surfaces: Stress-weighted percolation in the damage zone," *Physical Review Letters,* vol. 90, Jan 31 2003.

[169] P. K. V. V. Nukala, S. Simunovic, and S. Zapperi, "Percolation and localization in the random fuse model," *Journal of Statistical Mechanics-Theory and Experiment,* Aug 2004.

[170] J. Krim and J. O. Indekeu, "Roughness exponent: A parados resolved," *Physical Review E,* vol. 48, pp. 1576 - 1578, 1993.

[171] A. Rinaldi, D. Krajcinovic, P. Peralta, and Y.-C. Lai, "Lattice models of polycrystalline microstructures: A quantitative approach," *Mechanics of materials,* vol. 40, pp. 17 - 36, 2008.

[172] N. Sukumar and D. J. Srolovitz, "Finite element-based model for crack propagation in polycrystalline materials," *Computational & Applied Mathematics,* vol. 23, pp. 363-380, 2004.

[173] P. D. Zavattieri, P. V. Raghuram, and H. D. Espinosa, "A computational model of ceramic microstructures subjected to multi-axial dynamic loading," *Journal of the Mechanics and Physics of Solids,* vol. 49, pp. 27-68, Jan 2001.

[174] H. D. Espinosa and P. D. Zavattieri, "A grain level model for the study of failure initiation and evolution in polycrystalline brittle materials. Part I: Theory and numerical implementation," *Mechanics of Materials,* vol. 35, pp. 333-364, Mar-Jun 2003.

[175] A. Zimmermann, W. C. Carter, and E. R. Fuller, "Damage evolution during microcracking of brittle solids," *Acta Materialia,* vol. 49, pp. 127-137, Jan 8 2001.

[176] M. Grah, K. Alzebdeh, P. Y. Sheng, M. D. Vaudin, K. J. Bowman, and M. Ostoja-Starzewski, "Brittle-intergranular failure in 2D microstructures: Experiments and computer simulations," *Acta Materialia,* vol. 44, pp. 4003-4018, Oct 10 1996.

[177] R. Schwaiger, B. Moser, M. Dao, N. Chollacoop, and S. Suresh, "Some critical experiments on the strain-rate sensitivity of nanocrystalline nickel," *Acta Materialia,* vol. 51, pp. 5159-5172, Oct 6 2003.

[178] K. An, P. Barai, K. Smith, and P. P. Mukherjee, "Probing the thermal implicaions in mechanical degradation of lithium ion battery electrodes," *Journal of the Electrochemical Society,* vol. 161, pp. A1058 - A1070, 2014.

[179] A. K. Chopra, *Dynamics of structures: Theory and applications to earthquake engineering*. New Jersey, USA: Prentice Hall, 2007.

[180] D.-W. Chung, N. Balke, S. V. Kalinin, and R. E. Garcia, "Virtual electrochemical strain microscopy of polycrystalline LiCoO2 films," *Journal of the Electrochemical Society,* vol. 158, pp. A1083 - A1089, 2011.

[181] R. Wartena, A. E. Curtright, C. B. Arnold, A. Pique, and K. E. Swider-Lyons, "Li-ion microbatteries generated by a laser direct-write method," *Journal of Power Sources,* vol. 126, pp. 193 - 202, 2004.

[182] A. Tranchot, A. Etiernble, P. X. Thivel, H. Idrissi, and L. Roue, "In-situ acoustic emission study of Si-based electrodes for Li-ion batteries," *Journal of Power Sources,* vol. 279, pp. 259-266, Apr 1 2015.

[183] R. T. Purkayastha and R. M. McMeeking, "An integrated 2-D model of a lithium ion battery: the effect of material parameters and morphology on storage particle stress," *Computational Mechanics,* vol. 50, pp. 209-227, Aug 2012.

[184] V. Srinivasan and J. Newman, "Design and optimization of a natural graphite/iron phosphate lithium-ion cell," *Journal of the Electrochemical Society,* vol. 151, pp. A1530-A1538, 2004.

[185] D. Burch and M. Z. Bazant, "Size-dependent spinodal and miscibility gaps for intercalation in nanoparticles," *Nano Letters,* vol. 9, pp. 3795-3800, Nov 2009.

[186] N. Meethong, H. Y. S. Huang, S. A. Speakman, W. C. Carter, and Y. M. Chiang, "Strain accommodation during phase transformations in olivine-based cathodes as a materials selection criterion for high-power rechargeable batteries," *Advanced Functional Materials,* vol. 17, pp. 1115-1123, May 7 2007.

[187] J. W. Wang, F. F. Fan, Y. Liu, K. L. Jungjohann, S. W. Lee, S. X. Mao*, et al.*, "Structural evolution and pulverization of Tin nanoparticles during lithiation-delithiation cycling," *Journal of the Electrochemical Society,* vol. 161, pp. F3019-F3024, 2014.

[188] Y. Zeng and M. Z. Bazant, "Phase separation dynamics in isotropic ion-intercalation particles," *Siam Journal on Applied Mathematics,* vol. 74, pp. 980-1004, 2014.

[189] K.-J. Bathe, *Finite element procedures*. New Jersey, USA: Prentice Hall, 1996.

[190] J. N. Reddy, *An introduction to nonlinear finite element analysis*: Oxford University Press, 2004.

[191] Y. Qi, L. G. Hector, C. James, and K. J. Kim, "Lithium concentration dependent elastic properties of battery electrode materials from first principles calculations," *Journal of the Electrochemical Society,* vol. 161, pp. F3010-F3018, 2014.

[192] M. Pharr, Z. G. Suo, and J. J. Vlassak, "Measurements of the fracture energy of lithiated Silicon electrodes of Li-ion batteries," *Nano Letters,* vol. 13, pp. 5570-5577, Nov 2013.

[193] P. Johari, Y. Qi, and V. B. Shenoy, "The mixing mechanism during lithiation of Si negative electrode in Li-ion batteries: An ab initio molecular dynamics study," *Nano Letters,* vol. 11, pp. 5494-5500, Dec 2011.

[194] M. J. Chon, V. A. Sethuraman, A. McCormick, V. Srinivasan, and P. R. Guduru, "Real-time measurement of stress and damage evolution during initial lithiation of crystalline silicon," *Physical Review Letters,* vol. 107, Jul 21 2011.

[195] P. Barai, B. Huang, S. J. Dillon, and P. P. Mukherjee, "Creep deformation in Sn electrodes under electrochemical cycling," *Under preparation,* 2015.

[196] B. Huang and S. Dillon, "Creep deformation in Sn electrodes under electrochemical cycling," P. P. P. Mukherjee, Ed., ed, 2014.

[197] X. K. Lin, J. Park, L. Liu, Y. Lee, A. M. Sastry, and W. Lu, "A comprehensive capacity fade model and analysis for Li-ion batteries," *Journal of the Electrochemical Society,* vol. 160, pp. A1701-A1710, 2013.

[198] R. Dehoff, *Thermodynamics in materials science*. New York, United States of America: CRC Taylor and Francis Group, 2006.

[199] H. H. Girault, *Analytical and physical electrochemistry*: EPFL Press, 2004.

APPENDIX I

FUNDAMENTALS OF ELECTROCHEMISTRY AND ELECTRODE THEORY

Inside a battery chemical energy gets converted into electrical energy. Hence, it is very important to properly understand the thermodynamics to correctly estimate the amount of electrical energy that can be extracted from a certain combination of chemicals. Figure A1.3 shows a schematic representation of an electrochemical cell where discharge is going on. Here, A represents the anode and C signifies the cathode material. Flow of electron e^- happens from anode to cathode (A to C) through an external circuit. The anode phase is represented by α and the cathode phase is represented by β, whereas ε signifies the electrolyte phase.

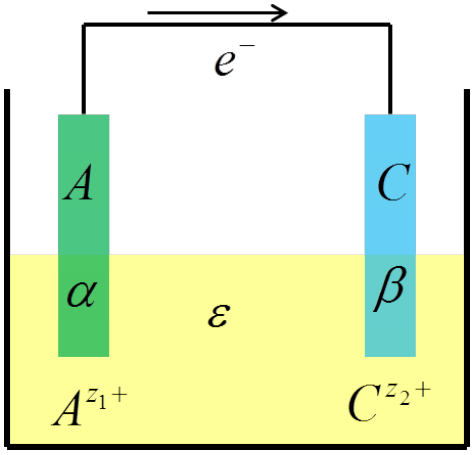

Fig: A1.1. *Schematic representation of an electrochemical cell going through discharge.*

The oxidation – reduction reaction that happens within the electrochemical cell has been provided in Eq. A1.1 (a) and (b). For each of the oxidation and the reduction reaction, expressions for equilibrium can be derived. Since both the reactions occur with

respect to the electrolyte, expressions of thermodynamic equilibrium are evaluated in comparison to the electrolyte phase.

$$n_1 A \rightarrow n_1 A^{z_1+} + n_1 z_1 e^- \tag{A1.1a}$$

$$n_2 C^{z_2+} + n_2 z_2 e^- \rightarrow n_2 C \tag{A1.1b}$$

Here, n_1 moles of anode material came out of the α phase and entered the electrolyte. On the other hand, n_2 moles of cathode material came out of the ε phase and entered the β phase. From basic charge conservation, it can be concluded that $n_1 z_1 = n_2 z_2$. In the next paragraph, thermodynamic equilibrium relation for the oxidation reaction (Eq. A1.1(a)) will be derived.

A1.1. Thermodynamics of electrochemical cells

From the combined relation of first and second law of thermodynamics (see [198]),

$$dU^\alpha = T^\alpha dS^\alpha - P^\alpha dV^\alpha + \sum \mu_i^\alpha dn_i^\alpha \tag{A1.2}$$

Rearranging the terms we can get an expression of the change in entropy in the α phase,

$$dS^\alpha = \frac{1}{T^\alpha} dU^\alpha + \frac{P^\alpha}{T^\alpha} dV^\alpha - \frac{1}{T^\alpha}\left(\mu_A^\alpha dn_A^\alpha + \mu_e^\alpha dn_e^\alpha\right) \tag{A1.3}$$

Similarly, an expression of the change in entropy for the ε phase gives,

$$dS^\varepsilon = \frac{1}{T^\varepsilon} dU^\varepsilon + \frac{P^\varepsilon}{T^\varepsilon} dV^\varepsilon - \frac{1}{T^\varepsilon} \mu_{A+}^\varepsilon dn_{A+}^\varepsilon \tag{A1.4}$$

For equilibrium, the total entropy of the system should be at a maximum, which renders,

$$dS^{sys} = dS^\alpha + dS^\varepsilon = 0 \tag{A1.5}$$

Combining all the terms from Eq. A1.3, A1.4 and A1.5, the equilibrium relations can be obtained as,

$$\frac{1}{T^{\alpha}}dU^{\alpha}+\frac{1}{T^{\varepsilon}}dU^{\varepsilon}+\frac{P^{\alpha}}{T^{\alpha}}dV^{\alpha}+\frac{P^{\varepsilon}}{T^{\varepsilon}}dV^{\varepsilon}-\frac{1}{T^{\alpha}}\left(\mu_{A}^{\alpha}dn_{A}^{\alpha}+\mu_{e}^{\alpha}dn_{e}^{\alpha}\right)-\frac{1}{T^{\varepsilon}}\mu_{A+}^{\varepsilon}dn_{A+}^{\varepsilon}=0 \tag{A1.6}$$

From the physical constraints and conservation of mass,

$$dV^{tot}=dV^{\alpha}+dV^{\varepsilon}=0 \tag{A1.7}$$

$$dn_{A+}^{\varepsilon}=-dn_{A}^{\alpha}\ and\ dn_{e}^{\alpha}=-z_{1}dn_{A}^{\alpha} \tag{A1.8}$$

Conservation of total energy must also take into consideration the electrical energy,

$$dE^{tot}=dU^{\alpha}+dU^{\varepsilon}-\varphi^{\alpha}z_{1}dn_{e}^{\alpha}+\varphi^{\varepsilon}z_{1}dn_{A+}^{\varepsilon}=0 \tag{A1.9}$$

Substituting expressions obtained from Eq. (A1.7), (A1.8) and (A1.9) into Eq. (A1.6),

$$\left(\frac{1}{T^{\alpha}}-\frac{1}{T^{\varepsilon}}\right)dU^{\alpha}+\left(\frac{P^{\alpha}}{T^{\alpha}}-\frac{P^{\varepsilon}}{T^{\varepsilon}}\right)dV^{\alpha}+\frac{1}{T^{\varepsilon}}\left(-\varphi^{\alpha}z_{1}dn_{A}^{\alpha}+\varphi^{\varepsilon}z_{1}dn_{A+}^{\varepsilon}\right)F-\frac{1}{T^{\alpha}}\left(\mu_{A}^{\alpha}dn_{A}^{\alpha}-z_{1}\mu_{e}^{\alpha}dn_{A}^{\alpha}\right)+\frac{1}{T^{\varepsilon}}\mu_{A+}^{\varepsilon}dn_{A}^{\alpha}=0 \tag{A1.10}$$

From the first and second terms, it can be concluded that at equilibrium,

$$T^{\alpha}=T^{\varepsilon}\quad and\quad P^{\alpha}=P^{\varepsilon} \tag{A1.11}$$

The rest of the Eq. (A1.10) yields that,

$$z_{1}F\left(\varphi^{\alpha}-\varphi^{\varepsilon}\right)=-\left(\mu_{A}^{\alpha}-z_{1}\mu_{e}^{\alpha}-\mu_{A+}^{\varepsilon}\right) \tag{A1.12}$$

Taking into consideration that the forward reaction is an oxidation reaction and the reference Gibbs free energy can be written as, $\Delta G_{ox}^{0}=z_{1}\mu_{e,0}^{\alpha}+\mu_{A+,0}^{\varepsilon}-\mu_{A,0}^{\alpha}$,

$$\varphi^{\alpha} - \varphi^{\varepsilon} = \frac{\Delta G_{ox}^{0}}{z_1 F} + \frac{RT}{z_1 F} \cdot \ln \frac{\left(a_e^{\alpha}\right)^{z_1} \cdot a_{A+}^{\varepsilon}}{a_A^{\alpha}} \tag{A1.13}$$

Similarly, for the reduction reaction going on between the cathode and the electrolyte phase, potential difference for the forward reaction can be written as,

$$\varphi^{\varepsilon} - \varphi^{\beta} = \frac{\Delta G_{red}^{0}}{z_2 F} + \frac{RT}{z_2 F} \cdot \ln \frac{a_C^{\beta}}{\left(a_e^{\beta}\right)^{z_2} \cdot a_{C+}^{\varepsilon}} \tag{A1.14}$$

Here, $\Delta G_{red}^{0} = \mu_{C,0}^{\beta} - z_2 \mu_{e,0}^{\beta} - \mu_{C+,0}^{\varepsilon}$ represents the reference Gibbs free energy for the reduction reaction. Assuming, $z_1 = z_2 = z$, and adding Eq. (A1.13) with (A1.14) gives,

$$-\left(\varphi^{\beta} - \varphi^{\alpha}\right) = \frac{\Delta G_{ox}^{0} + \Delta G_{red}^{0}}{zF} + \frac{RT}{zF} \cdot \ln\left(\frac{\left(a_e^{\alpha}\right)^{z_1} \cdot a_{A+}^{\varepsilon}}{a_A^{\alpha}} \frac{a_C^{\beta}}{\left(a_e^{\beta}\right)^{z_2} \cdot a_{C+}^{\varepsilon}} \right) \tag{A1.15}$$

Assume, $V = \varphi^{\beta} - \varphi^{\alpha}$, the difference between the electrical potential is known as the cell voltage, and $\Delta G_{ox}^{0} + \Delta G_{red}^{0} = \Delta G^{0}$ along with $\Delta G^{0} = -zFV^{0}$. Thus,

$$V = V^{0} - \frac{RT}{zF} \cdot \ln\left(\frac{\left(a_e^{\alpha}\right)^{z} \cdot a_{A+}^{\varepsilon}}{a_A^{\alpha}} \frac{a_C^{\beta}}{\left(a_e^{\beta}\right)^{z} \cdot a_{C+}^{\varepsilon}} \right) \tag{A1.16}$$

This equation is also known as the Nernst equation which correlates the equilibrium cell voltage with the concentration/activity of its components. Here, V signifies the cell potential and V^{0} denotes the reference potential. This Nernst equation gives an idea about the equilibrium configuration. It does not give any information about the kinetics of the oxidation – reduction reaction.

A1.2. Kinetics of electrochemical cells

Kinetics of most of the electrochemical cells is governed by the Butler-Volmer equation (see Ref. [199]). This expression helps to correlate the flow of current with the oxidation – reduction reaction that goes on inside the electrode. The Butler-Volmer equation for half cells is derived from the Nernst equation of each of the half cells. Then they are combined together to correlate the cell potential with the current flowing through the electrochemical cell. Suppose, the half reaction is given as,

$$C_O + e^- \rightarrow C_R \tag{A1.17}$$

For the half cell, the Nernst equation can be written as,

$$E = E^0 - \frac{RT}{zF} \ln \frac{C_R}{C_O} \tag{A1.18}$$

Here, E signifies the difference between the potential of the electrode and the electrolyte. C_R and C_O simply represents the concentration of the product and the reactant respectively. Eq. (A1.18) can be rearranged and written as,

$$\ln \frac{C_R}{C_O} = -\frac{zF}{RT}\left(E - E^0\right) \tag{A1.19}$$

The rate of forward reaction is given as, $R_f = k_f C_O$, and the rate of backward reaction is given as, $R_b = k_b C_R$. The flow of current per unit volume (i) is directly proportional to the rate of reaction,

$$R_{net} = R_f - R_b = k_f C_O - k_b C_R = \frac{i}{zF} \tag{A1.20}$$

At equilibrium, when there is no external current flowing $\left(i = 0, and\ k_f C_O = k_b C_R\right)$,

$$\ln k_b - \ln k_f = \ln \frac{C_O}{C_R} = \frac{zF}{RT}\left(E - E^0\right) \tag{A1.21}$$

Taking first derivative of Eq. (A1.21) with respect to E gives,

$$\frac{RT}{zF}\left[\frac{d}{dE}\ln k_b + \frac{d}{dE}\ln\frac{1}{k_f}\right] = 1 \tag{A1.22}$$

Assuming the first term on the LHS of Eq. (A1.22) equivalent to $\left(1-\alpha\right)$ and the second term in the LHS to be equal to α, one can write that,

$$\frac{RT}{zF}\frac{d}{dE}\left(\ln\frac{1}{k_f}\right) = \alpha \tag{A1.23}$$

Integrating Eq. (A1.23) under the condition that at $E = E^0$, $k_f = k_f^0$,

$$k_f = k_f^0 \exp\left(-\frac{z\alpha F}{RT}\left(E - E^0\right)\right) \tag{A1.24}$$

Similarly, for the backward reaction, it can be concluded that,

$$k_b = k_b^0 \exp\left(\frac{(1-\alpha)zF}{RT}\left(E - E^0\right)\right) \tag{A1.25}$$

Combining Eq. (A1.20), (A1.24) and (A1.25), the applied current can be written as,

$$i = zF\left[k_f^0 C_O \exp\left(-\frac{\alpha zF}{RT}\left(E - E^0\right)\right) - k_b^0 C_R \exp\left(\frac{(1-\alpha)zF}{RT}\left(E - E^0\right)\right)\right] \tag{A1.26}$$

When there is no externally applied current and internal equilibrium has not been achieved, there will be some current flowing internally to attain equilibrium. This internal current is known as the exchange current density $\left(i_0\right)$, which is written as,

$$i_0 = zFk_f^0 C_O^* \exp\left(-\frac{\alpha zF}{RT}\left(U - E^0\right)\right) = zFk_b^0 C_R^* \exp\left(\frac{(1-\alpha)zF}{RT}\left(U - E^0\right)\right) \tag{A1.27}$$

Here, the starred concentration values correspond to the bulk concentration. The non-starred values of the concentration correspond to the value at the surface of the electrode. From Eq. (A1.27), the ratio of the bulk concentration can be obtained as,

$$\frac{C_O^*}{C_R^*} = \exp\left(\frac{zF}{RT}\left(U - E^0\right)\right) \tag{A1.28}$$

Here, U is equivalent to the open circuit potential (OCP) of that electrode. Raising Eq. (A1.28) by $-\alpha$, and combining it with Eq. (1.27) one gets,

$$i_0 = zFk_0\left(C_O^*\right)^{1-\alpha}\left(C_R^*\right)^{\alpha} \tag{A1.29}$$

It has been assumed that the reference forward and the backward reaction rates are the same and given by, $k_0 = k_f^0 = k_b^0$. Combining Eq. (A1.26) and (A1.29),

$$\frac{i}{i_0} = \left[\left(\frac{C_O}{C_O^*}\right)\left(\frac{C_O^*}{C_R^*}\right)^{\alpha}\exp\left(-\frac{\alpha zF}{RT}\left(E - E^0\right)\right) - \left(\frac{C_R}{C_R^*}\right)\left(\frac{C_O^*}{C_R^*}\right)^{-(1-\alpha)}\exp\left(\frac{(1-\alpha)zF}{RT}\left(E - E^0\right)\right)\right] \tag{A1.30}$$

Combining Eq. (A1.28) with Eq. (A1.30),

$$\frac{i}{i_0} = \left[\left(\frac{C_O}{C_O^*}\right)\exp\left(-\frac{\alpha zF}{RT}\left(E - U\right)\right) - \left(\frac{C_R}{C_R^*}\right)\exp\left(\frac{(1-\alpha)zF}{RT}\left(E - U\right)\right)\right] \tag{A1.31}$$

If the concentration gradient due to the diffusion process can be neglected and the surface concentration can be assumed to be equal to the bulk concentration,

$$i = i_0 \cdot \left[\exp\left(-\frac{\alpha zF}{RT}\left(E - U\right)\right) - \exp\left(\frac{(1-\alpha)zF}{RT}\left(E - U\right)\right)\right] \tag{A1.32}$$

Estimation of the correct exchange current density is a challenge and has been explained here for general lithium ion battery applications. The reaction equivalent to Eq. (A1.17) that happens in lithium ion battery can be given as,

$$Li^+ + e^- + \theta_s \rightarrow Li\theta_s \tag{A1.33}$$

Here, θ_s represents an intercalation site for Li ions. Comparing Eq. (A1.33) with Eq. (A1.17), C_O consists of the concentration of Li+ in the electrolyte $\left(C_e\right)$ and the concentration of intercalation sites for lithium ions within the solid phase $\left(1-C_{Li}\right)$. On the other hand, C_R corresponds to the concentration of lithium ions inside the solid phase C_{Li}. Exchange current density gives,

$$i_0 = zFk_0\left(C_e\right)^{1-\alpha}\left(C_{\max.Li}-C_{Li}\right)^{1-\alpha}\left(C_{Li}\right)^{\alpha} = zFk_0C_{\max.Li}\left(C_e\right)^{1-\alpha}\left(1-x_{Li}\right)^{1-\alpha}\left(x_{Li}\right)^{\alpha} \tag{A1.34}$$

Here, x_{Li} signifies stoichiometry of Li ions at the surface of the electrode. Combining Eq. (A1.32) with Eq. (A1.34), the correct form of Butler-Volmer equation can be obtained.

$$i = zFk_0C_{\max.Li}\left(C_e\right)^{1-\alpha}\left(1-x_{Li}\right)^{1-\alpha}\left(x_{Li}\right)^{\alpha}\left[\exp\left(-\frac{\alpha zF}{RT}\left(E-U\right)\right)-\exp\left(\frac{\left(1-\alpha\right)zF}{RT}\left(E-U\right)\right)\right] \tag{A1.35}$$

A1.3. Multiplicative split of the axial stretch component

For the large deformation analysis reported in Chapter VI, the elastic and concentration dependent component of stretch must be estimated from the total amount of axial stretch. For large deformation analysis, multiplicative decomposition of the stretch tensor must be conducted. Let's denote the total stretch as λ, the elastic

component of the stretch tensor as λ^e, concentration dependent stretch as λ^c and initial, total, elastic and concentration dependent length as l_0, l, l_e and l_c respectively. The following relation always holds,

$$\lambda = \frac{l}{l_0}, \quad \lambda^e = \frac{l_e}{l_0}, \quad \lambda^c = \frac{l}{l_e} \quad \text{and} \quad \lambda = \lambda^e \lambda^c \tag{A1.36}$$

Magnitude of the concentration dependent stretch is defined as,

$$\lambda^c = 1 + \Omega \cdot \Delta\hat{c} \tag{A1.37}$$

Here, Ω is the partial molar volume multiplied by the maximum concentration, and $\Delta\hat{c}$ indicates the change in normalized lithium concentration. Combining Eq. (A1.36) and (A1.37) one can conclude that,

$$l_e = \frac{l}{1 + \Omega \cdot \Delta\hat{c}} \tag{A1.38}$$

A similar expression is also provided in Chapter VI. The increasing in length of the spring element along the axial direction is given as,

$$\Delta l = l_e - l_0 \tag{A1.39}$$

Following the same direction mentioned in the previous equations, incorporation of the creep strain can also be accomplished in a similar fashion.

$$l_e = \frac{l}{\left(1 + \Omega \cdot \Delta\hat{c}\right) \cdot \left(1 + \Delta\varepsilon^c\right)} \tag{A1.40}$$

Here, $\Delta\varepsilon^c$ indicates the creep strain increment at a given time interval. The magnitude of creep strain increment can be estimated from the following equation using the axial stress $\left(\sigma\right)$, creep coefficient $\left(A\right)$ and creep exponent $\left(n\right)$ and change in time Δt.

$$\Delta\varepsilon^c = A\cdot\sigma^n\cdot\Delta t \tag{A1.41}$$

Creep strain can be important while analyzing the lithiation induced deformation and fracture within Sn active materials, because melting point of Sn is much less than Si.

A1.4. Normalization of the momentum balance equation for large deformation

As provided in Eq. (6.16) given in Chapter VI, the virtual work statement can be written in the following form,

$$\int_{{}^tV}\begin{bmatrix} {}^{t+\Delta t}_{\ t}S_{xx} & \frac{1}{2}\,{}^{t+\Delta t}_{\ t}S_{xy}\end{bmatrix}\begin{bmatrix}\dfrac{\partial\delta_t u}{\partial x}\\ \dfrac{\partial\delta_t v}{\partial x}\end{bmatrix}d\,{}^tV+\int_{{}^tV}{}^{t+\Delta t}_{\ t}S_{xx}\begin{bmatrix}\dfrac{\partial_t u}{\partial x} & \dfrac{\partial_t v}{\partial x}\end{bmatrix}\begin{bmatrix}\dfrac{\partial\delta_t u}{\partial x}\\ \dfrac{\partial\delta_t v}{\partial x}\end{bmatrix}d\,{}^tV=0 \tag{A1.42}$$

The vector form of the two stresses can be modified according to,

$$\begin{bmatrix} {}^{t+\Delta t}_{\ t}S_{xx}\\ \frac{1}{2}\,{}^{t+\Delta t}_{\ t}S_{xy}\end{bmatrix}=\begin{bmatrix}E & 0\\ 0 & G\end{bmatrix}\begin{bmatrix}\dfrac{\partial_t u}{\partial x}\\ \dfrac{\partial_t v}{\partial x}\end{bmatrix} \tag{A1.43}$$

For the purpose of non-dimensionalizing the virtual energy expression, only one component of the equation will be analyzed here.

$$\begin{aligned}\int_{{}^tV}{}^{t+\Delta t}_{\ t}S_{xx}\frac{\partial\delta_t u}{\partial x}d\,{}^tV&=\int_{{}^tV}E\frac{\partial_t u}{\partial x}\frac{\partial\delta_t u}{\partial x}d\,{}^tV=\int_x{}^tAE\frac{\partial_t u}{\partial x}\frac{\partial\delta_t u}{\partial x}dx=\\ &=\int_{\tilde{x}}\frac{{}^tA}{A_0}\frac{E}{E_0}A_0E_0L_0\frac{\partial_t\tilde{u}}{\partial\tilde{x}}\frac{\partial\delta_t\tilde{u}}{\partial\tilde{x}}d\tilde{x}=\int_{\tilde{x}}{}^t\tilde{A}\tilde{E}A_0E_0L_0\frac{\partial_t\tilde{u}}{\partial\tilde{x}}\frac{\partial\delta_t\tilde{u}}{\partial\tilde{x}}d\tilde{x}\end{aligned} \tag{A1.44}$$

For this equation to be applicable in the context of large volume expansion, the product of reference cross-sectional area, reference elastic modulus and reference length should equal to unity.

$$A_0E_0L_0=1 \tag{A1.45}$$

Based on the analysis of fracture threshold energy, the total strain energy associated with each spring element is calculated as,

$$\psi_t \cdot A = \frac{1}{2} EA\,{}^{t+\Delta t}_{t}\varepsilon_{xx} \cdot u = \frac{1}{2}\frac{E}{E_0}\frac{A}{A_0}\,{}^{t+\Delta t}_{t}\varepsilon_{xx} \cdot \frac{u}{L_0} \cdot E_0 L_0 A_0 = \frac{1}{2}\tilde{E}\tilde{A}\,{}^{t+\Delta t}_{t}\varepsilon_{xx}\tilde{u} = \tilde{\psi}_t \tag{A1.46}$$

Here, A indicates the cross-sectional area of the spring element. The value of fracture threshold $\left(\psi_t\right)$ is provided in the units of J/m^2. Hence, multiplication with the cross sectional area of the spring element is very important. To satisfy the condition that $\tilde{A} = 1$ the value of A is equal to the value of A_0 must be satisfied. For the reference active particle of diameter 250nm, the reference length of each element turns out to be approximately 3.5714nm. Assuming that the reference elastic modulus is around 75GPa, the references cross sectional area can be estimated as,

$$A_0 = \frac{1}{E_0 L_0} = \frac{1}{75\times10^9 \times 3.5714\times10^{-9}} = 0.003733 m^2 \tag{A1.47}$$

Substituting this relation within the Eq. (A1.46), the normalized fracture threshold energy is obtained as,

$$\tilde{\psi}_t = \psi_t \cdot A = 5.0 \times 0.003733 = 0.018665 \approx 0.02 \tag{A1.48}$$

Similar normalization can also be applied to the other terms of the free energy functional given in Eq. (A1.42).